Shortcuts to adiabaticity for ultracold gases

Jean-François Schaff

Université de Nice-Sophia Antipolis - UFR Sciences
École doctorale de Sciences Fondamentales et Appliquées

Thèse

pour obtenir le titre de
Docteur en Sciences
de l'Université de Nice-Sophia Antipolis

Spécialité Physique Quantique

présentée et soutenue par
Jean-François Schaff

Shortcuts to adiabaticity for ultracold gases

Raccourcis aux transformations adiabatiques de gaz ultrafroids

Thèse dirigée par Guillaume Labeyrie et Patrizia Vignolo
soutenue le 30 septembre 2011 devant le jury composé de :

M.	Jean Dalibard	Président du jury
M.	Christopher J. Foot	Rapporteur
M.	Juan Gonzalo Muga	Rapporteur
M.	Anders Kastberg	Examinateur
M.	Guillaume Labeyrie	Directeur
M^{me}	Patrizia Vignolo	Co-directrice

Shortcuts to adiabaticity for ultracold gases

Raccourcis aux transformations adiabatiques de gaz ultrafroids

Jean-François Schaff

Institut non linéaire de Nice,
UMR6618, Université de Nice-Sophia Antipolis, CNRS,
1361 route des Lucioles, F-06560 Valbonne, France

December 10, 2011

Remerciements

Cette thèse est l'aboutissement d'un travail effectué à l'Institut non linéaire de Nice (INLN) entre octobre 2008 et septembre 2011. Au cours de ces trois années, j'ai eu le plaisir de faire la connaissance de nombreuses personnes qui ont, de manières diverses, contribué à la réussite de cette entreprise.

Guillaume Labeyrie et Patrizia Vignolo ont assuré la direction de cette thèse. J'ai trouvé en eux deux interlocuteurs privilégiés, toujours disponibles, et complémentaires par leurs regards d'expérimentateur et de théoricien. Je suis persuadé que cette codirection m'a été extrêmement bénéfique.

J'ai eu la chance de travailler au jour le jour avec Guillaume, toujours très présent en salle de manip. Je lui suis reconnaissant de m'avoir fait partager son amour de la physique expérimentale et de l'optique, et de m'avoir transmis, en fin pédagogue qu'il est, une part de sa grande expérience pratique. Avec lui, j'ai appris à dégager l'essentiel de problèmes qui semblent à première vue complexes, et à trouver les réponses par l'expérience. Je garde en exemple son approche résolument expérimentale de la physique. Merci Guillaume de m'avoir transmis tout cela.

Patrizia a joué un rôle crucial dans ma venue à l'INLN, et sans elle je n'aurais pas eu la chance de faire ma thèse dans ce laboratoire. Elle m'a ensuite suivi et conseillé avec beaucoup de bienveillance et de sens de la responsabilité. J'ai eu beaucoup de joie à travailler avec elle sur les problèmes de localisation, puis, ensuite, sur la théorie des raccourcis aux transformations adiabatiques. J'ai énormément profité de son expérience en théorie des gaz quantiques, et de sa disponibilité pour m'en transmettre une part. Mais Patrizia est aussi une personne exceptionnelle sur le plan humain. Sa force de caractère, sa bonne humeur permanente, et son enthousiasme à toute épreuve m'ont rendu ces trois années extrêmement riches et agréables. Merci pour tout.

Xiao-Li Song a travaillé en tant que post-doctorante sur l'expérience BEC pendant les deux premières années de ma thèse. Merci Xiao-Li d'avoir toujours su garder ta bonne humeur communicative, même dans les moments de doute. Merci à Pablo Cappuzi d'avoir tenu bon face à nos requêtes toujours changeantes de simulations pour les expériences de raccourcis. Merci à Jean-Charles Bery de l'atelier mécanique, et aux électroniciens Arnaud Dusaucy et

Jean-Claude Bernard, qui ont participé à la construction de l'expérience. Il n'y aurait pas non plus d'expérience BEC sans le soutien de toute l'équipe administrative et technique du laboratoire : Jean-Daniel Barde, Christian Taggiasco, Mathieu Barbieri, Nathalie Hamel, Isabelle Larochette, et François-Régis Huc, merci à vous tous.

Je suis infiniment reconnaissant à Juan Gonzalo Muga et à Christopher J. Foot de l'intérêt qu'ils ont témoigné pour ma thèse en acceptant d'en être les rapporteurs. Merci aussi à Jean Dalibard d'avoir présidé le jury, et à Anders Kastberg pour son rôle d'examinateur.

Merci aux "localisateurs" Nicolas Cherroret, Cord Müller, Benoit Grémaud, Tomasz Karpiuk, Christian Miniatura, et Dominique Delande de m'avoir fait partager leur expérience sur les problèmes de transport en milieu désordonné. Je suis particulièrement reconnaissant à Christian pour son soutien et sa confiance, ainsi que ses conseils avisés sur les questions de localisation et de transport cohérent.

Quelques personnes du laboratoire trouvent, au moment des remerciements, une place particulière : merci à Robin Kaiser pour sa bienveillance, son soutien, et ses conseils avisés en physique atomique et sur le domaine du refroidissement laser. Merci à William Guérin, dont les recommandations ont été précieuses sur la difficile route vers la condensation. L'INLN regroupe des théoriciens et expérimentateurs de divers domaines, ce qui est particulièrement appréciables pour les étudiants. Je suis reconnaissant à Mario Gattobigio de n'avoir pas compté le temps passé à répondre à mes nombreuses questions. Sa disponibilité et sa passion pour la physique, alliée à son intarissable culture théorique font de lui un collègue d'une valeur inestimable. Merci également à Michel Le Bellac pour ses conseils. Merci à Gian-Luca Lippi pour le rôle qu'il a joué dans ma venue à l'INLN, j'espère avoir été digne de la bourse qu'il m'a attribuée. Merci aussi à David Wilkovsky pour ses conseils, son soutien et sa confiance. Je lui souhaite bon courage pour son projet à Singapour.

Merci à tous mes camarades doctorants, ces années de thèse ont été agréables à l'intérieur comme en dehors du laboratoire grâce à vous ! Merci à Tom Bienaimé avec qui j'ai partagé mon bureau, qui a supporté mes questions incessantes et m'a fait profiter de ses réponses toujours instructives, et à Nicolas Mercadier : l'émulation et l'amitié qui s'est établie entre nous trois a été une force. Merci aussi à Maryvonne Chalony qui a été un exemple pour nous. Merci enfin à tous les autres : Marianne Corvellec, Louis Bellando, Quentin Baudouin, Axel Euverte, Laurent de Forges de Parny, Marta Wolak, Florence Haudin, Margherita Turconi, et aux post-doctorants de l'equipe de Robin, qui nous ont fait profité de leur expérience : Vera Guarrera, Giovanni Barontini, Riadh Rebhi, et Julien Chabé. J'ai éprouvé beaucoup de plaisir à faire ma thèse à vos côtés.

Cette thèse a bénéficié des corrections d'anglais de Bess Fang, merci in-

finiment ! Je lui souhaite une bonne continuation dans l'équipe d'Isabelle Bouchoule à l'Institut d'Optique.

Je tiens également à remercier, dans son ensemble, le groupe d'Optique Atomique dirigé par Alain Aspect, pour m'avoir permis de découvrir ce domaine de recherche lors de mon stage de M2. Merci en particulier à l'équipe "Pince" de l'époque : Alain Bernard, Patrick Cheinet, Philippe Bouyer, Juliette Billy et Vincent Josse. En fin de stage, Juliette m'avait pointé du doigt l'INLN, merci !

Merci enfin à mes parents et mes frères de m'avoir donné cet environnement favorable à ma construction. Merci aussi à mon partenaire Alexandre, qui m'a soutenu, a su me faire oublier mon travail quand j'en avais le plus besoin, et m'a donné tant depuis trois ans.

Je profite aussi de ces lignes pour remercier tous mes professeurs, surtout ceux du lycée Chaptal, et en particulier Pascal Brasselet qui, le premier, m'a fait découvrir la physique expérimentale.

Parce que la thèse n'est pas une fin, mais un commencement, je tiens à remercier les personnes qui m'ont fait confiance pour la suite : merci à Thorsten Schumm et Jörg Schmiedmayer de m'avoir accueilli dans leur équipe. Merci aussi à mes amis Tarik Berrada et Julia Tirler de l'aide qu'ils m'ont apportée pour l'installation en Autriche.

Vienne, Autriche, décembre 2011

Contents

Introduction

The control of quantum systems has become a major issue of modern physics. Physicists are now able to isolate simple quantum systems such as a few single atoms or ion chains, and to manipulate them with unprecedented precision [1–6]. These investigations have led to the development of the first quantum simulators [7–9], and may eventually see the birth of quantum computers [6, 10, 11]. In the past decades other systems such as electronic circuits [12] or mechanical resonators [13] — hitherto well described by classical physics — have been brought to the quantum level by various means, involving their cooling and the control of noise sources [14]. To be useful to practical applications such as quantum information processing or quantum simulation, one must be able to control these systems precisely and without inducing a decay of their coherence. This requires both a good understanding of the fundamental physics at play, and practical tools, methods, and algorithms to control their quantum state.

Within the past 15 years, ultracold gases have become model quantum objects that can be used to study a variety of effects. They have proven their ability to reproduce model systems of condensed matter physics [7, 15–17]. Ultracold gases are ideal tools to study quantum control: they are versatile, they can either be degenerate or not, they can be placed in a variety of potentials, dissipation can easily be added by using light, interactions can be tuned at will, etc. For instance, it has recently become possible to measure and control each atom of a degenerate ensemble individually [2–5].

An important parameter characterizing a given physical system in thermodynamical equilibrium is its entropy. For "isolated" systems containing a lot of particles that can be described by a time-dependent (Hermitian) Hamiltonian, the second principle of thermodynamics states that the entropy cannot decrease. If the system is initially in thermodynamical equilibrium, quantum adiabatic transformations are known to conserve the thermodynamical entropy when the final state is also an equilibrium state [18]. To that respect, such adiabatic transformations are thus "the best" one can achieve when bringing a system from an initial equilibrium state to a final one. Nevertheless these transformations generally have to be slow in order to be adiabatic, which can

be a real limit to their practical use. Indeed decoherence [14] or finite lifetimes of quantum systems are major issues of e.g. quantum computing.

In this thesis we have experimentally demonstrated transformations of a gas equivalent to quantum adiabatic transformations with respect to the initial and final states they connect, but which are not adiabatic. A consequence is that they can be performed much faster than their adiabatic counterparts. Such transformations have been named "shortcuts to adiabaticity" by Chen et al. [19] and this is the term we have kept for the title of this thesis.

This thesis

Three major themes can be found in this thesis. The first one is the practical implementation of the Bose-Einstein condensation (BEC) of a Rubidium-87 (^{87}Rb) gas. When I arrived at the Nonlinear Institute of Nice[1] (INLN) in October 2008, the Bose-Einstein condensate experiment, so far constructed by Guillaume Labeyrie alone, was not functional yet, and a lot of effort has been dedicated to obtaining our first BECs 11 months after my arrival. We were three people working on the experiment: Guillaume Labeyrie, Xiao-Li Song who worked with us as a postdoc for two years and had arrived one month earlier in the group, and I. We were helped by the electronic technicians of the laboratory Arnaud Dusaucy and Jean-Claude Bernard, and by the mechanical engineer Jean-Charles Bery. Such experiments have become standard in the past few years, and many groups around the world are now able to produce BECs. Nevertheless they are still quite challenging from an experimental point of view, especially because nobody of our group had had experience on a BEC setup. Since more than half of my time at INLN was dedicated to make it work, details on its construction are naturally included in this thesis. They are also there to stay as a reference for future researchers working on the setup.

During the construction of the experiment, I also worked on theoretical aspects with Patrizia Vignolo in order to prepare the experiments we had in mind. We wanted to study multiple scattering of matter waves in random potentials. I thus worked on a simple model of correlated disorder responsible for the partial breakdown of Anderson localization in a one-dimensional geometry.

When we were finally able to make the apparatus work, we could start investigate new physics. The study of shortcuts to adiabaticity arose from a very technical consideration: the transfer of the cloud from the magneto-optical trap to the quadrupole trap induces heating (and actually a decrease of phase-space density), and I wanted to try to optimize this transfer. I had seen the article of Chen et al. [19] on the arXiv and I thought I could find

[1] Institut non linéaire de Nice, UMR6618, CNRS, Université de Nice-Sophia Antipolis.

useful references in it. I realized we could also simply do the experiment if we were able to adapt it with gravity, which was not included in the original treatment of Chen et al. [19]. This was the beginning of a team work with Patrizia Vignolo — and later Pablo Capuzzi — on the theoretical side, and Guillaume and Xiao-Li on the experimental side.

Outline

This thesis is divided into four chapters: the first one contains the background needed to address the physics of Bose-Einstein condensates of neutral atoms, both from the theoretical and experimental point of view. Its first section gives a remainder of basic statistical physics. The stress is put on the results providing experimental tools. The basic equations useful to the description of BECs in various geometries are introduced. The most important techniques used to produce BECs are presented: laser cooling and radio-frequency evaporative cooling in a magnetic trap.

The second chapter details the construction of the experiment and its performances for the production of BECs. It is designed to provide a snapshot of the experiment at the moment of writing this thesis, and to stay as a reference for future people working on the setup. Since this is the first thesis concerning the INLN BEC experiment, and for the sake of completeness, some parts describe the work previously done by Guillaume Labeyrie before I joined him (design of the vacuum system, electronics for the lasers, etc.). I hope these considerations will be useful to future researchers working on the experiment.

Chapter 3 contains our study of shortcuts to adiabaticity with both a very dilute normal gas, which can be considered ideal, and a dense interacting Bose-Einstein condensate. This work is both theoretical and experimental. We believes such techniques may find a broad range of applications for the control of classical and quantum systems.

The last chapter is concerned with the initial project of the team: the study of matter wave transport with BECs. It is a theoretical work performed with Patrizia Vignolo on the effect of a particular model of correlations on one-dimensional Anderson localization.

Chapter 1

Theoretical basics and experimental techniques

The purpose of this chapter is twofold. On the one hand, it gives the basic theoretical ingredients needed to describe and analyze the objects we are going to work with: trapped cold gases of neutral atoms, either classical or degenerate. On the other hand, it gives an overview of the main experimental techniques used to produce such ultracold gases, with a stress on the fundamental limits of each of them, justifying their complementary use. The discussion will often be illustrated by examples involving the ^{87}Rb atom, which is the species I worked with during my thesis.

1.1 Bose-Einstein condensation

The indistinguishability of identical particles, which is the fact that the measurable quantities should not change when the positions of any two particles are swapped, together with the laws of quantum mechanics lead to the striking fact that quantum particles can be divided into two main categories: *bosons*, for which the many-body wave function is unchanged by the exchange of two particles, and *fermions*, for which the wave function changes sign.

The spin-statistics theorem [20, 21] states that particles with half-integer spins (in units of the reduced Planck constant $\hbar = h/2\pi \simeq 1.05 \times 10^{-34}$ J.s) are fermions, whereas particles with an integer spin are bosons.

This property of fundamental particles extends to composite particles such as neutrons, protons, nuclei, neutral atoms, ions, molecules, etc., under the condition that they are not distinguishable from one another, i.e. only when they are in the same internal state.

In simple words, and using a classical picture, a consequence is that two identical neutral atoms whose nuclei have an even number of neutrons (such

that they are bosons) can be put at the same position in space and with the same velocity, pointing in the same direction (same state). On the contrary, neutral atoms with odd number of neutrons follow Pauli's exclusion principle: they cannot be in the same state, just like two electrons cannot be on the same orbital around their nucleus in an atom.

Now let us now be a little more precise on what "being in the same state" means in quantum mechanics. In classical physics, the state of a point particle is simply given by its position and momentum, i.e. by six real numbers in a given set of axes. This six-dimensional space is often called the *phase space* of the system (here just one particle). In quantum physics, the components of the position q_i and momentum p_i in a given direction $i \in \{x, y, z\}$ follow the fundamental Heisenberg uncertainty principle

$$\sqrt{\langle q_i^2 \rangle - \langle q_i \rangle^2} \times \sqrt{\langle p_i^2 \rangle - \langle p_i \rangle^2} \geq \frac{\hbar}{2}, \tag{1.1}$$

where the brackets $\langle A \rangle$ denote the average of A over, e.g., many identical experiments. The word "uncertainty" is somewhat misleading: these inequalities state that there is a *certain* spread in position and velocity. In a way, the particles are not points anymore. Consequently, phase space can be seen as divided into unit cells of volume h^3. The uncertainty principle (1.1) states that particles cannot occupy a volume of phase space less than this elementary volume. This truly revolutionary idea that phase space is divided into such unit cells was first introduced by Bose [22] in 1924 for photons. With it, he could recover the properties of a gas of photons in thermal equilibrium (black body radiation). The difference between bosons and fermions is that many bosons can be put in the same unit cell of phase space, whereas only one fermion is allowed in each unit cell.

This quantum nature will thus play an important role when there is a good chance that particles want to stand in the same place, with the same velocity. In this case they have the same energy and the system is said to be *degenerate*[1]. For instance, for air at room temperature and atmospheric pressure, the density is on the order of[2] $n_0 \sim 10^{19}$ molecules/cm^3, and the width of the velocity distribution is $\Delta v \sim 100$ m/s. This corresponds to a typical number of atoms per unit cell of phase space (this is called the *phase-space density*) $D = (h/\Delta x \Delta p)^3 = h^3 n_0/(m\Delta v)^3 \sim 10^{-6}$. In these conditions, whether particles can or cannot be in the same state will not play any role, because the system is too dilute. Consequently, the gas is well described by classical mechanics. On the contrary, if the same reasoning is applied to electrons in a piece of metal at room temperature, one gets $D \sim 1$. This means

[1] This is obviously not possible for fermions, but in this case, one talks about degeneracy when a large number of adjacent energy levels are occupied by exactly one fermion.

[2] "on the order of" will often be abbreviated by the symbol $\sim$.

that even at room temperature the electrons of a metal are behaving quantum mechanically.

On the way to Bose-Einstein condensation, the gas we manipulate is classical most of the time. For instance, we start at room temperature and very low pressure (on the order of 10^{-12} bar). The corresponding phase-space density is $D \sim 10^{-18}$. Thus, it is worth first recalling a few basic results on non-degenerate gases. For this purpose we need to use the methods of equilibrium statistical mechanics.

1.1.1 Statistical description of the gas

This section recalls the standard description, and usual results of equilibrium statistical mechanics, which can be found in many textbooks (for instance Refs. [23–26]). It is strongly based on the course of Georges and Mézard [26].

In classical mechanics, a system of N particles is characterized by its Hamiltonian $H(\{q_l, p_l\})$, containing the coordinates q_l and momenta p_l of the particles ($l \in \{1, \cdots, 3N\}$), and the dynamics is governed by $6N$ canonical Hamilton equations.

In equilibrium statistical mechanics, instead of describing the system with these $6N$ degrees of freedom, the *phase space* (the $6N$ dimensional space in which $\{q_l, p_l\}$ is a point) is assumed to be randomly populated with a given probability density function $D(\{q_l, p_l\})$. The macroscopic observables are subsequently calculated as averages over this density function.

The microcanonical ensemble

For instance, in the *microcanonical ensemble* (isolated system with a fixed total energy E), this probability density function is chosen to be

$$D(\{q_l, p_l\}) = C\,\delta[H(\{q_l, p_l\}) - E], \tag{1.2}$$

C being a normalization constant. It means that all the possible states having a total energy E are assumed to have the same probability. This assumption is known as the *postulate of equiprobability*.

In quantum mechanics, the $6N$ conjugate momenta and Hamilton equations of classical physics are replaced by a many-body wave function $\Psi(\{q_l\})$ and a single Schrödinger equation governing its evolution. In trapped systems, the spectrum is discrete and if one fixes the total energy E, it is likely that no eigenstate of H will have an energy $E_n = E$. It is thus more practical to use the constraint

$$E \leq E_n \leq E + \delta E \tag{1.3}$$

on the eigenstates of energies E_n that can be populated, where δE is small compared to the macroscopic energies, but large compared to the level spacings. For the probability p_n of finding a particle in a state of energy E_n, the postulate of equiprobability simply becomes

$$p_n = \frac{1}{W(E, \delta E)}, \tag{1.4}$$

where $W(E, \delta E)$ is the number of states satisfying the constraint (1.3).

The classical equivalent of (1.3) is

$$E \leq H(\{q_l, p_l\}) \leq E + \delta E, \tag{1.5}$$

and the probability density function that follows is

$$D(\{q_l, p_l\}) = \frac{1}{\mathcal{V}(E, \delta E)}, \tag{1.6}$$

where $\mathcal{V}$ is the volume of the fraction of phase space accessible to the system

$$\mathcal{V}(E, \delta E) \equiv \int_{E<H(\{q_l,p_l\})<E+\delta E} \prod_l \mathrm{d}q_l \mathrm{d}p_l. \tag{1.7}$$

There is actually no satisfactory classical theory of statistical mechanics because such theories lead to contradictions with thermodynamics. A striking example is the Gibbs paradox: with a classical approach the free energy and the entropy are found not to be extensive quantities.

For N indistinguishable particles, a prescription that solves this problem and enables us to still use the classical formalism is the following: the classical limit is obtained by replacing the number of states $W(E, \delta E)$ by

$$W(E, \delta E) \to \frac{\mathcal{V}(E, \delta E)}{h^{3N} N!}. \tag{1.8}$$

The terms h^{3N} corresponds to the elementary phase-space volume of a system of N particles and accounts for the finite resolution of phase space discussed above. The term $N!$ accounts for the indistinguishability of the particles: for instance when $N = 2$, a situation with the two particles at different positions is counted twice by the integral (1.7), whereas it corresponds to a unique physical situation.

It can be shown that this approach, together with Boltzmann's definition of entropy

$$S = k_B \ln W, \tag{1.9}$$

is sufficient to recover all the results of standard thermodynamics ($k_B \simeq 1.38 \times 10^{-23}$ J/K is the Boltzmann constant).

The canonical ensemble

An alternative to the microcanonical ensemble is the *canonical ensemble*. In this picture, the system under study (say system 1, N_1 particles, energy E_1) can exchange energy with another one, much bigger (system 2, $N_2 \gg N_1$ particles, energy E_2). The total energy is fixed $E = E_1 + E_2$.

The probability that system 1 is in a state of energy E_1 is

$$p(E_1) = \frac{W_2(E - E_1)}{\sum_{E_1'} W_1(E_1')W_2(E - E_1')}. \tag{1.10}$$

Writing the entropy as in Eq. (1.9), developing at first order using the fact that $E \gg E_1$, and identifying $\partial_E S_2 = 1/T_2$ one obtains the probability of a state of system 1 as

$$p = \frac{1}{Z(T)} e^{-E_1/k_B T}, \tag{1.11}$$

where $Z(T)$ is called the *partition function* of system 1 and is

$$Z(T) = \sum_n e^{-E_1^{(n)}/k_B T}, \tag{1.12}$$

where the sum is on all the states of system 1, whose energies are $E_1^{(n)}$.

The quantum mechanical expressions of these two quantities are

$$D = \frac{1}{Z} e^{-H/k_B T}, \tag{1.13}$$

$$Z = \operatorname{tr} e^{-H/k_B T}, \tag{1.14}$$

and the classical, continuous version is

$$Z = \frac{1}{h^{3N} N!} \int \prod_l \mathrm{d}q_l \mathrm{d}p_l \, e^{-\beta H(\{q_l, p_l\})}. \tag{1.15}$$

The internal energy, the entropy and the free energy are given by

$$U = \langle H \rangle = k_B T^2 \frac{\partial \ln Z}{\partial T}, \tag{1.16}$$

$$S = k_B \ln Z + k_B T \frac{\partial \ln Z}{\partial T}, \tag{1.17}$$

$$F = -k_B T \ln Z. \tag{1.18}$$

The grand canonical ensemble

In the *grand canonical* description, the system under study (system 1, N_1 particles, energy E_1) can exchange energy and particles with another, which is much bigger (system 2, $N_2 \gg N_1$ particles, energy E_2). The total energy and particle number are fixed $E = E_1 + E_2$, $N_{\text{tot}} = N_1 + N_2$.

The probability that system 1 is in a state of energy E_1 with N_1 particles is

$$p(E_1, N_1) = \frac{W_2(E - E_1, N_{\text{tot}} - N_1)}{\sum_{E_1', N_1'} W_1(E_1', N_1') W_2(E - E_1', N_{\text{tot}} - N_1')}. \tag{1.19}$$

When writing the entropy of system 2, the temperature emerges as in the canonical ensemble. The chemical potential appears as

$$\mu = -T \frac{\partial S_2}{\partial N}. \tag{1.20}$$

It plays, for the exchange of particles, a role similar to the temperature for the exchange of energy. In the microcanonical and canonical descriptions, the chemical potential is interpreted as the work one has to give to the system in order to add a particle. In the following, we will use the usual notations $\beta \equiv 1/k_B T$ and $\alpha \equiv \beta\mu$.

The probability of a state of system 1 is

$$p = \frac{1}{Z_G(\alpha, \beta)} e^{-\beta E_1 + \alpha N_1}, \tag{1.21}$$

where $Z_G(\alpha, \beta)$ is the *grand canonical partition function* of system 1,

$$Z_G(\alpha, \beta) = \sum_n e^{-\beta E_1^{(n)} + \alpha N_1^{(n)}}, \tag{1.22}$$

and where the sum is on all the possible values of N_1, and for each of them, on all the states of system 1 whose energies are $E_1^{(n)}$. Writing $Z_N(\beta)$ the canonical partition function when there are N particles, we have

$$Z_G(\alpha, \beta) = \sum_{N=0}^{\infty} e^{\alpha N} Z_N(\beta). \tag{1.23}$$

The number of particles, the internal energy and the entropy are given by

$$N = \langle N_1 \rangle = \frac{\partial \ln Z_G}{\partial \alpha}, \tag{1.24}$$

$$U = \langle H \rangle = -\frac{\partial \ln Z_G}{\partial \beta}, \tag{1.25}$$

$$S = k_B \left(\ln Z_G + \beta U - \alpha N \right). \tag{1.26}$$

1.1.2 The classical gas

In a trap, the Hamiltonian reads

$$H = \sum_{j=1}^{N} \left[\frac{\mathbf{p}_j^2}{2m} + U(\mathbf{q}_j) \right] + V(\mathbf{q}_1, \cdots, \mathbf{q}_N), \tag{1.27}$$

where U is any trapping potential ($\lim_{|\mathbf{q}|\to\infty} U(\mathbf{q}) = +\infty$), and V represents the interactions between the particles.

In the canonical ensemble, the probability of finding a particle in a region of phase space of infinitesimal volume about the point $(\mathbf{q}_1, \cdots, \mathbf{q}_N, \mathbf{p}_1, \cdots, \mathbf{p}_N)$ is

$$\frac{1}{Z} \exp\left[-\beta H\right] \prod_j \mathrm{d}\mathbf{q}_j \mathrm{d}\mathbf{p}_j. \tag{1.28}$$

Performing the integration on all the position variables and all the momenta but one, we obtain the single-particle velocity distribution

$$g(\mathbf{v}) = \left(2\pi \frac{k_B T}{m} \right)^{-3/2} \exp\left[-\frac{m\mathbf{v}^2}{2k_B T} \right]. \tag{1.29}$$

This is the Maxwell-Boltzmann distribution. In particular, it does not depend on the interaction term, nor on the shape of the trap.

This provides us with a first experimental tool: for a *classical gas* the temperature is related to the root-mean-square (rms) width σ_v of the velocity distribution along any axis by

$$\sigma_v = \sqrt{\frac{k_B T}{m}}. \tag{1.30}$$

It is interesting to notice that this is a universal property of a classical ensemble of particles (when it can be described by such an H) which comes from the fact that $\exp[-\beta \times (\text{kinetic energy})]$ and $\exp[-\beta \times (\text{potential energy})]$ commute. It means that *non-Gaussian velocity distributions in the trap will be signatures of quantum behaviors.*

The ideal gas

Throughout the experimental cycle, the density and the temperature vary by orders of magnitude, but the gas is always very dilute (cf. Sec. 1.1.4). This condition, together with being far from degeneracy, allows the gas to be well described by the ideal gas model, upon which interactions are added in a somewhat ad hoc fashion. For an ideal gas, the interaction term is removed

$$V(\mathbf{q}_1, \cdots, \mathbf{q}_N) = 0. \tag{1.31}$$

A direct consequence is that the density profile, obtained by integrating (1.28) over all momenta and all positions but one (and normalizing the obtained density function to N instead of 1), directly reflects the shape of the trapping potential:

$$n(\mathbf{q}) = n_0 \exp\left[-\frac{U(\mathbf{q})}{k_B T}\right]. \tag{1.32}$$

For instance, for a harmonic confinement (angular frequency ω_{trap}), the density is Gaussian with a rms width

$$\sigma_q = \sqrt{\frac{k_B T}{m\omega_{\text{trap}}^2}}. \tag{1.33}$$

For a linear trap (i.e. $U(\mathbf{q}) \propto |\mathbf{q}|$, or $U(\mathbf{q}) = f_x|x| + f_y|y| + f_z|z|$), the width σ_q scales as T. Once again, the width in situ (in the trap) gives a measurement of the temperature.

The density at the center of a three-dimensional (3D) harmonic trap is given by the fact that the integral of (1.32) is the number of atoms. As a function of N and T, which are experimentally accessible quantities, it reads

$$n_0 = \left(\frac{m\bar{\omega}^2}{2\pi k_B}\right)^{3/2} N T^{-3/2}, \tag{1.34}$$

where $\bar{\omega} = (\omega_x \omega_y \omega_z)^{1/3}$ is the geometrical average of the angular frequencies of the harmonic trap. This expression can also be written as

$$n_0 \lambda_{\text{dB}}^3 = \left(\frac{\hbar\bar{\omega}}{k_B T}\right)^3, \tag{1.35}$$

where the *thermal de Broglie wavelength* $\lambda_{\text{dB}} = \sqrt{2\pi\hbar^2/mk_B T}$ has been introduced. It can be seen as a measure of the typical spatial extent of the atomic wave packets due to the thermal motion of particles. The right hand side of Eq. (1.35) is thus a dimensionless number measuring the ratio of the volume occupied by the atomic wave packets, to the volume in which one atom is found. It is actually the phase-space density $D = n_0 \lambda_{\text{dB}}^3$, and classically, it is seen to be close to 1 when $T \sim \hbar\bar{\omega}/k_B$. In Sec. 1.1.3 we will see that the quantum nature of particles dramatically modifies this and that the system can actually be degenerate below a critical temperature $T_c \gg \hbar\bar{\omega}/k_B$.

Time of flight of an ideal gas

We have seen that the width of the cloud in situ is a measurement of the temperature. Nevertheless, it is sometimes difficult to measure, either because the cloud is too small to be resolved, or because of other effects such as the

presence of a magnetic field. It is thus often more convenient to release the cloud from the trap and monitor its expansion. This technique is called the *time of flight*. In the experiments, we are able to manipulate the trapping potential and in particular, to turn it off abruptly. In a freely falling frame of reference, the cloud has a ballistic expansion. If the trap is harmonic, after a time t_f of free expansion, the density is the convolution of the initial Gaussian density, with the initial Gaussian velocity distribution. Consequently, it keeps a Gaussian profile with a rms width

$$\sigma_{\rm tof}(t_f) = \sqrt{\sigma_q^2 + \frac{k_B T}{m} t_f^2}. \tag{1.36}$$

Fitting this curve yields the temperature. If the trap is not harmonic, in the limit $\sigma_{\rm tof}(t_f) \gg \sigma_{\rm tof}(0)$, the slope of the curve $\sigma_{\rm tof}^2(t_f)$ vs t_f^2 is $\sigma_v^2 = k_B T/m$ which still yields the temperature.

1.1.3 Bose-Einstein condensation in harmonic traps

In this section, we consider N indistinguishable non-interacting bosons in a harmonic trap. Bose-Einstein statistics is recalled [22] together with its striking consequence discovered by Einstein [27]: the accumulation of most of the particles in the ground state when the temperature is decreased below a critical temperature $T_c \gg \hbar\bar{\omega}/k_B$.

Bose-Einstein statistics

For N bosons at sufficiently low phase-space density such that degeneracy can be neglected, the particles all have single-particle wave functions (SPW) φ_k $(1 \leq k \leq N)$ orthogonal to each other, and the many-body wave function can be written as

$$\Psi(\mathbf{q}_1, \cdots, \mathbf{q}_N) = \frac{1}{\sqrt{N!}} \sum_P \varphi_1(\mathbf{q}_{P(1)}) \times \cdots \times \varphi_N(\mathbf{q}_{P(N)}), \tag{1.37}$$

where the sum is over all the permutations P of $\{1, \cdots, N\}$ and is here to guarantee that Ψ is symmetric with respect to the exchange of particles. There are $N!$ permutations which explains the normalization factor. This shows that, because the particles are indistinguishable, the number of accessible states is dramatically reduced, by a factor of $N!$. Of course, any linear combinations of such Ψ would also be valid.

This expression also underlines how tricky writing wave functions can become. Indeed when a few particles are described by the same SPW, the normalization becomes much more complicated. An alternative to representing the system with its wave function is to use the *Schrödinger field* formalism (also

called *second quantization* formalism, see e.g. Ref. [28, Chap. 14] or Ref. [29]). In this case, the state is given by the number of particles n_k in each eigenstate ψ_k ($k \in \mathbb{N}$) of the single-particle Hamiltonian. In the microcanonical ensemble, the constraints satisfied by this sequence are $\sum_k n_k = N$ and $\sum_k n_k \epsilon_k = E$ (the ϵ_k's are the eigenenergies associated to the ψ_k). These two constraints are not convenient to work with and it is actually simpler to work in the grand canonical ensemble instead of the microcanonical one.

A grand canonical partition function can be derived when $\mu < \epsilon_0$, ϵ_0 being the energy of the single-particle ground state. It is then given by (1.23) and reads

$$\ln Z_G = -\sum_{k=0}^{\infty} \ln\left[1 - \exp(\alpha - \beta\epsilon_k)\right]. \tag{1.38}$$

The corresponding probability to find a particle in the kth eigenstate (the *occupation factor*) is obtained as

$$f_k = \frac{1}{e^{\beta(\epsilon_k - \mu)} - 1}. \tag{1.39}$$

This constitutes the *Bose-Einstein statistics*. It is indeed positive for all k because $\mu < \epsilon_0$.

Continuous limit, density of states

It is sometimes convenient to use continuous functions instead of discrete energy levels. This can be done by introducing the *density of states* $\mathcal{N}(\epsilon)$ (DOS), defined such that $\int_{E_1<\epsilon<E_2} \mathcal{N}(\epsilon)\mathrm{d}\epsilon$ coincides with the number of single-particle eigenstates ψ_k of energies $E_1 < \epsilon_k < E_2$ as soon as $E_2 - E_1$ is sufficiently large compared to the level spacing. In this case, discrete sums are replaces by integrals.

For instance, the average number of particles becomes

$$N = \sum_k f_k \simeq \int \mathcal{N}(\epsilon) f(\epsilon)\mathrm{d}\epsilon, \tag{1.40}$$

where $f(\epsilon)$ is a continuous version of (1.39):

$$f(\epsilon) = \frac{1}{e^{\beta(\epsilon - \mu)} - 1}. \tag{1.41}$$

For instance, the DOS of a 3D harmonic trap is [29]

$$\mathcal{N}(\epsilon) = \frac{\epsilon^2}{2(\hbar\bar{\omega})^3}. \tag{1.42}$$

Bose-Einstein condensation: saturation of the excited states

The maximal possible number of atoms in the excited states $N_{\max} = \max[N - N_0]$ (we define $N_0 \equiv n_0$ the occupation factor of the single-particle ground state ψ_0) can be calculated by using the continuous approximation. It is reached when the chemical potential has the same value as the ground state energy $\mu = \epsilon_0$. This yields [30]

$$N_{\max} = \zeta(3) \left(\frac{k_B T}{\hbar \bar{\omega}} \right)^3, \tag{1.43}$$

ζ being the Riemann zeta function[3], $\zeta(3) \simeq 1.202$. This number is seen to be finite, and to depend only on the temperature and trap geometry. It means that if the temperature is fixed and particles are added one after another, at some point all the added particles will not be able to be in either of the excited states. At this point, the excited states are *saturated*, and the consequence is that any additional particle has to be added to the lowest energy state. This saturation corresponds to the *Bose-Einstein condensation* of the gas[4]. Obviously, this also applies if N is fixed and T (initially high) is decreased: when $N_{\max}$ reaches N (from above), $N - N_{\max}(T)$ particles have to gather in the single-particle ground state.

The relationship between the total number of atoms N_c and the temperature T_c when this starts to happen is simply obtained by setting $N_c = N_{\max}$ ($N_0 = 0$) and $T = T_c$ in Eq. (1.43). This yields the *critical temperature*

$$T_c = \frac{\hbar \bar{\omega} N_c^{1/3}}{k_B \zeta(3)^{1/3}} \simeq 0.94 \frac{\hbar \bar{\omega}}{k_B} N_c^{1/3}. \tag{1.44}$$

For instance, for $N \sim 10^6$ atoms, we have $k_B T_c / \hbar \bar{\omega} \sim 100$. It is seen that contrary to the classical case in which D was found to approach unity when $k_B T_c / \hbar \bar{\omega} \sim 1$ [cf. Eq. (1.35)], this happens for much higher values of T. In the following chapters we will see that the typical number of atoms is $N \sim 10^6$, and the trap frequency is $\bar{\omega} = 2\pi \times 100$ rad/s. This corresponds to critical temperatures in the range $T_c \sim 100$ nK.

The proportion of atoms in the ground state is often called the *condensate or condensed fraction*. It is obtained from Eqs. (1.43) and (1.44) as

$$\frac{N_0}{N} = 1 - \left(\frac{T}{T_c} \right)^3, \tag{1.45}$$

[3]The Riemann zeta function is defined by $\zeta(s) \equiv \sum_{m=1}^{\infty} 1/m^s$.

[4]Notice that $N_{\max}$ is finite for a 3D harmonic trap, but could a priori be infinite with other trap geometries (i.e. different density of states). For instance, this is the case for strictly 2D box potentials and 1D harmonic traps because in both cases the density of state is a constant [29]. Condensation cannot occur in such traps.

for $T \leq T_c$, $N_0/N = 0$ otherwise.

Another instructive quantity to calculate is the density at the trap center. The number of atoms is given by Eq. (1.40) and reads

$$N = \left(\frac{k_B T}{\hbar\bar{\omega}}\right)^3 g_3(z), \tag{1.46}$$

where $z = \exp[\beta\mu]$ is called the *fugacity*, and g_3 is the Bose function[5]. When the system is far from degeneracy, the central density is simply $n_0 = N/(\sqrt{2\pi}\bar{\sigma})^3$, where $\bar{\sigma}$ is the geometrical average of the rms widths of the cloud along the three axes, given by Eq. (1.33). This gives

$$n_0 \lambda_{\mathrm{dB}}^3 = g_3(z). \tag{1.47}$$

where the thermal de Broglie wavelength λ_{dB} was introduced in Sec. 1.1.2. Here n_0 is the central density only when the system is far from degeneracy. The gas condenses when $z \to 1$, i.e. when $n_0\lambda_{\mathrm{dB}}^3 \to g_3(1) \simeq 1.202$. One thus sees that *condensation occurs when the typical inter-atomic distance is comparable to the extent of the atomic wave packets, i.e. when the wave packets start to overlap.*

1.1.4 Interactions

In practice, there are collisions, hence a cold and trapped ^{87}Rb gas is not an ideal gas. This is even an essential ingredient of condensation experiments because collisions are needed during evaporative cooling to bring the cloud back to equilibrium (cf. Sec. 1.4.2).

"Real potential" and pseudopotential

The interaction potential between two identical atoms has the typically shape of Fig. 1.1. It is strongly repulsive at short distances, because the electron clouds repel each other, attractive around a typical distance r_0 (bound states of this potential well correspond to molecules), and attractive for large distances $r \gg r_0$, with a $1/r^6$ dependence arising from induced dipole-dipole interactions (van der Waals potential).

In Sec. 1.4 we will see that we magnetically trap the atoms in the $|F = 2, m_F = +2\rangle$ sublevel of the ground state. The appropriate potential is thus the curve marked with "2 + 2" in the inset of Fig. 1.1. In the following discussion, we assume that the colliding atoms stay in the same internal states during the collision, which simplifies the collision problem.

[5] Also called Bose-Einstein integral, or polylogarithm function (by mathematicians), it is defined by $g_u(z) \equiv \frac{1}{\Gamma(u)}\int_0^\infty \frac{x^{u-1}}{z^{-1}e^x - 1}\mathrm{d}x = \sum_{m=1}^\infty z^m/m^u$. $\Gamma(u) = \int_0^\infty t^{u-1}e^{-t}\,\mathrm{d}t$ is the gamma function. In $z = 1$ the Bose function takes the value of the Riemann zeta function $g_u(1) = \zeta(u)$.

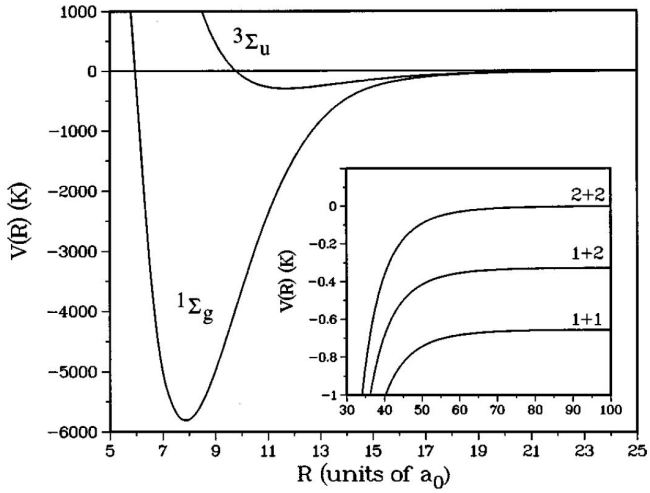

Figure 1.1: Figure of Weiner and Julienne [31] showing the "real" interaction potential of two ^{87}Rb atoms. The horizontal scale is the distance r between the two atoms in units of the Bohr radius $a_0 \simeq 0.53$ Å. The vertical one is the potential divided by k_B in K. The inset shows the potentials for large distances when the two atoms are either in the same hyperfine state $F = 1$ (curve marked "$1 + 1$") or $F = 2$ (curve "$2 + 2$"), or when there is one atom in each state (curve "$1 + 2$").

Scattering theory In quantum mechanics, collisions between particles are properly described by scattering theory [32]. One considers incoming wave packets scattered by the interatomic potential of Fig. 1.1. One defines the *differential cross-section* $\sigma(\theta, \varphi)$ of the collision by the relation $\mathrm{d}n = F_I \sigma(\theta, \varphi)\mathrm{d}\Omega$, counting the number $\mathrm{d}n$ of particles scattered per unit time in a given direction of space[6] characterized by the two angles (θ, φ) and a solid angle $\mathrm{d}\Omega$, F_I being the incident flux. The *scattering cross-section* is then obtained by integrating $\sigma(\theta, \varphi)$ over 4π steradians: $\sigma = \int \sigma(\theta, \varphi)\mathrm{d}\Omega$.

As often, it is more convenient to work in Fourier space. Far from the scatterer ($r \gg r_0$), the scattered wave function is [32]

$$v_k^{\mathrm{scat}}(\mathbf{r}) \sim_{\mathbf{r}\to\infty} e^{ikz} + f_k(\theta, \varphi)\frac{e^{ik\mathbf{r}}}{r}, \tag{1.48}$$

where the e^{ikz} is the incoming plane wave, and the second term is the scattered wave which propagates radially. The problem is to find the *scattering amplitude* $f_k(\theta, \varphi)$ characterizing the process. The differential scattering cross-section for a given energy (given k) is simply $\sigma(\theta, \varphi) = |f_k(\theta, \varphi)|^2$.

[6] Of course the particles which are still in the incident mode after the collision are not counted in $\mathrm{d}n$.

The scattering problem is simplified by the fact that the potential is central because this leads to the conservation of the orbital angular momentum $\mathbf{L}$ (quantum numbers l and m) during a collision. A consequence is that the wave functions can be decomposed as a linear combination of products of spherical harmonics and radial wave functions, and that the scattering amplitude is independent of φ [32]. One can show that it reads [33]

$$f_k(\theta) = \frac{1}{2ik} \sum_{l=0}^{\infty} (2l+1) \left(e^{2i\delta_l} - 1 \right) P_l(\cos\theta), \tag{1.49}$$

where the *phase shifts* $\delta_l(k)$ (defined modulo π) have been introduced, and the P_l's are the Legendre polynomials.

If the two colliding atoms are identical bosons, the wave functions have to be symmetric with respect to the exchange of positions. This restricts the acceptable solutions to even values of l and modifies the expression of the differential scattering cross-section: $\sigma(\theta) = |f_k(\theta) + f_k(\pi - \theta)|^2$ [33].

Another simplification comes from the fact that collisions occur at low energy $k \to 0$. The terms corresponding to $l \neq 0$ in (1.49) become negligible compared to the term $l = 0$, that is, *the scattering becomes isotropic*[7]. In this case one speaks about "s-wave scattering" because the only partial wave contributing to scattering is the s-wave ($l = 0$). The scattering cross-section then becomes

$$\sigma = 8\pi a_s^2, \tag{1.50}$$

where the *zero-energy scattering length* a_s is

$$a_s \equiv - \lim_{k \to 0} \frac{\tan \delta_0(k)}{k} = - \left[\frac{\mathrm{d}\delta_0(k)}{\mathrm{d}k} \right]_{k=0}. \tag{1.51}$$

For ^{87}Rb, the temperature below which only s-wave scattering occurs has been measured to be about 300 μK [34–36]. We will see that the temperature is below this value during most of the experimental cycle.

Pseudopotential Since the real potential $V(\mathbf{r})$ may be complicated (or even unknown) it is modeled by an effective potential V_{eff} yielding the same physics, i.e. the same scattering length for a given range of energy (in our case $E = k_B T \to 0$). The simpler *pseudopotential* one can think of is a "point scatterer" of the form

$$V_{\text{eff}}(\mathbf{r}) = g_{3\text{D}} \delta(\mathbf{r}), \tag{1.52}$$

where $g_{3\text{D}}$ is called the *interaction coupling constant*. Mathematical difficulties can arise from the use of a δ function (see e.g. Ref. [37]), in which case any

[7] Cf. e.g. Ref. [33] for a discussion of the validity of this statement, in particular the fact that only s-wave scattering occurs at low energy is not true for all central potentials.

other potential resulting in the same scattering length can be used, for instance Huang's pseudopotential $\tilde{V}_{\text{eff}}(\mathbf{r}) = g_{3\text{D}}\delta(\mathbf{r})\partial_r(r\cdot)$ [38] (see also Ref. [33] for a discussion on these pseudopotentials).

For this approach to be consistent, the expression of $g_{3\text{D}}$ must be [33]

$$g_{3\text{D}} = \frac{4\pi\hbar^2 a_s}{m}, \tag{1.53}$$

where a_s is the measured scattering length, and σ is still given by (1.50).

Of course, this approximation only reproduces the physics partially: it is only valid about $k \simeq 0$ (the relevant criterion being $ka_s \ll 1$), short-range correlations are not properly accounted for by this effective potential, other effects such as Efimov physics (three-body interaction) are not described by this effective theory, etc. In an instructive set of lectures, Lepage [39] shows how more sophisticated effective theories can be constructed to reproduce the experimental results.

It is remarkable that, depending on the details of the real potential, the zero-energy interaction coupling constant $g_{3\text{D}}$ can either be positive or negative, depending on the sign of the scattering length. This means that the effective interaction potential (1.52) can either be attractive ($a_s < 0$), repulsive ($a_s > 0$), or even vanishing ($a_s = 0$). This is exploited in Feshbach resonances: the potential can be deformed with external fields (often a static magnetic field) resulting in the modification of the phase shifts and of the scattering length.

In this thesis, we have worked with ^{87}Rb spin polarized in the $|5^2S_{1/2}, F = 2, m_F = +2\rangle$ state, for which the s-wave scattering length was measured to be $a_s \simeq 110\, a_0$ [34, 36, 40].

Collision rate

For a non-degenerate homogeneous gas with a density n_0, the elastic collision rate is [41]

$$\gamma_{\text{el}} = n_0 \sigma \bar{v}\sqrt{2}, \tag{1.54}$$

where $\bar{v} = \sqrt{8k_BT/\pi m}$ is the average thermal velocity. $\bar{v}\sqrt{2}$ is the average relative velocity between atoms. σ is the zero-energy s-wave scattering cross-section introduced above. In a trap, this gives the collision rate at the center, where the density is n_0. To obtain the cloud-averaged collision rate, one has to replace n_0 by the average density $\bar{n} = \int n^2(\mathbf{q})\,\mathrm{d}\mathbf{q}/N$. For instance, for a harmonic trap, the result is $\bar{n} = n_0/2\sqrt{2}$.

For ^{87}Rb in the $|F = 2, m_F = +2\rangle$ state at $T = 1$ μK, $\gamma_{\text{el}} = 1$ s^{-1} for $n_0 \simeq 5 \times 10^{10}$ atoms/cm^3.

Influence of interactions

In the following chapters we will see that we work in the *dilute regime*[8] characterized by $n_0|a_s|^3 \ll 1$. In this regime, interactions can sometimes be neglected. For instance, the critical temperature is just reduced by a few percents when the interaction is repulsive [30, 42]. On the contrary, in the following section we will see that interactions strongly affect the shape and the expansion of condensates released from the trap. They are also essential to superfluidity [43].

The results of Sec. 1.1.2 concerning the expansion from the trap during a time of flight were derived assuming no interactions, and indeed, interactions also modify the expansion, even when the cloud is non-degenerate. We observed such deviations which we generally neglected. They were studied in detail by Gerbier [44].

1.2 Mean field description of Bose-Einstein condensates

In principle, the state of N trapped bosons is fully described by the many-body wave function $\Psi(\mathbf{q}_1, \cdots, \mathbf{q}_N)$, which must be symmetric with respect to the exchange of any two particles. In the absence of interactions, the ground state is

$$\Psi(\mathbf{q}_1, \cdots, \mathbf{q}_N) = \prod_{j=1}^{N} \psi_0(\mathbf{q}_j) \tag{1.55}$$

which is indeed symmetric. Here, ψ_0 is the single-particle ground state. Under these conditions ($T = 0$, no interactions), the system is thus trivial because it is equivalent to a single particle. The wave nature is thus preserved, but quantum fluctuations are neglected and the system is somehow just like a classical field [the wave equation being the Schrödinger equation on $\psi_0(\mathbf{q}_j)$].

This approach can be generalized to the dilute case, as presented in the following section.

1.2.1 The Gross-Pitaevskii equation

For the reasons explained in Sec. 1.1.4, the interactions can be modeled by a pseudopotential

$$V(\mathbf{q}_1, \cdots, \mathbf{q}_N) = \sum_{j<k} g_{3\mathrm{D}} \delta(\mathbf{q}_k - \mathbf{q}_j), \tag{1.56}$$

where $g_{3\mathrm{D}} = 4\pi\hbar^2 a_s/m$ is the interaction coupling constant, expressed in terms of the atomic mass m and the zero-energy scattering length a_s.

[8] Also called "weakly interacting regime".

Taking the non-interacting case as a guide, the wave function is written as in (1.55), but this time, ψ_0 is not the single-particle ground state, but is left unknown (*Hartree approximation*). We will thus write it ψ instead of ψ_0. At this point, the expected value of the energy $E = \langle\Psi|H|\Psi\rangle$ is considered as a functional of this unknown function ψ. The state of this form having the lowest energy is found by minimizing this functional under the constraint that ψ is normalized: $\int |\psi(\mathbf{q})|^2 \mathrm{d}\mathbf{q} = 1$ (see for instance [45]). The Euler-Lagrange equation satisfied by ψ is called the Gross-Pitaevskii equation (GPE):

$$\mu\,\psi(\mathbf{q}) = \left[-\frac{\hbar^2}{2m}\Delta + U(\mathbf{q}) + g_{3\mathrm{D}}N|\psi(\mathbf{q})|^2\right]\psi(\mathbf{q}). \tag{1.57}$$

The energy μ is the Lagrange multiplier of this minimization problem. To obtain (1.57), the approximation $N-1 \simeq N$ has been used. It is valid because we always deal with large clouds containing at least $N \sim 10^4$ atoms.

This approach can be generalized to the time-dependent problems to obtain a time-dependent version which reads [46]

$$i\hbar\frac{\partial\psi(\mathbf{q},t)}{\partial t} = \left[-\frac{\hbar^2}{2m}\Delta + U(\mathbf{q}) + g_{3\mathrm{D}}N|\psi(\mathbf{q},t)|^2\right]\psi(\mathbf{q},t). \tag{1.58}$$

The effective particle described by $\psi(\mathbf{q},t)$ is seen to satisfy Schrödinger-like equations [Eqs. (1.57) and (1.58)], containing the usual kinetic energy term (second derivative with respect to the position) and trapping potential, but with an additional nonlinear term, which looks like a potential energy involving the density ($N|\psi(\mathbf{q},t)|^2$). It accounts for the mean field interaction with the other particles.

1.2.2 Thomas-Fermi approximation

From Eq. (1.57) it is seen that the energy of the trapped gas can be split into three terms:

1. the kinetic energy of the cloud

$$E_{\mathrm{k}} = N\frac{\hbar^2}{2m}\int |\nabla\psi|^2 \mathrm{d}\mathbf{q}, \tag{1.59}$$

2. its trapping energy

$$E_{\mathrm{trap}} = N\int U|\psi|^2 \mathrm{d}\mathbf{q}, \tag{1.60}$$

3. and its interaction energy

$$E_{\mathrm{int}} = \frac{N}{2}\int g_{3\mathrm{D}}N|\psi|^4 \mathrm{d}\mathbf{q}. \tag{1.61}$$

From the assumption that the interactions do not dramatically modify the wave function (it is thus expected to be close to a Gaussian with a typical width $\bar{a}_{\rm ho} = \sqrt{\hbar/m\bar{\omega}}$) one can evaluate the ratio of the interaction energy to the kinetic energy as [30]

$$\frac{E_{\rm int}}{E_{\rm k}} \propto N\frac{|a_s|}{\bar{a}_{\rm ho}}. \tag{1.62}$$

In our experiments, this is generally very large (for the experiments presented in this thesis this is always $> 10^3$) and despite the fact that the gas is dilute[9] ($n_0|a_s|^3 \ll 1$), interactions are dominant in the trap.

In this limit of negligible kinetic energy, known as the *Thomas-Fermi (TF) limit*, there is a simple solution for the stationary GPE (1.57):

$$\psi(\mathbf{q}) = \left(\frac{\mu - U(\mathbf{q})}{g_{\rm 3D}N}\right)^{1/2}, \tag{1.63}$$

where $\mu \geq U$, and $\psi = 0$ otherwise.

A few useful formulas in the case of harmonic traps

For a harmonic trap with angular frequencies $\omega_x, \omega_y, \omega_z$ (geometric average $\bar{\omega}$), the density is [$\mathbf{q} = (x, y, z)$]:

$$n(\mathbf{q}) = N|\psi(\mathbf{q})|^2 = n_0\left[1 - \left(\frac{x}{R_x}\right)^2 - \left(\frac{y}{R_y}\right)^2 - \left(\frac{z}{R_z}\right)^2\right], \tag{1.64}$$

where this is positive, and $n(\mathbf{q}) = 0$ otherwise. The condensate thus assumes the shape of an inverted parabola. The R_i's are called the *TF radii* of the condensate. Their expressions in terms of the number of atoms and the trap frequencies are

$$\forall i \in \{x, y, z\},\ R_i = \left(15N\frac{a_s\hbar^2\bar{\omega}^3}{m^2\omega_i^5}\right)^{1/5}. \tag{1.65}$$

The chemical potential μ is obtained from the normalization of the wave function and reads

$$\mu = \frac{1}{2}\hbar\bar{\omega}\left(15Na_s\sqrt{\frac{m\bar{\omega}}{\hbar}}\right)^{2/5}. \tag{1.66}$$

In experiments, we actually measure the column density [integration of $n(\mathbf{q})$ along one of the eigenaxes]

$$\tilde{n}(x, y) = \int N|\psi(x, y, z)|^2 dz = \frac{4}{3}n_0R_z\left[1 - \left(\frac{x}{R_x}\right)^2 - \left(\frac{y}{R_y}\right)^2\right]^{3/2}. \tag{1.67}$$

[9] I recall that the term "weakly interacting" is also commonly used.

The density profile obtained can be fitted by this 2D function. As a function of the fitting parameters $\tilde{n}_0 = 4n_0R_z/3$, R_x and R_y, the number of atoms is

$$N = \frac{2\pi}{5}\tilde{n}_0 R_x R_y. \tag{1.68}$$

It is sometimes more convenient to numerically integrate Eq. (1.67) before fitting (in practice this corresponds to summing the absorption images in one dimension) to obtain the twice integrated density

$$n_{1\mathrm{D}}(x) = \int N|\psi(x,y,z)|^2 dydz = \frac{\pi}{2} n_0 R_y R_z \left[1 - \left(\frac{x}{R_x}\right)^2\right]^2. \tag{1.69}$$

In this case the fitting parameters are $n_{1\mathrm{D}}(0) = \pi n_0 R_y R_z/2$ and R_x, and N reads

$$N = \frac{16}{15} n_{1\mathrm{D}}(0) R_x. \tag{1.70}$$

Finally, a last integration yields the number of atoms as a function of the central density and the TF radii

$$N = \frac{8\pi}{15} n_0 R_x R_y R_z. \tag{1.71}$$

As a function of the trap frequencies and N, the central density reads

$$n_0 = \frac{1}{\pi}\left(\frac{15}{128\sqrt{2}}\right)^{2/5}\left(N\frac{m^3\bar{\omega}^3}{\hbar^3 a_s^{3/2}}\right)^{2/5}. \tag{1.72}$$

The relation between the rms width of the density profile σ_i and the TF radius R_i ($i \in \{x,y,z\}$) is $R_i/\sigma_i = \sqrt{7}$.

1.2.3 Collective excitations

The collectives excitations of the gas resulting from an abrupt modification or a controlled modulation of a parameter can give some insight of the system. The simplest parameter that can be changed is the trapping potential which is generally harmonic. This has been the subject of intense studies very soon after the realization of the first BECs in 1995, both in theory [47–50] and in experiments [51–54]. For instance, the so called scissors mode was used to "probe the superfluidity" of BECs [55–57]. More recently the scattering length of a BEC was modulated to study the resulting collective modes [58], and the breathing mode of a unitary Fermi gas with imbalanced spin populations was used as a weighing scales to measure the effective mass of the Fermi polaron, a quasi-particle of the system [59]. Finally, it is worth mentioning that collective modes occur in a variety of physical systems, ranging from colloidal particles, to astrophysical systems [60].

In this section we only address the dipole, breathing, and scissors modes which are studied and revisited in the third chapter of this thesis.

Kohn's theorem and the dipole mode

We will only deal with harmonic potentials, which greatly simplifies the analysis. Indeed, in such traps the motion of the center of mass and of the "internal" degrees of freedom are not coupled, regardless of the binary interaction. This remarkable feature of harmonic confinements was discovered by Kohn [61] in the context of the cyclotron frequency of electrons in metals, and is commonly named Kohn's theorem. The Hamiltonian has the form[10]

$$H = \sum_{j=1}^{N} \left[\frac{\mathbf{p}_j^2}{2m} + U(\mathbf{q}_j, t) \right] + \sum_{j<l} V(\mathbf{q}_j - \mathbf{q}_l), \tag{1.73}$$

where V is any interaction between two particles. U is a time-dependent harmonic potential, that is, any second order polynomial in $\mathbf{q}$. For instance

$$U(\mathbf{q}, t) = \frac{1}{2} m \left[\omega_\perp^2(t) \left(x^2 + z^2 \right) + \omega_\parallel^2(t) y^2 \right] + mgz. \tag{1.74}$$

Kohn's theorem states that the system is equivalent to two independent systems:

1. a single particle in the potential $U(\mathbf{q}, t)$,
2. a system of $N-1$ interacting particles in a time-dependent harmonic potential whose center is not moving.

This result is obtained by defining the center of mass position and momentum operators $\mathbf{Q} = \sum_j \mathbf{q}_j / N$ and $\mathbf{P} = \sum_j \mathbf{p}_j$ and by a canonical transformation using the Jacobi coordinates $(\boldsymbol{\varrho}_j, \boldsymbol{\pi}_j)$, $j \in [1, N-1]$, constructed from the $\mathbf{q}_j$'s and $\mathbf{p}_j$'s (cf. e.g. Ref. [62] or Ref. [63] in which a similar treatment is directly performed on the GPE). The Hamiltonian of the center of mass is

$$H_{\mathrm{cm}} = \frac{\mathbf{P}^2}{2Nm} + NU(\mathbf{Q}, t), \tag{1.75}$$

and the relative motion Hamiltonian is

$$\begin{aligned} H_{\mathrm{rel}} = & \sum_{j=1}^{N-1} \left\{ \frac{j+1}{j} \frac{\boldsymbol{\pi}_j^2}{2m} + \frac{j}{j+1} \frac{m}{2} \left[\omega_\perp^2(t) \left({\varrho_x}_j^2 + {\varrho_z}_j^2 \right) + \omega_\parallel^2(t) {\varrho_y}_j^2 \right] \right\} \\ & + \sum_{j<l} V\left(\boldsymbol{\varrho}_j - \boldsymbol{\varrho}_l \right). \end{aligned} \tag{1.76}$$

[10] The Hamiltonian (1.73) is often sufficient to describe our trapped atoms, but the theorem actually holds as long as the non-interacting part of (1.73) is a second order polynomial in the variables q_l, p_l, $l \in [1, 3N]$, the coefficients of the polynomial being time-dependent.

Note that the linear terms of the potential are still present in the center-of-mass Hamiltonian (indeed such terms are needed for the oscillation of the center to be possible), but not in the relative Hamiltonian. These two Hamiltonians satisfy $H = H_{\rm cm} + H_{\rm rel}$ and commute $[H_{\rm cm}, H_{\rm rel}] = 0$, i.e. no energy can be transfered from the center of mass to the relative motion or vice versa. The full wave function can thus be written as a superposition of wave functions of the form

$$\varphi(\boldsymbol{\varrho}_1, \ldots, \boldsymbol{\varrho}_{N-1}, \mathbf{R}, t) = \psi_{\rm cm}(\mathbf{R}, t)\psi(\boldsymbol{\varrho}_1, \ldots, \boldsymbol{\varrho}_{N-1}, t), \tag{1.77}$$

where $\psi_{\rm cm}(\mathbf{R}, t)$ is the center-of-mass wave function, and $\psi(\boldsymbol{\varrho}_1, \ldots, \boldsymbol{\varrho}_{N-1})$ is the wave function associated with the internal degrees of freedom. Notice that this is not an approximation, it is exact.

From this discussion, one sees that simply displacing a harmonic trap (i.e. having a time-dependent linear term $\alpha(t)\mathbf{q}$ in U, but a constant curvature of the potential) does not change the dynamics in the frame of reference of the center of mass and simply excites the center-of-mass motion. The oscillation of the center of mass is often referred to as the *dipole mode*, and its frequency along each trap eigenaxis equals the trap frequency.

Similarly, when the harmonic trap is switched off and the cloud is in free fall, the acceleration of gravity does not modify the expansion in the accelerated frame of reference of the center of mass[11].

Breathing modes

We now focus on the internal degrees of freedom. We will see in Chap. 3 that the motion is simply governed, to some extent, by scaling equations for the widths of the cloud.

Breathing of a non-interacting gas For a non-interacting gas (normal, BEC, Fermi gas, etc.), this statement is exact (no approximations of any kind) when the harmonic trap does not rotate [e.g. the Hamiltonian (1.74)] and the scaling equation governing the cloud width is (cf. Chap. 3)

$$\ddot{b} + \omega^2(t)b = \omega_0^2/b^3. \tag{1.78}$$

For instance, if the cloud was initially at equilibrium with a width $\sigma(0)$ in a trap with a frequency $\omega(0) = \omega_0$, the time-dependent cloud width is given by $\sigma(t) = b(t)\sigma(0)$. The fact that a constant ω_0 appears in the equation is a matter of convention, as can be seen from doing the change of variable $b(t) \to Cb(t)$, which just turns the ω_0 into ω_0/C^2 in Eq. (1.78).

[11] This is true as long as the measurement is unable to "resolve" the curvature and inhomogeneity of the gravity field at the surface of the earth.

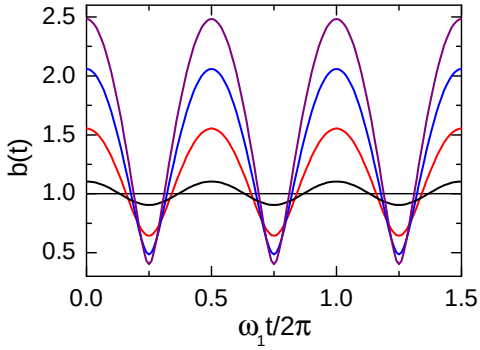

Figure 1.2: Breathing mode of a non-interacting gas [Eq. (1.79)] for $\omega_0/\omega_1 = 1$ and increasing amplitude $A = 0$, $A = 0.2$, $A = 1$, $A = 2$, and $A = 3$. The frequency is twice the trap frequency.

When the angular frequency of the trap is constant $[\omega(t) = \omega_1]$ the general solution of Eq. (1.78) is found by multiplying it by $\dot{b}$ and integrating, and is

$$b(t) = \left[\sqrt{A^2 + \frac{\omega_0^2}{\omega_1^2}} - A + 2A\cos^2(\omega_1 t + \phi)\right]^{1/2}, \tag{1.79}$$

which is a periodic oscillating function with an angular frequency $2\omega_1$. A plays the role of an amplitude. This is called the *breathing mode* or *quadrupole mode*, and for a non-interacting gas, it is at twice the trap frequency. This function is plotted in Fig. 1.2. For small amplitudes $A \ll \omega_0/\omega_1$ it reduces to a sine function with an average value $\sqrt{\omega_0/\omega_1}$, while for large amplitudes $A \gg \omega_0/\omega_1$ it reduces to $b(t) \simeq \sqrt{2A}|\cos(\omega_1 t + \phi)|$.

Breathing of interacting BECs Since the scaling equations describing the evolution of BECs in time-dependent traps are derived in Chap. 3 and App. C, we just give here the frequencies of the various low-energy modes previously studied (cf. Refs. [51–53]). The breathing modes of interacting BECs are similar to the non-interacting case discussed above, but modified by the non-linearity which induces a modification of their frequencies. Since the axes are coupled by the interaction, the frequency of the breathing in one direction depends on the trap frequencies in the other directions. Theses modes can be obtained either from the scaling equations of App. C, from the collisionless hydrodynamic equations, or by a Bogoliubov approach [30].

In a cylindrically symmetric trap with an axis having an axial (angular) frequency $\omega_\parallel$ and the other two axes a radial frequency $\omega_\perp > \omega_\parallel$ [as the potential (1.74) but static], one finds a *surface mode* with a frequency [64] $\Omega_0 = \sqrt{2}\omega_\perp$ and the two frequencies

$$\Omega_\pm^2 = \left\{2 + 3\lambda^2/2 \pm \left[\left(2 + 3\lambda^2/2\right)^2 - 10\lambda^2\right]^{1/2}\right\}\omega_\perp^2, \tag{1.80}$$

corresponding to a radial (+ sign) and an axial (− sign) breathing mode respectively. λ is the ratio $\omega_\parallel/\omega_\perp$. For very elongated traps, $\lambda \ll 1$, they simplify to $\Omega_+ = 2\omega_\perp$ and $\Omega_- = \sqrt{5/2}\omega_\parallel$.

Scissors modes

Scissors modes correspond to an angular oscillation of the cloud in the trap and can be excited if the trap is anisotropic and slightly rotated, e.g., around one of its eigenaxes. They were first investigated theoretically by Guéry-Odelin and Stringari [65] who underlined the difference between the scissors mode of a superfluid BEC (for which interactions are needed) and the one occurring in non-interacting systems (either strictly non-interacting or thermal non-condensed at high temperatures). This mode is derived in the limit of $T \to 0$ for interacting BECs in App. C. Note that all the modes discussed here are obtained in the limit of small perturbations of the cloud, and can actually be coupled when they have sizable amplitudes (for instance the scissors and breathing modes are coupled). They were investigated experimentally in details by Maragò et al. [55, 56] in both the $T \to 0$ limit and at nonzero temperatures.

Assuming we rotate the trap (1.74) around the z axis, an interacting BEC would display an angular oscillation in the x-y plane (scissors mode) whose angular frequency is given by

$$\omega_{\rm sc}^2 = \left(1 + \lambda^2\right) \omega_\perp^2, \tag{1.81}$$

this mode being *undamped*. Differently, a thermal gas in the collisionless regime would display undamped oscillations at the two frequencies $\omega_\pm = (1 \pm \lambda)\omega_\perp$. In the presence of collisions, these two modes are damped [65].

1.2.4 Reduction of dimensionality

In Chap. 4, we will consider condensates trapped in very elongated geometries, where the interesting physics happens in the long direction. In very flat or elongated traps, one can be interested in the dynamics happening in the two or one less confined directions only. In this case the system is considered as an effective two- or one-dimensional system. Effective 2D or 1D equations where the transverse dynamics has been "integrated out" can be derived from the 3D GPE[12] [70].

[12] This kind of approach is not always valid: an example is the case of a very strong transverse confinement and small number of atoms which is a realization of a Tonks gas, not described by a GPE [37, 66–69].

Effective one-dimensional equation

The trap is assumed to be harmonic in the radial directions (x-y plane) with an angular frequency $\omega_\perp$. The wave function is written as a product of radial and axial components

$$\psi(\mathbf{q},t) = \phi(x,y,t;\sigma(z,t))\varphi(z,t), \tag{1.82}$$

and a Gaussian ansatz is used for $\phi(x,y,t;\sigma(z,t))$, $\sigma(z,t)$ being its position dependent (transverse) rms width. We use the usual normalization conventions $\int |\phi|^2 \mathrm{d}x\mathrm{d}y = 1$ and $\int |\varphi|^2 \mathrm{d}z = 1$. We will not go into the details of the different regimes which depend on the density and the ratio between the typical transverse size and the scattering length. We only consider the regime characterized by

$$\left(\frac{a_s}{a_\perp}\right)^2 \ll n_{1\mathrm{D}}|a_s| \ll 1, \tag{1.83}$$

where $n_{1\mathrm{D}} \equiv N|\varphi|^2$ is the linear atomic density and $a_\perp \equiv \sqrt{\hbar/m\omega_\perp}$ is the transverse harmonic oscillator length. The first inequality excludes the Tonks limit which has proven to be very difficult to reach in actual experiments with ultracold gases [37, 66–69]. Under these conditions, the transverse width can be considered constant and is approximately the harmonic oscillator length $\sigma(z,t) = a_\perp$. Then the dynamics in the longitudinal direction is also well described by the 1D nonlinear Schrödinger equation [70]

$$i\hbar\frac{\partial\varphi}{\partial t} = \left[-\frac{\hbar^2}{2m}\frac{\partial^2}{\partial z^2} + U(z) + g_{1\mathrm{D}}N|\varphi|^2\right]\varphi. \tag{1.84}$$

The potential is assumed to be invariant by translation in the x-y plane. Note that the interaction coupling constant has been renormalized

$$g_{1\mathrm{D}} \equiv g_{3\mathrm{D}}\int |\phi|^4 \mathrm{d}x\mathrm{d}y = \frac{g_{3\mathrm{D}}}{2\pi a_\perp^2} = 2\hbar\omega_\perp a_s. \tag{1.85}$$

1.3 Laser cooling and trapping of neutral atoms

The second half of the 20th century has seen the development of amazing techniques, in which light is used to control both the internal and external degrees of freedom of neutral atoms, ions, molecules, etc. One of the pioneers was Frisch [71] who first demonstrated that shining light on an atomic beam could deflect it. This is an experimental proof that light carries momentum. Later, Kastler [72] showed that the internal state of atoms could be controlled by shining polarized light on atomic beams (optical pumping).

More generally, these techniques are based on the fact that, just like massive objects, light carries energy, momentum, and angular momentum, and can

interact strongly with matter. In any process theses quantities are conserved: they can be exchanged between the field and the matter. As a consequence, a good control of the light translates into a good control of the dynamics of the atoms.

The control of the polarization can be easily done with natural materials, such as mica sheets and other crystals. In the 60's, the invention of lasers, which provide intense and directional sources of monochromatic light, has made the control of the pulsation ω of the light very precise (and consequently, the control of its energy $\hbar\omega$ and its momentum $\hbar\omega/c$).

In this section, some basics are given concerning the experimental techniques to control the dynamics of the atoms using light.

1.3.1 Atom-field interaction

An important notion to have in mind is the behavior of a two-level atom illuminated by the light of a laser. The two levels have an energy separation $\hbar\omega_0$. The excited state is unstable, and decays back into the ground state with a time constant $\tau = 1/\Gamma$. Γ is called the *linewidth* of the atomic transition. The laser is assumed to emit light with a pulsation ω. The difference $\delta = \omega - \omega_0$ is called the laser *detuning* with respect to the atomic transition. On the scale of the atomic wave packet, the light intensity I is supposed constant.

The number of scattered photons per unit time is [73]

$$\Gamma_{\mathrm{sc}} = \frac{\Gamma}{2}\frac{s}{1+s}, \tag{1.86}$$

where $0 \leq s < \infty$ is the saturation parameter:

$$s = \frac{I/I_{\mathrm{sat}}}{1 + 4(\delta/\Gamma)^2}, \tag{1.87}$$

$$I_{\mathrm{sat}} = \frac{2\pi^2 c}{3\lambda^3}\hbar\Gamma. \tag{1.88}$$

The saturation intensity is an important parameter. Indeed, $s = 1$ separates two different regimes of light scattering by the atom: for $s \ll 1$ (linear regime), light scattering is essentially elastic. On the contrary, for $s > 1$ (nonlinear regime), the scattered light spectrum exhibits several lines centered at frequencies different from that of the laser, known as the Mollow triplet [74]. When the atom is saturated, it spends on average half its time in the excited state, while for $s \ll 1$ the population of the excited state stays low.

The radiation pressure force

Every time a photon is absorbed (respectively emitted) by an atom, its momentum $\hbar\mathbf{k}$ ($\mathbf{k}$ is the light wave vector) is transfered to (or subtracted from)

the atom. The transferred velocity is called the *recoil velocity*

$$v_{\mathrm{r}} = \frac{\hbar k}{m}. \tag{1.89}$$

For instance, for the D_2 line of ^{87}Rb, $v_{\mathrm{r}} \simeq 5.88$ mm/s.

Since spontaneous emission occurs with the same probability in two opposite directions, the transfer of momentum averaged over a large number of absorption-emission cycles (duration $\Delta t \gg 1/\Gamma_{\mathrm{sc}}$) is $\Delta P = \Gamma_{\mathrm{sc}} \Delta t \, \hbar \mathbf{k}$. This corresponds to a force

$$\mathbf{F} \equiv \frac{\Delta P}{\Delta t} = \Gamma_{\mathrm{sc}} \hbar \mathbf{k} \tag{1.90}$$

called the *radiation pressure* force. Obviously, it is always repulsive. A similar force appears when light is reflected by a mirror: this transfers $2\hbar\mathbf{k}$ to the mirror and pushes it away from the source.

The corresponding acceleration can be important: for instance, at resonance, for a strongly saturated ^{87}Rb atom ($\Gamma_{\mathrm{sc}} = \Gamma/2$) this yields an acceleration $a = F/m \sim 10^5$ m/s^2.

The dipole force

Another force appears when an atom is illuminated. In a classical picture, it comes from the interaction of the dipole induced by the electric field $\mathbf{p} \propto \mathbf{E}$ with the electric field itself. Since the energy of this interaction is $-\mathbf{p} \cdot \mathbf{E}$, the corresponding potential is seen to be proportional to $|\mathbf{E}|^2$, i.e. to the intensity of the radiation[13]. The quantum mechanical expression of the *dipole potential* (also called the ac-Stark shift) is [75]

$$U_{\mathrm{dip}}(\mathbf{r}) = \frac{\hbar\delta}{2} \ln\left[1 + s(\mathbf{r})\right], \tag{1.91}$$

where the spatial dependence of s comes from the fact that the light field may be inhomogeneous. A remarkable aspect is that the dipole potential is positive when $\omega > \omega_0$: it means that the atoms will be repelled from high intensity regions. In this case, the light is said to be *blue detuned* from the transition. On the contrary, when the light is *red detuned* ($\delta < 0$), the regions of higher intensity attract the atoms. The corresponding force is the gradient of this potential, and contrary to the radiation pressure force, it is not oriented in the direction of $\mathbf{k}$.

In the limit of low saturation, a remarkable relationship between the scattering rate and the dipole potential is

$$U_{\mathrm{dip}}(\mathbf{r}) = \frac{\delta}{\Gamma} \hbar \Gamma_{\mathrm{sc}} = \frac{\hbar\delta}{2} \frac{I(\mathbf{r})/I_{\mathrm{sat}}}{1 + 4(\delta/\Gamma)^2}. \tag{1.92}$$

[13] This classical and linear interpretation is valid only in the linear regime, i.e. when $s(\mathbf{r}) \ll 1$. Indeed Eq. (1.91) gives a dipole potential linear in the intensity in this limit.

It shows that, given a desired dipole potential, the scattering rate can be rendered negligible by using larger detunings. This can be done at the cost of increasing the intensity in the same proportion as the detuning ($I/\delta =$ constant in the limit of large detunings $\delta \gg \Gamma$).

In this regime, the dipole force is commonly employed to realize conservative traps for cold atoms, with various geometries obtained by tailoring the light intensity distribution (cf. Ref. [76] and references therein).

The dipole force on real atoms

For real, multi-level atoms such as ^{87}Rb and other alkali atoms, an expression of the dipole force can be obtained in the experimentally relevant limit of unresolved hyperfine splitting, for which the atoms are assumed to be in the state $|5^2S_{1/2}, F\rangle$, and the detunings δ_1 with respect to the center of the hyperfine split of the D_1 line and δ_2 with respect to the center of the hyperfine split of the D_2 line are large compared to the excited state's hyperfine splitting ($\delta_1, \delta_2 \gg \Delta'_{\mathrm{HFS}}$). In this case, the dipole potential is given by [76]

$$U_{\mathrm{dip}}(\mathbf{r}) = \frac{\hbar\Gamma^2}{24}\left(\frac{2+\mathcal{P}g_F m_F}{\delta_2} + \frac{1-\mathcal{P}g_F m_F}{\delta_1}\right)\frac{I(\mathbf{r})}{I_{\mathrm{sat}}}, \tag{1.93}$$

where $\mathcal{P}$ characterizes the light polarization ($\mathcal{P} = 0, \pm 1$ for linearly and $\sigma^{\pm}$ polarized light respectively). g_F is the Landé g-factor of the hyperfine manifold $|5^2S_{1/2}, F\rangle$, and m_F is the quantum number associated with the projection of the atomic angular momentum $\mathbf{F}$ on the light's wave vector. For instance, for the state $|F = 2, m_F = +2\rangle$ and σ^+ polarized light, a two-level system is isolated ($|F = 2, m_F = +2\rangle \leftrightarrow |F' = 3, m'_F = +3\rangle$) and, as expected, one recovers the two-level expression (1.92) taken in the limit $\delta/\Gamma \gg 1$.

1.3.2 Doppler cooling

From everyday experience, the fact that light can be used to cool, and not to heat matter is not intuitive. Indeed in nature, light is generally absorbed by matter, non-radiative processes convert this energy into heat before radiative processes can occur once again (black body radiation for instance). The difference with isolated atoms is that they are simpler than most materials: unlike for instance molecules in which ro-vibrational states can be excited, with single atoms, only radiative processes can occur. A photon absorbed will always be re-emitted at some point.

Doppler cooling is based on two ingredients: a resonance of the form discussed in Sec. 1.3.1, and the Doppler effect [78], i.e. the fact that in the frame of reference of an atom moving with a velocity $\mathbf{v}$, the pulsation of the light is shifted by

$$\Delta\omega = -\mathbf{k}\cdot\mathbf{v}. \tag{1.94}$$

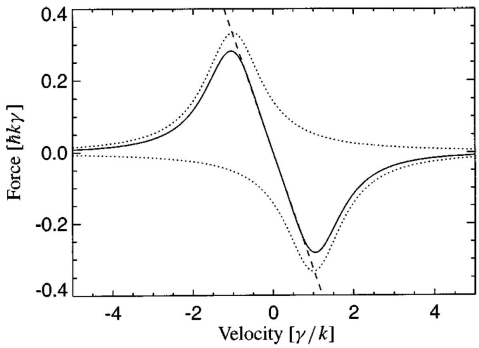

Figure 1.3: Figure of Metcalf and van der Straten [77] showing how the force depends on the velocity in optical molasses. The dotted lines are the forces of each beams, the solid line is their sum. The straight line shows how this force mimics a pure damping force over a restricted velocity range.

If the laser is red detuned and does not saturate the transition, it is seen that, because of the Doppler effect, the atoms moving towards the source scatter more photons than the ones moving away from the source. By using two counterpropagating red-detuned lasers, the force exerted by the light is thus strongly velocity dependent (cf. Fig. 1.3). It mimics friction ($\mathbf{F} = -\alpha\mathbf{v}$) and thus tends to slow the atoms, i.e. to cool the ensemble. This idea was proposed independently by Hänsch et al. [79] for neutral atoms, and Wineland and Dehmelt [80] for trapped ions.

Since the Doppler force is $\mathbf{F} = -\alpha\mathbf{v}$, one would expect the atoms to slow down until $\mathbf{v} = \mathbf{0}$, i.e. until the temperature has reached absolute zero. But this is actually true only for the average velocity (averaged on many absorption emission cycles). Since the atoms continuously absorb photons and re-emit them in random directions, they perform a random walk in momentum space, which leads to diffusion of the momentum distribution of the cloud. This corresponds to heating. A precise analysis [46, 81–84] shows that the steady-state temperature (when the cooling and heating effects cancel each other) is the smallest if one chooses the detuning $\delta = -\Gamma/2$, and is

$$T_{\mathrm{D}} = \frac{\hbar\Gamma}{2k_B}. \tag{1.95}$$

This is called the *Doppler temperature*. It is the fundamental limit on temperature that can be achieved with this mechanism. For the D_2 line of ^{87}Rb which we use, this limit is $T_{\mathrm{D}} \simeq 146\ \mu$K.

A set of pairs of counterpropagating red-detuned beams (either one, two or three) used to Doppler cool a sample is often called an *optical molasses*. Because of the spatial diffusion, the cloud gets more and more dilute and is lost once all the atoms have escaped the region where the lasers cross.

1.3.3 The magneto-optical trap

The invention of the magneto-optical trap (MOT) was motivated by the fact that the cold samples produced by optical molasses were quickly lost. The idea

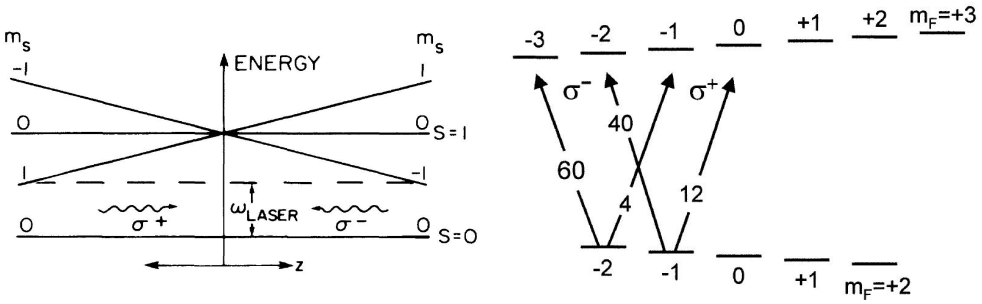

Figure 1.4: Figures of Raab et al. [85] and Chu [86] explaining the principle of a magneto-optical trap, and showing the actual magnetic sublevel structure of the transition used in this thesis. Two counterpropagating red-detuned laser beams with the same circular polarization (with respect to their wave vector) respectively drive σ^+ and σ^- transitions. A static magnetic field with a linear dependence on the position (a gradient) shifts some Zeeman sublevels (left: $m_S = \pm 1$, right: $m_F \neq 0$). This cools and traps the atoms about the center where $\mathbf{B} = \mathbf{0}$ (see text).

is to make an optical molasses, but to render the velocity-dependent force also position-dependent in order to trap the cloud. For this, one takes advantage of the Zeeman substructure of the atomic transition and of the Zeeman effect: the fact that these levels are shifted by a static magnetic field. An inhomogeneous static magnetic field is thus added to bring the atoms closer to resonance with the laser that tends to push them towards the center, thus increasing the radiation pressure force, when they are far from the trap center. Since two Zeeman sublevels with opposite m_F number are shifted equally, but with opposite signs, the light is circularly polarized to address only the transition which is closer from resonance with the laser. The idea of adding a magnetic field to an optical molasses was proposed by Dalibard[14] to Raab et al. [85] who did the first experimental realization. This principle is illustrated in Fig. 1.4.

Since the cooling mechanism is just Doppler cooling, the expected fundamental limit on T is still the Doppler temperature (1.95).

Sub-Doppler cooling

In experiments, it was soon realized that optical molasses could produce much lower temperatures than the Doppler limit [88] (40 μK instead of the expected $T_{\mathrm{D}} = 240$ μK for Na). It was a real surprise to the community and directly attracted a lot of attention [86]. The accepted mechanism accounting for such low temperature is called *Sisyphus cooling* or *polarization gradient cooling*.

[14]This is reported in Refs. [85] and [86].

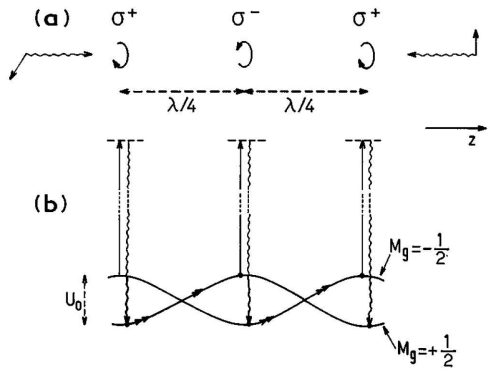

Figure 1.5: Figure of Cohen-Tannoudji [87] explaining the principle of the "Sisyphus cooling" mechanism. Laser configuration formed by two counter-propagating plane waves along the z axis with orthogonal linear polarizations (a). The polarization of the resulting electric field is spatially modulated with a period $\lambda/2$. Every $\lambda/4$, it changes from σ^+ to σ^- and vice versa. For an atom with two ground state Zeeman sublevels $M_g = \pm 1/2$, the spatial modulation of the laser polarization results in correlated spatial modulations of the light shifts of these two sublevels and of the optical pumping rates between them (b). Because of these correlations, a moving atom runs up potential hills more frequently than down [double arrows of (b)].

The interference of the counterpropagating beams with identical circular polarizations produces a periodic structure of the polarization along the propagation axis. This is illustrated in Fig. 1.5 for the simpler case of two orthogonal linear polarizations. A simple explanation of the mechanism can be found in Cohen-Tannoudji [87]. It relies on the correlation between the probability of optical pumping between the light-shifted Zeeman sublevels, and the spatial periodicity of the light-shifts: an atom climbing uphill is losing kinetic energy and then pumped to another sublevel having a lower energy, where the process starts over (cf. Fig. 1.5). The theory is detailed in Refs. [89–92].

In this process, the atoms are continuously scattering photons, and the subsequent limit on temperature is a few times the recoil energy $E_\mathrm{r} = \hbar^2 k^2/2m$, the energy gained by an atom at rest when it absorbs a photon. The corresponding limit on the temperature is thus related to the recoil temperature[15] $T_\mathrm{r} = 2E_\mathrm{r}/k_B$. For ^{87}Rb, this is $T_\mathrm{r} \simeq 362$ nK. In practice, the coldest temperatures achieved are on the order of a few tens of recoils, i.e. a few μK for ^{87}Rb. For large MOTs such as employed in this thesis, the typical temperature is even higher, on the order of a few tens of μK.

[15] Sometimes defined without the factor 2. The definition used in this thesis is $T_\mathrm{r} = \hbar^2 k^2/mk_B$.

Limit on the density and big magneto-optical traps

We have seen the temperature limits of the two laser cooling mechanisms we are going to use in Chap. 2 as the first stage of cooling. But the important parameters for Bose-Einstein condensation is not the temperature, but the peak phase-space density $D = n_0\lambda_{\mathrm{dB}}^3$ introduced in Sec. 1.1.2. The natural question arising is thus: "What limits the density of MOTs?".

The two dominant effects which must be considered are:

1. the "attenuation force" $\mathbf{F}_A$ [93] resulting from the depletion of the beams by the cloud. This cannot be neglected when the optical thickness $b(\delta)$ is not $\ll 1$,

2. the repulsive force $\mathbf{F}_R$ induced by emission and reabsorption of photons by different atoms of the cloud (multiple scattering). It is negligible when only single scattering events are likely to happen, namely when $b(\delta) \ll 1$.

The attenuation force is given by [94]

$$\nabla \cdot \mathbf{F}_A = -6\sigma_L^2 n I_\infty / c, \tag{1.96}$$

while the repulsive force for two atoms separated by a distance r is

$$|\mathbf{F}_R| = \frac{\sigma_R \sigma_L n I}{4\pi c r^2}. \tag{1.97}$$

Here, σ_L is the absorption cross-section of atoms for the trapping light, I_∞ is the intensity outside the cloud (not attenuated yet), n the density and σ_R is the absorption cross-section for the scattered light, which is different from σ_L because of the change of polarization. Note that the repulsive force resembles the well known gravitational and Coulomb interactions. This opens the possibility to study gravitational or charged plasma physics with sufficiently large MOTs [94–99].

A consequence of the interplay of these two forces with the trapping force $-k_{\mathrm{M}}\mathbf{r}$ of the MOT is that the density is limited to [94]

$$n_{\max} = \frac{c k_{\mathrm{M}}}{2\sigma_L(\sigma_R - \sigma_L) I_\infty}. \tag{1.98}$$

This simple model is in good agreement with the experiments (cf. Refs. [94, 100]) and can be used to measure the ratio σ_R/σ_L. When the MOT loads, once the density has reached $n_{\max}$, the MOT size keeps increasing as $L \sim N^{1/3}$ (i.e. constant density). This behavior is different from the one of an ideal gas maintained at a constant temperature in a harmonic trap in which the density would keep increasing when atoms are added (cf. Sec. 1.1.2).

For MOTs with large number of atoms, the interplay between these forces can also lead to MOT instabilities [94, 95, 101], which translate into large fluctuations of the density.

Since we work with large MOTs, in which the atom number can reach 10^{11}, and the optical density $b_0 \equiv b(\delta = 0) = 300$, we use larger detunings (i.e. smaller σ_L) than the optimal value for Doppler cooling ($\delta \simeq -3.5\ \Gamma$ instead of $-0.5\ \Gamma$). With our parameters (cf. Sec. 2.2.1), the typical limit on the density is $\sim 10^{10}$ atoms/cm^3.

1.4 Magnetic trapping and evaporative cooling

A MOT can simply be loaded from a room temperature vapor at a low pressure of typically 10^{-12} bar. The phase-space density of such a vapor is $n_0\lambda_{\rm dB}^3 \sim 10^{-18}$. In Sec. 1.3 we have seen how laser cooling techniques suffer from fundamental limits on both the attainable temperatures and densities. The corresponding limit on the phase-space density is $n_0\lambda_{\rm dB}^3 \lesssim 10^{-4}$ which is 14 orders of magnitude higher than that of the initial gas, but still far from $n_0\lambda_{\rm dB}^3 \sim 1$ required for Bose-Einstein condensation to occur[16]. For this reason, the pioneers of Bose-Einstein condensates [102–107] had the idea to use laser techniques only as a first stage to collect, pre-cool, and isolate the system from the hot environment, followed by a second stage of trapping in a conservative trap in which evaporative cooling could be performed. Evaporation implies losing most of the atoms, but at the same time the temperature decreases, and with an appropriate choice of the trap geometry, the density can increase. Consequently, the phase-space density of the remaining ensemble can be made to increase. In this section, we give an idea of how magnetic trapping and evaporative cooling work.

1.4.1 Magnetic trapping

Neutral atoms with nonzero permanent magnetic moments $\boldsymbol{\mu}$ can be trapped by an inhomogeneous static magnetic field $\mathbf{B}(\mathbf{r})$ via the interaction with the field

$$U(\mathbf{r}) = -\boldsymbol{\mu} \cdot \mathbf{B}(\mathbf{r}). \tag{1.99}$$

In the weak field limit (i.e. when the Larmor frequency $\nu_L = U(\mathbf{r})/h$ is much smaller than the fine and hyperfine splittings [108]) this interaction leads to a shift of the atomic energy levels linear in $\mathbf{B}$ known as the Zeeman shift:

$$U(\mathbf{r}) = g_F m_F \mu_B |\mathbf{B}(\mathbf{r})|, \tag{1.100}$$

[16] Note that this phase-space density is just 2 orders of magnitude larger than that of a gas at room temperature and atmospheric pressure.

where μ_B is the Bohr magneton ($\mu_B/h \simeq 1.4$ MHz/G), g_F is the Landé g-factor of the hyperfine manifold characterized by the number F, and m_F is the quantum number associated to the projection F_z of the atomic angular momentum $\mathbf{F}$ on the static field. The trapping potential will thus have the form given by Eq. (1.100) if the atom stays in a given m_F state. This occurs when the Larmor frequency is much bigger than the rate of change of the magnetic field axis: in this case the orientation of the atomic spin follows adiabatically the field orientation.

In a vacuum, Maxwell's equations do not allow $|\mathbf{B}|$ to have a local maximum (Wing's theorem [109]). Thus, static magnetic traps can only be formed by a field configuration exhibiting a local minimum of $|\mathbf{B}|$. It follows that only the Zeeman states for which the product $g_F m_F > 0$ can be trapped. An important consequence is that neutral atoms cannot be trapped in their fundamental internal state (because the high-field-seeking state $|F, -m_F\rangle$ has a lower energy than the trapped, weak-field-seeking $|F, m_F\rangle$). This means that magnetically trapped neutral atoms are intrinsically in a metastable state.

In the ground state $|5^2S_{1/2}\rangle$ of ^{87}Rb, three such states can be found: $|F = 1, m_F = -1\rangle$ (because $g_1 \simeq -1/2$) and the two states $|F = 2, m_F = +1\rangle$ and $|F = 2, m_F = +2\rangle$ ($g_2 \simeq +1/2$).

Majorana losses

The first cause of losses in magnetic traps is Majorana spin flips[17] that occur when the adiabaticity criterion discussed above is not fulfilled. This is inevitable in quadrupole traps because the magnetic field has a zero in the center. This motivated experimentalists to move to harmonic traps with a non vanishing field minimum [103] or to prevent the atoms from reaching the low-field region [107]. In a quadrupole, the dependence of the losses on the temperature is not trivial, because although higher temperatures correspond to higher velocities which allow spin flips to be more likely, the density is lower about the field minimum than that at lower temperatures. Nevertheless, simple arguments show that the loss rate γ_{flip} scales as [103]

$$\gamma_{\text{flip}} \propto T^{-2}. \tag{1.101}$$

Even if these losses are small at the beginning of the evaporation, they become significant as the temperature decreases. This prevents condensation in static quadrupole traps.

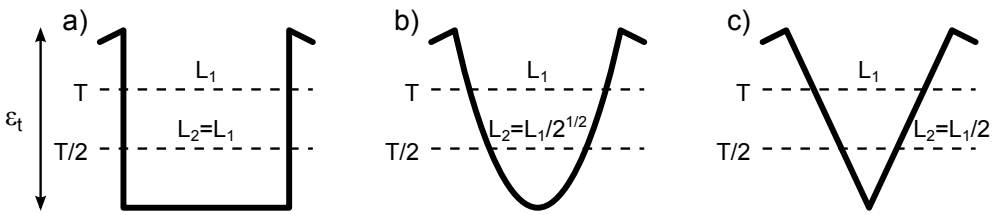

Figure 1.6: Three traps with a finite depth ϵ_t and a different shape are represented (the vertical axis is the potential, the horizontal one the position). In a box potential (a) the volume L^3 is independent of T and the density $n_0 = N/L^3$ scales as N. In a harmonic trap (b) $L \propto \sqrt{T}$ and $n_0 \propto NT^{-3/2}$. In a linear trap (c) $L \propto T$ and $n_0 \propto NT^{-3}$. These different scaling laws illustrate the importance of the trap shape for evaporative cooling.

1.4.2 Forced radio-frequency evaporative cooling

Forced evaporative cooling is the truly magical step in BEC experiments, because it permits to gain the 6 missing orders of magnitude[18] in the phase-space density. Surprisingly, except for the outcoupling mechanism (radio-frequency induced spin flips) this process is completely classical.

Principle

The principle is in fact straightforward: the gas is held close to equilibrium in a trap of finite depth[19] ϵ_t. In the tails of the velocity distribution, some atoms have an energy higher than this trap depth, and subsequently escape from the trap. Their energy is thus removed from the cloud. Since it is higher than the average energy per particle, this process induces a reduction of the average energy per (remaining) particles, i.e. the cooling of the remaining cloud.

Scaling laws

Now let us suppose that the trap is a simple box potential with a volume L^3 as in Fig. 1.6a, the walls being "reflecting" below a certain kinetic energy ϵ_t and "transparent" above. The corresponding density N/L^3 can only decrease during the evaporation. Since T also decreases (i.e. λ_{dB} increases), it is not clear yet how the phase-space density will evolve. On the contrary, if the trap

[17] Also called "Majorana flops" [104].

[18] Recall that $D \sim 10^{-4}$ at best in a MOT, but the imperfect transfer to a magnetic trap generally reduces D.

[19] This statement seems paradoxical because strictly speaking, no equilibrium is possible in a trap of finite depth. Nevertheless, when $k_B T \ll \epsilon_t$, there is a quasi-equilibrium [110], and T is the effective temperature of this quasi-equilibrium.

Parameter	Scaling	Scaling with N, T		
		Box	Harmonic	Linear
Width L		1	$T^{1/2}$	T
Velocity v	$T^{1/2}$	$T^{1/2}$	$T^{1/2}$	$T^{1/2}$
Density n_0	N/L^3	N	$NT^{-3/2}$	NT^{-3}
Collision rate $\gamma_{\rm el}$	$n_0 v$	$NT^{1/2}$	NT^{-1}	$NT^{-5/2}$
Phase-space density D	$n_0\lambda_{\rm dB}^3$	$NT^{-3/2}$	NT^{-3}	$NT^{-9/2}$
$(\alpha^{-1})_{\max}$		3/2	3	9/2

Table 1.1: This table shows how the different parameters characterizing the cloud scale with the number of atoms N and the temperature T. The three traps considered are 3D box, harmonic, and linear potentials (as in Fig. 1.6 but in 3D). The cloud is assumed to be at equilibrium, which is strictly speaking not possible if the depth ϵ_t is finite. Nevertheless, it is a good approximation when $\eta = \epsilon_t/k_B T \gg 1$, T being the effective temperature.

has a different shape, say it is harmonic (Fig. 1.6b) or linear ($U(\mathbf{r}) \propto |\mathbf{r}|$, Fig. 1.6c) we have seen that the cloud width is related to the temperature [cf. Eq. (1.33)]. Consequently, the density can in principle increase during the evaporation. It is thus important to understand how the parameters describing the cloud scale with N and T [20]. This is summarized in Tab. 1.1 for the three traps of Fig. 1.6.

In the (hypothetical) absence of other losses than the "evaporated atoms", the considerations of Tab. 1.1 are sufficient to implement efficient evaporative cooling. Indeed, the only thing needed is to increase phase-space density. From the scaling laws of Tab. 1.1, it is seen that starting from a cloud at equilibrium with N atoms and a temperature T, a small loss of $\mathrm{d}N$ atoms leading to a new equilibrium with a reduction of the temperature by $\mathrm{d}T$ will correspond to an increase of D if $\mathrm{d}\log D/\mathrm{d}\log T < 0$ (notice that $\mathrm{d}\log T < 0$). From the scaling of D with respect to N and T (Tab. 1.1), one can express this condition as

$$\frac{\mathrm{d}\log N}{\mathrm{d}\log T} < (\alpha^{-1})_{\max} \tag{1.102}$$

where $(\alpha^{-1})_{\max}$ depends on the trap shape and is given in Tab. 1.1 (we use the same notation as Refs. [41] and [111]: $\alpha \equiv \mathrm{d}\log T/\mathrm{d}\log N$).

The ingredients of evaporative cooling are thus the following:

1. a way to selectively remove the most energetic atoms,

[20] We express them with N and T and not (N, D), (D, T), (n_0, T), etc. because these are the quantities that we can directly measure.

2. enough collisions for the cloud to reach a new equilibrium after some atoms have been removed.

We will see that other loss mechanisms also play an important role.

Radio-frequency outcoupling

In magnetic traps, one can take advantage of the Zeeman substructure to selectively remove the most energetic atoms. Indeed the Zeeman shift between adjacent Zeeman sublevels of a given hyperfine manifold F was given in Sec. 1.4.1 and is $\Delta E(\mathbf{r}) = g_F \mu_B |\mathbf{B}(\mathbf{r})|$. With the magnetic fields needed to trap the atoms, this corresponds to radio-frequencies (rf) $\nu_{\rm rf} = \Delta E/h$ in the range $1 \leq \nu_{\rm rf} \leq 50$ MHz. If one shines such rf on the magnetically trapped atoms, on the surface defined by

$$\mathcal{S}(\nu_{\rm rf}) = \{\mathbf{r} \text{ such that } \Delta E(\mathbf{r}) = h\nu_{\rm rf}\}, \tag{1.103}$$

the rf is resonant with the transitions $|F, m_F\rangle \rightarrow |F, m'_F = m_F \pm 1\rangle$. For instance, if the atoms are trapped in $|F = 2, m_F = +2\rangle$, they can emit (stimulated emmission) a resonant rf photon and be transfered to the $|F = 2, m_F = +1\rangle$ state. For magnetic traps as discussed in Sec. 1.4.1 the surface $\mathcal{S}$ is exactly an isopotential surface (in the absence of gravity) and looks like a "bubble" surrounding the trapped atoms. Only the atoms with an energy higher than $m_F h\nu_{\rm rf}$ can cross this surface and be transfered to another Zeeman substate. Strictly speaking the selection is spatial and not energetic, but still, only a subset of the most energetic atoms can reach $\mathcal{S}$ and be evaporated. This provides a way to selectively remove the atoms which have more energy than the average energy per particle.

The resonance condition mentioned above is actually not sufficient because if the oscillating rf field has the same orientation as the static magnetic field, then it cannot drive the transitions $m_F \rightarrow m_F \pm 1$. In Ioffe-Pritchard magnetic traps, for large distances from the center, the field is oriented in all directions and evaporation occurs preferentially around an "equator". On the contrary, close from the potential minimum, the magnetic field is preferentially oriented along the direction of the field at the trap minimum. Thus the rf radiation should have its magnetic field generated perpendicular to this direction to be efficient at all energies.

Collisions and losses

Collisions are needed for the cloud to reach a new equilibrium. The relevant corresponding timescale for equilibrium is thus $\tau = 1/\gamma_{\rm el}$, where $\gamma_{\rm el}$ is the elastic collision rate. In practice, *magnetic traps exhibit losses, mainly due*

to collisions with the background gas. The number of magnetically trapped atoms thus decreases exponentially with a time constant τ_{trap}. Since these losses are not energy dependent, they do not contribute to cooling. They tend to decrease the phase-space density D (because $D \propto N$). Thus there is a competition between the "good" (elastic) collisions and the "bad" (inelastic) collisions with the background gas. Evaporative cooling will be all the more efficient if there are a lot of good collisions for one bad collision, i.e. if the ratio $\tau_{\text{trap}}/\tau \gg 1$. This is the difficult criterion to fulfill because it requires a lot of atoms to be trapped in a place where the vacuum is good (cf. Sec. 2.2 for values), and a sufficiently large cross-section for elastic collisions.

Runaway evaporation

One talks about *runaway evaporation* when both the phase-space density and the collision rate increase during the evaporation. From Tab. 1.1, one sees that this is not possible in a box potential, but it is with other traps such as linear or harmonic traps. It is also important to note that, since $\gamma_{\text{el}} \propto DT^2 \propto NT^{2-\alpha^{-1}}$ (cf. Tab. 1.1), the condition for runaway evaporation is

$$\frac{\mathrm{d}\log N}{\mathrm{d}\log T} \leq (\alpha^{-1})_{\max} - 2, \tag{1.104}$$

which is more constraining than the criterion (1.102) for an increasing phase-space density. This shows that the elastic collision rate can remain constant during evaporation while the phase-space density can increase by orders of magnitude.

Kinetics and forced evaporative cooling

Because evaporation relies on the exponential wings of the velocity distribution, the rate of evaporation depends exponentially on the truncation parameter $\eta = \epsilon_t/k_BT$ (ϵ_t is the trap depth). It can be shown that if η is not too close to 1 ($\eta \sim 10$), the velocity distribution inside the trap is well approximated by a truncated Maxwell-Boltzmann distribution [110]. The evaporation rate has a complex expression proportional to the elastic collision rate and to $e^{-\eta}$. Evaporation with a constant depth ϵ_t is thus slower and slower as the temperature decreases. Since the inelastic losses have a constant rate $1/\tau_{\text{trap}}$, at some point the phase-space density starts to decrease. Moreover, even in the absence of inelastic losses, the time to reach BEC would have to be exponentially long. Evaporation must thus be *forced*, i.e. the trap depth ϵ_t is decreased as the temperature decreases, keeping η more or less constant.

The full dynamics of forced evaporative cooling is treated in Ref. [111]. A set of coupled differential equations is derived for the evolution of the internal

energy, the number of atoms and the effective temperature of the gas. This analysis relies on the strong assumption that the evaporation process is energy dependent and not spatially dependent, i.e. that any atom reaching an energy ϵ_t is instantaneously lost. This is obviously not the case for the outcoupling mechanism discusses above, because atoms colliding near the trap center can gain high energies without being removed. Despite the fact that this assumption is too strong to predict the correct times needed for evaporation[21], the model is instructive. It greatly simplifies when η is supposed to be constant, since most of the parameters such as the density, the energy lost per particle, etc., have a nonlinear dependence on η through uneasy incomplete gamma functions. In this case, quantitative criteria on the ratio $\tau_{\rm trap}/\tau$ can be derived, and an optimal value of η can be determined, which is typically $5 < \eta < 10$.

Evaporative cooling in practice

In practice, the considerations of Tab. 1.1 are sufficient in the laboratory. The goal is to have D increase while keeping a significant elastic collision rate. At the same time, the peak density should not be too large in order to prevent losses such as three-body losses. The upper bound on n_0 is of course strongly dependent on the atom considered (its collisional properties). For ^{87}Rb, three-body losses become non-negligible for densities[22] $n_0 \sim 10^{14}$ atoms/cm^3.

The optimization of the rf ramps (frequency and amplitude) can thus be performed step by step by maximizing D under the constraint that the density stays below a certain threshold, imposed by three-body losses. As noted above, when the trap is static[23], maximizing D is the same as maximizing the elastic collision rate $\gamma_{\rm el}$ while decreasing both N and T.

1.5 Conclusion

This chapter has given a minimal "toolbox" to attack the problem of designing a setup for the Bose-Einstein condensation of a neutral gas. Elements of theory concerning trapped classical and degenerate Bose gases have been recalled,

[21] One can readily check that this model predicts durations smaller than a fraction of second for situations where experimentalists report much longer times, on the order of a few seconds or even a minute.

[22] For instance, if the lifetime in the trap is 60 s, the rate of three-body losses equals the rate of background gas induced losses when $n_0 \simeq 6.5 \times 10^{13}$ atoms/cm^3 (cf. Ref. [112]).

[23] This assumption is implicit in this discussion, but is not satisfied for optical traps, which have to be decompressed to reduce ϵ_t [for a single Gaussian beam, the potential must be scaled by a factor $\epsilon_t(t)/\epsilon_t(0)$, consequently reducing the trap oscillation frequency by the square root of this factor (harmonic approximation)]. In this case, one should include the scaling with the trap geometry in Tab. 1.1.

with a focus on the ones providing practical experimental methods. The main experimental techniques used in this thesis, namely the laser manipulation of the cloud, magnetic trapping, and evaporative cooling, have been briefly presented. The reasons why each of these various techniques is not sufficient, and why they are needed together has been underlined.

Many important aspects, not investigated within the duration of this thesis, have been omitted. For instance, Bose-Einstein condensates exhibit amazing coherence properties arising from the fact that all the atoms are described by the same wave function. Bloch et al. [113] showed experimentally how first order coherence emerges when the phase transition is crossed. They also demonstrated that this coherence extends over the whole BEC. Higher order correlations have not been discussed either, for example, the density-density correlation function of BECs is different from that of a non-degenerate gas. This was investigated e.g. by Schellekens et al. [114]. Neither the thermodynamical properties of Bose gases, nor the fact that Bose-Einstein condensation is a phase transition have been discussed. The question of the dynamics of the formation of the BEC when the phase transition is crossed has also attracted attention. It was first predicted to be so slow that BECs would never have time to form [115, 116], before Stoof [117] showed that this time is actually small. Experiments confirmed this prediction. Recently, Weiler et al. [118] observed the spontaneous formation of vortices during condensation. Effects that cannot be understood with the mean-field theory are also subjects of intense studies.

The following chapter presents the construction of an experiment for the condensation of ^{87}Rb. Both the design of the apparatus and the achievement of Bose-Einstein condensation are guided by the contents of this first chapter.

Chapter 2

Bose-Einstein condensation of Rubidium-87

This chapter details the key points involved in the production of Bose-Einstein condensates (BECs). It is divided in two parts: the first part gives an overview of the apparatus which was (partially) constructed during this thesis, with technical details. Its main elements are the vacuum system, in which the physics takes place, the lasers used for the first stage of cooling, for imaging, and to apply various forces on the atoms, and the magnetic trap in which the BECs are produced. Some details on the radio-frequency source used for evaporative cooling are also given.

The second part is dedicated to the various steps that bring a very dilute gas of Rubidium at room temperature (density $n_0 \sim 10^7$ atoms/cm^3) to a ^{87}Rb BEC containing 5×10^5 atoms at a peak density of 5×10^{14} atoms/cm^3. This involves laser cooling, optical pumping, magnetic trapping, and radio-frequency induced evaporative cooling in the magnetic trap.

2.1 The experimental setup

The first atomic BECs where produced in 1995 by three American groups: Anderson et al. [105] first condensed ^{87}Rb, then Bradley et al. [106] condensed ^{7}Li, and Davis et al. [107] condensed ^{23}Na. The three setups had a lot in common: they all used a first stage of laser cooling followed by magnetic trapping and radio-frequency or microwave evaporative cooling in the magnetic trap. They used three different chemical elements, which were all alkali metals. This is because alkali metals have a broad cycling transition, making them particularly suitable to laser cooling. There were important differences though. First, the magnetic trap of Anderson et al. [105] was not static (time-averaged, orbiting potential [103]), Davis et al. [107] used a hybrid trap combining a static

magnetic field and a repulsive dipole laser beam (a "plug"), while Bradley et al. [106] used permanent magnets in a Ioffe-Pritchard configuration [102] (instead of electro-magnets for the others). This latter strategy proved to be inconvenient because the time of flight technique could not be used. The methods to prepare the cloud for evaporative cooling were also distinct: two used a Zeeman slower [119] to load a magneto-optical trap (MOT), while Anderson et al. [105] directly loaded the MOT from the room temperature, low pressure vapor (vapor-loaded MOT, first realized by Monroe et al. [120]). Because of the low loss rate needed to evaporate, they had to work at very low pressure, and consequently the loading time of the MOT had to be long (5 minutes).

Nowadays, most of the existing Bose-Einstein condensation apparatus in the world are refinements of these original setups[1]. To date only two groups were able to produce atomic BECs with other strategies, i.e. without a first stage of laser cooling [121, 122], and in both cases they also used evaporative cooling in a magnetic trap in the end.

Nevertheless, since 1995, experimental techniques have been improved, and new techniques have emerged. The improvements are of various aspects: reduction of the duty cycle (which makes a real difference in the laboratory for practical purposes), condensation of many new species [121, 123–132], cooling of fermions to degeneracy (see e.g. Refs. [133–135]), ability to load the BECs into various trap geometries to explore the analogy with laser physics [113, 136–138], or more recently, to simulate condensed-matter physics [2–5, 7, 43, 69, 139–145].

Some remarkable evolutions of the experimental techniques are the development of a variety of magnetic traps [146–151] and the possibility to dress them with a radio-frequency field [152–154], the loading of BECs in optical traps of various geometries [155], the production of BECs with all-optical techniques [156] (the magnetic trap is replaced by a dipole force trap), or the use of novel cooling schemes [157]. An important technique which has become commonly used in the past few years is the possibility of changing the scattering length through Feshbach resonances (see e.g. Refs. [158–160]). This allows one to tune the interactions between the atoms from the strongly interacting regime to the weakly, or even, non-interacting regime, the interaction being either attractive or repulsive. The existence and the properties of Feshbach resonances depends on the species considered and, unfortunately, no convenient resonance has been found in ^{87}Rb so far.

Due to the lack of experience of the INLN group with BECs, the choice was made to use ^{87}Rb, by far the most documented species for Bose-Einstein condensation. This sections describes the experimental setup constructed during this thesis, and is followed by one that details the experimental sequence

[1] This is also true for experiments on degenerate Fermi gases.

used to produce BECs.

When I arrived in the group the two MOTs were operating. I had to develop the magnetic trap and its control electronics, to set up the hardware and develop the softwares for the computer control of the experiment and the imaging. With our team of three, it took us 11 months to produce our first BEC. The various sources of instabilities which often affect such complex experiments were then continuously identified and fixed. The experiment is now very stable and fully operational to study the physics. This section includes technical details aimed at giving other research groups elements to guide them in the production of BECs, in the manner of Ref. [161] which we found useful as a basis. Some are reported in App. B which contains the list of the key elements of the experiment.

2.1.1 The vacuum system

To take advantage of the group's experience with big MOTs, it was decided to use a double MOT setup, similar to the one introduced by Myatt et al. [162] (but without magnetic guiding). This is a way to bring together a fast loading of a MOT and a good vacuum needed for evaporative cooling. A first vapor-loaded MOT (MOT1) is produced in a chamber with a relatively high Rubidium pressure (i.e. too high to perform evaporative cooling) $P_1 \sim 10^{-9}$ Torr (1 Torr $\sim$ 1 mbar $\sim$ 100 Pa). The captured atoms are then transfered to a second MOT (MOT2) located in another chamber where the pressure is lower, typically $P_2 \sim 10^{-11}$ Torr, which is sufficient to ensure long lifetimes of the atomic sample, on the order of the minute. MOT1 is a 3D MOT. This choice was made to still be able to explore the interesting physics of large MOTs, which is the historical research subject of the group (long range interactions in MOTs, instabilities, light propagation and localization in MOTs, cf. e.g. Refs. [95–97, 100, 163–173]).

The two chambers are connected by a thin long tube. In this very low pressure regime, the typical time needed for the pressure to equilibrate between both parts is long, typically tens of minutes or hours, and since the two chambers are independently pumped, the system remains out of equilibrium. When the geometry of the tube and the pumping rates are well chosen, the steady state corresponds to the above mentioned pressure imbalance. With a laser beam going through the two MOTs and the differential pumping tube, the atoms of MOT1 are pushed and recollected by MOT2. Once MOT2 is loaded with enough atoms, all the remaining steps are performed in the second chamber. The design is sketched in Fig. 2.1.

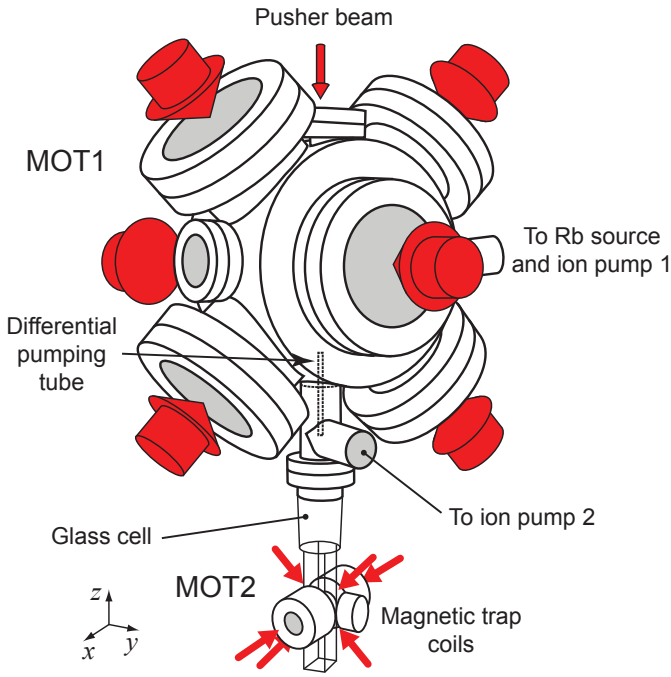

Figure 2.1: Schematic representation of the apparatus with the two magneto-optical trap chambers, the differential pumping tube, and the magnetic trap coils. The red arrows represent collimated laser beams.

Steel chamber

The upper chamber is made of ultra-high vacuum compatible 316L stainless steel and was assembled by the company Meca2000. A precise technical drawing of this part is given in App. A. The viewports have a broadband anti-reflecting coating on both sides, reducing the reflection below 1% on typically 100 nm around the specified wavelegth (780 nm). Six 100 CF viewports are used for the large MOT1 beams[2], and three 38 CF viewports are used for the vertical pushing beam and two additionnal ports for imaging and probe beams. One of the ports is connected to a 27 L/s ion pump, a valve separating the chamber from a copper tube containing solid Rubidium, and a valve to connect the turbo pump used during the bake-out procedure. There is also a bypass tube, generally closed by a valve, connecting the upper chamber to the lower one through the lower ion pump. This is opened only during bake-out to equally pump the two chambers.

[2]The references of the key components of the setup are listed in App. B.

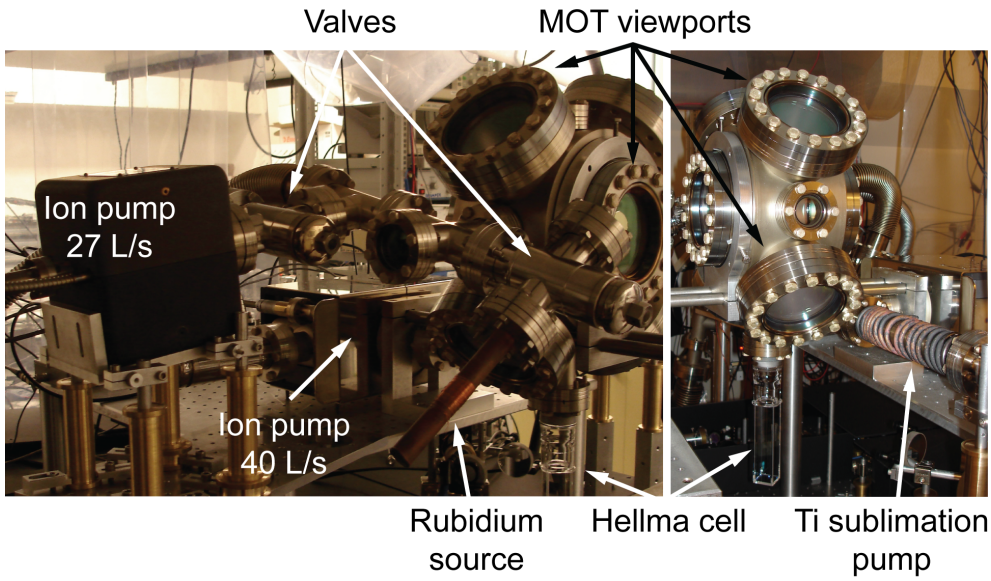

Figure 2.2: Photographs of the two sides of the vacuum system before any optical elements were placed.

Hellma glass cell

The lower chamber is a Vycor glass cell constructed by the company Hellma. Vycor is a glass with high temperature and thermal shock resistance, which can be baked without risks of breaking. It has an anti-reflecting coating on the outer surface ($R < 0.5\%$) but not on the inside. The lower part of the cell, in which the MOT and BEC are created, is made of 3 mm thick walls and has an outer square section of 30 mm. The choice of this size is the result of a compromise: on the one hand, we need enough space for the MOT beams, additionnal optical access for other elements such as dipole trap beams or probe beams, on the other hand, the magnetic trap coils need to be close to the atoms if we want them to be of reasonable sizes and carry low currents. For simplicity, we chose to have no elements (such as coils) inside the vacuum chamber. A technical drawing of the cell is given in App. A.

Differential pumping

The lower part of the upper chamber is closed by a welded piece of metal holding the differential pumping tube (length 10 cm, inner diameter 5 mm). This tube has a low conductance for gases which allow the two chambers to have different pressures when pumped by the two ion pumps. A pipe connected to a 40 L/s ion pump and a Titanium sublimation pump (TSP) is connected

below this separation, and the Hellma cell is connected below by a 35 CF flange.

For pressures below typically 10^{-3} Torr, the mean free path for molecular (atomic) collisions is bigger than the size of the apparatus, and the gas is in the so called *molecular flow* regime. The conductance of the differential pumping tube is then defined by [174]

$$U = \frac{Q}{P_1 - P_2}, \tag{2.1}$$

where Q is the gas flow, homogeneous to a power. The pumping speed S is defined by the same equation: $S = Q/P$, where P is the pressure of the pumped region. Pumping speeds and conductances are homogeneous to a volume per unit time and are often given in L/s. For a cylindrical tube with a radius r and a length $l \gg r$, the conductance is [174]

$$U = \frac{8\pi}{3}\frac{r^3}{l}\sqrt{\frac{k_B T}{2\pi m}}, \tag{2.2}$$

where m is the molecular mass and T the temperature. For instance, for Nitrogen gas, whose pumping speed is given by the pump constructors, and for our tube, we obtain $U \simeq 0.2$ L/s at room temperature. The pressure difference is given by the fact that, in a stationary regime, the flow through the second pump is the same as the flow through the tube. This yields

$$\frac{P_1}{P_2} \simeq \frac{S_2}{U}. \tag{2.3}$$

For our lower pump, $S_2 \simeq 45$ L/s (pressure between 10^{-11} and 10^{-9} Torr) and the corresponding differential pumping is thus $P_1/P_2 \simeq 200$. We will keep in mind that this tube leads to a drop of the pressure by two orders of magnitude.

Bake-out

When I arrived in the group we soon realized that the lower ion pump was dysfunctional. The pressure was thus much too high in the glass cell. The vacuum had to be broken and the experiment baked again (most of the optical elements had to be removed for that). The whole vacuum system was baked for one week at 250°C with a turbo pump connected to both chambers, while the ion pumps were off. When the turbo was connected, the inner pressure and gas composition could be monitored with a mass spectrometer. The turbo was then isolated from the chambers by a valve, the ion pumps were switched on and the TSP was used. When it was first switched on, the pressure increased dramatically, as indicated by the current increase of the ion pump, probably

due to the presence of dirt on the Titanium filament, which was cold during bake-out (it would have been better to heat them during bake-out to avoid this problem). After repeatedly switching the TSP on and off to clean the filament, and waiting for the dirt to be pumped, we could use it for 70 s with a moderate increase of the pressure. The use of the TSP clearly reduced the background gas pressure, as indicated by a subsequent increase of the lifetime of magnetically trapped atoms from a few seconds to more than 30 s. Since this initial use of the TSP, we never had to switch it on again.

Pressure

There is no pressure gauge on the apparatus, but the pressure (or at least the pressure variations) can be inferred from the evolution of the currents of the ion pumps and, most importantly, from the lifetime of the magnetically trapped samples. Another way to have an insight on the pressure, or to diagnose dysfunctional pumps is to look at how the MOTs load. Indeed the loading of a MOT from a room-temperature vapor can be simply modeled by a rate equation for the number N of trapped atoms [120]

$$\frac{dN}{dt} = R - N/\tau, \tag{2.4}$$

where R is the loading rate and depends on the MOT parameters (detuning, intensity, alignment, etc.), the gas temperature, and is proportional to the Rubidium pressure P_{Rb}, and τ is the loading time, which depends on both P_{Rb} and the background gas pressure P_{bg}. The steady-state number of atoms is obviously $N_\infty = \tau R$. When $P_{\mathrm{bg}} \ll P_{\mathrm{Rb}}$, the loss rate from the trap $1/\tau$ is also proportional to P_{Rb}, and N_∞ is thus independent of P_{Rb}. On the contrary, when P_{bg} cannot be neglected, N_∞ increases with an increasing P_{Rb}. In practice, these considerations were used to detect a dysfunctional pump by monitoring both τ and N_∞ while switching the pumps on and off, or closing and opening the Rubidium valve (i.e. changing P_{Rb}). Comparison of τ and N_∞ before and after using the TSP also gave some insight on the efficiency of the process.

We have seen that the pressure in the lower chamber is at least 100 times smaller than that in the upper one. From the MOT loading considerations, we know that the partial pressures of gases other than Rubidium are negligible (because the steady state number of atoms N_∞ is independent of P_{Rb}). At room temperature (20°C), the Rubidium contained in the chamber is mainly solid. At equilibrium with the solid phase, the vapor pressure is on the order of 10^{-7} Torr [108], which is too high. The upper Rubidium pressure is thus adjusted by measuring the loading time of MOT1. If it is too long, the Rubidium valve is opened, if it is too short, the valve is closed. After a few

days of adjustment, the MOT loading time converges to a value which allies sufficiently fast loading of MOT1, while the pressure in the glass cell is kept low enough.

2.1.2 The lasers

At least two frequencies are needed to laser cool ^{87}Rb. The first one is slightly red-detuned from the $|5^2S_{1/2}, F = 2\rangle \rightarrow |5^2P_{3/2}, F' = 3\rangle$ cycling transition (cooling light), whereas the second one is tuned to the $|5^2S_{1/2}, F = 1\rangle \rightarrow |5^2P_{3/2}, F' = 2\rangle$ transition (repumping light) and prevents atoms from accumulating in the lowest energy state $|5^2S_{1/2}, F = 1\rangle$ which is dark to the cooling light. These two transitions are part of the 780 nm D_2 line, and have a frequency difference of 6.567 GHz (mainly due to the hyperfine splitting of the ground state $\Delta_{\mathrm{HFS}}/2\pi = 6.835$ GHz). Such a difference is out of reach of acousto-optic modulators but could be obtained with electro-optic modulators [175] or by direct current modulation. For simplicity, we employ two separate diodes described in the following.

The DFB diode lasers

The light is thus provided by two distributed feedback (DFB) diode lasers. The gain region of DFBs is periodically structured as a Bragg mirror, providing feedback for a given frequency. This results in a narrow, monomode laser. The diodes are specified for 780 nm, and have a typical linewidth of 2 MHz, which is smaller but comparable to the linewidth of the D_2 line of ^{87}Rb, $\Gamma/2\pi = 6.067$ MHz.

Many groups use external cavity diode lasers (ECDLs, cf. e.g. Ref. [176] and the end of this section). Compared to them, DFBs have the advantage of being much more simple to build and to use (no grating and almost no settings needed, this is obvious from the comparison of Figs. 2.3 and 2.7). Contrary to ECDLs, DFBs do not exhibit mode hopping. Their main drawbacks are their great sensitivity to feedback, which is handled by a proper use of optical isolators, but more importantly, their linewidth is larger (typically 2 MHz for the ones we use, compared to 0.1 MHz for ECDLs). The consequences are discussed in more details in Sec. 2.1.7.

The output frequency can be tuned by playing on both the temperature and the current. The typical frequency variations are 1.5 MHz/μA and 30 GHz/°C. In order to maintain the laser frequency on the atomic transitions, both the temperatures and the current have to be precisely controlled. For this purpose, the diodes are mounted in homemade holders shown in Fig. 2.3. The setup is very simple: the diode is held in a small mounting containing a collimation lens, which is placed in a metal holder. The temperature of

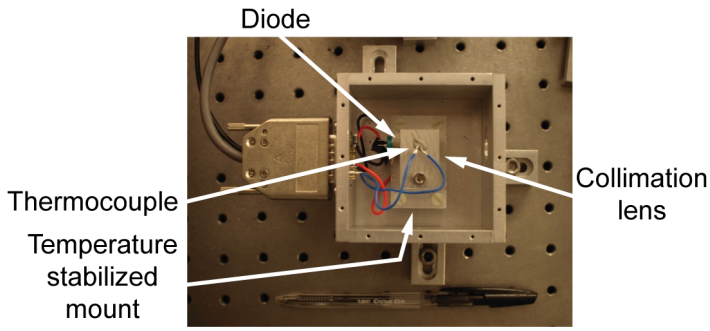

Figure 2.3: Photograph of a DFB diode laser. Two such lasers are used for the production of the BEC and imaging.

the whole thing is measured by a thermocouple positioned close to the diode, and controlled by a Peltier element which is under the mounting. The two lasers typically output 75 mW when maintained around room temperature and operating currents of 130 mA.

Saturated absorption, temperature and frequency stabilization

The temperature is servo-controlled to a constant value with a proportional-integral-derivative (PID) controller. The error signal is the subtraction of a constant set point from the output of the thermocouple, and the feedback is provided by heating or cooling the diode with the Peltier element.

The frequency stabilization is realized by modulating directly the diode's current (typical frequency 20 kHz, amplitude in the μA range) and using a lock-in amplifier taking the saturated absorption photodiode signal as an input, to obtain an error signal proportional to the derivative of the curve absorption vs current (the curves of Fig. 2.4). This error signal is maintained to 0 by a PID controller acting on the diode's current. This system can thus lock the laser on any sufficiently intense absorption line. Figure 2.4 shows the absorption signals used to lock the two lasers.

These techniques have been commonly used for decades, and the circuits we use, which are made by the laboratory's electronics engineers, are not given in this thesis. For instance Ref. [177, p. 46] contains a basic explanation of saturated absorption signals, and more information about the use of diode lasers for atomic physics can be found in Refs. [176, 178] (including electronic circuits). Reference [179] also contains detailed electronic circuits of PID controllers and interesting considerations on diode lasers stabilization.

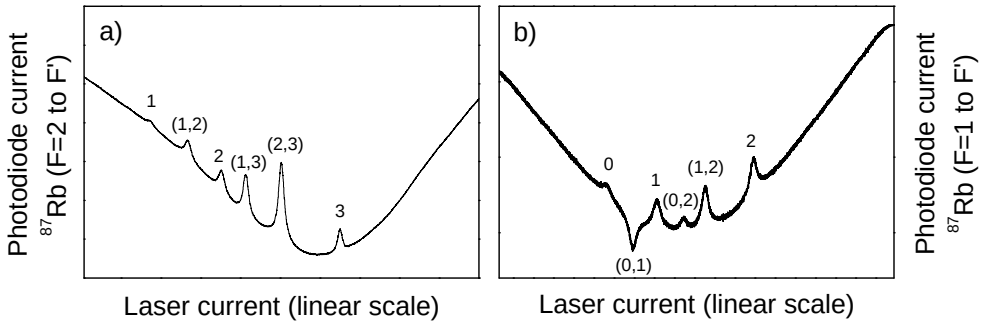

Figure 2.4: Saturated absorption signals used to lock the two lasers. In both cases the six lines corresponding to the three transitions $F \to F' = F$, $F \to F' = F \pm 1$ and the three crossovers are visible. DFB1 and 2 are respectively locked on the $F = 2 \to (F' = 2, F' = 3)$ and $F = 1 \to (F' = 1, F' = 2)$ crossovers of ^{87}Rb.

Required frequencies

In addition to the cooling and repumping light, many frequencies are needed throughout the experimental cycle: a detuned pushing beam is needed to transfer the atoms from MOT1 to MOT2, optical pumping between the Zeeman states of the $|5^2S_{1/2}, F = 2\rangle \to |5^2P_{3/2}, F' = 2\rangle$ transition requires a pump and a repumper, and a beam is needed to image the atoms. All the laser frequencies corresponding to these beams, together with the structure of the D_2 line of ^{87}Rb are represented in Fig. 2.5. They are obtained by frequency shifting the light of the two DFBs with AOMs, as shown in Fig. 2.6.

As indicated in Fig. 2.4, the lasers (DFB1 and DFB2) are respectively locked on the $F = 2 \to (F' = 2, F' = 3)$ and $F = 1 \to (F' = 1, F' = 2)$ crossovers of ^{87}Rb.

Laser setup

A schematic of the laser setup used to produce all these frequencies is given in Fig. 2.6. The power needed for the two MOTs is obtained by injecting both the cooling and repumping light into a single 1.4 W tapered amplifier (TA). The beam is then split in two, one for each MOT.

The laser system sketched in Fig. 2.6 is on the same optical table as the vacuum system. To prevent stray light from illuminating the atoms, a black cardboard box covers all the optical elements. Obviously most of them are not shown in Fig. 2.6 (mirrors, lenses, etc.). All the beams are finally injected into single-mode polarization-maintaining fibers. Because magnetic trapping is very sensitive to resonant stray light (which induces losses of atoms), the

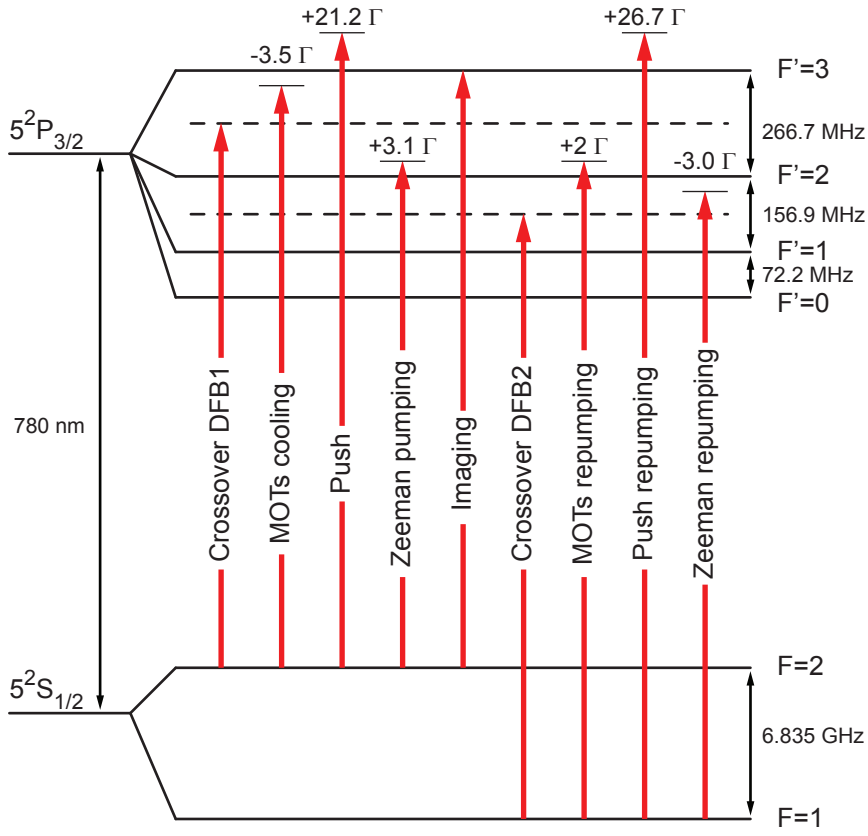

Figure 2.5: Rubidium-87 D_2 line structure and laser frequencies used on the BEC setup. All the frequencies are produced from two DFB diode lasers locked on the indicated crossovers. The detunings with respect to the closest lines (defined as $\omega_{\text{laser}} - \omega_{\text{line}}$) are given in units of the natural linewidth $\Gamma = 2\pi \times 6.067 \times 10^6$ rad/s.

fibers input couplers are preceded by telescopes with homemade mechanical shutters positioned at the focal points. This allows complete extinction of the light. The shutters typically have delays around 10 ms, which are calibrated and compensated in the control program, and jitters of 0.1 to 0.5 ms. Precise and fast switching is thus provided by the single pass AOMs, while the shutters provide a complete extinction (with a delay).

For each MOT the light is delivered by six polarization-maintaining optical fibers, ensuring a good long-term stability of the alignment. We used to split the beam into six with five half-wave plates followed by cubes. The resulting six beams were then injected into six independent fibers. This setup worked well and was used for almost all the data presented in this thesis, but it

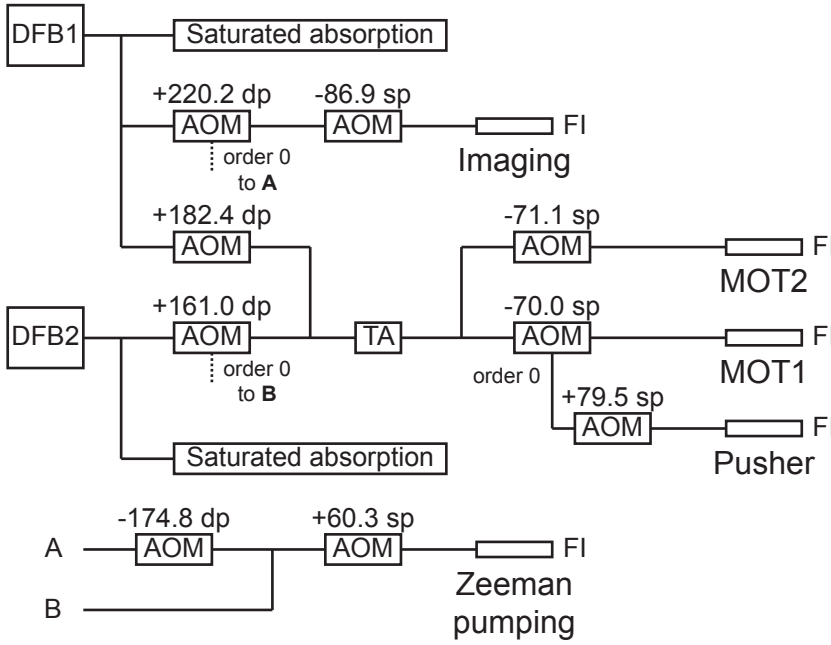

Figure 2.6: Schematic representation of the laser system. Acousto-optic modulators (AOMs) are used in double pass (dp) or single pass (sp) configuration to control the laser frequencies and amplitudes. The frequency shifts, indicated above, are given in MHz. The order 0 of two AOMs in double pass configuration are "recycled" for the Zeeman optical pumping beams. A single 1.4 W tapered amplifier (TA) is used to provide enough power for the two MOTs. All the beams are finally injected into single-mode polarization maintaining fibers (FI), or fibered splitters.

was quite sensitive to day-to-day fluctuations (probably room temperature fluctuations) and had to be checked, and the power balanced, everyday (we had one photodiode per fiber output to check the power balance). Only two mirrors positioned before the splitting of the beam into six were used to inject the six fibers, and it was sometimes tricky to get the full power back after it had dropped. The total coupling efficiency of the splitting was between 50 and 60% at best, mainly because of the poor output beam profile of the TA and also because of the limited degrees of freedom we had to inject the six fibers.

An important improvement of the experiment consisted of replacing these homemade splitters by commercial one-to-six fibered splitters. Since only one input fiber has to be injected, it is much easier to set. The day-to-day stability is also better. A drawback is that the balance cannot be adjusted (the difference between the two most imbalanced beams is 20%).

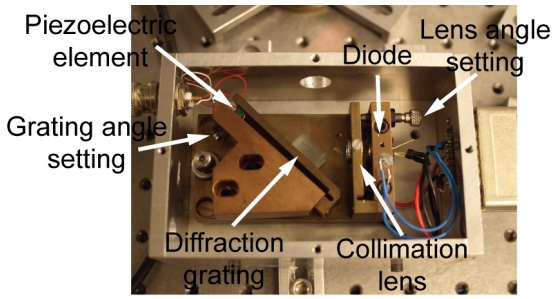

Figure 2.7: Photograph of an ECDL used for the blue detuned dipole trap. The temperature of the whole copper part is regulated by a Peltier element (not visible).

Finally, the outputs of the MOT fibers are simply positioned at the focal points of collimation lenses. For MOT1, they have a diameter of 10 cm and focal length of 30 cm. The collimated beams have a resulting waist ($1/e^2$ radius) of 2.7 cm inside the steel chamber. Because of this large size, the quarter-wave plates of this MOT are positioned directly after the fibers outputs, where the beams are not collimated. More details on the MOTs are given in Sec. 2.2.1.

Blue-detuned laser for dipole potentials

The external cavity diode laser (ECDL) shown in Fig. 2.7 was constructed and used for dipole potential experiments. The output surface of the diode is coated to reduce the reflectivity so that the diode itself does not behave as a cavity. The laser cavity is formed by the diode's back face and the diffraction grating, used in Littrow configuration. This means that one of the first-order diffracted beams is sent back to the chip, while the zeroth-order reflected beam is the output beam. In order to stabilize such lasers, the temperature is regulated (diode and cavity) with a single Peltier element. For frequency stabilization, a fast servo loop acts on the current while a slower one acts on the grating's angle. In practice, we use this ECDL 15 nm away in the blue of the D_2 transition (i.e. the detuning is $\delta/2\pi \sim +10^3$ GHz) and since the frequency variations are less than 1 GHz, there is no need to lock this laser when we use it as a dipole trap (only the temperature is stabilized).

By changing the grating angle with the adjustment screw, the laser can be tuned as far as 20 nm away from the maximum of the gain curve with still a reasonable output power. We use a diode specified for 780 nm which is pulled to 765 nm. Stabilized around room temperature, the laser has an output power of 26 mW for a current of 68 mA. It is then amplified by a TA specified for 770 nm. It can output up to 1.5 W when injected with 24 mW.

In addition to the intense narrow peak at 765 nm, the output beam spectrum also contains a broad, much less intense component reflecting the gain curve of the TA diode (pedestal). It typically contains 1% of the total power with a FWHM of $\sim$ 15 nm. It thus contains a non-negligible quantity of resonant light (780 nm) which can have dramatic effects on the atoms when they are trapped in the dipole potential, since absorption/spontaneous emission cycles induce heating and losses from the trap. We use an interferometric band-stop filter to block this resonant light. The wavelengths between 767 and 800 nm are reflected (optical density > 6) while the rest of the spectrum is well transmitted ($T > 93\%$ between 400 and 1600 nm). The edges at 767 and 800 nm are sharp (the transmission drops from 90% to 10% on ~ 1 nm).

2.1.3 The magnetic trap

As we have seen in Sec. 1.4, magnetic trapping is an essential step in the preparation of BECs. We have built the trap ourselves, with the help of the group mechanical engineer Jean-Charles Bery. The key features of a magnetic trap are its depth, its volume and the fact that its minimum has a non-vanishing magnetic field. The trap shape (harmonic, linear, etc.) also plays an important role during evaporative cooling, as presented in Sec. 1.4.2. Another important practical consideration is the optical access left by the trap coils to add other laser beams for imaging, optical trapping and so on.

Requirements

The trap was designed for ^{87}Rb atoms in the $|5^2S_{1/2}, F = 2, m_F = +2\rangle$ states. Two other levels can be trapped magnetically ($|F = 2, m_F = +1\rangle$ and $|F = 1, m_F = -1\rangle$) but their Zeeman shift is twice smaller, and thus, twice higher fields would be required to obtain the same potential. For this state, the Zeeman shift is 1 Bohr magneton $\mu_B/h = 1.4$ MHz/G $\simeq 70$ μK/G $\times$ (k_B/h) (1 G $= 10^{-4}$ T). In order to hold the atoms against gravity, the vertical magnetic field gradient must be greater than $mg/\mu = 15.3$ G/cm. Since the atoms are first cooled in a MOT ($T \sim 100$ μK), a typical trap depth of 1 mK is sufficient to trap the atoms without "spontaneous" evaporation, which corresponds to a magnetic depth of ~ 15 G. Moreover, the minimal field value must not be too small (~ 1 G) in order to prevent non-adiabatic spin flips [103]. In practice, most of the macroscopic magnetic traps used for neutral atoms have higher peak values than those imposed by the requirements mentioned above (on the order of 500 G). This is because the trap volume must be small in order to obtain the large densities required for evaporative cooling (that is high gradients or trap frequencies).

The QUIC trap

The trap we have built is a quadrupole-Ioffe-configuration trap (QUIC), very similar to the original version introduced by Esslinger et al. [149]. It is composed of two coils in anti-Helmholtz configuration (quadrupole coils) which generate a spherical quadrupole field, plus a smaller additional coil (the Ioffe coil) which almost cancels the quadrupole field close to its tip, to produce a non-zero field minimum. Because the coils are made of a lot of turns of wire and are positioned quite close to each other, it requires a low current (less than 30 A). The consumed electrical power is low (below 1 kW), and the associated thermal problems are reduced. The price to pay for using lots of turns is the high trap inductance (on the order of 0.1 mH) which complicates fast switching.

The main idea of this trap is to first use the spherical quadrupole to capture the atoms of the MOT (at this point there is no current in the Ioffe coil), and then to convert this quadrupole into a Ioffe-Pritchard-like trap (harmonic with non-vanishing magnetic minimum) by ramping the current in the Ioffe coil. After capturing the cloud in the quadrupole, the temperatures is too high for non-adiabatic spin flips to be consequent, and the corresponding losses are negligible. Because the final Ioffe-Pritchard trap has a non-vanishing minimum, it is appropriate for evaporative cooling. Since the atoms are first trapped in a quadrupole, the same coils can be used before for the MOT, and the two traps are automatically superimposed, which simplifies the transfer. Figure 2.8 shows the arrangement of the three coils and the corresponding magnetic field when the Ioffe coil current is gradually increased.

Design and construction

A top view of the three coils and their position with respect to the glass cell is shown in Fig. 2.9. Each quadrupole coil is made up of 180 turns of 1.7 mm thick enameled copper wire, wound and glued on water cooled copper mountings. The glue is an aluminum-filled epoxy that is highly heat conducting to improve heat transport to the water-cooled mountings. The Ioffe coil is made up of the same materials, and is conical to allow access to the MOT beams. Its 176 turns create a field opposed to the quadrupole (on the y axis) and more intense. This yields a minimum at a distance of 8 mm from the quadrupole center (on the y axis). Around this trap minimum, the projection of $\mathbf{B}$ on y is quadratic ($\partial_y B_y = 0$, $\partial_{yy} B_y \neq 0$) and the projections on x and z are linear with position, with the same gradient (because $\nabla \cdot \mathbf{B} = 0$). At the trap minimum, the field is aligned in the y direction and its value is $B_0 \simeq 1$ G. The design of the trap (coil size, number of turns, etc.) was achieved using a numerical calculation of the field. Cuts of the field magnitude along three

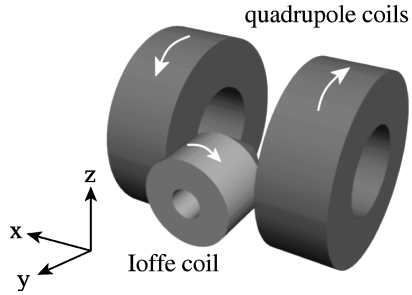

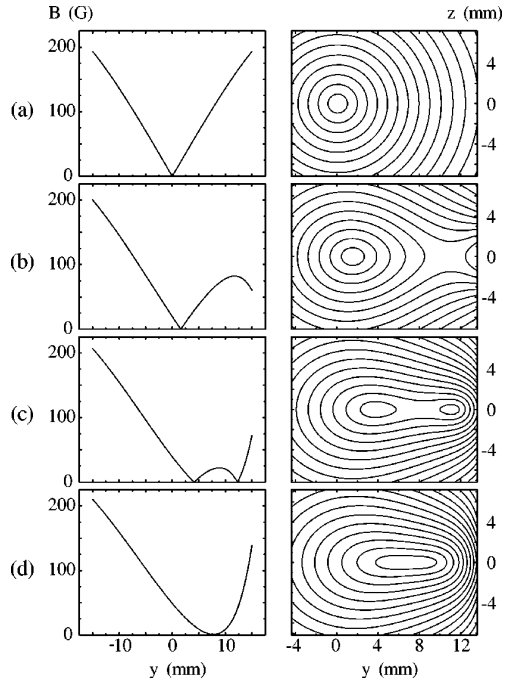

Figure 2.8: Both figures are from Esslinger et al. [149]. (Left) Sketch of the three coils of the QUIC trap. The arrows indicate the direction of the current flowing through the coils. (Right) Absolute values of the magnetic field along the y axis (left column) and in the y-z plane (right column) are shown, calculated for a fixed current of 25 A in the quadrupole coils and increasing currents in the Ioffe coil [(a) 0 A to (d) 25 A]. Each contour in the right column corresponds to an increase of 15 G of the field magnitude.

orthogonal planes are represented in Fig. 2.10.

Because of the difficulty of accurately winding conical coils, the actual coils were slightly different from the design, resulting in a double minimum such as in Fig. 2.8c. This was solved by adding a few turns to the Ioffe coil.

Field measurement and expression

Once the coil assembly was completed, the trap parameters were directly measured with Hall probes. The figures are given in Tab. 2.1.

As seen on Fig. 2.8 and 2.10, the potential does not have a simple shape (not simply harmonic or linear). When $k_BT \gg \mu B_0$, the potential is somehow linear in the z-x plane and harmonic on the y axis. Nevertheless, for $k_BT \ll \mu B_0$, which is the case close to degeneracy (cf. Sec. 2.1.5), the trap is a three-dimensional harmonic potential, whose frequencies are obtained by expanding the field magnitude about its minimum. It is important to know these frequencies because they determine the quantum level spacings, enter the transition temperature, and so on. The expression of the IP field magnitude

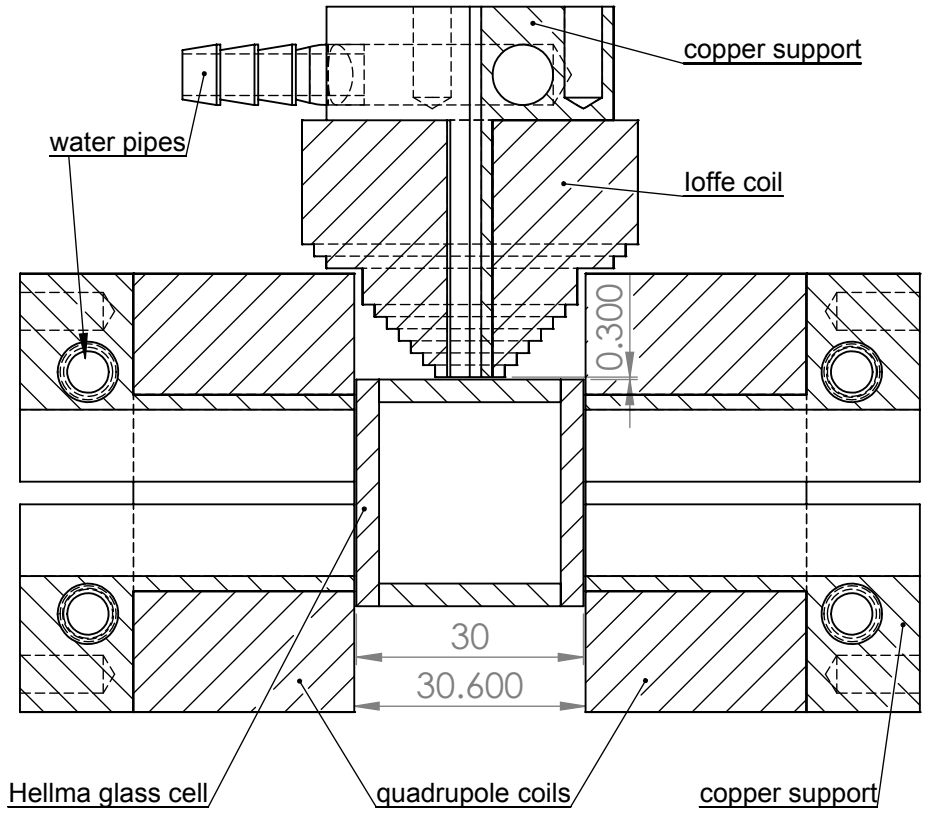

Figure 2.9: Top view of the magnetic trap (cut through the coil centers).

in the neighborhood of the minimum is [180]

$$B(x,y,z) = B_0 + \frac{1}{2}\left(\frac{B'^2}{B_0} - \frac{B''}{2}\right)\left(x^2+z^2\right) + \frac{1}{2}B''y^2, \tag{2.5}$$

and the trap frequencies are given by

$$\nu_x^2 = \nu_z^2 = \frac{\mu}{(2\pi)^2 m}\left(\frac{B'^2}{B_0} - \frac{B''}{2}\right), \tag{2.6}$$

$$\nu_y^2 = \frac{\mu}{(2\pi)^2 m}B''. \tag{2.7}$$

The second term in (2.6) can often be neglected (with our parameters, $B_0 B''/2B'^2 \simeq 0.6\%$). With the measured values of Tab. 2.1, this yields a

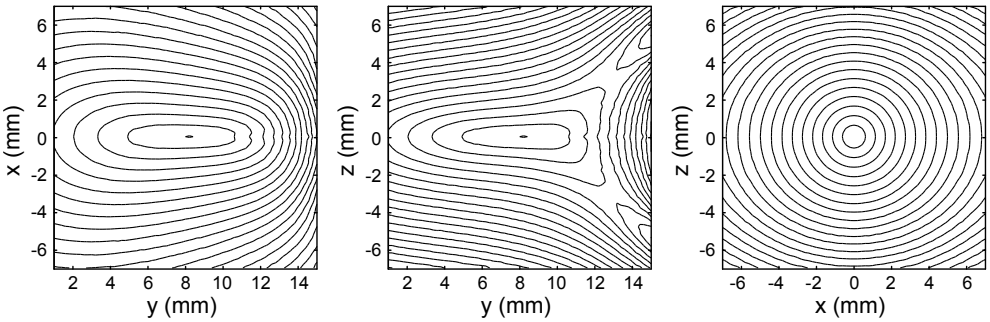

Figure 2.10: Contour plots of the magnetic field magnitude in the IP configuration for a current $I = 26.7$ A (numerical calculation): cut through $z = 0$, $x = 0$ and $y = 8$ mm. Each contour corresponds to an increase of 15 G. The origin $(x = 0, y = 0, z = 0)$ is the quadrupole center.

radial frequency $\nu_r \equiv \nu_{x,z} = 177$ Hz and an axial one $\nu_y = 19$ Hz. These values are smaller (by 30% and 12% for ν_r and ν_y respectively) than those directly measured using the oscillations of the trapped atoms (see Sec. 2.2.2). The finite size of the Hall detectors, which yields a convolution of the measured profiles may have something to do with this mismatch. Nevertheless, it is mainly due to the fact that B_0 is overestimated by these direct measurements (a more precise value of $B_0 \lesssim 1.7$ G was measured by evaporating the atoms) and the great sensitivity of ν_r to a small reduction of B_0. For instance, taking the same values, but $B_0 = 1$ G gives $\nu_r = 245$ Hz. Also these expressions do not take into account gravity. If the magnetic field were perfectly harmonic, gravity would not change the oscillation frequency, but here, the influence of the anharmonicity on the vertical frequency cannot be neglected.

Power supply and control electronics

On the one hand, in order to convert the quadrupole into a IP trap, one must be able to set the Ioffe current independently of the quadrupole current. On the other hand, in the final configuration (IP), the three coils must be in series in order for the field fluctuations to be correlated[3]. The three coils of the QUIC trap are thus powered by a single stable 48V/50A generator connected to a homemade analog current control box. A sketch of the electronics is given in Fig. 2.11.

The quadrupole coils are in series with the Ioffe coil, but the latter is also in parallel with a shunt in which all the current can be transfered. The current

[3]When the three coils are powered by independent generators, the current noises are not correlated and lead to a fluctuation of the trap center position and shape. This generally leads to high heating rates even with stable generators ($\Delta I/\bar{I} \sim 10^{-3}$).

Configuration	Parameter	Value (G/cm/A)	Value @ 26.7 A (G/cm)
Quadrupole	$\partial_z B_z$	5.2	139
	$\partial_x B_x$	10.4	278
	$\partial_y B_y$	5.2	139
IP	B_0	0.072 G/A	1.9 G
	$B' \equiv \partial_z B_z$	7.28	194
	$\partial_x B_x \simeq B'$	7.12	190
	$B'' \equiv \partial_{yy} B_y$	8.24 G/cm^2/A	220 G/cm^2

Table 2.1: Measured parameters of the quadrupole and Ioffe-Pritchard (IP) traps. The quadrupole is characterized by its gradients along the three axes around the trap center (point where $\mathbf{B} = \mathbf{0}$). The IP is characterized by two gradients and one curvature around the field minimum (point where $\mathbf{B} = B_0 \mathbf{u}_y$). The units are G/cm/A and G/cm unless specified. The center of the IP is positioned 8.1 mm away from the quadrupole center on the y axis.

in the three arms can be controlled independently by three servo loops, with the obvious constraint $I_{\text{Ioffe}} + I_{\text{shunt}} = I_{\text{Quad}}$. The main issues in designing the circuit of Fig. 2.11 were: (i) making the the servo loops stable on a wide range of set points (from 0 to 30 A), because of the non-linearity of the feedback loops (due to the response of the transistors), (ii) properly handling heat dissipation in the power transistors (which would burn after some time of use, this was fixed by using several in parallel for the control of I_{Quad}), (iii) having a fast switch-off. In the current setup, it is still quite long, on the order of 1 ms. The design of this circuit is not detailed in this thesis.

2.1.4 Other coils

The coils of MOT1 are made of hundreds of turns of 1.7 mm thick enameled wire positioned around two opposite viewports of the steel chamber. They are powered by a 30V/20A generator connected to a homemade switch (controlled by a TTL signal). They produce of a gradient of 7.8 G/cm/A (tighter axis).

In order to compensate the residual magnetic field (important for the optical molasses), or to slightly displace MOT2, three orthogonal pairs of compensation coils in Helmholtz configuration are present in MOT2 (not in MOT1). They are made up of approximately 20 turns of 1.7 mm thick wire and can be powered with a few amperes of current. They are large (tens of centimeters of diameter) to produce homogeneous fields on the order of 1 G/A and not to reduce optical access. The resulting field does not change by more than a few percents on 1 cm. They are powered by stable 30V/3A power supplies connected to homemade two-value boxes or, for one of the pairs (on the y

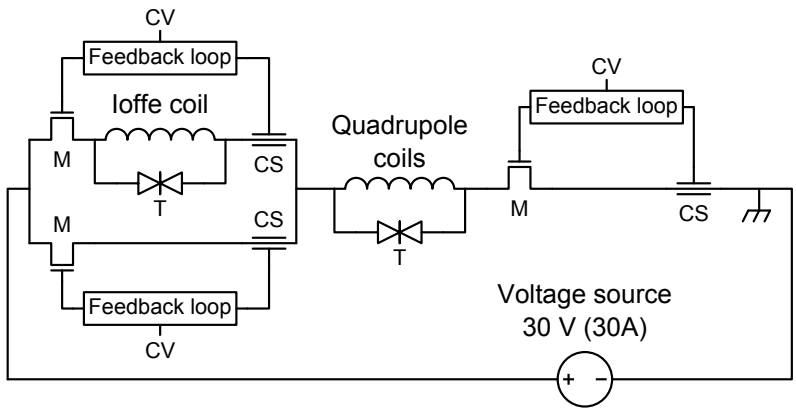

Figure 2.11: Sketch of the QUIC trap current control electronics. The currents in the three arms are controlled by servo loops consisting of Hall current sensing elements (CS) and power field-effect transistors (M). The set points of the servo loops (i.e. the currents) are set by control voltages (CV) generated by the computer. Transient voltage suppression diodes (T) are used for fast current cut off and to protect the transistors from high voltages.

axis), an analog current control electronic circuit. The pair aligned on the y axis can be used to change B_0 independently of the gradient and curvature of the magnetic trap.

2.1.5 The radio-frequency source

Let us first recall a few important values: the recoil velocity is the change of velocity when absorbing or emitting a resonant photon

$$v_\mathrm{r} = \frac{\hbar k}{m} \simeq 5.88 \text{ mm/s} \tag{2.8}$$

for the D_2 line of ^{87}Rb. The kinetic energy of an atom with a velocity v_r is called the recoil energy:

$$E_\mathrm{r} = \hbar\omega_\mathrm{r} = \frac{1}{2}mv_\mathrm{r}^2 = \frac{\hbar^2k^2}{2m}, \quad \omega_\mathrm{r}/2\pi \simeq 3.77 \text{ kHz}. \tag{2.9}$$

The corresponding temperature is the recoil temperature:

$$T_\mathrm{r} = \frac{mv_\mathrm{r}^2}{k_B} = \frac{\hbar^2k^2}{mk_B} \simeq 362 \text{ nK}. \tag{2.10}$$

It is sometimes defined with an additional factor 1/2. We use the definition (2.10) such that during a time of flight, the temperature of a cloud whose rms width expands with a velocity v_r is T_r.

The typical temperature of the cloud just before starting the evaporation is about 400 μK $\simeq 10^3 \times T_\mathrm{r}$. This means that the atoms typically explore the region of the trap where their potential energy varies between 0 (at the trap center) and $10^3 \times E_\mathrm{r} \simeq h \times (4\ \mathrm{MHz})$. Since the atoms are trapped in the $|F = 2, m_F = +2\rangle$ state, two rf photons of the same energy are required to drive the transitions $|F = 2, m_F = +2\rangle \to |F = 2, m_F = +1\rangle \to |F = 2, m_F = 0\rangle$ and expel them. The rf frequency needed to evaporate the atoms is thus typically $4/2 = 2$ MHz. As we have seen in Sec. 1.4.2, evaporative cooling is most efficient when the parameter $\eta = (\text{trap depth})/k_B T$ is on the order of 10. The initial frequency needed is thus about 20 MHz. In this discussion, we have neglected the additional ~ 0.7 MHz, which comes from the fact that the trap minimum has a nonzero magnetic field, on the order of 1 G.

Efficient evaporation leads to the formation of a BEC when the critical temperature is reached. For $N \sim 10^6$ atoms and our trap parameters, this temperature is about 500 nK $\simeq T_\mathrm{r}$. Evaporation of such a cold cloud with $\eta = 10$ requires a final frequency $\nu_\mathrm{stop} \simeq 10 \times 3.77/2 + 700$ kHz. The first term corresponds to the trap depth $10\, k_B T$ (assuming $T = T_\mathrm{r}$), while the second one is the offset due to the bias field $B_0 = 1$ G. From this expression it is clear that B_0, which can be neglected at the beginning of the evaporation, is dominant at the end.

To illustrate the role of the rf frequency stability, let us assume that $\Delta\nu_\mathrm{stop}/\nu_\mathrm{stop} = 1\%$. This leads to a fluctuation of η by almost 40%. The same argument applies if ν_stop is stable but B_0 is fluctuating.

This underlines the requirements for a good rf source:

- ability to perform frequency ramps between 20 and 1 MHz within seconds or tens of seconds,
- the possibility to choose the absolute value of the final frequency to better than a few kHz,
- relative frequency fluctuations in the 10^{-3} range.

Moreover, the optimization of evaporative cooling requires the ability to manipulate the shape of the frequency ramp and the rf amplitude during the ramp.

In the experiment, the rf is produced by a digital function generator which meets the above requirements. In the "3D mode", arbitrary ramps can be used to control the amplitude, frequency and phase vs time, without degrading the quality of the spectrum. It is followed by a 25 W amplifier which has a relatively flat gain curve on the range used to evaporate, and has been chosen to be completely tolerant to impedance mismatch between its output and the antenna. The antenna is a 4 cm square loop of 1.7 mm-thick copper wire with

5 turns. It is positioned at the bottom of the Hellma cell, with its symmetry axis aligned vertically (the coil center is thus 5 cm away from the quadrupole center). In this way, the magnetic field created by the coil is perpendicular to the magnetic trap bias field. Since the symmetry axis of the rf antenna is perpendicular to the axes of the magnetic trap coils, the induction of rf in these coils is reduced.

2.1.6 Computer control

As it will be presented in Sec. 2.2, the production of BECs involves a variety of experimental steps which have to follow each other with precise timing. Moreover, the timescales involved vary between the full sequence time on the order of the minute (thermal effects can have even longer characteristic times), down to times related to the atomic response (the lifetime of the excited state $5^2P_{3/2}$ of ^{87}Rb is 26.2 ns). This requires an efficient control of the experiment with computers and fast electronics.

Hardware

The computer control is based on a single cheap National Instrument (NI) analog output card inserted in a standard personal computer running Windows Vista. This card has 32 analog outputs, and 8 digital (TTL) outputs, which are not currently used. The analog outputs are directly accessible through a series of BNC connectors. The output voltage is between -10 and $+10$ V, and is encoded on 13 bits (resolution of 2.4 μV). The card has its own internal clock and the sample rate can be adjusted on a wide range, which depends on the number of outputs used. We use all the outputs, and a sample rate of 10 kS/s (i.e. a time step of 100 μs). This choice corresponds to a trade-off between the short time step needed for some operations (the shortest event is the imaging pulse) and the relatively important quantity of data which results from the sampling of 32 analog channels when the total cycle duration is on the order of 30 s. From this point of view, using only analog outputs is not optimal.

Software

The NI card is controlled by Matlab via the Data Acquisition Toolbox, which considerably simplifies the programming of the card (only a few matlab functions are needed to talk to the card). A Matlab graphical user interface (GUI) was developed to easily program the signals. The GUI programming is object oriented, and its class structure was designed in a way which makes adding other devices (such as function generators or other similar cards) relatively easy.

The main features of this user interface are the following: various devices (corresponding to physical output cards or function generators) can be configured by selecting the channels to be used, giving them names, physical units, and calibration functions (to convert the physical values entered by the user into voltages). The main object is a *sequence*, which corresponds to a given experiment, for instance the production of a BEC. The default behavior is to loop identical sequences. A sequence is made of a series of *events* which follow each other. For instance, a first event is used to load the two MOTs, another one for the compressed MOT, and so on. For each event, the user chooses what channels are going to be used, and defines the signals by entering a series of times and values, or functions to be output. Each channel has its "default signal" which is used by default when the channel is not used in an event.

Instead of real numbers, the boxes in which the times and values are given can contain words, defining *variables*, or *parameters*. In the main panel of the GUI, these parameters can be given values. They can also contain vectors instead of single values, so that scans can be done. In this case, each time a sequence is completed, the parameters take the next value in the vector, and the sequence is started again with new values. "Multi-dimensional" scans can be done, and priorities can be attributed to the parameters to define the order in which they will be changed.

This software has been developed from scratch during the three years of my thesis. Most of the experiments presented in this thesis were done before automated scans could be performed. At this time, the setup was stopped for a few seconds (all the channel's voltages went to 0 V) every time a parameter was changed. When adding the "scan" feature, the program was also modified to suppress this dead time between two sequences. This dramatically improved the reproducibility and stability of the experiment, probably because, with the new system, the AOMs are never stopped. Indeed, when an AOM is stopped (the frequency control voltages were set to 0 V which induced a jump of the detunings), its temperature changes, and the output polarization turns, which leads to laser intensity fluctuations from shot to shot.

2.1.7 Detection and imaging

Various probes are used to set the experiment and to monitor what is happening when it runs: photodiodes to measure laser intensities, Hall probes to monitor the magnetic fields, thermocouples to check the temperatures of the coils, CCD cameras for imaging, etc. Most of these detectors are standard. We give here a few details on the imaging techniques, and on the cameras used.

We use different models of CCD cameras for imaging and to look at laser beam profiles. They are controlled via a homemade matlab software. A library

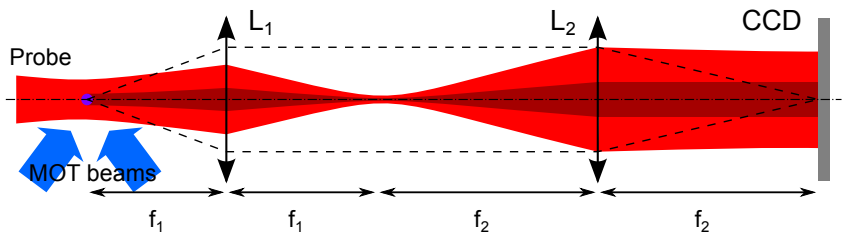

Figure 2.12: Principle of fluorescence and absorption imaging. For absorption imaging, a Gaussian probe beam (red) is sent on the optical axis and the shadow of the cloud is imaged onto a CCD. For fluorescence imaging, this probe is not used, but the cloud is illuminated by the MOT beams (blue) and the scattered photons are captured by the same imaging system. The lenses are positioned in a $4f$ configuration such that both the geometrical image and the image waist of the probe laser are positioned on the CCD.

of functions coded in C and compiled in a way that makes them accessible to matlab (so called "MEX-files" in matlab's jargon) was developed to talk to the cameras (set the shutter, gain, binning, retrieve the images, etc.). They are always triggered with an external TTL signal.

The main ways to measure the atomic cloud we have used are absorption and fluorescence imaging. A sketch illustrating these two techniques is presented in Fig. 2.12.

Fluorescence imaging

The principle of fluorescence imaging is to shine a near resonant laser beam on the cloud and to image the scattered photons (the *fluorescence*) on a CCD. The resulting image will reflect the atomic density integrated along the direction perpendicular to the CCD plane if all the atoms scatter on average the same number of photons, and that these photons reach equally the CCD. This can be achieved in two distinct regimes: (i) in the linear regime, when the cloud is not optically thick, depletion of the pump beam and multiple scattering effects are avoided, or (ii) in the opposite regime of strong saturation where the cloud has become transparent to the pump light and all the atoms scatter the maximum number of photons (i.e. with a rate $\Gamma/2$). This requires a saturation parameter $s \gg b$, where b is the optical thickness of the cloud. We always operate in the first regime. The pump beams we use are directly the beams of the MOTs, and the optical thickness can be reduced by detuning by a few linewidths on either side of the atomic transition. A major drawback of quantitative fluorescence imaging (in the linear regime) is that it requires a careful calibration of the detection (including CCD, detection solid angle, light intensity).

In practice we always take two images: the first one captures the fluorescence and the second is a background image taken some time after the cloud has fallen. It is subtracted to the first one to get rid of stray light. Examples of fluorescence images can be found in Fig. 2.18.

Absorption imaging

Absorption imaging is the technique commonly used to image the cloud at the end of evaporation, and the BEC. It consists in measuring the shadow cast by the cloud on a laser beam. Three images are taken: the shadow, the probe beam without atoms and a background image (no probe beam), which is subtracted to the two others (to remove stray light). The ratio of the two resulting images give the spatially resolved transmission $T(x, y)$. The optical thickness $b(x, y)$ (also called optical depth, optical density or absorbance) is defined by the Beer-Lambert law

$$T(x, y) = \exp\left[-b(x, y)\right]. \tag{2.11}$$

This expression is valid for a purely monochromatic probe laser. The optical density is directly related to the cloud's column density $\tilde{n}(x, y) = \int \mathrm{d}z\, n(x, y, z)$, by [181]

$$b(x, y) = \frac{\sigma_0}{1 + 4\,\delta^2}\,\tilde{n}(x, y), \tag{2.12}$$

where σ_0 is the resonant scattering cross-section and δ is the laser detuning with respect to the transition in units of the linewidth Γ.

We image the atoms on the $|5^2S_{1/2}, F = 2\rangle \rightarrow |5^2P_{3/2}, F' = 3\rangle$ transition, in the absence of a significant magnetic field. For such an atomic transition with a Zeeman substructure, the resonant scattering cross-section is

$$\sigma_0 = g\frac{3\lambda^2}{2\pi} \tag{2.13}$$

where g depends on the Zeeman substate and the laser polarization. For instance, if the atoms are in $m_F = +2$ (with respect to the light propagation axis) and only σ^+ transitions are driven (clean circular polarization) the system is a two-level atom ($|F = 2, m_F = +2\rangle \rightarrow |F' = 3, m_{F'} = +3\rangle$) and $g = 1$. Since we do not control the field during imaging, we do not know the population in the different Zeeman sublevels. We assume $g = 7/15$ which is the appropriate value when the Zeeman substates are equally populated and these populations are stationary (no optical pumping), and is independent of the light polarization. This is a crude assumption, and, since the measured number of atoms is proportional to g, our number measurement is not absolute.

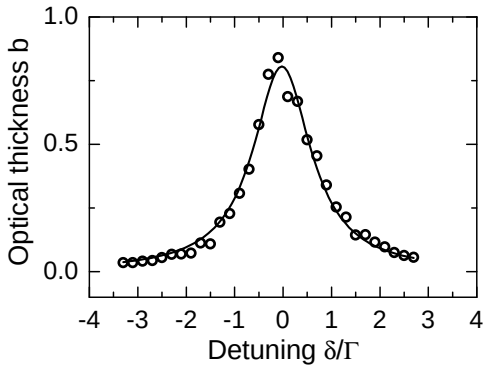

Figure 2.13: Indirect measurement of the imaging probe linewidth. A cloud of resonant optical thickness $b_0 \simeq 0.8$ is prepared and the optical thickness b is measured vs the laser detuning. The resulting curve is close to a Lorentzian (fitted line) with a width $\Gamma_m = 1.4\,\Gamma$. This broadening is attributed to a laser linewidth of a fraction of Γ, consistent with the diode's specifications (typical value $\Gamma_L/2\pi = 2$ MHz).

Effect of the probe's linewidth

We assume the probe beam is centered on the atomic transition (angular frequency ω_0) and has a Lorentzian spectrum with a linewidth Γ_L:

$$S_L(\omega) = \frac{2}{\pi\Gamma_L}\,\frac{1}{1+4\left(\frac{\omega-\omega_0}{\Gamma_L}\right)^2}. \tag{2.14}$$

The measured transmission is thus the average

$$T = \int \mathrm{d}\omega\, e^{-b(\omega)} S_L(\omega), \tag{2.15}$$

where $b(\omega)$ is given by Eq. 2.12. At first order in b [$b(\omega_0) \ll 1$], this yields a measured, effective optical thickness

$$b_{\text{eff}} \simeq 1 - T \simeq \frac{b_0}{1+\Gamma_L/\Gamma}. \tag{2.16}$$

As expected, for a very broad laser, the cloud is completely transparent, while for a narrow one ($\Gamma_L \ll \Gamma$), $b_{\text{eff}} = b_0$.

This underlines the kind of error made on N when the probe's linewidth is not negligible compared to the atomic linewidth. When $b_{\text{eff}} \gtrsim 1$, multiple scattering and cooperative effects may play a role, and the problem becomes more complicated (cf. e.g. Ref. [182]).

Calibration

For both techniques, the system is focused by looking at the fluorescence of a small object and minimizing the image size. The calibration of the sizes measured in the object plane is done either by placing a mirror on the optical

path and imaging a ruler or, whenever possible, by doing a time of flight of a small freely falling thermal cloud. Knowing the value for the gravity of Earth $g = 9.81$ m/s^2, and fitting the 2D trajectory with a parabola gives a precise calibration, together with a measurement of the angle with respect to the vertical axis.

Other considerations for imaging

For absorption imaging saturation should be avoided, which gives an upper bound on the laser intensity.

All the atoms must be measured without being sent off resonance, that is the Doppler shift induced by the probe's pushing must be small compared to the atomic linewidth:

$$N_{\mathrm{p}}\, k v_{\mathrm{r}} \ll \Gamma \tag{2.17}$$

where N_{p} is the number of photons absorbed by each atom, k the probe's wave vector, and v_{r} the recoil velocity. This gives $N \ll 800$ for the cycling transition of ^{87}Rb. This number is comparable to the number of photons needed to escape from the cycling transition and populate $|5^2S_{1/2}, F = 1\rangle$. There is no repumper in the imaging beam, so this should be avoided. These two conditions give the same constraint on the total energy of the imaging pulse.

The cloud does not just absorb the probe light, it also shifts its phase. This is exploited in other imaging techniques such as phase contrast imaging [181]. Thus, a small and dense cloud acts like a lens and can focus or defocus the probe beam. This phase shift is proportional to the detuning, therefore this effect can be avoided by using resonant light.

2.2 Bose-Einstein condensation in a QUIC trap

This section describes the steps involved in the production of BECs. In simple words it can be summarized as: (i) collect a lot of atoms in a region where the vacuum is good enough, (ii) increase the density and collision rate, (iii) bring the atoms into an internal state which can be held in a conservative trap (no dissipation) preventing exchange of heat with the outside world, (iv) cool the cloud while increasing its density.

2.2.1 The two magneto-optical traps

To avoid MOT instabilities that can occur in large MOTs with retro-reflected beams [101], both MOTs are produced using six independent beams. The total laser powers in MOT1 and 2 are 360 mW and 73 mW respectively, and the beam waists are 2.7 cm and 6.7 mm. The peak intensity of each MOT

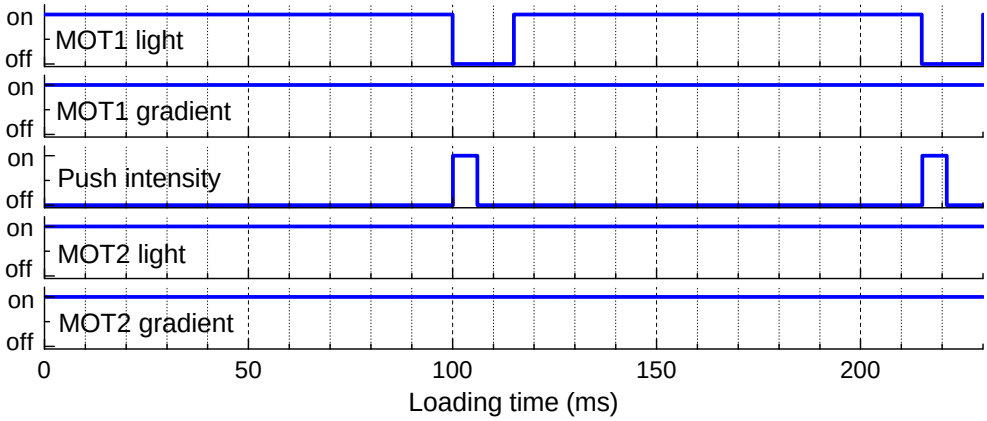

Figure 2.14: Temporal diagram of the pulsed loading of MOT2 from MOT1 (2 periods).

beam is respectively $I_1 = 3\,I_{\text{sat}}$ and $I_2 = 10\,I_{\text{sat}}$, $I_{\text{sat}} = 1.67$ mW/cm^2 being the saturation intensity of the $|F = 2, m_F = \pm 2\rangle \rightarrow |F = 3, m_F = \pm 3\rangle$ cycling transition of ^{87}Rb. The magnetic field gradients of MOT1 and 2 are respectively $B'_1 = 11$ G/cm and $B'_2 = 14.6$ G/cm (gradient along the tighter axes of the quadrupoles). The two MOTs almost have the same detunings $\delta = -3.5\,\Gamma$, which results in respective saturation parameters $s_1 = 0.06$ and $s_2 = 0.20$. When running continuously without the pushing beam, MOT1 can contain up to a few 10^{11} atoms with a peak density of a few 10^{10} atoms/cm^3.

While MOT2 is continuously on, MOT1 is operated in a pulsed regime, as shown on the temporal diagram of Fig. 2.14. First, the trapping light and magnetic field are on and MOT1 loads from the surrounding Rubidium vapor. After 100 ms of such loading, MOT1's size has reached the differential pumping tube's diameter, and the light is switched off. At this point the blue-detuned pushing laser beam, aligned on the vertical axis linking the two MOTs and passing through the tube, is turned on for 6 ms. Its waist is 1.6 mm and its peak intensity $596\,I_{\text{sat}}$. Its detuning is $+21.2\,\Gamma$ and the saturation parameter is $s_{\text{push}} = 0.33$. Because of the radiation pressure force, this light pulse transfers the atoms captured by MOT1 to MOT2 within 15 ms. The force exerted by the pushing beam is not strong enough to overcome the trapping force of MOT2 and thus does not induce atom losses. After a few seconds of such loading, MOT2 contains $\sim 10^{10}$ atoms and MOT1 is then switched off (light and magnetic field). Figure 2.15 shows the fluorescence signals of the two MOTs during the loading.

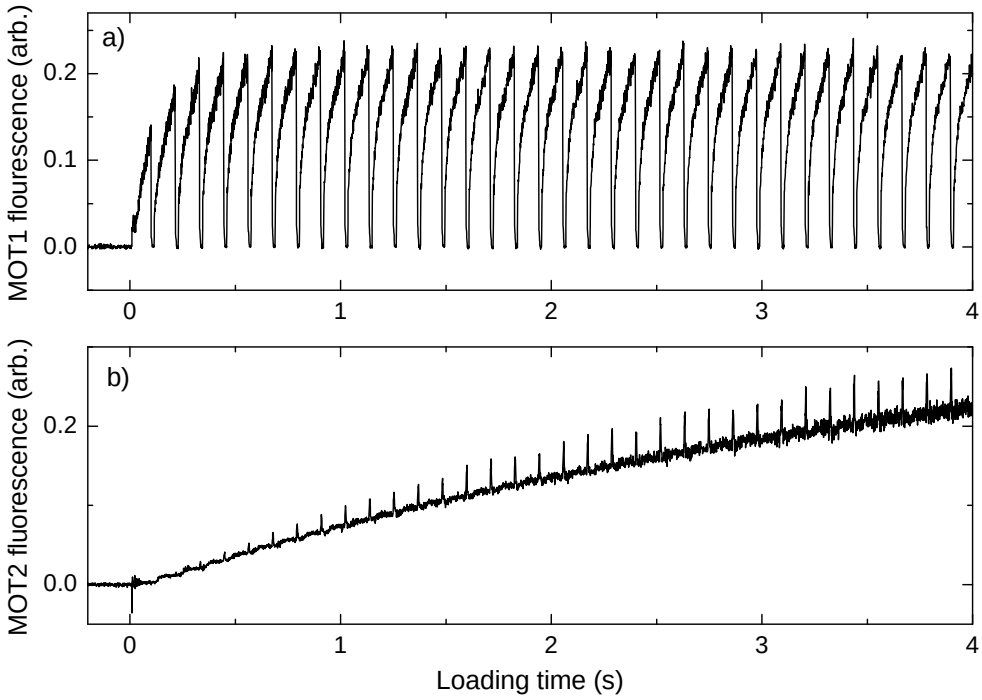

Figure 2.15: Fluorescence signals of (a) MOT1 and (b) MOT2 during the pulsed loading.

Compressed magneto-optical trap

The cloud is then compressed by a compressed MOT phase (CMOT, also called temporal dark MOT): the cooling light detuning is changed from $\delta = -3.5\ \Gamma$ to $\delta = -8\ \Gamma$ and the magnetic field gradient is increased to $B_2' = 65.5$ G/cm. The change of detuning reduces the multiple-scattering-induced repulsive interaction between atoms, while increasing the gradient increases the trap spring constant. This causes the cloud to shrink, thus increasing the density and collision rate by a factor of 3. This phase also gives the MOT a nicer, more symmetric shape. By playing on the compensation fields, the CMOT position can be precisely adjusted to optimize the transfer to the magnetic trap.

Molasses

The cloud is then further cooled to 80 μK by a 3-ms-long optical molasses phase (the magnetic field is turned off, and the detuning changed to $\delta = -10\ \Gamma$). This temperature is rather high compared to the Sisyphus limit and could probably be further reduced.

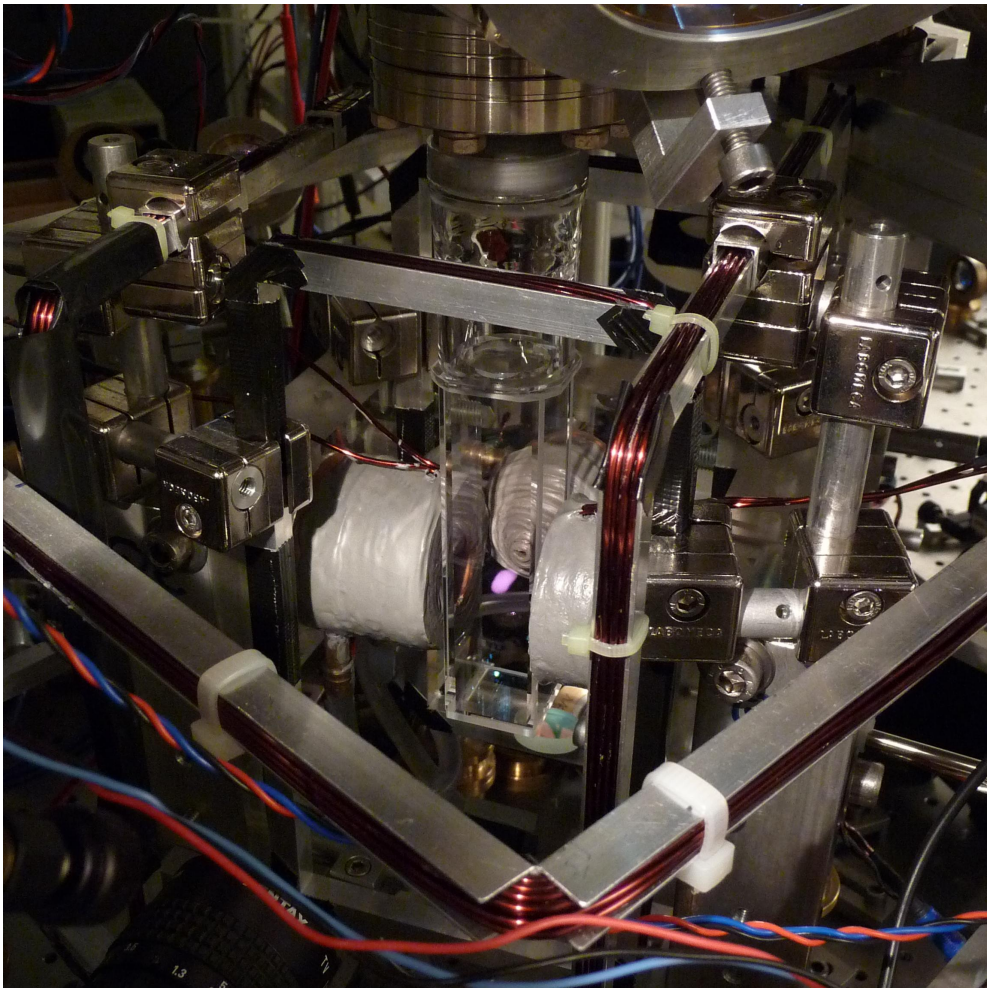

Figure 2.16: Photograph of the lower magneto-optical trap (MOT2). The thin coils are the compensation coils. The gray parts are the coils of the magnetic trap. The MOT is visible (the bright purple spot) in the center of the glass cell. When seen with the naked eye, it appears less intense than on this picture and dark red instead of purple.

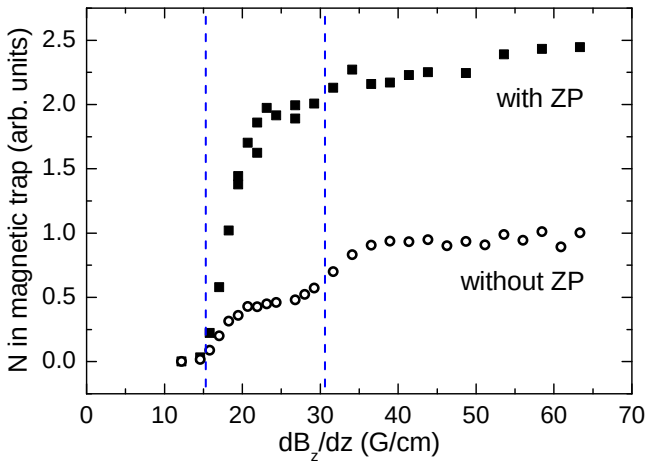

Figure 2.17: Influence of the Zeeman optical pumping stage (ZP) on the number of trapped atoms. The number of atoms is measured after transfer to the magnetic trap and adiabatic compression as a function of the "catch value" (initial vertical gradient). Without ZP, atoms in $|F = 2, m_F = +2\rangle$ are first trapped when the gradient compensates gravity (first vertical dashed line at $\partial_z B_z = mg/\mu_B = 15.3$ G/cm). For $\partial_z B_z = 30.6$ G/cm (second dashed line) atoms in $|F = 2, m_F = +1\rangle$ and $|F = 1, m_F = -1\rangle$ with a magnetic dipole moment twice smaller are also captured.

Optical pumping

For magnetic trapping, the atoms are optically pumped to the $|5^2S_{1/2}, F = 2, m_F = 2\rangle$ Zeeman substate by a circularly polarized beam, detuned by $\delta_{\mathrm{ZP}} = +3.2\ \Gamma$ from the $|5^2S_{1/2}, F = 2\rangle \rightarrow |5^2P_{3/2}, F = 2\rangle$ transition. When atoms end up in the $|F = 2, m_F = +2\rangle$ state, they do not interact anymore with the pumping laser (dark state). Since the pumping transition is not cycling, a superimposed repumper beam is used, detuned by $\delta_{\mathrm{ZP\ rep.}} = -3\ \Gamma$ from the $|5^2S_{1/2}, F = 1\rangle \rightarrow |5^2P_{3/2}, F = 2\rangle$ transition. The lasers are detuned to reduce multiple scattering. A homogeneous magnetic field of ~ 0.5 G is aligned with the light wave vector to define the quantization axis. This optical pumping stage lasts 300 μs. Using optical pumping increases the number of atoms captured by the magnetic trap by a factor of 4 (slightly smaller than the expected factor of 5), as illustrated by Fig. 2.17. The present setup uses a single Zeeman pumping beam (not retro-reflected), which results in a velocity of $3.6\, v_r$ along the beam direction, consistent with the fact that just a few photons are needed to bring the atoms into the $|F = 2, m_F = +2\rangle$ dark state.

2.2.2 Magnetic trapping

Finally, all the light is turned off and the quadrupole magnetic field is abruptly turned on to trap the cloud. The initial value of the gradient is $\partial_x B_x = 54.1$ G/cm which corresponds to a vertical gradient (twice smaller) large enough to compensate gravity only for atoms in the $|5^2S_{1/2}, F = 2, m_F = +2\rangle$ state (cf. Fig. 2.17). This value is kept constant for 100 ms to let the atoms in the other states fall ($|F = 2, m_F = +1\rangle$ and $|F = 1, m_F = -1\rangle$). This is followed by an adiabatic compression of the cloud, performed by linearly increasing the magnetic gradient to 278 G/cm within 500 ms. Without decreasing the phase-space density, this compression stage increases the elastic collision, an important ingredient of evaporative cooling (cf. Sec. 1.4). At this point, the number of atoms is $N \simeq 5 \times 10^9$, and the temperature $T \simeq 400$ μK. Figures 2.18c and 2.18d show how the cloud looks before and after the adiabatic compression.

Transfer to the Ioffe-Pritchard trap

In order to suppress Majorana losses, which become important for cold clouds [103], the quadrupole magnetic trap is converted into a Ioffe-Pritchard trap by ramping the current in the Ioffe coil within 500 ms. In the final configuration, the three coils are in series and have the same current. During this process, the cloud center shifts horizontally by 8 mm towards the Ioffe coil. The center of the cloud is thus 4 mm away from the cell wall. Figure 2.19 shows how the cloud is displaced during this transfer.

If the atoms are too hot, or the magnetic field not steep enough on the side of the Ioffe coil, the tail of the atomic cloud can touch the glass cell, which leads to evaporative cooling and subsequent losses. This is what happens with our trap because of the relatively high temperature after compression (400 μK). Figure 2.20 displays the corresponding effective sample lifetime together with the evolution of the cloud width after time of flight (temperature measurement). The number of atoms decay is clearly not exponential, and has a shape typical of evaporation at constant trap depth (the loss rate decreases as the temperature lowers). Because of this, the number of atoms is reduced by a factor of 10 in the Ioffe-Pritchard trap, compared to the quadrupole trap. These losses are not that tragic because the cloud also cools. The efficiency of this *contact evaporative cooling* has not been investigated.

Lifetime in the magnetic trap

The lifetime of the magnetically trapped atoms is an important parameter, because it is the ultimate limit on the duration of the experiments. More importantly, it is also an essential ingredient for efficient evaporative cooling

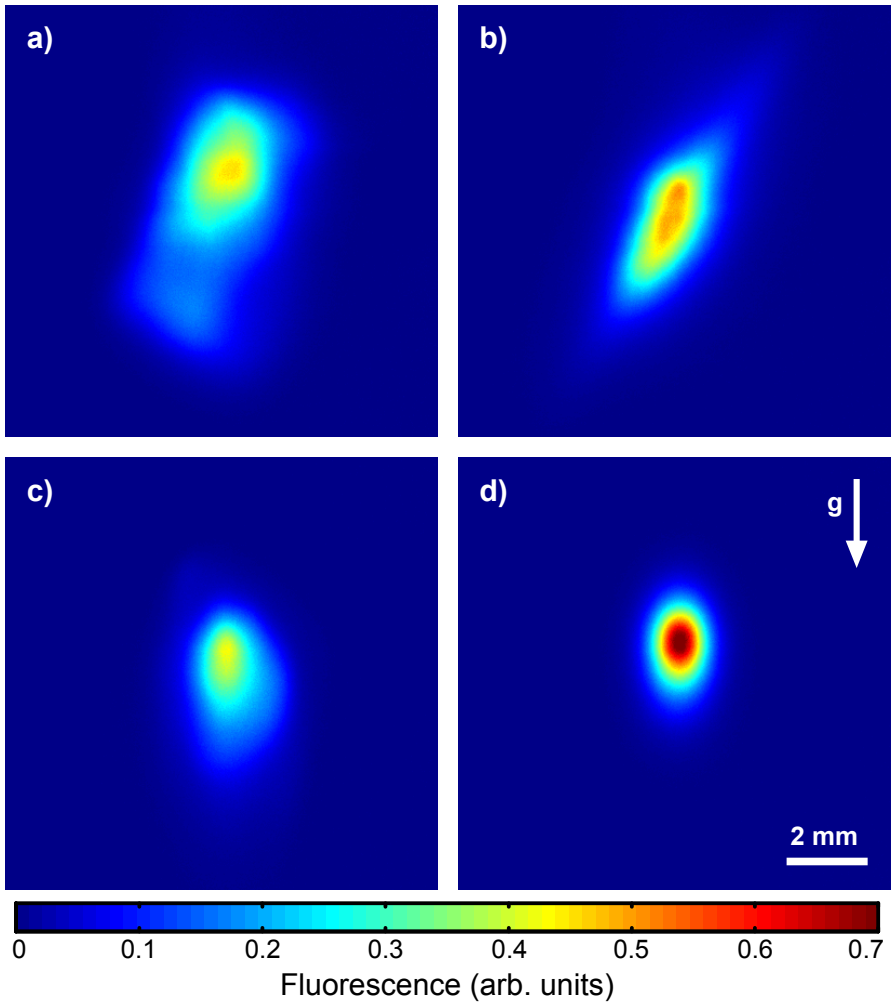

Figure 2.18: Fluorescence pictures of the trapped cloud (a) during the loading of MOT2, (b) after the compressed MOT, (c) after the cloud has been caught in the magnetic trap and (d) after the adiabatic compression. The spatial and color scales remain the same throughout the 4 pictures.

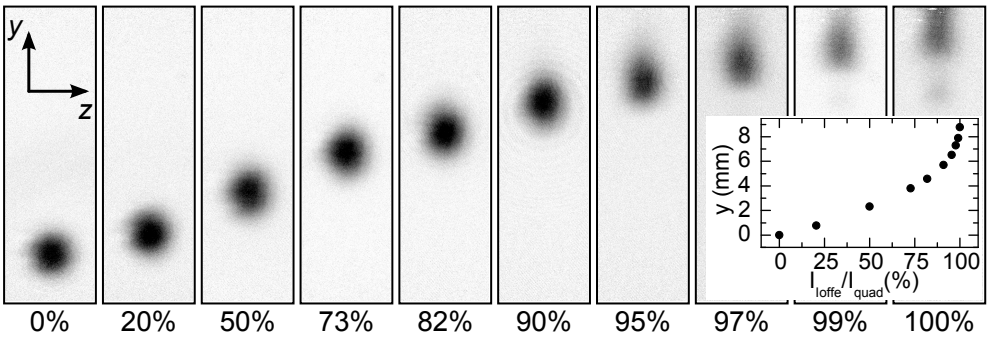

Figure 2.19: Absorption images of the transfer from the quadrupole to the Ioffe-Pritchard trap (after a small time of flight of 3 ms) when the Ioffe current is gradually increased. The numbers in percentage are the ratios of the Ioffe current to the quadrupole current $I_{\mathrm{Ioffe}}/I_{\mathrm{quad}}$. The vertical field of view is about 9.5 mm. The cloud has first been precooled to $T \simeq 100$ μK to be able to pinpoint the magnetic field minimum. The y axis is actually horizontal in the laboratory and the z axis vertical. During the transfer, the cloud center moves by 8 mm towards the Ioffe coil (inset).

(cf. Sec. 1.4.2). It is simply measured by monitoring the decay of the number of atoms when the cloud is held in the trap. Figure 2.21 shows these decays in the compressed quadrupole and in the Ioffe-Pritchard trap. For the latter, the cloud has first been rf cooled to a temperature where evaporation on one of the cell walls has become negligible. The measurement in the quadrupole trap is performed at $T \simeq 400$ μK, where Majorana losses can safely be neglected [103]. In both cases the lifetime is about 30 s.

Trap frequencies

The trap frequencies are measured by monitoring the center-of-mass oscillations after a small displacement of the trap center. For the x and z axis, along which the projections of $\mathbf{B}$ are linear with position, the displacement is simply induced by adding a homogeneous field with the compensation coils. On the y axis, along which the gradient cancels about the trap center, adding a homogeneous field does not shift the position of the center. A displacement can instead be induced by slightly decreasing the Ioffe current. Figure 2.22 shows an example of such measurement of the vertical frequency of the compressed trap (in which the BEC is produced) and of a "decompressed trap" (the QUIC current has been reduced by a factor of 6 and the bias decreased from 2 G to 7.8 G with the compensation coils). Some damping is observed which is attributed to the trap anharmonicity, and subsequent transfer of energy between the 3 dimensions.

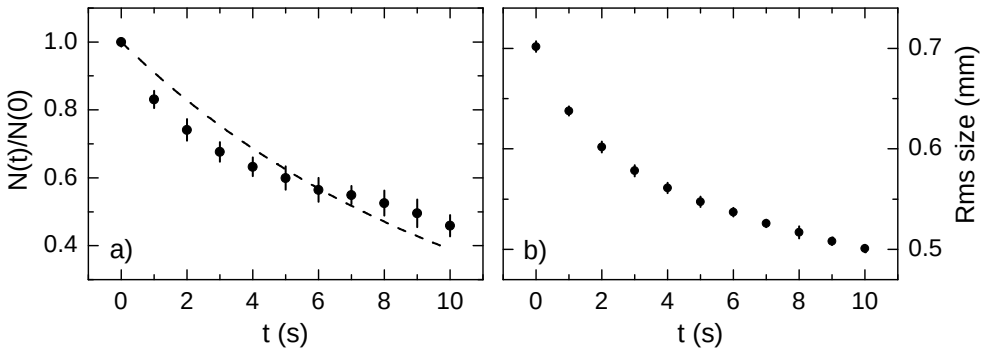

Figure 2.20: Evaporation on the cell wall. After complete conversion of the quadrupole trap into a Ioffe-Pritchard ($t = 0$), (a) the number of atoms and (b) the temperature (given by the cloud size after a 4.5 ms time of flight) are seen to decrease. An exponential fit to $N(t)$ (dashed line) shows that the decay is not exponential, and yields a time constant of 10 s, which is 3 times smaller than the trap lifetime. The error bars are ±rms of 10 realizations.

2.2.3 Evaporative cooling and condensation

Once the cloud is in the Ioffe-Pritchard trap, rf evaporative cooling is performed by ramping the rf frequency from $\nu_{\text{start}} = 20$ MHz to $\nu_{\text{stop}} = 1.2$–1.4 MHz (depending on the precise value of B_0 which can be adjusted) within typically 10 s. Most of the experiments presented in this thesis were done with linear frequency ramps followed by 100 or 200 ms of evaporation at a constant frequency ν_{stop}. The rf amplitude is kept constant on the generator, but since the coupling to the antenna may be frequency dependent, we do not know the precise amplitude sent onto the atoms.

The influence of the stability of the rf frequency, as discussed in Sec. 2.1.5, is easily seen in the production of BECs. We initially employed an analog Tabor generator in VCO mode (an external voltage is used to control the frequency), with which no BEC could be obtained (in this mode, a small noise on the control voltage yields large fluctuations of the frequency, cf. Sec. 2.1.5). Switching to the internal sweep mode yielded BECs, but only after using a final evaporation stage at constant frequency. During this final stage, the fact that the rf spectrum was broad was compensated by evaporating at constant trap depth (i.e. using a larger η). Using either a Tabor or Agilent DDS generator, we can obtain BECs without this final stage, either with linear or exponential frequency ramps.

We noticed that with our initial conditions, exponential ramps always give bigger BECs (up to 60%), but so far, no systematic optimization of the frequency and amplitude ramps have been performed. During the redaction of

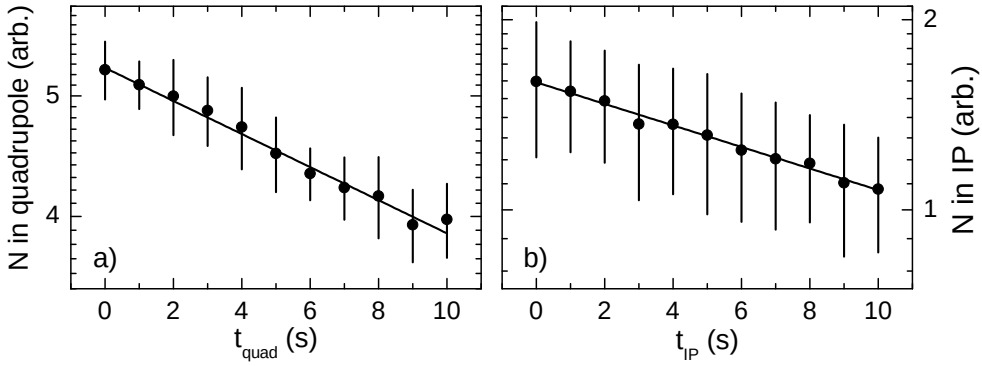

Figure 2.21: Number of atoms in (a) the quadrupole and (b) Ioffe-Pritchard magnetic traps vs holding time (semi-log scale). The lines are exponential fits and yield the decay time constants $\tau_{\rm quad} = 33$ s and $\tau_{\rm IP} = 25$ s. The error bars are $\pm$rms of 10 realizations.

this thesis, the cycle time has been reduced (from 35 s to 15.3 s), and identical BECs can now be prepared with only 4 s of evaporation using a nearly exponential frequency ramp. A precise optimization of the ramps, together with a decompression of the trap during evaporation (to reduce the density and the possible three-body losses [112, 155, 183–186]) could still be done to improve both the duty cycle and the atom number in the condensate.

We routinely produce "pure" BECs (no discernible thermal fraction with our absorption imaging) in the fully compressed magnetic trap, containing 5×10^5 atoms. Figure 2.23 shows how the cloud parameters evolve during the last 2 seconds of a 10 s-long evaporation ramp. The temperature is inferred from the width of the thermal fraction after a single 20 ms time-of-flight image. The number of atoms is directly obtained from the same absorption images, and all the other parameters are calculated assuming that the trap is harmonic (the trap frequencies are known from the measurements of Sec. 2.2.2). On the images corresponding to the last 3 points of these curves, a clear *bump* appears in the center of the density profile, as in Fig. 2.24. Condensation occurs at the expected critical phase space density $n_0 \lambda_{\rm dB}^3 \simeq 1.2$ (indicated by the blue horizontal line in the last graph).

Figure 2.24 shows absorption images of the cloud after the rf ramp and a 30 ms time of flight, for different values of the final rf frequency $\nu_{\rm stop}$. Above $\nu_{\rm stop} = 1.43$ MHz, the density is well fitted by a Gaussian, whereas for $\nu_{\rm stop} \leq 1.42$ MHz, the distribution is clearly bimodal. It is well fitted by the sum of a Gaussian and a Thomas-Fermi profile despite the fact that T/T_c is not that small (in principle the TF profile is valid in the limit $T \to 0$). The fact that the density still follows a TF profile after the 30 ms of expansion is not trivial,

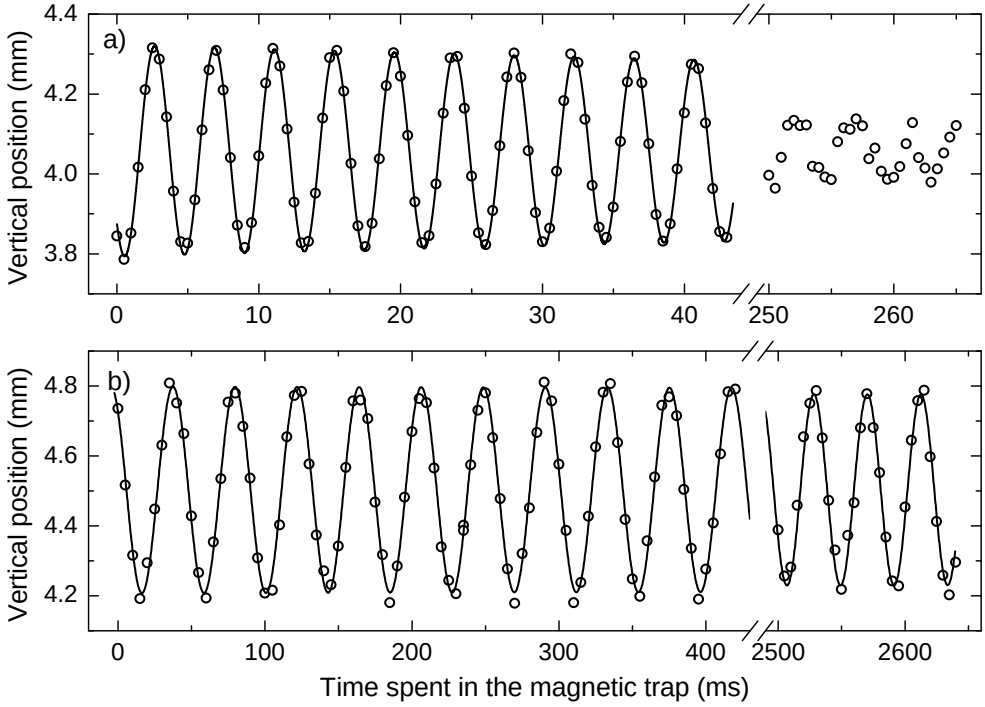

Figure 2.22: Measurement of the trap frequencies. A small magnetic field offset is slowly applied, and abruptly switched off. The cloud position is measured after a variable time of free evolution in the trap plus a constant time of flight (here 27 ms). Vertical trap frequency of (a) the fully compressed trap in which the BEC is produced, (b) a decompressed trap. The lines are exponentially damped sine fits yielding (a) $\nu_z = 237$ Hz and (b) $\nu_z = 23.7$ Hz.

and is discussed in Sec. 2.2.4.

Efficiency of evaporative cooling

The efficiency of evaporative cooling is directly measured by interrupting the evaporation at various times and plotting N vs T in log-log scale (Fig. 2.25 shows this plot for the last 2 seconds of a 10-s-long evaporation ramp). As explained in Sec. 1.4.2, the slope of this curve is a direct measurement of the efficiency of evaporative cooling. Indeed, in a harmonic trap, the phase space density scales as $n_0\lambda_{\mathrm{dB}}^3 \propto NT^{-3}$, it thus increases when $\mathrm{d}\log N/\mathrm{d}\log T < 3$. The condition for runaway evaporative cooling is even more stringent: $\mathrm{d}\log N/\mathrm{d}\log T < 1$ (cf. Sec. 1.4.2). If it is met, the phase-space density is assured to increase by at least 2 orders of magnitude when the temperature decreases by 1 order of magnitude. Typical experimental values characterizing

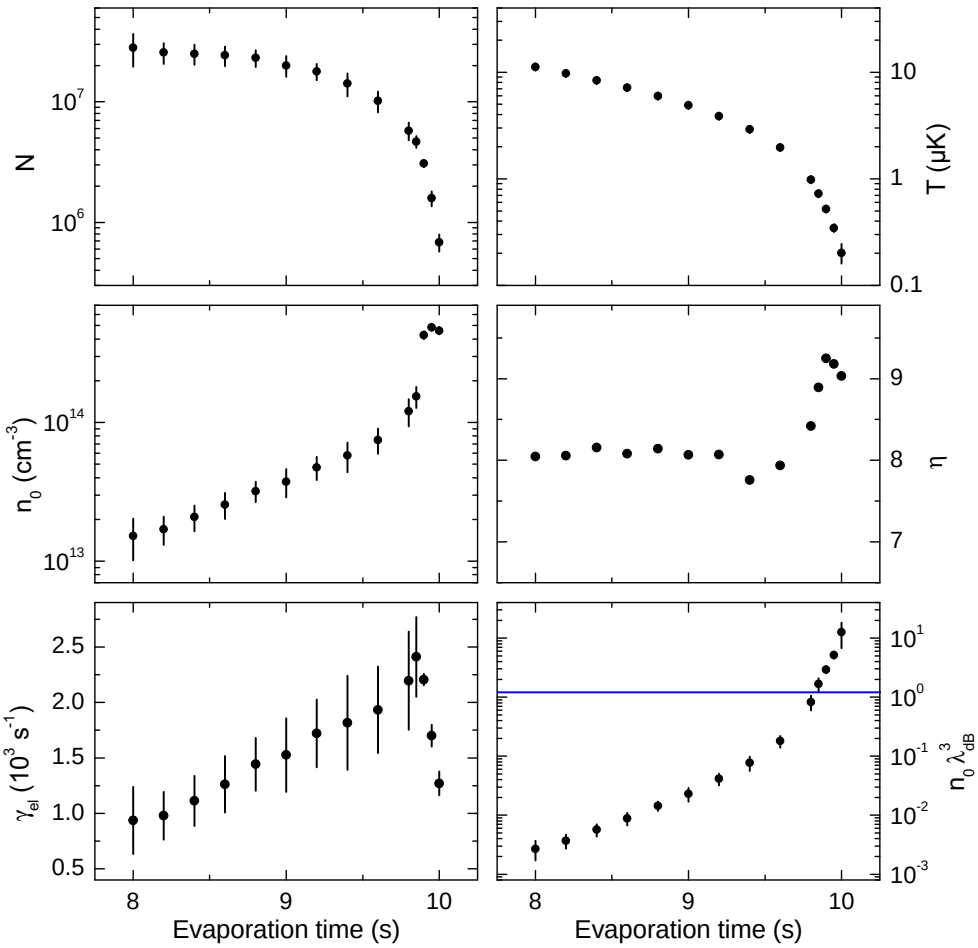

Figure 2.23: Evolution of the number of atoms N, the temperature T, the truncation parameter η, the peak density n_0, the peak elastic collision rate $\gamma_{\rm el}$, and the peak phase-space density $n_0\lambda_{\rm dB}^3$ during the last 2 seconds of evaporation. The blue horizontal line in the last graph corresponds to the critical phase-space density of 1.2 for which condensation is expected to occur (cf. Sec. 1.1.3). The collision rate is calculated from the density and temperature of the thermal fraction, which is why the curve decreases after condensation. The error bars are ±rms of 6 realizations.

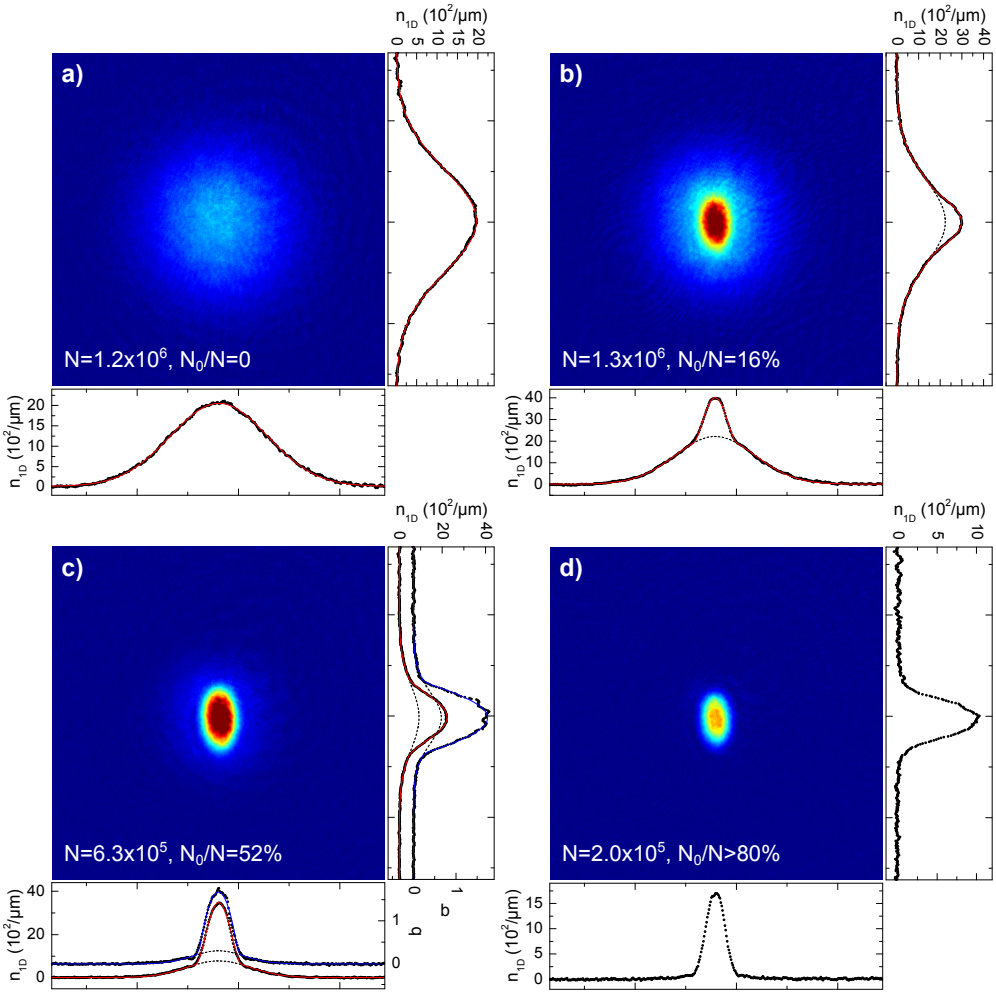

Figure 2.24: Bose-Einstein condensation when the final rf frequency is reduced. (a) $\nu_{\mathrm{stop}} = 1.44$ MHz, (b) $\nu_{\mathrm{stop}} = 1.42$ MHz, (c) $\nu_{\mathrm{stop}} = 1.40$ MHz, (d) $\nu_{\mathrm{stop}} = 1.39$ MHz. These absorption images are taken after 30 ms of time of flight. The field of view of each image is 1.65×1.65 mm. The profiles are the integrals of the column density along the two axes. They are fitted (red lines) with a bimodal distribution which is the sum of a Gaussian component (dashed line) and a Thomas-Fermi component [expression (1.69)]. In (c) are also shown cuts of the image through the center, fitted with the expression (1.67) (blue lines).

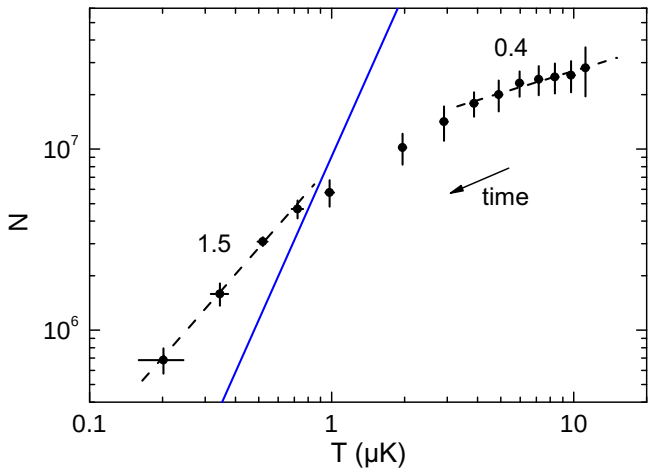

Figure 2.25: The efficiency of evaporative cooling is given by the slope of the curve N vs T in log-log scale. The numbers are the slopes obtained from fits to the first 7 points (on the right) and the last 4 points (on the left). The concavity of the curve seems to indicate that the efficiency decreases during evaporation (see text). The solid blue line corresponds to the phase transition [Eq. (1.44)]. The errors bars are ±rms of 6 realizations.

efficient evaporation are thus less than 1. As seen in Fig. 2.25, the efficiency seems to decrease during the process. These measurements were done with a constant time of flight (20 ms) and because of the increase of the optical thickness throughout evaporation to high values (up to 3), the number of atoms may be underestimated in the BEC. Also, the density reaches high values after condensation, and three-body losses may be consequent. This effect could be suppressed by decompressing the magnetic trap at the end of the rf ramp.

2.2.4 Inversion of the aspect ratio

A striking signature of condensation is the sudden growth of this *bump* in the center of the density profile (cf. Fig. 2.24). It is a direct observation of the population of the single-particle ground state, which starts to be macroscopically populated at the phase transition. In a harmonic trap and in the absence of interactions, this peak is expected to have a Gaussian shape (harmonic oscillator ground state), with different rms widths along the three axes, related to the harmonic oscillator lengths. For instance, $\Delta z = a_{\mathrm{ho},z}/\sqrt{2} = \sqrt{\hbar/2m\,\omega_z}$. The rms width of the momentum distribution along the same axis is $\Delta p_z = \sqrt{\hbar m\,\omega_z/2}$, such that the Heisenberg inequality is saturated: $\Delta z \Delta p_z = \hbar/2$, as expected for the HO ground state. Measuring the aspect ratio, that is the ratio of two widths (for instance $\Delta y/\Delta z$) of this peak in situ (inside the trap)

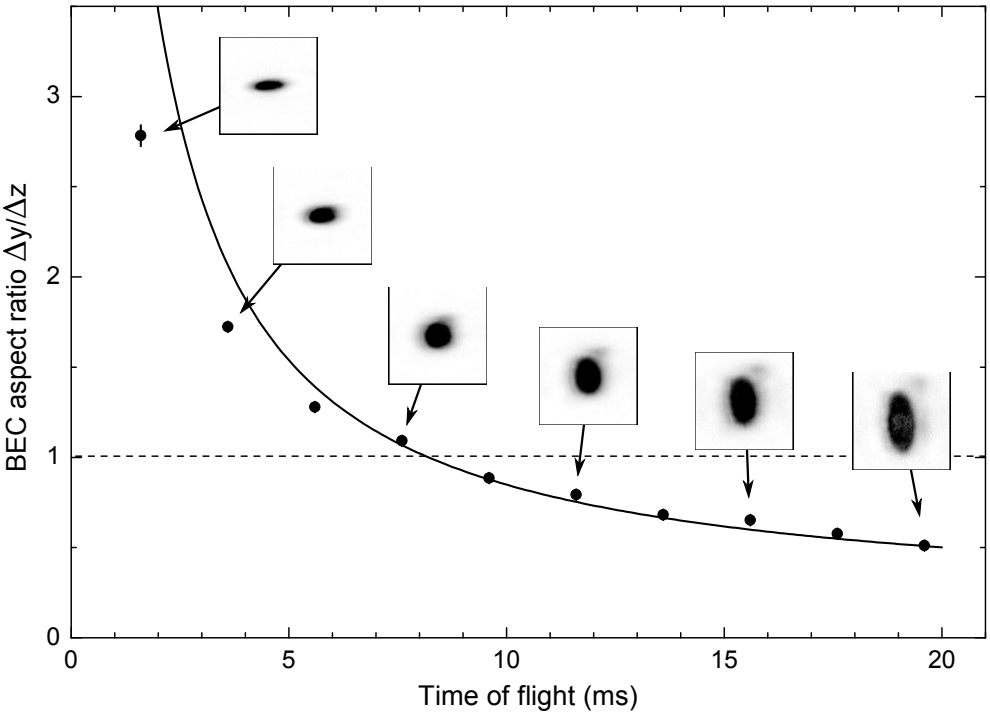

Figure 2.26: Inversion of the aspect ratio of a pure BEC during time of flight. The absorption images correspond to the points indicated by the arrows. The field of view is 359×359 μm. The errors bars are $\pm$rms of 5 realizations. The continuous line corresponds to the model of Ref. [49] [Eq. (2.19)] without any fitting parameter. For small times the optical thickness is too high to properly measure the widths, which explains the observed discrepancy.

would thus lead to the value $\sqrt{\omega_z/\omega_y}$. On the contrary, if the trap is switched off and the wave packet is first left to expand freely before the measurement, the density profile after an asymptotically long evolution reflects the initial velocity distribution and the value of the aspect ratio is $\Delta p_y/\Delta p_z = \sqrt{\omega_y/\omega_z}$, the inverse of the in situ value. This shows how the aspect ratio of a non-interacting BEC inverts during a time of flight.

Interactions quantitatively modify the expansion but the behavior is qualitatively the same. For instance, in the TF limit and at zero temperature, the width in the direction $j \in \{x, y, z\}$ is enlarged by the repulsive interactions by a factor

$$\frac{\Delta r_j^{\mathrm{TF}}}{\Delta r_j^{\mathrm{ideal}}} = \frac{R_j/\sqrt{7}}{a_{\mathrm{ho},j}/\sqrt{2}} = 15^{1/5}\sqrt{\frac{2}{7}}\left(\frac{m\, a_s^2\, \bar{\omega}^6}{\hbar \omega_j^5}\right)^{1/10} N_0^{1/5}. \tag{2.18}$$

The numerator and denominator are respectively the rms widths of the density

profiles of a TF BEC (TF radius R_j) and of a non-interacting BEC. a_s is the scattering length, $\bar{\omega} = (\omega_x\omega_y\omega_z)^{1/3}$, and N_0 is the number of atoms in the BEC. For our trap frequencies, and with $N_0 = 10^5$ atoms, this factor is about 2 in the radial directions, and 7 on the long axis. The expansion itself is modified by the interactions. During a time of flight, the density keeps a TF shape (inverted parabola) but the TF radii are rescaled by time-dependent increasing factors (see Ref. [49] and Chap. 3). For short times, the aspects ratio of a cylindrically symmetric BEC evolves as [49]

$$\frac{\Delta y}{\Delta z} \simeq \frac{1 + \epsilon^2 \left[\tau \arctan(\tau) - \ln\sqrt{1+\tau^2}\right]}{\epsilon\sqrt{1+\tau^2}} \tag{2.19}$$

where $\epsilon = \omega_y/\omega_\perp$ and $\tau = \omega_\perp t$. This shows that the aspect ratio of an interacting BEC also inverts during a time of flight. A measure of this effect is shown in Fig. 2.26.

Despite the seemingly quantum nature of this inversion in the non-interacting case, this behavior is not a signature of the presence of a BEC when there are interactions. Indeed non-degenerate systems can exhibit the same kind of behaviors in the hydrodynamic regime, i.e. when collisions are predominant [187].

2.2.5 Condensate heating and lifetime

Many effects can lead to a heating of the atomic sample. For instance, random fluctuations of the magnetic field can shake the atoms and heat them. An interesting quantitative study of this effect is presented in Ref. [188]. It shows that the most dramatic effect is parametric heating, i.e. heating due to trap fluctuations at twice the oscillation frequency. For this reason, trap current fluctuations should be kept as low as possible.

Other possible sources of heating are collisions with the background gas, collisions with a dilute cloud of hot atoms which have not been evaporated (sometimes called the "Oort cloud", cf. Ref. [189, Chap. 8] for a study of this effect), three-body losses which release some energy that can be transfered to the trapped atoms, etc.

In practice, heating in magnetic traps is not well understood [190], probably because of the variety of possible sources. For instance, the simple model of Ref. [188] predicts an exponential increase of the temperature, while we have always observed temperature dependent heating rates, that decrease when the temperature increases (at more or less constant total number of atoms). This heating may be due to three-body losses which are expected to be important at these high densities of 5×10^{14} atoms/cm^3. To avoid this effect the cloud should be decompressed at the end of the evaporation.

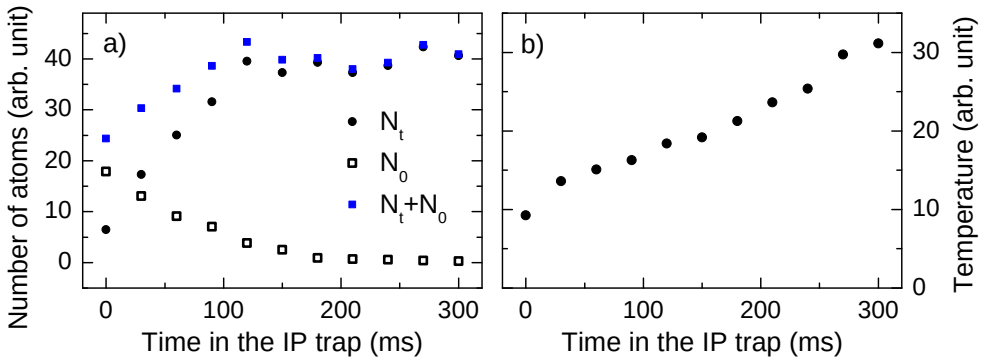

Figure 2.27: Melting of the BEC held in the compressed IP trap. On (a) the condensate (N_0) and normal (N_t) fractions and the total number of atoms ($N = N_t + N_0$) are plotted vs the time spent in the trap. On (b) the temperature is plotted. The BEC completely melts within 200 ms. The initial increase of N (for $0 \leq t \lesssim 100$ ms) is attributed to the fact that N is underestimated when the optical thickness is large.

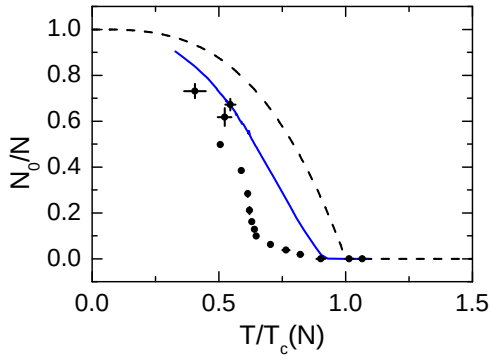

Figure 2.28: Condensed fraction vs rescaled temperature. Most of the error bars (± rms of 5 realizations) are smaller than the points. The dashed line corresponds to the theory of the non-interacting gas in the thermodynamic limit, while the solid blue line is a result of the semiclassical two-fluid model of Ref. [191]. This model takes into account the interactions, the finite number of atoms and its variation during the evaporation.

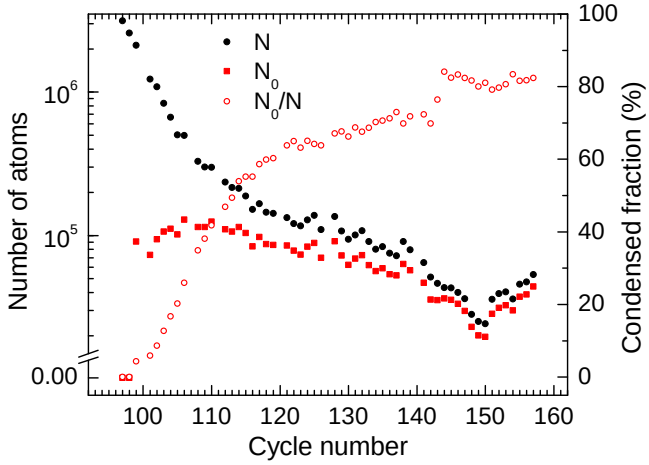

Figure 2.29: Evolution of the total number of atoms N, condensate number N_0 and condensed fraction when the experiment is turned on with the parameters for the production of pure BECs. The points correspond to successive realizations of the experiment (cycles). At the time these data were taken, each cycle was about 35 s.

The fact that the BEC is not at equilibrium just after the evaporation, probably because of this high heating rate, is also observable in Fig. 2.28 displaying the condensate fraction vs the temperature [the expected curve is Eq. (1.45)]. The measured critical temperature is lower than the one expected taking into account finite size effects and interactions. Since atoms are lost during the evaporation, the horizontal scale has to be rescaled by $T_c(N)$, where N is the absolute atom number. We have seen that our number measurement is not absolute, but even if we assume an error on N, this does not account for the strange shape of the measured curve.

2.2.6 Reproducibility

Since our measurement technique (time of flight followed by absorption imaging) is destructive, every study involves the repetition of the same experiment while varying at least one parameter. Ideally, the shots should be as *identical* as possible. In practice, this is not an easy thing to do, because the production of BECs involves many steps which are chained, and the fluctuations of all steps are added to each other.

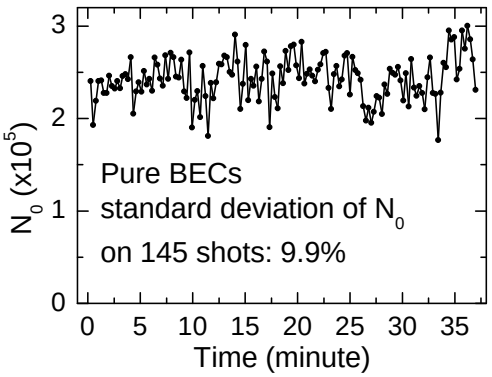

Figure 2.30: Evolution of the number of atoms N_0 of pure BECs in steady state. The curve corresponds to 145 shots, each cycle taking 15.3 s.

Turn-on behavior

When the experiment is turned on, a transient regime lasts for the first 30 repetitions of the experiment (cycles). This is shown in Fig. 2.29 which was taken soon after we could produce our first BECs. At this time the rf source was an unstable analog function generator which was then changed for the one of App. B, the one-to-six splitters had not been installed yet, and the cycle duration was longer (35 s, instead of the current 15.3 s). This transient regime was mainly due to the fact that the magnetic trap coils have to reach their steady state temperature of 55–60°C, and that the bias B_0 depends strongly on the coils' temperature (probably due to a dilatation of the coils). This is the reason why N and N_0 fluctuate so much. Because of the various sources of instability (MOT power, final rf frequency, coils temperature and value of the bias), the experiment never really reached a steady state at this time. It is seen that the turn-on behavior lasted approximately half an hour.

Reproducibility

With the improvements made continuously during this thesis, it still takes a few cycles to stabilize, but the experiment is much more reproducible in steady state. This is illustrated in Fig. 2.30, where the fluctuations of the number of atoms of pure BECs are recorded over 145 successive shots.

Finally it is also worth pointing out that the day-to-day fluctuations are low. It takes a few minutes to turn the experiment on, and with the same parameters as the day before, we are in steady state (Fig. 2.30) after less than half an hour.

2.3 Outlook

This chapter has presented the experiment constructed during this thesis and its performance to produce BECs. Some improvements could still be made. For instance the absorption imaging does not give an absolute number of atoms for three reasons: (i) the population of the various Zeeman substates and the orientation of the magnetic field during the imaging pulse are not controlled. This results in an uncertainty in the absorption cross-section. This could be improved by controlling the rotation of the magnetic field during switch off to orient it along the imaging axis, and checking that only the $|F = 2, m_F = +2\rangle$ substate is populated with a Stern-Gerlach separation. (ii) The probe is spectrally large and the number of atoms is probably underestimated. This should be fixed by using another laser for imaging. (iii) The optical thickness is often too large. The probe cannot be detuned because of lensing effects, and the solution is thus to increase the time of flight (this cannot be done simply with the current imaging beam). These improvements are currently being implemented. The trap should be decompressed during the evaporation to reduce three-body losses. Another problem is the switching off of the fully compressed magnetic trap. On the one hand it is too long, on the order of 1 ms, which must deform the cloud. On the other hand, the three coils were measured to switch off with different time constants, which kicks the cloud giving it a velocity of a few recoils. This may not be a problem if the BEC is produced in a looser trap (the switch off time constant was measured to be lower in a decompressed trap).

In addition to the improvements discussed above, the blue-detuned laser is currently being used to trap the atoms in a two-dimensional geometry and study matter wave transport in disordered potentials. In the following chapter we present some experiments performed in the magnetic trap only (no dipole trap).

Chapter 3

Shortcuts to adiabaticity for trapped ultracold gases

In quantum mechanics, the evolution of a system described by a time-dependent Hamiltonian $H(t)$ is *adiabatic* when the transition probabilities between the time-dependent eigenstates of H are negligible. This happens when H is either time-independent, or when its rate of change is *slow* compared to the typical time-scales involved [192–194]. Nevertheless, thinking in terms of instantaneous eigenstates is often much easier than looking for the solutions of time-dependent problems. In the field of atomic physics, going from the semi-classical approach of atom-field interaction to the celebrated dressed state picture [73] illustrates the convenience of such adiabatic representations.

For this reason, many adiabatic schemes to prepare interesting quantum states were proposed. For instance, non-classical states [195, 196], or new strongly correlated states [197] can be prepared by adiabatic passage. Quantum adiabatic computation has recently been demonstrated [11]. Yet adiabatic techniques are typically slow [194], while experimentalists are often constrained by finite lifetimes or coherence times of their samples. This motivated the search for fast schemes reproducing or approaching adiabatic transformations. Some methods use minimization techniques to optimize the transition to a target state [198–201], whereas others yield the exact same state that would have been reached after an adiabatic transformation [19, 202]. The latter are referred to as *shortcuts to adiabaticity*.

In this chapter, we detail how such methods can be used on the motional degrees of freedom of ultracold gases confined in time-dependent harmonic traps, and experimentally demonstrate the validity of the approach. Two direct applications of the procedure are the fast cooling of atomic samples, and the suppression (or reduction) of any *parasitic excitations* which occur in experiments on ultracold gases when the trap geometry or the interactions are

modified. Since the method is not restricted to equilibrium states, it could be used in a variety of situations as discussed at the end of the chapter.

The first part is theoretical and recalls how harmonically confined gases react to the variation of the trap. Both the one-dimensional non-interacting gas, and the three-dimensional Bose-Einstein condensate with repulsive contact interaction between particles are treated. In the second part, the method to realize shortcuts to adiabaticity are detailed for theses two systems, and examples are given. The third part focuses on the experimental realization of these methods. Rapid decompressions have been performed on both a non-interacting gas and a Bose-Einstein condensate. The practical limitations which degrade the performances are discussed. In the last part, we attempt to generalize the problem to an arbitrary variation of the three-dimensional harmonic potential and give other examples of shortcuts which may be of experimental relevance. For clarity, some details concerning the calculations have been moved to App. C.

3.1 Quantum adiabatic transformations

The term *adiabatic* is a confusing one in physics because it has different meanings. The word itself has a Greek root and means "not passing through" [194]. In the context of thermodynamics, it is the *heat* that is not passing through the walls of the container: this word describes a process in which no heat is exchanged. In that sense, thermodynamical adiabatic transformations need by no means be slow.

In quantum mechanics, *the meaning is different*: a process is adiabatic when the probabilities for the system to make transitions between the time-dependent (or "instantaneous") eigenstates of the Hamiltonian are negligible. This condition may be very constraining and can be weakened if one assumes that the system is initially in a given instantaneous eigenstate $|\lambda;t\rangle$ of the Hamiltonian (the λ's denote all the necessary quantum numbers). The evolution will then be said adiabatic in the time interval $t \in [0, t_f]$ if the populations of all the other time-dependent eigenstates stay low during this interval.

In the next sections, we recall the adiabatic theorem of quantum mechanics and give a few useful criteria for particular transformations to be adiabatic. They will be useful as a reference in the rest of the chapter.

3.1.1 The adiabatic theorem

The precise formulation of the adiabatic theorem was first given by Born and Fock [192], and later refined by others (see e.g. Refs. [193, 203, 204]). Suppose we have a varying Hamiltonian $H(t)$ of which $\{|\lambda;t\rangle\}$ is a basis of time-dependent eigenstates (the spectrum is written $\{\hbar\omega_\lambda(t)\}$). The adiabatic

theorem states that if this Hamiltonian is slowed down — mathematically, this is achieved by evolving the system with the new one $H_\epsilon(t) \equiv H(\epsilon t)$ with $\epsilon < 1$ — then the solutions $|\Psi_\epsilon; t\rangle$ of the Schrödinger equation associated to $H_\epsilon(t)$ satisfy

$$|\Psi_\epsilon; t\rangle - \exp\left\{-i \int_0^t \left[\omega_{\lambda_\epsilon}(t') - i\langle\lambda_\epsilon; t'|\frac{\partial}{\partial t'}|\lambda_\epsilon; t'\rangle\right] \mathrm{d}t'\right\} |\lambda_\epsilon; t\rangle = O(\epsilon), \quad (3.1)$$

where we have written $\{|\lambda_\epsilon; t\rangle\}$ a basis of instantaneous eigenstates of $H_\epsilon(t)$ and $\{\hbar\omega_{\lambda_\epsilon}(t)\}$ its spectrum. This means that when the evolution is *infinitely slow* ($\epsilon \to 0$) the instantaneous eigenstates, chosen with this appropriate phase, coincide with the solutions of the Schrödinger equation. This is quite intuitive.

3.1.2 Criteria for adiabaticity

One sees that the adiabatic theorem is not often relevant to practical problems, because it is just valid in the limit $\epsilon \to 0$. For instance, if one wants to use it in a problem involving a two-level atom interacting with a classical field oscillating with a pulsation ω, the theorem can only be applied in the limit $\omega' \equiv \epsilon\omega \to 0$, which is not very useful since it corresponds to a static field.

Nevertheless, one can calculate the criteria on the rate of evolution for the transformation to be nearly adiabatic. If the initial state is $|\lambda; t = 0\rangle$ and the spectrum is discrete, the criteria often used is

$$\sum_{\lambda' \neq \lambda} \left|\frac{\langle\lambda'; t|\partial_t|\lambda; t\rangle}{\omega_\lambda(t) - \omega_{\lambda'}(t)}\right| \ll 1, \quad (3.2)$$

where the sum is over all the instantaneous eigenstates other than $|\lambda; t\rangle$. It is important to remember that this condition is generally neither necessary nor sufficient for adiabaticity, as explained in Ref. [194]. Nevertheless, for the problem we will consider in this chapter, i.e. the decompression of a harmonic potential with a monotonously decreasing frequency $\omega(t)$, condition (3.2) is sufficient for the transformation to be adiabatic.

Criterion for the decompression of a harmonic potential

We first consider a 1D harmonic potential whose center is not moving. The Hamiltonian is thus $H(q, p, t) = p^2/2m + m\,\omega^2(t)q^2/2$. We assume that the particle is initially in the ground state $|0; t = 0\rangle$. The eigenstates $\{|n; t\rangle, n \in \mathbb{N}\}$ are the usual orbitals of the harmonic oscillator (HO), but the frequency which is usually constant is now time-dependent. The calculation of the left-hand side of Eq. (3.2) gives the criterion

$$\left|\frac{1}{4\sqrt{2}}\frac{\dot{\omega}}{\omega^2}\right| \ll 1. \quad (3.3)$$

For instance, if one uses what we will call in the rest of the chapter a "linear decompression", i.e., a decompression of the form[1] $\omega^2(t) = \omega^2(0) - [\omega^2(0) - \omega^2(t_f)]t/t_f$, where t_f is the duration of the decompression and $\omega(t_f) < \omega(0)$, the criterion (3.3) is more constraining at the end of the decompression when ω is smaller and thus becomes, expressed on t_f,

$$t_f \gg \frac{1}{8\sqrt{2}\,\omega(t_f)} \left[\frac{\omega^2(0)}{\omega^2(t_f)} - 1\right]. \tag{3.4}$$

As underlined in Ref. [19], a more efficient strategy to perform an adiabatic decompression (or compression) is to distribute $\dot{\omega}/\omega^2$ uniformly along the trajectory, i.e., to impose $\dot{\omega}/\omega^2 = c$, where c is a constant. This yields the trajectory

$$\omega(t) = \frac{\omega(0)}{1 + \frac{t}{t_f}\left(\frac{\omega(0)}{\omega(t_f)} - 1\right)}, \tag{3.5}$$

and the condition (3.3) becomes

$$t_f \gg \frac{1}{4\sqrt{2}} \left|\frac{1}{\omega(t_f)} - \frac{1}{\omega(0)}\right|. \tag{3.6}$$

These conditions will be useful in Sec. 3.3 where we will see that our shortcuts can in principle lead to the same final state as obtained after an adiabatic decompression, but still strongly violate these criteria.

3.2 Scaling properties of harmonically confined ultracold gases: two examples

In this section, we recall how the density and velocity distributions of a one-dimensional (1D) non-interacting gas are affected by a change of the harmonic confinement. In 1D, the harmonic trap is fully described by its time-dependent angular frequency $\omega(t)$, and minimum position $q_0(t)$. We show that the dynamics is fully described by two scaling functions, one associated to the size of the cloud, the other to its center-of-mass position, and exhibit the exact solutions of the Schrödinger equation. This will be used in the rest of the chapter to realize shortcuts to adiabaticity (cf. Sec. 3.3). Similar scaling properties are also recalled for Bose-Einstein condensates (BECs) with interactions strong enough to be well described by the Thomas-Fermi regime. The analogy between the invariant method used for the non-interacting gas [205], and the scaling often used for BECs [48–50] is underlined.

[1] We call this a "linear decompression" because in the experiment, it corresponds to decreasing the current I of the magnetic trap linearly with time, since $\omega^2(t) \propto U(\mathbf{q}, t) \propto |\mathbf{B}(\mathbf{q}, t)| \propto I(t)$.

3.2.1 The non-interacting gas

We consider a 1D non-interacting gas confined in the most general time-dependent harmonic potential, described by the one-particle Hamiltonian

$$H(q,p,t) = \frac{p^2}{2m} + \frac{1}{2}m\,\omega^2(t)\,[q - q_0(t)]^2\,, \tag{3.7}$$

where q and p are conjugate variables, and m is the mass of a particle. We first recall how dynamical invariants can be used to find the general solutions of the Schrödinger equation.

Definition and properties of dynamical invariants

In 1969 Lewis and Riesenfeld [205] generalized the concept of invariant of motion to the case of explicitly time-dependent Hamiltonians $H(q,p,t)$. Such Lewis invariants (also called dynamical invariants, or first integrals) can be used to solve the Schrödinger equation

$$i\hbar\frac{\partial|t\rangle}{\partial t} = H(q,p,t)|t\rangle. \tag{3.8}$$

Given a time-dependent Hamiltonian $H(q,p,t)$, a time-dependent hermitian operator $I(q,p,t)$ is a dynamical invariant of the system described by H if it is constant under Hamiltonian evolution, that is if

$$\frac{\mathrm{d}I}{\mathrm{d}t} \equiv \frac{\partial I}{\partial t} + \frac{1}{i\hbar}[I,H] = 0\,. \tag{3.9}$$

In this case, the following properties hold [205]:

1. if $|t\rangle$ is a solution of (3.8), then $I|t\rangle$ is also a solution of (3.8),
2. the eigenvalues $\lambda(t)$ and associated eigenvectors $|\lambda;t\rangle$ of I are *a priori* time-dependent. We assume they form a complete set. It turns out that the eigenvalues are actually constant: $\lambda(t) = \lambda$. They are real because I is hermitian.
3. The eigenvectors of I satisfy

$$\text{for all } \lambda,\lambda' \text{ such that } \lambda \neq \lambda', \quad \langle\lambda';t|i\hbar\frac{\partial}{\partial t}|\lambda;t\rangle = \langle\lambda';t|H|\lambda;t\rangle. \tag{3.10}$$

4. If we assume that I does not contain the operator $\partial/\partial t$, then the set of vectors $\{e^{i\alpha_\lambda(t)}|\lambda;t\rangle,\ \alpha_\lambda(t) \in \mathbb{R}(t)\}$ is also a complete set of eigenvectors of I. If these functions are chosen to solve the equations

$$\frac{\mathrm{d}\alpha_\lambda}{\mathrm{d}t} = \langle\lambda;t|i\frac{\partial}{\partial t} - \frac{H}{\hbar}|\lambda;t\rangle, \tag{3.11}$$

equation (3.10) also holds for $\lambda' = \lambda$. Using the fact that the set is complete, this gives the general solutions of the time-dependent Schrödinger equation as

$$|t\rangle = \sum_{\lambda} c_\lambda \, e^{i\alpha_\lambda(t)} |\lambda; t\rangle \,, \tag{3.12}$$

where the c_λ's are constant complex numbers.

The solutions of the Schrödinger equation are thus given by the knowledge of an invariant $I(q, p, t)$, any set of its time-dependent eigenvectors, and the phases $\alpha_\lambda(t)$ which must solve Eqs. (3.11).

Derivation of a dynamical invariant

In this section, we give a simple derivation of the invariants of a 1D time-dependent HO described by (3.7). We use the classical formalism to derive the invariant, which is also an invariant of the corresponding quantum system.

The canonical Hamilton equations of motion associated with the Hamiltonian (3.7) are

$$\frac{\mathrm{d}q}{\mathrm{d}t} = \{q, H\} = \frac{p}{m}, \tag{3.13a}$$

$$\frac{\mathrm{d}p}{\mathrm{d}t} = \{p, H\} = -m\,\omega^2(t)[q - q_0(t)], \tag{3.13b}$$

where $\{A, B\} \equiv \frac{\partial A}{\partial q}\frac{\partial B}{\partial p} - \frac{\partial A}{\partial p}\frac{\partial B}{\partial q}$ are the Poisson brackets of two observables A and B.

When the angular frequency $\omega(t)$ and trap center $q_0(t)$ vary, one expects the cloud to be displaced and to change its size, thus one can introduce a canonical change of variables

$$Q = \frac{q - q_{\mathrm{cm}}(t)}{b(t)}, \quad P = P(q, p, t), \quad \tau = \tau(t), \tag{3.14}$$

leading to a new Hamiltonian H'. One has to derive conditions on the real dimensionless function b, and the displacement function q_{cm} such that the transformation is canonical. For this, we look for a new Hamiltonian of the form

$$H' = \frac{P^2}{2m} + \frac{1}{2} m\,\omega_0^2\, Q^2 + f(\tau), \tag{3.15}$$

where ω_0 is a constant angular frequency. The Hamiltonian explicitly depends on time only through the function $f(\tau)$ (which does not contain the variables Q and P). The transformation (3.14) is canonical if

$$\frac{\mathrm{d}Q}{\mathrm{d}\tau} = \{Q, H'\}, \tag{3.16a}$$

$$\frac{\mathrm{d}P}{\mathrm{d}\tau} = \{P, H'\}. \tag{3.16b}$$

From Eq. (3.16a) one deduces that

$$\mathrm{d}\tau = b^{-2}\,\mathrm{d}t \tag{3.17}$$

and that

$$P = b(p - m\dot{q}_{\mathrm{cm}}) - m\dot{b}(q - q_{\mathrm{cm}}), \tag{3.18}$$

where the dot denotes the derivation with respect to time t. From Eq. (3.16b), one finds that the functions b and q_{cm} must obey the two differential equations

$$\ddot{b} + \omega^2(t)\, b = \frac{\omega_0^2}{b^3}, \tag{3.19}$$

$$\ddot{q}_{\mathrm{cm}} + \omega^2(t)[q_{\mathrm{cm}}(t) - q_0(t)] = 0. \tag{3.20}$$

When these two equations are satisfied, the quantity

$$I = \frac{P^2}{2m} + \frac{1}{2} m\,\omega_0^2\, Q^2, \tag{3.21}$$

which appears in the new Hamiltonian is a Lewis invariant. This can be proved directly by checking that Eq. (3.9) is verified.

The choice of the function $f(\tau)$ in H' is irrelevant for the dynamics, since doing the change of Hamiltonian

$$H' \to H' - f(\tau) = I \tag{3.22}$$

corresponds to a gauge transformation which changes the phase of the wave function in the following manner:

$$\psi_{H'}(Q,\tau) \to \psi_I(Q,\tau) = e^{\frac{i}{\hbar}F(\tau)}\psi_{H'}(Q,\tau), \tag{3.23}$$

where F is a primitive of f.

Classical generating function of the transformation

Canonical transformations modify the Lagrangian and the action. If the least action principle is

$$L_H(q+\delta, \dot{q}+\dot{\delta}, t) - L_H(q,\dot{q},t) \simeq \delta \int (p\mathrm{d}q - H\mathrm{d}t) = 0, \tag{3.24}$$

with the initial Hamiltonian, δ being the function giving the distance between the actual trajectory and a neighbor one, it reads

$$L_{H'}(Q+\delta', \dot{Q}+\dot{\delta}', \tau) - L_{H'}(Q,\dot{Q},\tau) \simeq \delta' \int (P\mathrm{d}Q - H'\mathrm{d}\tau) = 0, \tag{3.25}$$

with the new Hamiltonian H'. The operator $\dot{\cdot}$ is the differentiation with respect to the new time τ. The two terms under the integrals are the exact differentials of the actions $\mathrm{d}S_H$ and $\mathrm{d}S_{H'}$. These two least action principles correspond to the same dynamics (i.e. the transformation is canonical) if the least actions of any trajectory differ by a constant in the two formulations, i.e. if the actions are the same up to an exact differential of a function G of the canonical variables [206]. Such a function is called the *generating function* of the canonical transformation. As explained above, it is defined by

$$\mathrm{d}G = \mathrm{d}S_{H'} - \mathrm{d}S_H. \tag{3.26}$$

A canonical transformation is thus not fully specified by its corresponding canonical change of variables [of the kind of Eqs. (3.14)]. For instance, it does not say how the time-dependent origin of the energy is chosen in the new Hamiltonian (if H' is admissible, then any $H' + f(\tau)$ is also admissible). In classical physics, this is not a problem because such a time-dependent factor does not change the trajectories, but in quantum mechanics, the phase of the wave function changes if such a term is added to H'.

We look for a generating function expressed with the variables q, P, and t. It thus satisfies

$$\frac{\partial G}{\partial q} = p, \quad \frac{\partial G}{\partial P} = Q, \quad \frac{\partial G}{\partial t} = H' \frac{\mathrm{d}\tau}{\mathrm{d}t} - H. \tag{3.27}$$

From these identities and Eq. (3.17), we obtain the generating function up to a time-dependent function $g(t)$

$$G(q, P, t) = \left(\frac{q - q_{\mathrm{cm}}}{b} \right) P + \frac{m\dot{b}}{2b} q^2 + m \left(\dot{b} q_{\mathrm{cm}} + b \dot{q}_{\mathrm{cm}} \right) q + g(t). \tag{3.28}$$

At this point, the new Hamiltonian is $H'(t) = I/b^2 + \alpha(t)$. By fixing $g(t)$, $\alpha(t)$ will be fixed. We impose $\alpha(t) = 0$, which gives the following form for g:

$$g(t) = -\frac{m}{2} \int_0^t \left[\left(\dot{b} q_{\mathrm{cm}} + b \dot{q}_{\mathrm{cm}} \right)^2 - \frac{\omega_0^2}{b^2} q_{\mathrm{cm}}^2 \right] \frac{\mathrm{d}t'}{b^2}. \tag{3.29}$$

We have chosen $\alpha = 0$ such that the eigenstates of I transformed by G are directly the time-dependent solutions of the initial Hamiltonian, with the appropriate phase.

Wave functions

Once an invariant has been found, the results of Sec. 3.2.1 can be used to calculate the wave functions of the time-dependent HO (3.7). We use Dirac's

method to calculate the wave function of the time-independent HO (3.21). We define dimensionless variables

$$\xi = \sqrt{\frac{m\,\omega_0}{\hbar}}Q, \quad \pi = \frac{1}{\sqrt{m\hbar\omega_0}}P, \tag{3.30}$$

satisfying the commutation relation $[\xi, \pi] = i$, and introduce the lowering and raising operators

$$a = \frac{1}{\sqrt{2}}(\xi + i\pi), \quad a^\dagger = \frac{1}{\sqrt{2}}(\xi - i\pi), \tag{3.31}$$

satisfying $[a, a^\dagger] = 1$. The invariant reads

$$I = \hbar\omega_0(a^\dagger a + 1/2). \tag{3.32}$$

The eigenstates $|n\rangle$ of the number operator $\hat{n} \equiv a^\dagger a$ are the eigenstates of I and satisfy

$$a|n\rangle = \sqrt{n}|n-1\rangle, \quad a^\dagger|n\rangle = \sqrt{n+1}|n+1\rangle, \quad n \in \mathbb{N}, \tag{3.33}$$

and $a|0\rangle = 0$. The eigenvalues of I are

$$\lambda_n = \left(n + \frac{1}{2}\right)\hbar\omega_0, \quad n \in \mathbb{N}. \tag{3.34}$$

The wave function $\psi_0(q,t) \equiv \langle q|0\rangle$ is calculated by solving the equation

$$a|0\rangle = 0 \tag{3.35}$$

in $|q\rangle$ representation. The expression of π is obtained from $p = -i\hbar\,\partial_q$, Eqs. (3.14) and (3.30), and reads

$$\pi = -i\frac{\partial}{\partial\xi} - \frac{b\dot{b}}{\omega_0}\xi - \sqrt{\frac{m}{\hbar\omega_0}}\,b\,\dot{q}_{\rm cm}. \tag{3.36}$$

Imposing the normalization condition $\int \mathrm{d}q\,|\psi_0(q,t)|^2 = 1$, and calculating the time-dependent phase corresponding to the initial Hamiltonian (3.7), we obtain the wave function

$$\psi_0(q,t) = \frac{\pi^{-1/4}}{\sqrt{a_{\rm ho}b}}\exp\left[-\frac{1}{2}\left(\frac{q-q_{\rm cm}}{a_{\rm ho}b}\right)^2\right]e^{-\frac{i}{\hbar}F(t)}e^{i\phi(q,t)}e^{-\frac{i}{\hbar}\lambda_0\int_0^t \mathrm{d}t'/b^2}, \tag{3.37}$$

where

$$\phi(q,t) = \frac{m}{\hbar}\left[\frac{\dot{b}}{2b}q^2 + \frac{1}{b}\left(\dot{q}_{\rm cm}b - q_{\rm cm}\dot{b}\right)q\right], \tag{3.38}$$

$$F(t) = \frac{m}{2}\int_0^t \mathrm{d}t'\left[\frac{1}{b^2}\left(\dot{q}_{\rm cm}b - q_{\rm cm}\dot{b}\right)^2 - \omega_0^2\frac{q_{\rm cm}^2}{b^4} + \omega^2(t')q_0^2\right], \tag{3.39}$$

and q_0, b, $q_{\rm cm}$, and their derivatives are functions of t (t' when they are under an integral symbol) and are linked by Eqs. (3.19) and (3.20). $a_{\rm ho} = \sqrt{\hbar/m\omega_0}$ is the HO length of I.

From this expression, we see the physical meaning of the two scaling functions: $q_{\rm cm}(t)$ is the center of the wave function (center of mass of a cloud which was initially at equilibrium), and $a_{\rm ho}b$ is the width of the wave function.

The wave function associated to the eigenvalue λ_n of I is expressed in terms of the nth Hermite polynomial H_n as

$$\psi_n(q,t) = \frac{1}{\sqrt{2^n n!}}\psi_0(q,t)H_n\left(\frac{q-q_{\rm cm}}{a_{\rm ho}b}\right)e^{-\frac{i}{\hbar}(\lambda_n-\lambda_0)\int_0^t \mathrm{d}t'/b^2}. \tag{3.40}$$

3.2.2 The case of an interacting Bose-Einstein condensate

For the corresponding three-dimensional (3D) interacting system of N particles, the Hamiltonian is

$$H = \sum_{i=1}^{N}\left[\frac{\mathbf{p}_i^2}{2m} + U(\mathbf{r}_i,t)\right] + \sum_{i<j} V(\mathbf{r}_j-\mathbf{r}_i). \tag{3.41}$$

The potential U is supposed to be a time-dependent 3D HO, and the rotation of this harmonic confinement is excluded for the moment (the trap keeps the same eigenaxes):

$$U(\mathbf{r},t) = \sum_{i\in\{x,y,z\}} \frac{1}{2}m\,\omega_i^2(t)\left[r_i - r_i^0(t)\right]^2, \tag{3.42}$$

V is the interaction potential between two particles, which is well approximated by a delta function (cf. Sec. 1.1.4).

The procedure described in Sec. 3.2.1 cannot be easily adapted, because it would require the knowledge of an invariant of this many-body system. However, when dealing with a BEC, as we have seen in Sec. 1.2, the dynamics is well described by a single-particle wave function whose evolution obeys the Gross-Pitaevskii equation (GPE).

Scaling approach

Let us consider a quantum system described by the wave function $\psi(\mathbf{r},t)$, whose time evolution is given by the GPE

$$i\hbar\frac{\partial}{\partial t}\psi(\mathbf{r},t) = \left[-\frac{\hbar^2}{2m}\Delta + U(\mathbf{r},t) + g_{\rm 3D}N|\psi(\mathbf{r},t)|^2\right]\psi(\mathbf{r},t), \tag{3.43}$$

with m being the mass of the particles, N the number of particles, and $g_{\rm 3D}$ the interaction coupling constant. Analogously to the non-interacting case,

we wish to write the solution of the time-dependent GPE as a function of the solution of a time-independent one expressed in a suitable frame of reference. Following this line, a strategy to solve Eq. (3.43) is to find a change of variables $\boldsymbol{\rho}(\mathbf{r}, \{b_i(t)\}, \{r_i^{\rm cm}(t)\})$ where the b_i's and the $r_i^{\rm cm}$'s are scaling and translation functions such that Eq. (3.43) can be written as a time-independent equation (i.e. a GPE with a *time-independent* potential) on the wave function $\chi(\boldsymbol{\rho}, \tau)$, defined by the relation

$$\psi(\mathbf{r}, t) = \mathcal{A}(t)\chi(\boldsymbol{\rho}, \tau)e^{i\phi(\mathbf{r},t)}, \tag{3.44}$$

where $\mathcal{A}(t)$ is a time-dependent normalization factor and $\phi(\mathbf{r}, t)$ a space- and time-dependent phase. All the dynamics induced by the time-dependent potential is *transferred* to the functions $\{b_i(t)\}$ and $\{r_i^{\rm cm}(t)\}$, and the differential equations they have to satisfy (similar to Eqs. (3.19) and (3.20)). If one can solve the new time-independent equation on χ, one solves Eq. (3.43) and knows the wave function $\psi(\mathbf{r}, t)$.

Equation (3.43) is invariant under the transformation

$$\forall i \in \{x, y, z\}, \quad \rho_i = \frac{r_i - r_i^{\rm cm}(t)}{b_i(t)} \tag{3.45}$$

in any of the following cases:

1. in the non-interacting limit [48, 207]: in this case the system is equivalent to three independent HO of the kind treated in Sec. 3.2.1,

2. for a suitable driving of the interaction term $g_{3\rm D}$ [207], that is, assuming one can control $g_{3\rm D}(t)$ at will (this can be done using Feshbach resonances),

3. in the TF limit [49].

This third case, which is detailed in the following section, is used in the rest of this chapter.

Condensate wave function in the Thomas-Fermi approximation

Given a time-dependent GPE, the TF approximation consists in neglecting the kinetic-energy-like term in the $\boldsymbol{\rho}$-frame of reference, i.e. $-\hbar^2/(2m)\sum_i b_i^{-2}\partial^2\chi/\partial\rho_i^2$, supposed to be small compared to the interaction term [49, 50]. In this regime, provided that $\mathcal{A}(t) = (\Pi_i b_i)^{-1/2}$ and that

$$\phi(\mathbf{r}, t) = \frac{m}{\hbar}\left\{\sum_i \left[\frac{r_i^2}{2}\frac{\dot{b}_i}{b_i} + \frac{r_i}{b_i}\left(\dot{r}_i^{\rm cm} b_i - r_i^{\rm cm}\dot{b}_i\right)\right]\right\} + \phi_0(t), \tag{3.46}$$

with

$$\phi_0(t) = -\frac{m}{2\hbar}\sum_i \int_0^t \mathrm{d}t' \left\{ \frac{1}{b_i^2}\left(\dot{r}_i^{\mathrm{cm}} b_i - r_i^{\mathrm{cm}}\dot{b}_i\right)^2 - \omega_i^2(0)\frac{(r_i^{\mathrm{cm}})^2}{b_i^4} + \left[\omega_i(t')r_i^0(t')\right]^2 \right\}, \tag{3.47}$$

where the scaling and translation functions are solutions of

$$\forall i \in \{x,y,z\}, \quad \ddot{b}_i + \omega_i^2(t) b_i = \frac{\omega_i^2(0)}{b_i b_x b_y b_z}, \tag{3.48}$$

$$\ddot{r}_i^{\mathrm{cm}} + \omega_i^2(t)\left[r_i^{\mathrm{cm}} - r_i^0(t)\right] = 0, \tag{3.49}$$

one gets the following equation on χ:

$$i\hbar\frac{\partial}{\partial\tau}\chi(\boldsymbol{\rho},\tau) = \left[U(\boldsymbol{\rho},0) + g_{3\mathrm{D}}N|\chi(\boldsymbol{\rho},\tau)|^2\right]\chi(\boldsymbol{\rho},\tau), \tag{3.50}$$

where we defined a rescaled time

$$\tau(t) = \int_0^t \frac{dt'}{\Pi_i b_i(t')}. \tag{3.51}$$

If at $t = 0$ the condensate is at equilibrium, the solution of Eq. (3.50) is

$$\chi(\boldsymbol{\rho},\tau) = \left[\frac{\mu - U(\boldsymbol{\rho},0)}{g_{3\mathrm{D}}N}\right]^{1/2} e^{-i\frac{\mu}{\hbar}\tau}, \tag{3.52}$$

where μ is the chemical potential. This gives the typical inverted parabola density profile whose sizes evolve in time as $R_i(t) = R_i(0)b_i(t)$, where the $R_i(0) = \sqrt{2\mu_0/m\omega_i^2(0)}$ are the initial TF radii.

3.3 Shortcuts to adiabaticity

In this section, the definition of a shortcut to adiabaticity is given, and the results of Sec. 3.2 are used to derive angular frequency trajectories realizing such shortcuts, for both non-interacting gases and interacting BECs confined in time-dependent harmonic traps.

3.3.1 Shortcut to adiabaticity based on an invariant of motion

For a system described by a Hamiltonian $H(t)$, a *shortcut to adiabaticity* is realized when another Hamiltonian $H'(t)$ can be found, such that the state obtained after a finite time of evolution with $H'(t)$ is *identical* (up to a global phase factor) to the final state of the adiabatic evolution with $H(t)$. Shortcuts to adiabaticity are generally *not* adiabatic; only the final state is identical to that obtained after an adiabatic evolution.

The possibility of such shortcuts has been known for a long time. Indeed, in the case of a HO with a time-dependent frequency $\Omega(t)$ treated by Lewis and Riesenfeld [205], when discussing the transition probability P_{sm} between two instantaneous eigenstates $|s\rangle$ and $|m\rangle$ after a given time of evolution with $H(t)$, the authors noticed:

> "[Assuming some conditions on $\Omega(t)$] yields
>
> $$P_{sm} = \delta_{sm},$$
>
> which also is the result given by the adiabatic approximation. We conclude that the rigorous transition probability coincides with the adiabatic transition probability [...]. It is clear that only a restricted class of $\Omega(t)$ functions will produce such a result, but the members of this class need by no means satisfy any adiabaticity requirement. The time evolution of such systems [...] will in general be non-adiabatic."

Such *shortcuts to adiabaticiy* can thus be realized by simply engineering the time-dependent parameters of the Hamiltonian (in this case, the angular frequency).

A practical method to find a class of appropriate $\omega(t)$ was detailed by Chen et al. [19]. In this case, the Hamiltonian is chosen to be time-independent (but with different frequencies) outside the time interval $t \in [0, t_f]$. An invariant is engineered to commute with the Hamiltonian outside this interval. This yields a specific $\omega(t)$ for which all the eigenstates of $H(t \leq 0)$ are exactly mapped to the corresponding ones of $H(t \geq t_f)$ after the evolution for $t \in [0, t_f]$. Up to a global phase and a rescaling of the energies and lengths, the final state (at time $t = t_f$) is *identical* to the initial one ($t = 0$), i.e. if the initial state is

$$|\psi\,;\, t \leq 0\rangle = \sum_n c_n |n\,;\, t = 0\rangle e^{-i\omega_n(0)t}, \tag{3.53}$$

where $\{|n\,;\, t\rangle, n \in \mathbb{N}\}$ is a basis of instantaneous eigenstates of $H(t)$, with $\{\hbar\omega_n(t)\}$ the corresponding eigenvalues, and $\sum_n |c_n|^2 = 1$, the final state is

$$|\psi\,;\, t \geq t_f\rangle = e^{i\Phi} \sum_n c_n |n\,;\, t_f\rangle e^{-i\omega_n(t_f)t - i\delta_n}, \tag{3.54}$$

where $\delta_n = \lambda_n/\hbar \int_0^{t_f} \mathrm{d}t'/b^2$. This is true *even if the initial state is not an equilibrium state.*

Frequency trajectory for a non-interacting gas

The Hamiltonian is assumed to have the form

$$H = \frac{p^2}{2m} + \frac{1}{2} m\,\omega^2(t) q^2 + mgq, \tag{3.55}$$

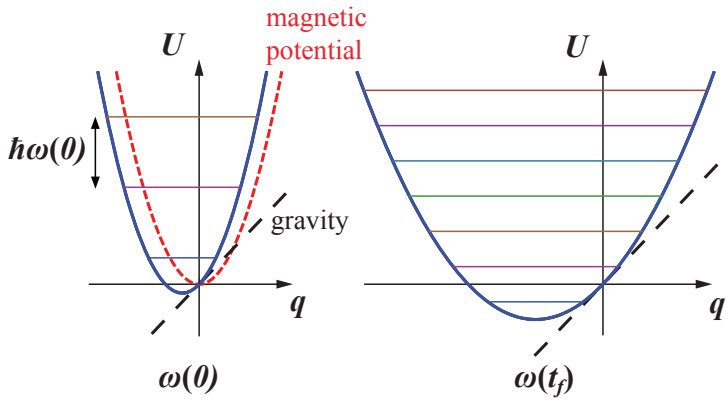

Figure 3.1: Schematic representation of the trap decompression. The potential (plain blue line) is the sum of the gravitational potential (dashed black line) and the harmonic magnetic potential (dashed red line). When the trap frequency is changed from $\omega(0)$ to $\omega(t_f)$, the lengths are multiplied by $\gamma = \sqrt{\omega(0)/\omega(t_f)}$, and the energies divided by γ^2. Because of gravity, the trap center shifts vertically by $\Delta q = -g\left[1/\omega^2(t_f) - 1/\omega^2(0)\right]$.

which is identical to (3.7), with the additional constraint $q_0(t) = -g/\omega^2(t)$ (and a gauge transformation consisting in adding $-m\,\omega^2(t)\,q_0^2(t)/2$ to H). It describes a single particle in a harmonic trap subject to a constant force, which, in the experiments presented in Sec. 3.4, comes from gravity. The angular frequency $\omega(t)$ is assumed to be constant outside the interval $t \in [0, t_f]$. During this interval, the problem is to find the appropriate frequency trajectory $\omega(t)$, connecting the initial trap of initial frequency $\omega(0)$ to a final trap of frequency $\omega(t_f)$, for the decompression [or compression if $\omega(0) < \omega(t_f)$] to implement a shortcut to adiabaticity. Figure 3.1 shows the initial and final situations assuming a decompression $[\omega(t_f) < \omega(0)]$.

We used the strategy introduced by Chen et al. [19]. If the invariant commutes with the Hamiltonian

$$[I, H] = 0 \tag{3.56}$$

for $t \leq 0$ and $t \geq t_f$, and provided that the functions b and $q_{\rm cm}$ are sufficiently continuous, the stationary states of $H(t \leq 0)$ will be transferred to the corresponding ones of $H(t \geq t_f)$.

It is convenient to use the dimensionless function

$$c(t) = -\frac{\omega_0^2}{g}\frac{q_{\rm cm}(t)}{b(t)} \tag{3.57}$$

instead of q_{cm}, and to rewrite Eq. (3.20) using the rescaled time τ [Eq. (3.17)]. Equation (3.20) becomes

$$\mathrm{d}^2c/\mathrm{d}\tau^2 + \omega_0^2\, c = \omega_0^2\, b^3. \tag{3.58}$$

If one chooses to set $\omega_0 = \omega(0)$, and the conditions

$$b(0) = 1, \qquad \dot{b}(0) = 0, \tag{3.59a}$$
$$c(0) = 1, \qquad \dot{c}(0) = 0, \tag{3.59b}$$

then $I(0) = H(t \leq 0)$, and if

$$b(t_f) = \gamma, \qquad \dot{b}(t_f) = 0, \tag{3.59c}$$
$$c(t_f) = \gamma^3, \qquad \dot{c}(t_f) = 0, \tag{3.59d}$$

where $\gamma \equiv \sqrt{\omega_0/\omega_f}$, then $I(t_f) = \gamma^2 H(t \geq t_f) + h(t)$, where h is a function of time only. These boundary conditions thus fulfil the condition (3.56). Since the functions b and c must be solutions of Eqs. (3.19) and (3.58), four additional boundary conditions must be satisfied:

$$\ddot{b}(0) = 0, \qquad \ddot{b}(t_f) = 0, \tag{3.59e}$$
$$\ddot{c}(0) = 0, \qquad \ddot{c}(t_f) = 0. \tag{3.59f}$$

Polynomial ansatz In order to construct the functions b and c satisfying these boundary conditions and the two differential equations (3.19) and (3.58), it is convenient to write all the boundary conditions on the function c and its derivatives with respect to the rescaled time τ. Using Eqs. (3.17) and (3.19), and differentiating Eq. (3.58) twice with respect to τ, one finds the ten conditions

$$c(0) = 1, \tag{3.60a}$$
$$c(\tau_f) = \gamma^3, \tag{3.60b}$$

and, for all $k \in \{1, 2, 3, 4\}$,

$$\frac{\mathrm{d}^k c}{\mathrm{d}\tau^k}(0) = 0, \tag{3.60c}$$
$$\frac{\mathrm{d}^k c}{\mathrm{d}\tau^k}(\tau_f) = 0, \tag{3.60d}$$

which are sufficient for the twelve boundary conditions (3.59). τ_f is the rescaled time corresponding to t_f: $\tau_f = \int_0^{t_f} b^{-2}(t')\,\mathrm{d}t'$.

Under this form, the boundary conditions are well suited to use a polynomial ansatz for $c(\tau)$, deduce $b(\tau)$ with Eq. (3.58), compute $\tau(t)$ by numerically integrating Eq. (3.17), and obtain $b(t)$. The final step consists in using Eq. (3.19) to obtain the time-dependent trap frequency as $\omega^2(t) = \omega_0^2/b^4 - \ddot{b}/b$.

An example of this procedure is given in Fig. 3.2 for particular values of the initial and final frequencies. The final rescaled time τ_f can be chosen at will, it can be arbitrarily small, but one important constraint on the function c is that it must not lead to vanishing values of b which give infinite $\omega^2(t)$. Additional constraints on c arise from experimental requirements, such as positive $\omega^2(t)$ (attractive potentials), the maximal and minimal frequencies attainable with a given setup, the *rate* at which $\omega(t)$ can be varied etc. Since all these depend on a particular experimental setup, no mathematical analysis of the *best* ansatz to use was done.

For the experiments presented in Sec. 3.4 and in Refs. [208, 209], a polynomial of order fifteen was used,

$$c(\tau) = \sum_{k=0}^{15} c_k \left(\frac{\tau}{\tau_f}\right)^k . \tag{3.61}$$

The first coefficient is fixed to 1 by Eq. (3.60a) and $c_1, \cdots, c_4$ are fixed to 0 by Eqs. (3.60c). We arbitrarily impose $c_5 = c_6 = \cdots = c_{10} = 0$, which leaves five coefficients which are uniquely determined by the remaining boundary conditions (3.60b) and (3.60d). The calculation of these remaining coefficient is done by inverting the linear system corresponding to these five equations.

In principle, since there are ten boundary conditions, a 9th order polynomial can be used, which yields a unique solution for the ten coefficients of c. Nevertheless, the obtained trajectory was not well behaved enough to be realized experimentally (the frequency was decreasing too fast in the beginning compared to what could be achieved by the apparatus). This is the reason why a higher order polynomial was used and six coefficients were fixed to 0.

Since the polynomial can be of any order greater than 9, and the boundary conditions only impose a linear relation between ten of its coefficients, there is obviously an infinity of different solutions connecting two given initial and final states. Moreover, other functions than polynomials could be used for c, as long as they provide enough free parameters.

The obtained nonzero coefficients of (3.61) are given in Tab. 3.1.

Example

In this section we determine the trajectory used in Sec. 3.4.2 and in Ref. [208]. The parameters are given in Tab. 3.2. Figure 3.2 shows the functions $c(\tau)$, $b(\tau)$, $t(\tau)$ and $\omega(t)/2\pi$ corresponding to this decompression.

Table 3.1: Nonzero coefficients of the polynomial ansatz $c(\tau)$ calculated from the boundary conditions (3.60).

c_0	c_{11}	c_{12}	c_{13}	c_{14}	c_{15}
1	$1365(\gamma^3-1)$	$5005(\gamma^3-1)$	$6930(\gamma^3-1)$	$4290(\gamma^3-1)$	$1001(\gamma^3-1)$

Table 3.2: Parameters of the 1D decompression of a non-interacting thermal gas.

Initial frequency $\omega(0)/2\pi$	235.8 Hz
Final frequency $\omega(t_f)/2\pi$	15.67 Hz
Final rescaled time τ_f	5.65 ms
Corresponding duration t_f	35.0 ms

Since the exact wave functions are known, all the properties of the atomic cloud during the decompression can be calculated. For instance, Fig. 3.3 displays the size and center-of-mass position of a cloud initially at equilibrium in the compressed trap. These are compared to the same values if the decompression were done very slowly as in the adiabatic theorem. The clear difference between the solid and dashed curves illustrates the fact that the decompression is not adiabatic.

3.3.2 Shortcut to adiabaticity for an interacting Bose-Einstein condensate in the Thomas-Fermi limit

Let us suppose that $\psi(\mathbf{r}, t \leq 0)$ is a stationary state of Eq. (3.43). We can engineer the parameters of the potential $U(\mathbf{r}, t)$ such that $\psi(\mathbf{r}, t_f)$ is also a stationary state for $t \geq t_f$. This implies that $\chi(\rho, \tau \geq \tau_f)$, with $\tau_f = \tau(t_f)$, must be a stationary state of Eq. (3.50) and that $\nabla_{\mathbf{r}}\phi(\mathbf{r}, t_f) = 0$. If these two conditions hold, $\psi(\mathbf{r}, t)$ can evolve between two stationary states during the time interval $[0, t_f]$, even if it is strongly different from the "adiabatic stationary state" during the evolution. In our experiment, the time-dependent trapping potential has a cylindrical symmetry of the form

$$U(\mathbf{r}, t) = \frac{1}{2} m\, \omega_\perp^2(t) \left(r_x^2 + r_z^2\right) + \frac{1}{2} m\, \omega_\parallel^2(t) r_y^2 + m g r_z \,, \tag{3.62}$$

with initial and final angular frequencies $\omega_{\perp,\parallel}(0)$ and $\omega_{\perp,\parallel}(t_f) = \omega_{\perp,\parallel}(0)/\gamma_{\perp,\parallel}^2$ respectively. This case corresponds to fixing $\forall\ t,\ r_{x,y}^0(t) = 0$ in Eq. (3.42) and $r_z^0(t) = -g/\omega_\perp^2(t)$. By introducing the dimensionless function

$$c(t) = -\frac{\omega_\perp^2(0)}{g} \frac{r_z^{\rm cm}(t)}{b_\perp(t)}, \tag{3.63}$$

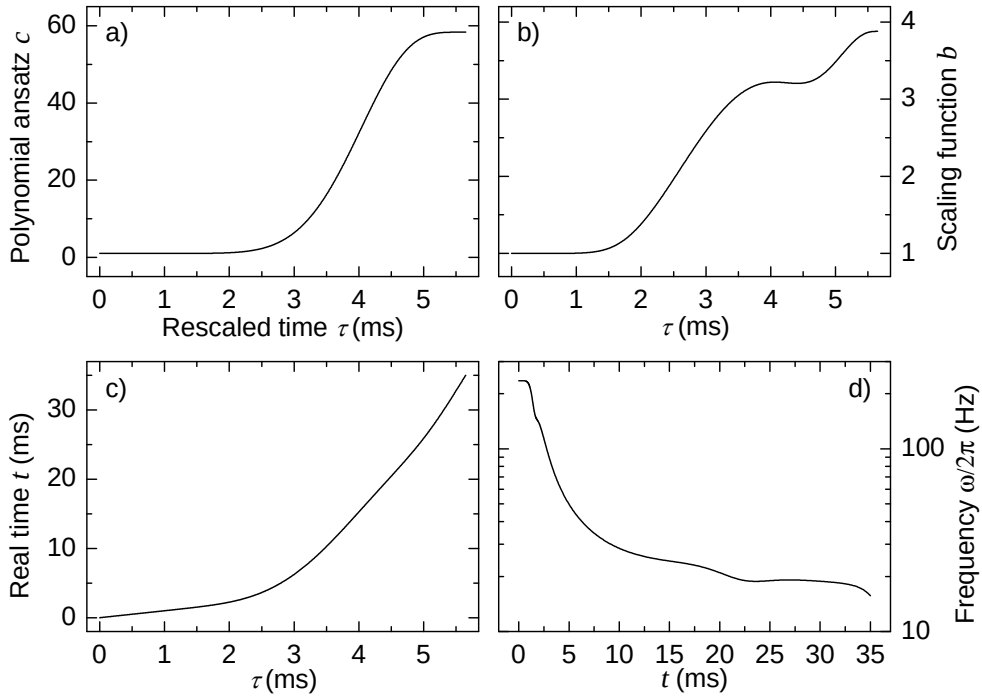

Figure 3.2: Determination of the frequency trajectory when the trap is decompressed from $\omega(t=0)/2\pi = 235.8$ Hz to $\omega(t_f)/2\pi = 15.67$ Hz within 35 ms (cf. parameters of Tab. 3.2). (a) A fifteenth order polynomial ansatz is used for the displacement function $c(\tau)$, which gives (b) the scaling function $b(\tau)$ through Eq. (3.58); (c) real time $t(\tau)$ is calculated by numerically integrating Eq. (3.17); (d) Eq. (3.19) is used to determine the time-dependent frequency $\omega(t)/2\pi$ (note the logarithmic scale).

the differential equations (3.48) and (3.49) take the form

$$\ddot{b}_\perp(t) + b_\perp(t)\omega_\perp^2(t) = \omega_\perp^2(0)/[b_\perp^3(t)b_\parallel(t)], \tag{3.64}$$

$$\ddot{b}_\parallel(t) + b_\parallel(t)\omega_\parallel^2(t) = \omega_\parallel^2(0)/[b_\parallel^2(t)b_\perp^2(t)], \tag{3.65}$$

$$b_\perp^4(t)b_\parallel(t)\ddot{c}(t) + 2b_\perp^3(t)b_\parallel(t)\dot{b}_\perp(t)\dot{c}(t) + \omega_\perp^2(0)c(t) - \omega_\perp^2(0)b_\perp^3(t)b_\parallel(t) = 0. \tag{3.66}$$

The final state is an equilibrium state if (i) the final TF radii satisfy that $R_{\perp,\parallel}(t_f)/R_{\perp,\parallel}(0) = \gamma_{\perp,\parallel}^2$, (ii) the vertical center-of-mass position fulfills the condition $r_z^{\rm cm}(t_f)/r_z^{\rm cm}(0) = \gamma_\perp^4$, and (iii) the condensate flow is null, namely $\nabla\phi = 0$. These constraints yield the boundary conditions $\dot{c}(0) = \dot{c}(t_f) = \dot{b}_{\perp,\parallel}(0) = \dot{b}(t_f)_{\perp,\parallel} = 0$ and $c(0) = 1$, $c(t_f) = \gamma_\perp^{14/5}\gamma_\parallel^{2/5}$, $b_{\perp,\parallel}(0) = 1$, $b_\perp(t_f) = \gamma_\perp^{6/5}\gamma_\parallel^{-2/5}$ and $b_\parallel(t_f) = \gamma_\perp^{-4/5}\gamma_\parallel^{8/5}$. These latter imply that $\ddot{b}_{\perp,\parallel}(0) = \ddot{b}_{\perp,\parallel}(t_f) =$

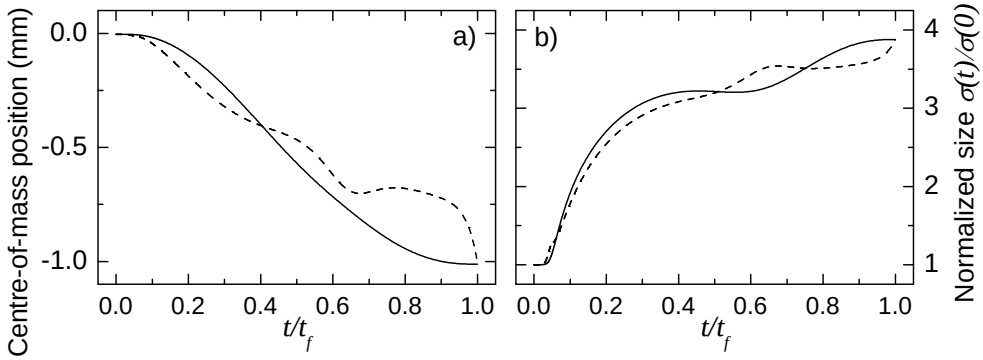

Figure 3.3: Expected (a) center-of-mass position and (b) cloud size during a fast decompression (same parameters as Tab. 3.2 and Fig. 3.2). The dashed curves correspond to the same values in the adiabatic limit $t_f \to \infty$. The adiabatic center-of-mass position is the trap minimum $q_{\mathrm{ad.}}(t) = -g/\omega^2(t)$, and the adiabatic size is $\sigma_{\mathrm{ad.}}(t) = \sqrt{\omega_0/\omega(t)}\sigma(0)$.

0 must hold as well, giving sixteen independent boundary conditions.

Our procedure to engineer $\omega_{\perp,\parallel}(t)$ is to reduce the dimensionality of the problem by only considering the trajectories that lead to a constant axial size. This corresponds to keeping $b_\parallel(t) = b_\parallel(0)$ for any t, fixing a trap decompression with $\gamma_\perp = \gamma_\parallel^2$. This choice simplifies the determination of the trajectories, but it does not reflect a restriction of the range of application of the method. In this case, Eqs. (3.64)–(3.66) reduce to

$$\ddot{b}_\perp(t) + b_\perp(t)\omega_\perp^2(t) = \omega_\perp^2(0)/b_\perp^3(t), \tag{3.67}$$

$$\omega_\parallel(t) = \omega_\parallel(0)/b_\perp(t), \tag{3.68}$$

$$b_\perp^4(t)\ddot{c}(t) + 2b_\perp^3(t)\dot{b}_\perp(t)\dot{c}(t) + \omega_\perp^2(0)c(t) - \omega_\perp^2(0)b_\perp^3(t) = 0. \tag{3.69}$$

Equation (3.67) is identical to Eq. (3.19) and Eq. (3.69) is nothing but Eq. (3.58) expressed in terms of the real time t [the rescaled time being given by Eq. (3.51) instead of Eq. (3.17)]. Thus we can exploit for $b_\perp(t)$ and $c(t)$ the solutions obtained for the non-interacting gas, provided that the axial frequency is varied according to Eq. (3.68).

Example

As an example of the procedure described above, we determine the trajectories used in Sec. 3.4.3 and in Ref. [209]. The decompression parameters are given in Tab. 3.3. The radial frequency is reduced by a factor of 9, and the axial frequency by a factor of 3. The obtained trajectories are represented in Fig. 3.4.

Table 3.3: Parameters of the 3D decompression of an interacting Bose-Einstein condensate.

Initial radial frequency $\omega_\perp(0)/2\pi$	235.8 Hz
Final radial frequency $\omega_\perp(t_f)/2\pi$	26.2 Hz
Initial axial frequency $\omega_\parallel(0)/2\pi$	22.2 Hz
Final axial frequency $\omega_\parallel(t_f)/2\pi$	7.4 Hz
Final rescaled time τ_f	11.555 ms
Corresponding duration t_f	30.0 ms

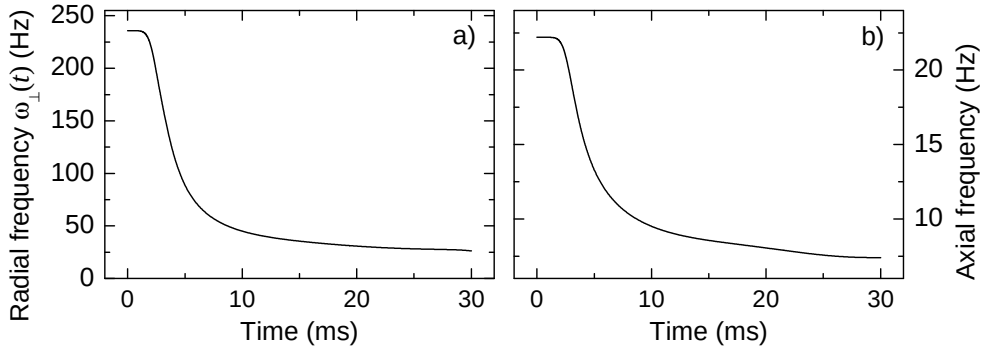

Figure 3.4: (a) Radial and (b) axial trap frequencies for the shortcut decompression of a BEC in $t_f = 30$ ms.

Validity of the Thomas-Fermi approximation

To check the validity of the Thomas-Fermi approximation that led to the trajectories of Fig. 3.4, three-dimensional Gross-Pitaevskii simulations have been performed and compared with the analytical results of Sec. 3.3.2. In the numerical solution we use a split step operator in time combined with a fast Fourier transformation in space. The results are presented in Fig. 3.5 and show that this approximation is well justified for our experimental parameters (decompression of Fig. 3.4, number of atoms $N \sim 10^5$, scattering length of ^{87}Rb of $a_s \simeq 110\, a_0$, a_0 being the Bohr radius).

3.4 Experimental realization of shortcuts to adiabaticity

The procedure described above was tested experimentally by quickly decompressing a trapped ultracold gas of ^{87}Rb atoms. In this section, we describe the experimental sequence, how the decompression is controlled, monitored, and compared to simpler (non-optimal) schemes.

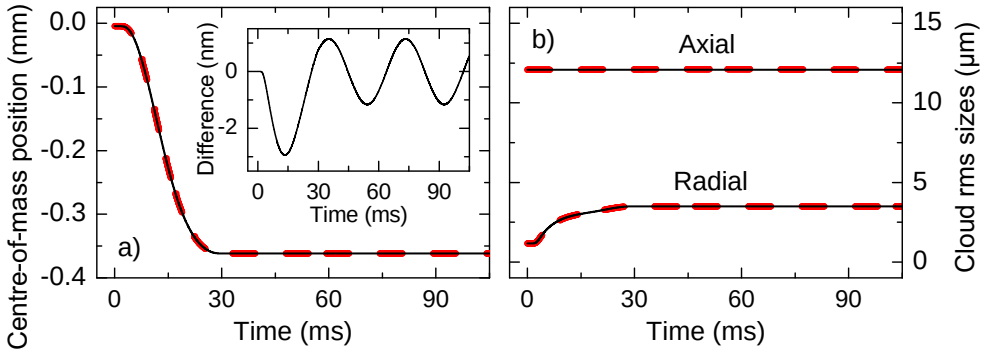

Figure 3.5: Comparison between the GPE simulations (dashed red lines) and the scaling solutions given by the Thomas-Fermi approximation (solid black lines) showing its validity. (a) Center-of-mass position; (b) axial and radial sizes. The peak relative difference between the scaling solution and the GPE simulations are respectively 0.3 % and 0.2 % for the axial and radial sizes. The decompression occurs during the first 30 ms, after which the cloud evolves in the static final trap.

3.4.1 Control of the trapping frequencies

As we have seen in Chap. 2, the trap is well approximated by a 3D harmonic potential for sufficiently low temperatures $T \ll \mu_B B_0/k_B$. This temperature is approximately 100 μK for our typical bias of 1.5 G. In the initial compressed trap , the frequencies are measured to be $\omega_x(0)/2\pi = 228.1$ Hz, $\omega_y(0)/2\pi = 22.2$ Hz and $\omega_z(0)/2\pi = 235.8$ Hz, the z axis being the vertical one.

Implementing shortcuts to adiabaticity requires a precise control of the trapping frequencies, in a dynamical fashion. In our QUIC magnetic trap, this can be achieved by varying the current i_Q running through the three coils, and the current i_{B_0} running through an additional pair of Helmoltz coils positioned along the axial dimension of the trap (compensation coils). The resulting potential is

$$U(x,y,z) = \mu|\mathbf{B}| \simeq \mu\left[B_0 + \frac{1}{2}\frac{B'^2}{B_0}\left(x^2+z^2\right) + \frac{1}{2}B''y^2\right], \tag{3.70}$$

where $\mu/h = 1.4$ MHz/G for atoms in $|5^2S_{1/2}, F=2, m_F=+2\rangle$. B' is the radial magnetic field gradient while B'' corresponds to its curvature along y. We recall that the radial and axial angular frequencies are

$$\omega_\perp \equiv \omega_z \simeq \omega_x \simeq \sqrt{\frac{\mu}{m}}\frac{B'(i_Q)}{\sqrt{B_0(i_Q,i_{B_0})}}, \quad \omega_\parallel \equiv \omega_y = \sqrt{\frac{\mu}{m}}\sqrt{B''(i_Q)}. \tag{3.71}$$

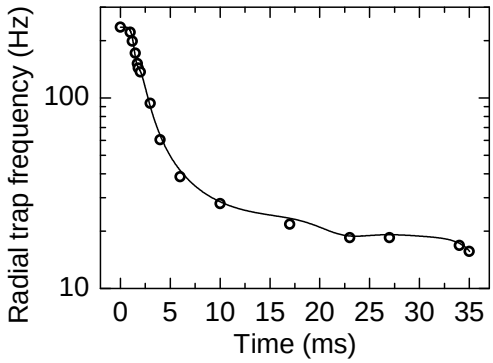

Figure 3.6: Vertical trap frequency calibration. The solid line is the theoretical shortcut decompression trajectory, the circles are the measured frequencies. The parameters of the decompression are given in Tab. 3.2.

These expressions show that the radial and axial frequencies can be controlled independently to some extent. The experimental realization of the shortcut trajectories requires a careful preliminary calibration of the frequencies versus currents, which is achieved by monitoring the cloud's center-of-mass oscillations after a small excitation (cf. Sec 2.2.2). Due to the finite time response of the control circuit, it is also necessary to check the behavior of the frequency during an actual trajectory. This is illustrated in Fig. 3.6, where we compare the theoretical decompression trajectory of Fig. 3.2 (line) to measured experimental values (circles). In this example, the deviation is below 5%.

3.4.2 Shortcut to adiabaticity for a non-interacting gas

In order to produce an ultracold thermal cloud sufficiently dilute for collisions to be negligible, the loading time of MOT2 is reduced. Then an evaporation ramp similar to the one used to obtain BECs is applied. This produces a dilute thermal gas, with a low elastic collision rate. It contains $N \simeq 10^5$ atoms at a temperature of $T_0 = 1.6$ μK. This corresponds to an average collision rate per particle of $\gamma_{\rm el} \simeq 8$ Hz, and a collision time of 125 ms. This is 30 times the oscillation period, and more than 3 times the decompression time, which justifies the non-interacting approximation. The 3 dimensions of the trap are thus not coupled and the system is equivalent to N simultaneous realizations of 3 independent HOs.

We use here the decompression trajectory discussed in Sec. 3.3.1, adapted to the vertical axis (Oz), with the parameters of Tab. 3.2. To maximize the decompression factor $\gamma^2 = \omega_z(0)/\omega_z(t_f)$, the compensation coils current i_{B_0} is increased from $i_{B_0}(t=0) \simeq 0$ A to $i_{B_0}(t_f) = 3.0$ A, while the QUIC current is decreased from $i_Q(t=0) = 26.7$ A to $i_Q(t_f) = 3.6$ A (see the resulting trajectory in Fig. 3.6). The decompression duration is $t_f = 35$ ms.

In theory, starting from a gas at equilibrium and temperature T_0 in the compressed trap, a shortcut to adiabaticity should lead to an equilibrium state in the final trap, with a temperature $T_f = T_0\,\omega(t_f)/\omega(0)$. This corresponds

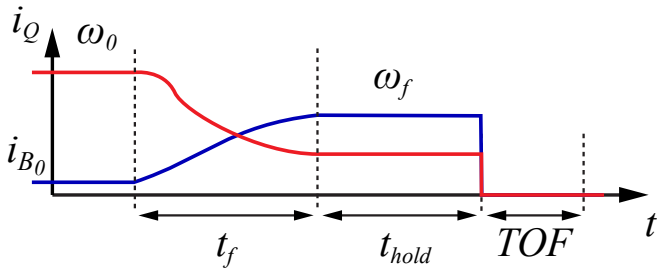

Figure 3.7: A cloud is first prepared in the compressed trap (frequency ω_0), which is then decompressed within a time t_f by simultaneously decreasing the QUIC current i_Q and increasing the compensation coils current i_{B_0} in a controlled way. The cloud then freely evolves in the decompressed trap for a variable amount of time t_{hold} before a time of flight measurement is performed (TOF).

to a situation where entropy has not increased. On the contrary, for a non-optimal decompression, one expects to observe oscillations of the cloud's size and center of mass in the decompressed trap, once the decompression is completed.

To evaluate the efficiency of our shortcut, we thus perform the fast decompression, and hold the cloud in the decompressed trap for a variable amount of time. The trap is then abruptly switched off, and an absorption image is taken after a constant time of free expansion (6 ms). This is illustrated in Fig. 3.7. The amplitude of the dipole (oscillation of the center of mass) and breathing modes (oscillation of the size) give access to the excess energy provided to the cloud, as compared to an adiabatic modification of the potential. If the cloud is reasonably at equilibrium after decompression, one can also directly measure the final temperature by measuring the evolution of the size during a free expansion.

In the following, we compare four decompression trajectories:

1. the shortcut, given in Figs. 3.2d and 3.6,

2. a linear decompression of the same duration (35 ms),

3. an abrupt decompression, which, somehow, corresponds to a worst case scenario (in practice, the decompression time is 0.1 ms and $\omega(t)$ is not controlled, and is imposed by the response of the magnetic trap control electronics),

4. a 6-s-long linear decompression, which can be considered nearly adiabatic.

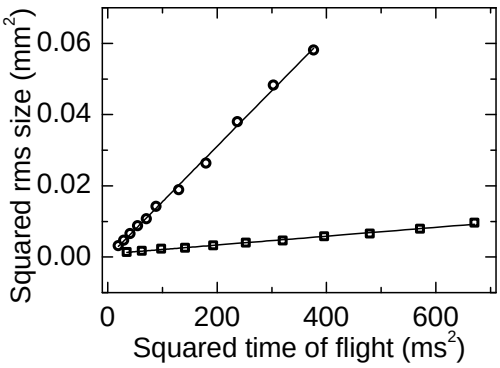

Figure 3.8: Temperature measurements before (circles) and after decompression (squares). The lines are linear fits. The initial temperature is measured to be $T_0 = 1.63$ μK, and the final temperature $T_f = 130$ nK, which is a factor of 12.5, close to the expected $\omega_z(0)/\omega_z(t_f) = 15$ (the measurement is done after the 6-s-long linear decompression).

What is referred to as "linear decompression" corresponds to both control currents being varied linearly with time. The corresponding frequency trajectory *is not linear*[2].

The experimental results are summarized on Fig. 3.9. In the case of the 6-s-long linear ramp (filled squares), very little residual excitation is observed (although the residual dipole mode is still measurable), and the temperature directly measured by time of flight is close to the expected value for an adiabatic decompression (cf. Fig. 3.8). In the shortcut case (open circles), clear oscillations of the cloud width and center-of-mass position are seen, but they are much reduced compared to the fast linear ramp (diamonds) and abrupt decompression (open squares).

Compared to the linear decompression in 35 ms, the shortcut reduces the amplitude of the dipole mode by a factor of 7.2 (obtained from the sine fits) and the amplitude of the breathing mode by a factor of 3 (comparison of the standard deviations of the two sets of data). The excess energy, which is dominated by the center-of-mass energy, is thus reduced by a factor of ~ 52. In the case of the 6-s-long ramp, we measured a final temperature of the cloud of 130 nK, a factor 12.5 below the initial one. This is consistent with the expected value of 15. The small difference may arise from a small heating rate due to the fluctuations of the magnetic trap.

The fact that the shortcut decompression still produces sizeable excitations is due to experimental imperfections. Several possible causes can be invoked. Firstly, as seen on Fig. 3.6, there are still small deviations from the ideal trajectory. These may have an impact, especially in the last phase of the trajectory where the cloud is subject to a large acceleration (see Fig. 3.3). Second, as can be seen again in Fig. 3.3, during the trajectory the cloud

[2]Cf. the expressions of the trap frequencies (3.71) knowing that the magnetic fields are proportional to the currents

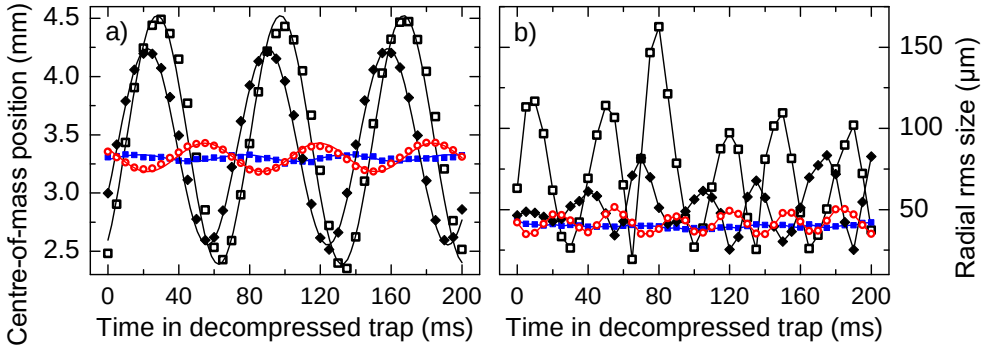

Figure 3.9: Comparison between different trap decompression schemes (along the vertical axis). Open red circles: shortcut decompression in 35 ms; black diamonds: linear decompression in 35 ms; solid blue squares: linear decompression in 6 s; open black squares: abrupt decompression. The decompression is performed, and then, the cloud is held in the decompressed trap for a variable time. We monitor (a) the vertical center-of-mass position (dipole mode) and (b) the cloud size (breathing mode), after 6 ms time of flight. In (a), the solid lines are sine fits, in (b) they just connect the points to guide the eye.

wanders quite far (several hundred μm) from the trap center and feels the non-harmonic region of the potential. This effect is difficult to quantify since our knowledge of the potential shape is not sufficiently accurate (however, the anharmonicity could be inferred from variations of the oscillation frequency with amplitude).

Fig. 3.10 shows the behavior of the axial size of the cloud in the conditions of Fig. 3.9b. Since the shortcut trajectory was designed only for the radial dimensions, the resulting axial breathing mode is of the same magnitude as for the linear decompression.

We compare in Fig. 3.11 the results of the shortcut decompression to linear ramps of various durations. The vertical axis in this figure represents amplitudes of oscillations after trap decompression, either of the center-of-mass position (filled symbols) or of the cloud radius (open symbols), scaled by their values for an abrupt decompression ($t_f \sim 0.1$ ms). The horizontal axis is the duration of the decompression t_f (notice the logarithmic scale). The circles correspond to linear decompressions while the stars are the shortcut results. As can be seen, fulfilling the adiabaticity criterion is easier for the breathing mode (size oscillation) than for the dipole mode (center-of-mass oscillation): the oscillation amplitude is reduced by a factor of 2 for $t_f = 20$ ms for the earlier, and for $t_f \simeq 150$ ms for the latter. Using the amplitude of the dipole mode as a criterion to compare the linear and shortcut schemes, one sees that

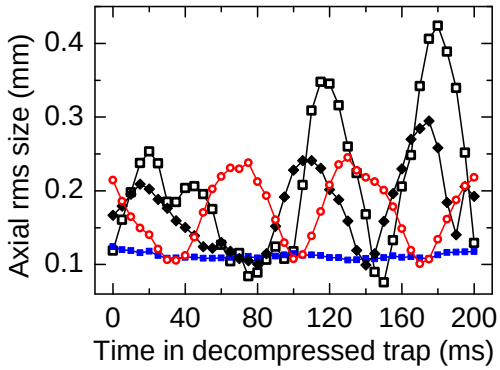

Figure 3.10: Impact of the vertical decompression schemes on the axial size (y direction). The same colors and symbols as in Fig. 3.9 are used. The amplitude of the axial breathing mode is not affected by the use of a shortcut trajectory adapted to the radial dimensions.

the decompression time is reduced by a factor of 37.

3.4.3 Shortcut to adiabaticity for an interacting condensate

As opposed to the previous case of non-interacting atoms, the decompression of a BEC is an intrinsically 3D problem because of the interactions. As a result, both the radial and axial frequencies have to be varied following Eqs. (3.67) and (3.68) in order to realize a shortcut to adiabaticity. In the present section, we describe a decompression experiment based on the trajectories discussed in Sec. 3.3.2 and represented in Fig. 3.4. In this scheme, the radial frequency is decreased by a factor of 9, while the axial frequency is adjusted to maintain the *axial size* of the BEC *fixed* during the whole trajectory. Accordingly, the axial frequency is decreased by a factor of 3.

We start from an initial BEC containing 1.3×10^5 atoms in the condensed fraction, and 7×10^4 non-condensed atoms at a temperature of 130 nK. The experimental scheme is similar to that employed for the thermal cloud. Here, we use a longer time of flight of 28 ms to characterize the various excitations generated by rapid decompressions. Three decompression schemes are compared:

1. the shortcut to adiabaticity in 30 ms,
2. the linear decompression in 30 ms,
3. an abrupt decompression.

Contrary to the previous case of a thermal cloud, the BEC cannot be held for more than 150 ms in the compressed magnetic trap because of a relatively high heating rate. Thus, we cannot compare our scheme to the adiabatic limit corresponding to a slow linear decompression in this case.

Figure 3.12 shows the temporal behaviour of the cloud following the linear and shortcut decompressions. These absorption images are taken in the (y, z)

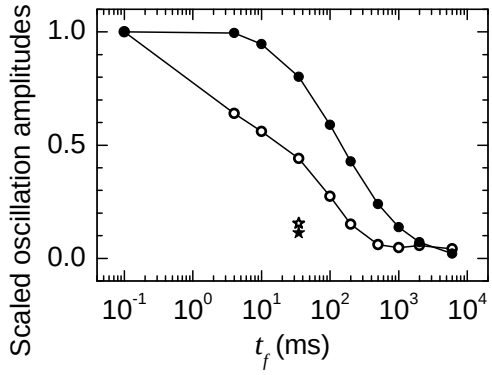

Figure 3.11: Comparison between linear and shortcut decompression schemes. We plot the scaled oscillation amplitudes of the breathing (cloud size, open symbols) and dipole (center-of-mass position) modes versus the decompression time t_f. The circles and stars correspond to linear and shortcut decompressions, respectively.

plane, after a certain holding time in the decompressed trap (indicated in the figure) plus a 28-ms-long time of flight. The field of view is $545\,\mu\text{m} \times 545\,\mu\text{m}$. The center-of-mass motion has been subtracted from these data for better clarity. In the linear case the BEC (yellow central part) undergoes large deformations and oscillations of its aspect ratio, whereas in the shortcut case it remains nearly perfectly stationary. Surprisingly, in the case of the linear decompression the BEC also oscillates *angularly*. We attribute this to an uncontrolled tilt of the trap axes during the decompression. This will be discussed in more details later. The nearly isotropic aspect of the BEC after the shortcut decompression is due to the value of the time of flight, which is close to the critical time of inversion of the aspect ratio. The thermal component surrounding the BEC (red halo) is also visible. Its temporal evolution is discussed at the end of the section.

Analysis of the absorption images

To provide a more quantitative analysis, the column densities obtained from the absorption images were fitted with a 2D bimodal distribution of the form

$$\tilde{n}(y,z) = \tilde{n}_{\text{th}}(Y_1, Z_1) + \tilde{n}_{\text{bec}}(Y_2, Z_2), \tag{3.72}$$

where the first term accounts for the thermal fraction and is assumed Gaussian

$$\tilde{n}_{\text{th}}(Y_1, Z_1) = \tilde{n}_{\text{th}}(0,0) \exp\left[-\frac{Y_1^2}{2\sigma_Y^2} - \frac{Z_1^2}{2\sigma_Z^2}\right], \tag{3.73}$$

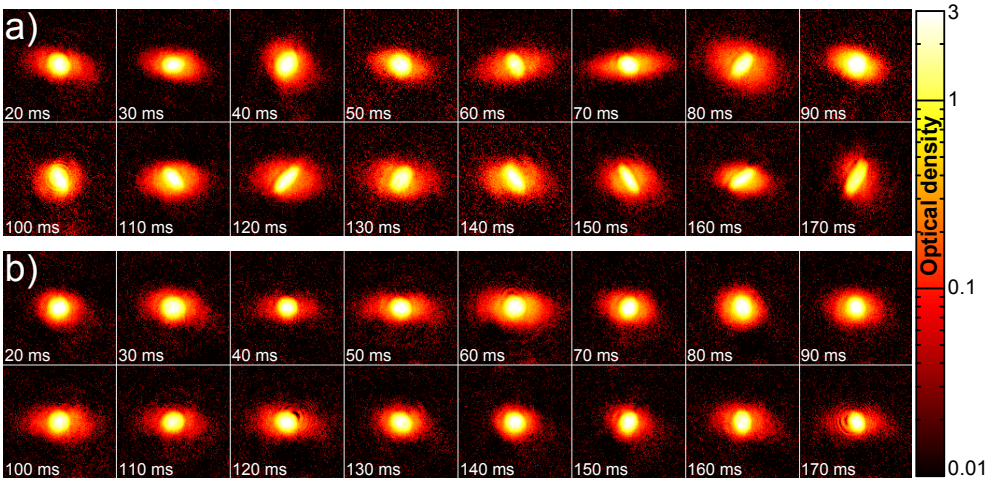

Figure 3.12: Comparison of linear and shortcut BEC decompressions. We compare the time evolution of the BEC after two different decompression schemes: (a) a 30-ms-long linear ramp and (b) the shortcut trajectory (see text). The center-of-mass motion has been subtracted from these time-of-flight images for clarity. On each image, the region where the optical density is highest (yellow and white) correspond to the condensate, while the red halo is the thermal component.

and the second term is the 2D TF profile given by Eq. (1.67). The y and z axes have been rotated differently for the two components by the angles α_1 and α_2 to account for a rotation of the clouds: for $i \in \{1, 2\}$

$$\begin{bmatrix} Y_i \\ Z_i \end{bmatrix} = \begin{pmatrix} \cos\alpha_i & \sin\alpha_i \\ -\sin\alpha_i & \cos\alpha_i \end{pmatrix} \begin{bmatrix} y - y_c \\ z - z_c \end{bmatrix}. \tag{3.74}$$

The fitting parameters are the cloud center (y_c, z_c), the two angles α_1, α_2, the rms widths of the thermal component σ_Y, σ_Z, the two TF radii of the BEC R_Y, R_Z, and the amplitudes of the two components (number of atoms in each).

Because of the large number of fitting parameters the fit is performed in four steps: first the whole image is fitted with a Gaussian to find a guess of the center, then the central region is excluded and the cloud is fitted with a Gaussian, then this result is subtracted from the data and the remaining peak is fitted with a pure TF profile. Finally the full absorption image is fitted with the bimodal distribution discussed above, using the results of the previous fits as guesses to start the optimization routine.

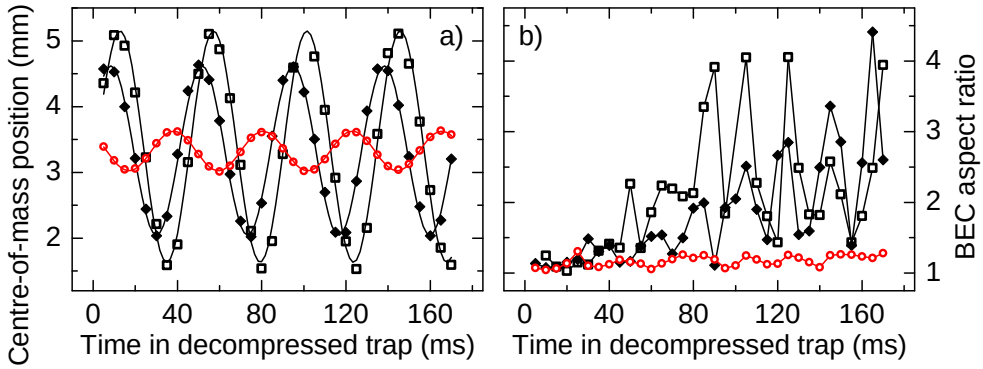

Figure 3.13: Decompression-induced excitations of the BEC. We report the temporal evolution of (a) the center-of-mass position and (b) the aspect ratio of the BEC after three different decompression schemes: an abrupt decompression (black squares); a 30 ms linear ramp (black diamonds); the 30 ms shortcut trajectory (red circles). All measurement are performed after 28 ms of time of flight.

Results

Figure 3.13a shows the center-of-mass oscillations (dipole mode) for the abrupt (squares), linear (diamonds) and shortcut (circles). Figure 3.13b shows the oscillations of the BEC's aspect ratio (breathing mode). All measurements are performed after a 28 ms time of flight. As in the case of the non-interacting cloud, the shortcut scheme reduces the amplitude of the dipole mode compared to a standard linear decompression, here by a factor of 4.3. For our relatively long time of flight, the measured positions reflect the atomic velocities. Thus, using the shortcut scheme reduces the kinetic energy associated with the dipole mode by a factor of 18.5 compared to the linear one (and 36 compared to the abrupt decompression). The residual energy after the shortcut decompression is 580 nK. As can be seen in Fig. 3.13b, both non-optimal schemes induce very large oscillations of the BEC's aspect ratio, with a rather complicated dynamics. A Fourier analysis reveals a main oscillation frequency of 47 Hz, consistent with a radial breathing mode at $2\omega_\perp$ (cf. Sec. 1.2.3). A smaller contribution at 12.5 Hz corresponds to the axial breathing mode at $\sqrt{5/2}\omega_\parallel$ (cf. Sec. 1.2.3). The shortcut scheme suppresses strikingly these breathing oscillations, yielding a BEC close to the targeted equilibrium state.

Behavior of the thermal component

As emphasized in Sec. 3.3.2, the shortcut trajectory employed in this experiment is also valid for the thermal fraction, in the radial dimensions only.

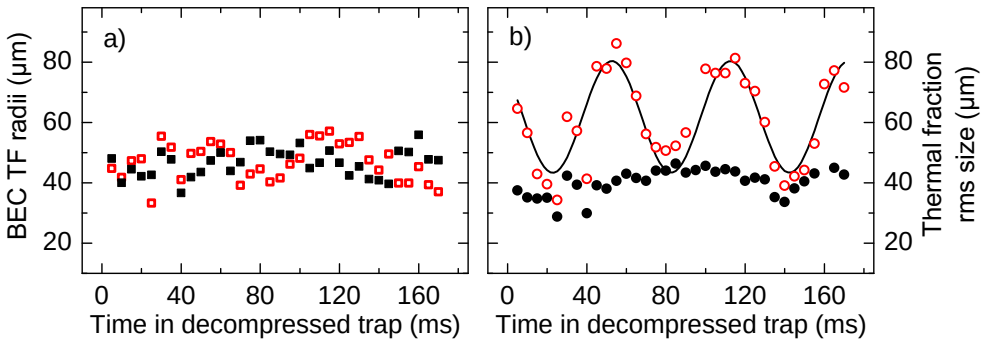

Figure 3.14: BEC versus thermal cloud decompression. We plot the sizes of (a) the BEC and (b) thermal component versus the time spend in the decompressed trap for the shortcut trajectory. The filled and empty symbols correspond to the radial (vertical) and axial directions respectively. The line is a sine fit to the axial size of the thermal fraction.

This is demonstrated in Fig. 3.14, where we compare the oscillations of the radial (open symbols) and axial (filled symbols) sizes of (a) the BEC, and (b) the thermal fraction, after the shortcut decompression. The BEC's TF radius is stationary with an average value of 46.8 μm close to the theoretical value (43μm). As can be observed in Fig. 3.14b, the radial size of the thermal fraction is also quite stationary as expected from a shortcut trajectory. Thus, this experiment demonstrates that both a non-interacting thermal gas and an interacting BEC can be decompressed simultaneously using an appropriate shortcut trajectory. The observed behavior is also qualitatively consistent with our initial assumption that the BEC and thermal fraction are independent. However, we expect that ultimately the validity of this approach will be limited by the interaction between the condensed and non-condensed fractions. The temperature inferred from the radial size of the thermal component is 22 nK, a factor of 6 below the initial one. This factor is smaller than the expected one $[\omega_\perp(0)/\omega_\perp(t_f) = 9]$, and even if we had improved the experimental setup to realize the ideal frequency trajectory we would probably be limited by the transfer of energy from the axial breathing mode via the interaction with the condensate. Indeed, the axial size of the thermal fraction presents clear breathing oscillations, reflecting the fact that the shortcut trajectory $\omega_\parallel(t)$ is not valid in this case, as expected.

Scissors mode

A striking feature in Fig. 3.12a is the large angular oscillation of the BEC after the linear decompression. This unexpected effect is due to a slight tilt of the

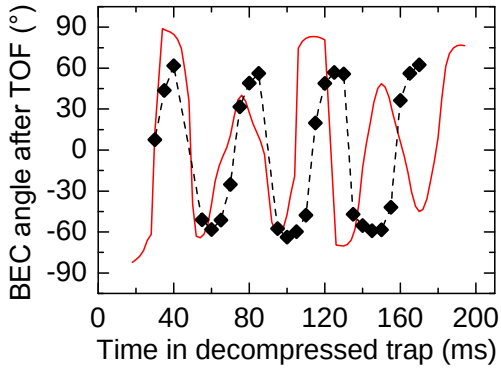

Figure 3.15: Experimental observation of a scissors mode excitation following the linear decompression (diamonds). The red line is a GPE simulation. The oscillation is not quantitatively reproduced because it depends on the precise way the trap is rotated during decompression, which is not known for the whole trajectory. Only the final tilt of 3° was measured. For the GPE simulation, the trap angle was assumed to be proportional to the trap bottom displacement from its original position.

QUIC trap eigenaxes (3°) in the (y, z) plane as the trap center moves downwards due to gravity. Because of this, an angular momentum is imparted to the atoms during the decompression, exciting a scissors mode (see Sec. 1.2.3). Our nearly critical time of flight then results in a magnification and a deformation of the scissors oscillations [210, 211]. Figure 3.15 shows an example of these oscillations, together with a GPE simulation (red line).

3.5 Other possible applications

In this section, we attempt to generalize the shortcut decompression of Bose-Einstein condensates to other situations which may find applications in experiments where a fast and large modification of the width of the velocity distribution or of the chemical potential is required.

3.5.1 Arbitrary variation of a harmonic potential

Let us consider the time evolution of a condensate in the time-dependent harmonic potential of the form

$$U(\mathbf{r}, t) = \frac{1}{2} m\, \mathbf{r}^t W(t) \mathbf{r} + \mathbf{r}^t \boldsymbol{u}(t) \tag{3.75}$$

where the symmetric matrix $W(t) = R^{-1}(t)\tilde{W}(t)R(t)$ represents the harmonic potential of stiffness

$$\tilde{W} = \begin{pmatrix} \omega_x^2(t) & 0 & 0 \\ 0 & \omega_y^2(t) & 0 \\ 0 & 0 & \omega_z^2(t) \end{pmatrix}, \tag{3.76}$$

rotated by a rotation matrix $R(t)$. The column vectors $\mathbf{r}$ and $\boldsymbol{u}$ respectively represent the position and a spatially homogeneous force which may depend on time. The superscript ^{t} indicates the transpose of vectors or matrices.

To solve Eq. (3.43) we look for a linear change of variables $\boldsymbol{\rho}(\mathbf{r}, \{b_{ij}(t)\}, \{r_i^{\rm cm}(t)\})$ where the b_{ij}'s are scaling and rotation functions for the r_i's. Let B be a 3×3 matrix whose elements are the functions b_{ij}. The transformation is

$$\boldsymbol{\rho} = B^{-1}(t)\left(\mathbf{r} - \mathbf{r}^{\rm cm}(t)\right) = B^{-1}(t)\mathbf{r} + \boldsymbol{a}(t). \tag{3.77}$$

In the TF limit, and if the matrix $\dot{B}B^{-1}$ is symmetric, Eq. (3.43) is invariant under this transformation. The full derivation is given in C.1, but we give here the key elements.

The TF approximation consists in neglecting the kinetic-energy-like term

$$\sum_{i,j,k} [B^{-1}]_{ij}[B^{-1}]_{kj}\frac{\partial^2\chi}{\partial\rho_i\partial\rho_k}, \tag{3.78}$$

with $\chi(\boldsymbol{\rho}, \tau)$ being defined as in Eq. (3.44). In this regime, the condensate wave function $\chi(\boldsymbol{\rho}, \tau)$ satisfies the equation of motion Eq. (3.50), under the action of the time-independent potential

$$U(\boldsymbol{\rho}, 0) = \frac{1}{2}m\boldsymbol{\rho}^t W(0)\boldsymbol{\rho}, \tag{3.79}$$

if the generic scaling functions satisfy

$$\ddot{B}^t B + B^t W B = \frac{W(0)}{\det B}, \tag{3.80}$$

$$\ddot{\mathbf{r}}^{\rm cm} + W(t)\boldsymbol{r}^{\rm cm} - \frac{1}{m}\boldsymbol{u} = \mathbf{0}. \tag{3.81}$$

It is worthwhile recalling that, as shown by the above equations, the evolution of B is decoupled from the center-of-mass motion which evolves with the net external force. The phase of the wave function is chosen as

$$\phi(\mathbf{r}, t) = \frac{m}{\hbar}\left\{\frac{1}{2}\mathbf{r}^t\dot{B}B^{-1}\mathbf{r} - \mathbf{r}^t B\dot{\boldsymbol{a}}\right\} + \phi_0(t), \tag{3.82}$$

with

$$\phi_0 = -\frac{m}{2\hbar}\int_0^t \mathrm{d}t' \left(\dot{\boldsymbol{a}}^t B^t B \dot{\boldsymbol{a}} - \boldsymbol{a}^t \frac{W^0}{\det B} \boldsymbol{a} \right). \tag{3.83}$$

The wave function normalization is

$$\mathcal{A} = (\det B)^{-1/2}, \tag{3.84}$$

and the time τ is defined by

$$\frac{\mathrm{d}\tau}{\mathrm{d}t} = \frac{1}{\det B}. \tag{3.85}$$

The derivation of the scaling equations (C.1) relies on the particular choice of the above phase ϕ which verifies

$$\boldsymbol{\nabla}_r \phi = -\frac{m}{\hbar} B \frac{\partial \boldsymbol{\rho}}{\partial t} \quad \text{or} \quad \boldsymbol{v}(\mathbf{r}) = \dot{B}B^{-1}\,\mathbf{r} - \dot{B}B^{-1}\,\mathbf{r}^{\mathrm{cm}} + B^{-1}\dot{\mathbf{r}}^{\mathrm{cm}}, \tag{3.86}$$

$\boldsymbol{v}(\mathbf{r})$ being the velocity field of the condensate, and on the assumption that the matrix $\dot{B}B^{-1}$ is symmetric. The first condition imposes that there are no terms linear in momentum in the GPE in the $\boldsymbol{\rho}$-coordinate frame; once the first condition is fulfilled the second imposes that the velocity field is irrotational, namely, the condensate is a superfluid everywhere. This implies that our scaling ansatz does not take into account the presence of quantized vortices and thus can describe the dynamics of a rotated condensate only below the critical angular velocity $\dot{\alpha}_c \simeq 0.7\omega_x$ for a slightly anisotropic confinement [212], or in general, for a metastable configuration [213]. It is possible to relax the first condition and allow for terms in the GPE that contain for instance the angular momentum components. These extensions are deferred for future studies.

Equations (3.80) and (3.81) can be used to determine the dipolar, compressional and scissors modes for a harmonically-trapped superfluid condensate (see C.2). Replacing $\det B$ with $(\det B)^\beta$ in Eq. (3.80), the same equation describes the compression and the scissors dynamics of a superfluid characterized by an equation of state $\mu(n) \propto n^\beta$, as it has been already shown for the quadrupolar modes [214], and as it can be easily deduced from Eq. (C.8) of App. C. In the following, we present three possible shortcut trajectories based on these scaling equations and adapted to compress or decompress and rotate a BEC in the absence and in the presence of gravity.

3.5.2 Uniform decompression or compression of a condensate

We now consider the particular case of $\boldsymbol{u} = \mathbf{0}$ and W diagonal. If one wants to compress or decompress the condensate without modifying the condensate

aspect ratio, the condition $\omega_i(t_f) = \omega_i(0)/\gamma^2$ must hold for any i. The boundary conditions for the shortcut solution are: $\dot{b}_{ii}(0) = \dot{b}_{ii}(t_f) = 0$, $b_{ii}(0) = 1$, $b_{ii}(t_f) = \gamma^{4/5}$ and $\ddot{b}_{ii}(0) = \ddot{b}_{ii}(t_f) = 0$. One possible solution is to set all $b_{ii}(t)$'s equal to a unique function

$$b(t) = \sum_{k=0}^{5} c_k \left(\frac{t}{t_f}\right)^k, \tag{3.87}$$

with $c_0 = 1$, $c_1 = c_2 = 0$, $c_3 = 10(\gamma^{4/5}-1)$, $c_4 = -15(\gamma^{4/5}-1)$, $c_5 = 6(\gamma^{4/5}-1)$. The time evolution of the trap frequencies $\omega_i(t)$ will be given by the equation

$$\omega_i^2(t) = \frac{\omega_i^2(0)}{b^5} - \frac{\ddot{b}}{b}. \tag{3.88}$$

If the kinetic energy is negligible during the whole decompression, the final state is a BEC at equilibrium with a chemical potential that has been divided by a factor of $\gamma^{16/5}$ [because $\mu \propto (\Pi_i \omega_i)^{2/5}$].

3.5.3 General compression or decompression in the presence of gravity

We now consider the case where $W(t)$ is diagonal with $\omega_x(t) = \omega_z(t) = \omega_\perp(t)$, $\omega_y(t) = \omega_\parallel(t)$, and $u_z = mg$. A general compression or decompression of a condensate confined in this axially-symmetric trap (3.62) can be realized in two steps: (i) in the first step ($t \in [0, \bar{t}\,]$), $b_\parallel$ is kept fixed as outlined in Sec. 3.3.2, while the desired final value of $b_\perp = b_\perp(t_f)$ is reached; (ii) then ($t \in [\bar{t}, t_f]$) $b_\perp$ is fixed and $b_\parallel$ evolves according to the set of equations:

$$\omega_\perp^2(t) = \frac{\omega_\perp^2(\bar{t})}{b_\parallel(t)}, \tag{3.89}$$

$$\ddot{b}_\parallel(t) + b_\parallel(t)\omega_\parallel^2(t) = \frac{\omega_\parallel^2(\bar{t})}{b_\parallel^2(t)}, \tag{3.90}$$

$$b_\parallel(t)\ddot{c}(t) = \omega_\perp^2(\bar{t})\left[c(t) - b_\parallel(t)\right], \tag{3.91}$$

where $c(t) = -\omega_\perp^2(\bar{t}) r_z^{\rm cm}(t)/[g b_\perp(t)]$ as in Eq. (3.63). Also in this case, one can write the function $c(t)$ as a polynomial of order ≥ 9 [see Eq. (3.61)] with the first coefficient fixed to one and the following four coefficients fixed to zero. The other coefficients are fixed by the boundary conditions at the time t_f of the function $c(t)$ and of the function $b_\parallel(t)$, that from Eq. (3.91) can be written as

$$b_\parallel(t) = -\frac{\omega_\perp^2(\bar{t})c(t)}{\ddot{c}(t) - \omega_\perp^2(\bar{t})}, \tag{3.92}$$

and by the boundary conditions of their derivatives at the same time t_f.

3.5.4 Rotation of the BEC in the presence of gravity

Now we propose a shortcut trajectory to rotate an axially-symmetric BEC of an angle $\bar{\alpha}$, in the presence of the gravity. In this case

$$W(0) = \begin{pmatrix} \omega_\perp^2(0) & 0 & 0 \\ 0 & \omega_\parallel^2(0) & 0 \\ 0 & 0 & \omega_\perp^2(0) \end{pmatrix}, \tag{3.93}$$

and $W(t_f) = R_{\bar{\alpha}}^{-1} W(0) R_{\bar{\alpha}}$, with

$$R_{\bar{\alpha}} = \begin{pmatrix} 1 & 0 & 0 \\ 0 & \cos\bar{\alpha} & \sin\bar{\alpha} \\ 0 & -\sin\bar{\alpha} & \cos\bar{\alpha} \end{pmatrix}. \tag{3.94}$$

Let us suppose, for instance, $\omega_\perp(0) < \omega_\parallel(0)$, with $\omega_\parallel(0) = \lambda\omega_\perp(0)$. The tilted ground-state for the potential $W(t_f)$ can be obtained in two steps: (i) during a time $\bar{t}$, fixing $b_\parallel$, decompressing the BEC in the radial direction up to the value $b_\perp(\bar{t}) = \lambda^{-1}$. At $t = \bar{t}$ the trap is spherical with frequency $\tilde{\omega} = \lambda\omega_\parallel(0)$ and the BEC is spherical with a TF radius equals to $R_\parallel(0)$. (ii) Fixing $b_\parallel$ along the direction y', compressing in the direction x' and z', where the axis $\mathbf{r}'$ are defined by $\mathbf{r}' = R_{\bar{\alpha}}\mathbf{r}$. Using the new coordinate reference frame, and setting $c_z(t) = -\tilde{\omega}^2 r_z^{\rm cm}(t)/[g b_\perp(t)\cos\bar{\alpha}]$, and $c_y(t) = -\tilde{\omega}^2 r_y^{\rm cm}(t)/[g\sin\bar{\alpha}]$, we obtain the set of equations

$$\ddot{b}_\perp(t) + b_\perp(t)\omega_\perp^2(t) = \tilde{\omega}^2/b_\perp^3(t), \tag{3.95}$$

$$\omega_\parallel(t) = \tilde{\omega}/b_\perp(t), \tag{3.96}$$

$$b_\perp^4(t)\ddot{c}_z(t) + 2b_\perp^3(t)\dot{b}_\perp(t)\dot{c}_z(t) + \tilde{\omega}^2\left[c_z(t) - b_\perp^3(t)\right] = 0, \tag{3.97}$$

$$b_\perp^2(t)\ddot{c}_y(t) + \tilde{\omega}^2\left[c_y(t) - b_\perp^2(t)\right] = 0, \tag{3.98}$$

the latter describing the center-of-mass motion in the y' direction. The boundary conditions for such a problem are: $b_\perp(\bar{t}) = c_z(\bar{t}) = c_y(\bar{t}) = 1$, $b_\perp(t_f) = \lambda$, $c_z(t_f) = \lambda^3$, $c_y(t_f) = \lambda^2$, and all the first and second derivatives with respect to time are null at $t = \bar{t}$ and t_f. In this case a finite-order polynomial ansatz in τ for c_i was found to be inadequate as a solution of the scaling equations due to the coupling of c_y and c_z. A full numerical solution of the dynamical equation using, e.g., a shooting method [215] may be needed to find a shortcut trajectory.

3.6 Conclusion

We have experimentally demonstrated the controlled transfer of trapped ultracold atoms between two stationary states using processes which strongly

violate the criteria for adiabaticity. This has enabled us to greatly reduce the transfer time compared to more commonly used adiabatic methods. The transfer is achieved by engineering specific trajectories of the external trapping frequencies that take explicitly into account the spatial shift introduced by gravity. This scheme was successfully applied to both a thermal gas with negligible interactions and an interacting Bose-Einstein condensate. The scheme used is flexible enough to be adapted to both situations even though, in the thermal gas, interactions do not play a significant role while the Bose-Einstein condensate is strongly affected by the s-wave repulsion between atoms. The residual excitations observed after the shortcut decompressions in the present demonstration experiments are due to our imperfect control over the time-varying magnetic trapping potential, and could be substantially reduced in future realizations.

Theoretically, the design of the transfer process was based on the invariant of motion and scaling equations techniques which turned out to be possible thanks to the harmonic shape of the external potential. In our scheme, the invariant of motion technique (for non-interacting particles) and the scaling equations technique (valid for both the non-interacting and the interacting gas) are tightly connected. The invariant of motion we used is a time-independent HO Hamiltonian that can be obtained by a time-dependent canonical transformation of the initial Hamiltonian. In the scaling equations technique, we looked for a transformation involving both a scaling and a displacement of the coordinates that allowed the equations of motion of the system to be time-independent. In both cases the whole dynamics is included in the new set of coordinates, that depend on the trap frequencies. We also showed that these techniques can be generalized to include the rotation of the eigenaxes.

In experiments with ultracold gases, samples are often prepared by transferring atoms from some confinement to another, e.g., from a magneto-optical trap to a magnetic quadrupole, from a quadrupole trap to a Ioffe-Pritchard trap, from a harmonic confinement to an optical lattice, etc. the major limitation being that, for short transfer times, parasitic excitations may show up. The main application of our scheme is thus to guide this transfer in order to prepare a very cold sample in a very short time with the desired geometry and without undesired excitations. The shortcut-to-adiabaticity scheme proposed here could be applied to non-interacting particles such as cold gases or ultracold spin-polarized fermions, to normal or superfluid (bosonic or fermionic as well) gases in the hydrodynamic regimes, and to strongly correlated systems such as the Tonks gas. In this chapter we focused on explicit solutions to transfer atoms between two stable states, but the same strategy could be applied to control the generation of metastable states, vortex states, or some exotic out-of-equilibrium states. We plan to explore these possibilities in future studies.

Finally, we believe that such methods are not restricted to this field and could find applications in many different physical systems. For instance, the exact same method — demonstrated here on the thermal gas — was proposed for the fast cooling of a mechanical resonator to its ground state [216]. Recently, similar methods have been proposed for atoms interacting with electromagnetic fields [217] and for non-hermitian Hamiltonians [218]. The recent surge of interest in the field of quantum control and the development of optimization methods (see e.g. Refs. [198–201, 219–224]) which could be combined to such exact solutions suggest that these techniques will play a central role in the future.

Chapter 4

Towards matter waves transport experiments

The INLN BEC experiment was initially constructed to study matter wave transport in disordered potentials. This was a natural evolution for the group which had studied the propagation and weak localization of light in disordered atomic media, namely in laser cooled clouds of Rubidium and Strontium atoms (cf. e.g. Refs. [170, 225]). These studies led to the first observations of coherent backscattering in such media [163, 225].

In this chapter, we present a theoretical work related to these topics, more precisely, to Anderson localization (AL) in one-dimensional (1D) systems. We have studied a particular model of correlations leading to the partial delocalization of some eigenstates, which is not expected in standard disordered 1D systems. We show that ultracold mixtures are particularly relevant to study such effects by evaluating the transport properties in a realistic experimental scenario.

4.1 Weak and strong localization of waves

The propagation of waves in complex random media is often well described by diffusion, that is, the particles constituting these waves (photons for light, phonons for sound, etc.) can be seen as performing a random walk in the medium. In such a description, assuming an initially localized ensemble of particles, and for sufficiently long times, the distribution becomes Gaussian with a mean square position increasing as

$$\langle \mathbf{r}^2 \rangle \sim Dt, \tag{4.1}$$

where D is called the *diffusion coefficient* or *diffusion constant*. This is true when the probability law of the lengths X of the steps of the random walk

has a finite variance. When this is not the case, diffusion is modified. For instance, the broad class of Lévy flights [226, 227] is characterized by X having a law $p_X(x)$ decreasing as $1/x^\alpha$, with $\alpha < 3$ for $x \to \infty$. This leads to a so called *superdiffusive transport* characterized by $\langle \mathbf{r}^2 \rangle \sim D' t^\beta$, with $\beta > 1$. Such models [226–231] were shown to accurately reproduce experimental observations in various situations [226, 232–234].

Since the energy of the wave is proportional to the density of particles, the transport of energy is diffusive or superdiffusive. In the context of electronic transport, a consequence is that the medium is conducting because the current carriers can move from one side of the medium to the other. Another important consequence of the diffusive behavior of electrons in solids is the electrical resistance of conductors given by Ohm's law.

What about interferences?

Surprisingly the underlying wave nature is often not visible in such processes and the particle picture is sufficient to account for the observations. There can be many causes [235]: coherent effects are often averaged to zero by the disorder, decoherence can be present in the medium, and the waves cannot interfere anymore after a few scattering events. This is for instance the case if the scattering is inelastic and leads to frequency redistribution (e.g. the Doppler effect in a hot gas; for electrons, decoherence is induced by the interaction with the underlying lattice which has a nonzero temperature).

Nevertheless the wave nature can sometimes dramatically modify the transport properties. In the following, we introduce two such effects, in which disorder and phase coherence either slow down or completely inhibit the transport.

4.1.1 Coherent backscattering and weak localization

Coherent backscattering (CBS) is the first, and probably the most robust effect arising from coherence (cf. Ref. [236] and references therein). When a wave is sent onto a disordered medium, it is scattered in all directions. If the scattering is sufficiently isotropic, or if a sufficient number of scattering events occur, the direction of propagation is redistributed in 4π steradians. The interference of the scattered waves, which is expected to look like a speckle, gives the same value $\langle I \rangle$ in all the directions after the configuration average. Nevertheless, in the backward direction, the interference between the outgoing scattered waves is always constructive and the result is an angular *cone* of "backscattered" light having a peak intensity $2\langle I \rangle$. The medium can be seen as an interferometer which is automatically aligned in the backward direction. The factor of 2 is the ratio between the peak intensity $2\langle I \rangle$ of a two-wave interference pattern to the spatial average of the fringes intensity $\langle I \rangle$ (see Fig. 4.1).

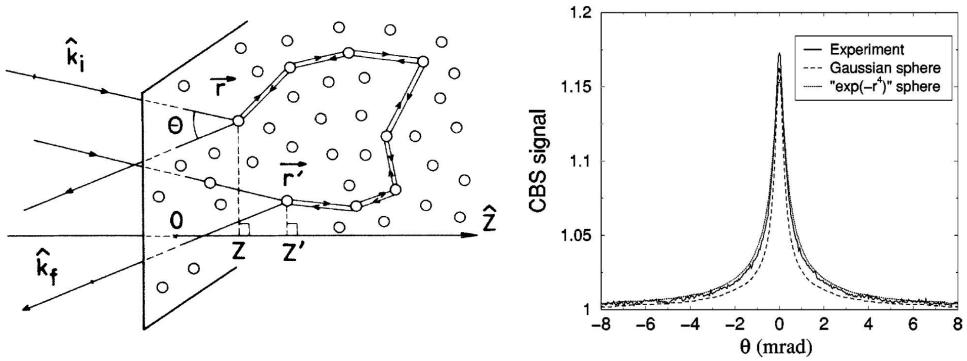

Figure 4.1: (Left) In the backward direction (i.e. when $\hat{\mathbf{k}}_\mathbf{f} = -\hat{\mathbf{k}}_\mathbf{i}$) two scattering paths followed in opposite directions have exactly the same length, leading to a constructive interference. On the contrary in other directions, interferences can either be constructive or destructive, which results in no enhancement after configuration averaging over the disorder. (Right) Coherent backscattering cone on a cold cloud of ^{85}Rb atoms. The enhancement factor is not 2 because of a breakdown of time-reversal symmetry induced by the multi-level structure of the atoms. Figures from Akkermans et al. [236] (left) and Labeyrie et al. [168] (right).

Similar interference effects can slow down the propagation of waves and e.g. lead to a reduction of the diffusion constant D. Indeed, from the CBS effect, one can see that interferences tend to increase the return probability compared to the diffusive case.

4.1.2 Anderson localization

It was first realized by Anderson [237] in the context of electronic transport that disorder could actually completely inhibit transport. With a simple model, he showed that even a small amount of disorder could turn a conductor into an insulator. This phenomenon is called *strong localization* or *Anderson localization*, from the name of its discoverer. It took some time for physicists to realize that the only ingredients needed for AL were waves and disorder, and that AL could actually occur with any wave, be it quantum or classical [238].

Localization is often studied in two distinct regimes: the *tight-binding (TB) regime* which is most suited to describe the propagation of electrons in crystals and can be reduced to a discretized Schrödinger equation (that is the Anderson model used in the following sections), and continuous models in a regime of weak disorder, described by a standard Schrödinger equation.

In the TB regime, the ordered system is a periodic potential in which the

particles can travel thanks to quantum tunneling. Anderson localization was first introduced with this description [237]. It is well known from condensed matter physics that the eigenstates of such a problem are Bloch waves, which are delocalized on the whole system. Disorder is induced by imperfections of the crystal which shift the energies of the sites and/or the hopping probabilities.

In the continuous description and in the absence of disorder, the particles are propagating in free space (no potential energy term) and the eigenstates are plane waves. Disorder is induced by adding a random potential $U(\mathbf{r})$. The counter intuitive result of AL is that, even if the typical amplitude[1] of $U(\mathbf{r})$ is negligible compared to the kinetic energy of the particle, disorder and interferences can lead to the spatial localization of the wave. This is in complete opposition with the result of classical mechanics, in which the velocity of the particle would only fluctuate with time about its mean value and the particle would propagate. This happens because, with waves, even a small modification of the potential results in a partial reflection (counterpart of tunneling). As we will see, AL is generally characterized by an exponential decay of the envelopes of the eigenstates.

4.1.3 Correlations

The meaning of "random" needs to be clarified. Indeed a rigorous way to define a random medium[2] is to say that the potential $U(\mathbf{r})$ is a *stochastic process* of the space variable $\mathbf{r}$.

Consequently the system under study is not just a single realization of $U(\mathbf{r})$ (each realization would indeed give different physical results), but many realizations of $U(\mathbf{r})$ characterized by a unique probability law. The typical properties of such a system are thus obtained by performing configuration averages over many realizations obtained from the same probability law.

To that respect, a simple example of an acceptable stochastic process is

$$U(\mathbf{r}) = U_0, \tag{4.2}$$

where U_0 is a random variable described by a given law. This is indeed random, but not "disordered", and of course, such a potential does not induce localization.

This underlines the importance of *correlations* in the random potential, i.e. conditional probabilities between different points. The system is disordered if the conditional probabilities of the potential at two different positions $\mathbf{r}_1 \neq \mathbf{r}_2$

[1] The typical amplitude of $U(\mathbf{r})$ is, e.g. the rms value $\sqrt{\langle U^2(\mathbf{r})\rangle - \langle U(\mathbf{r})\rangle^2}$, assumed to be independent of the position $\mathbf{r}$, where the brackets $\langle\cdot\rangle$ denote the ensemble average.

[2] We will only consider static (i.e. time-independent) media, sometimes called "quenched" media [230].

are not trivial, unlike that in the example above. In principle, higher order correlations (involving more points) can also play a role.

In standard localization problems [237], the disorder is assumed to be delta-correlated, i.e. the two-point correlation function satisfies

$$\langle U(\mathbf{r}_1)U(\mathbf{r}_2)\rangle = C + A\delta(\mathbf{r}_2 - \mathbf{r}_1), \tag{4.3}$$

where C and A are constants and $\langle\cdot\rangle$ is the ensemble average [i.e. average over the joint probability law of the stochastic processes $U(\mathbf{r}_1)$ and $U(\mathbf{r}_2)$]. For instance, this is the case if the two random variables $U(\mathbf{r}_1)$ and $U(\mathbf{r}_2)$ are independent as soon as $\mathbf{r}_1 \neq \mathbf{r}_2$.

Since the delta-correlated case (4.3) does not seem very physical, at least when the system is continuous ($\mathbf{r} \in \mathbb{R}^3$), and because a lot of natural systems exhibit strong correlations, a sensible question is: "Can AL survive the presence of correlations?". This is the subject of Secs. 4.3 and 4.4 of this chapter.

4.1.4 One-dimensional Anderson localization

The physics of wave transport and AL has been studied extensively during the past 60 years. The book of Akkermans and Montambaux [235] is a reference in this domain. The recent lectures of Müller and Delande [239] give a good introduction to this subject. The theoretical theses of Lemarié [240] and Lugan [241] also contain a lot of references and give an overview of the current developments of this field. In this section, we just recall the basic elements needed for 1D AL.

The length scales involved in the transport are represented below (inspired by Ref. [239]).

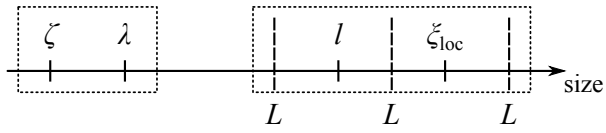

At short distances, there is the wavelength λ and the *correlation length* of the disorder ζ. The latter is the typical width of the correlation function (4.3), which may not be a delta function (in which case $\zeta = 0$) and which is assumed to have a finite support for simplicity[3]. The potential is well approximated by a delta-correlated one when $\zeta \ll \lambda$. At larger scales there is the *transport mean free path* l, the localization length ξ_{loc} and the size of the system L.

The transport mean free path l is the average length traveled by a particle before one scattering event occurs. For a given disorder it is generally energy

[3]Long-range correlated disorders have also been studied but are not discussed for the moment (see e.g. Ref. [242]).

dependent. In the 1D diffusive regime, it is related to the diffusion constant by $D = vl$, with v being the velocity of the particle. A simple model of randomly positioned identical point scatterers (see e.g. Ref. [239]) can be used to show that, in 1D, the density of particles $n_{1D}(z)$ (for light that would be the transmission coefficient T of the energy) decreases exponentially at large distances as

$$\exp\langle \ln [n_{1D}(z)] \rangle \sim_{|z|\to\infty} e^{-2\gamma|z|}. \tag{4.4}$$

Since the density is the modulus square of the wave function $n_{1D}(z) = |\varphi(z)|^2$, the latter decreases on a typical length $\xi_{loc} = 1/\gamma$, called the *localization length*. Its inverse γ is called the *Lyapunov exponent*.

A remarkable feature of 1D AL is that the localization length is essentially the transport mean free path:

$$\xi_{loc} = 4l. \tag{4.5}$$

One can show that with delta-correlated disorders, all the eigenstates are localized, independently of their energy. In the following sections we will see that correlations can modify this behavior.

4.1.5 Why matter waves?

Coherent effects and AL in complex media have been studied with a variety of waves such as ultrasounds [243], microwaves [244, 245], infra-red or visible light in various media [246–255].

Most of these systems suffer from two main issues:

1. absorption is difficult to cancel, and results in exponential decays (Beer-Lambert law). Thus it has been difficult to differentiate the two effects and to obtain clear signatures of AL.

2. The propagation media are solid material which have to be engineered in order to contain a controlled amount of disorder. This can be difficult to realize in practice.

Recently, atomic matter waves coming from either Bose-Einstein condensates or magneto-optical traps have been used to demonstrate AL in 1D [142, 143] and 3D [145, 256–258]. Robert-de-Saint-Vincent et al. [259] are also approaching the 2D Anderson regime. As we have seen in Chap. 1, light can be used to produce potentials for cold atoms. Two interfering counter-propagating lasers produce a lattice in which atoms can tunnel, reproducing in an almost perfect fashion the periodic potential of a crystal. Random light distribution can easily be produced with laser speckle [260] or with spatial light modulators, enabling an almost total control of the statistics and correlations of the disorder, with the ultimate limit being diffraction. Feshbach

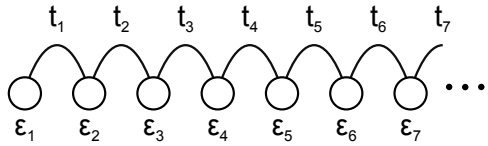

Figure 4.2: Schematic representation of the Hamiltonian (4.6).

resonances can be used to span a large range of interaction regimes, from the ideal gas to the strongly correlated regime. Finally, there is no absorption in such potentials. By controlling the spontaneous emission, or adding other perturbations (time-dependent potentials, breaking time-reversal symmetry, etc.) one could imagine to also tune the decoherence to study its effects on AL. Another advantage compared to other waves is the possibility to directly measure the density of particles, i.e. the modulus of the wave function. The phase may be accessible via interference with a reference wave. Moreover, correlations measurement can easily be performed. Finally, the time-dynamics is also accessible. For all these reasons, we believe that ultracold atoms are well adapted to the study of such effects.

4.2 One-dimensional Anderson localization in the tight-binding regime

4.2.1 A toy model for one-dimensional Anderson localization

Probably the most simple Hamiltonian describing a 1D system in which AL can occur is Anderson's TB Hamiltonian:

$$H = \sum_{n=1}^{N_s} \epsilon_n |n\rangle\langle n| + \sum_{n=1}^{N_s-1} t_n \left(|n\rangle\langle n+1| + |n+1\rangle\langle n| \right). \tag{4.6}$$

This Hamiltonian can be considered as describing a single particle traveling through a lattice, whose sites are indexed by n, and have energies ϵ_n. Moreover, the particle can only hop to nearest-neighbor sites. Each site has one orbital $|n\rangle$. In the basis of the lattice site's orbitals $\{|n\rangle,\ n \in [1, N_s]\}$, this Hamiltonian is tridiagonal. This kind of Hamiltonian can be represented in the way of Fig. 4.2.

4.2.2 The Green's function operator

There are various ways to analyze such a physical problem. For instance, in Anderson's original paper [237], he considered the time dynamics of a particle initially localized on one site, and showed that the particle could not propagate

to large distances, even in the limit $t \to \infty$. An alternative is to directly look at the spectral properties of the Hamiltonian, together with the average spatial properties of its eigenstates. We use this second strategy. For this purpose, we use the *Green's function operator* formalism, which is introduced below.

The Green's function operator, also called *resolvent*, associated with the Hamiltonian H is defined by

$$G(E) \equiv (E \cdot \mathbb{1} - H)^{-1}\,,\ E \in \mathbb{C}\,. \tag{4.7}$$

The symbol $\mathbb{1}$ is the identity operator of the Hilbert space $\mathcal{H}$. As we will see, the fact that the Hamiltonian is tridiagonal makes the use of the Green's function operator particularly relevant. Most of the properties describing the system have simple expressions involving only a few matrix elements of this operator.

Density of states

The *density of states* (DOS) of a system is the function $\mathcal{N}(E)$ such that for all energies $\epsilon_1 < \epsilon_2$, the quantity $\int_{\epsilon_1}^{\epsilon_2} \mathcal{N}(E)\mathrm{d}E$ is the number of eigenstates of energies $E \in [\epsilon_1, \epsilon_2]$. For instance, if $\{\epsilon_n, n \in \mathbb{N}\}$ is the spectrum of a Hamiltonian which is not degenerate, $\mathcal{N}(E) = \sum_n \delta(E - \epsilon_n)$.

The DOS is calculated as a function of the Green's function operator as

$$\mathcal{N}(E) = -\frac{1}{\pi} \lim_{\epsilon \to 0^+} \mathrm{Im}\left\{\mathrm{tr}\left[G\left(E + i\epsilon\right)\right]\right\}, \tag{4.8}$$

where E is now a real number. This can be shown by starting from Eq. (4.8) and writing the trace in a basis where H is diagonal. One gets $\mathcal{N}(E) = \sum_n \lim_{\epsilon\to 0^+} \frac{1}{\pi}\frac{\epsilon}{(E-\epsilon_n)^2+\epsilon^2}$. The limit then turns the Lorentzian functions into the delta functions $\delta(E-\epsilon_n)$. In the following, limits of the kind $\lim_{\epsilon\to 0^+} f(i\epsilon)$ will be written $f(i0^+)$.

Another expression of the DOS, valid for tridiagonal Hamiltonians with non-vanishing hoppings was given by Kirkman and Pendry [261]:

$$\mathcal{N}(E) = \frac{1}{\pi}\mathrm{Im}\left[\frac{\partial \ln G_{1,N_s}(E + i0^+)}{\partial E}\right] \tag{4.9}$$

where $G_{m,p}(E) \equiv \langle m|G(E)|p\rangle$.

Lyapunov exponent

The Lyapunov exponent of a 1D disordered system can be calculated, in the limit of an infinite system, as a function of two matrix elements of the Green's operator [262]:

$$\gamma(E) = \lim_{n\to+\infty} \frac{1}{n} \ln\left|\frac{G_{n,n}(E + i0^+)}{G_{1,n}(E + i0^+)}\right|. \tag{4.10}$$

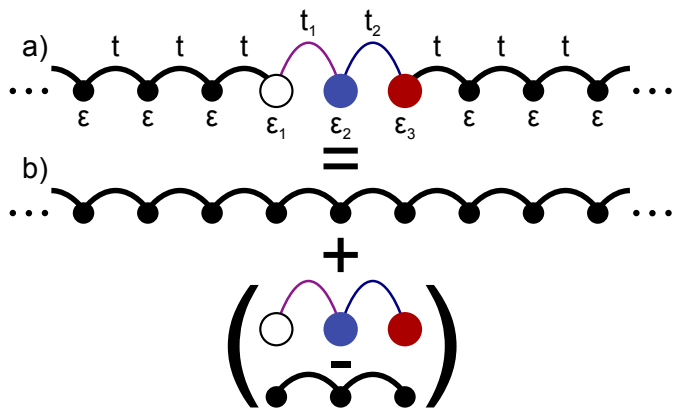

Figure 4.3: Computation of the transmission coefficient. (a) To compute the transmission coefficient, the system under study (here the three sites 1, 2, 3) is connected to two semi-infinite perfect lattices playing the role of electrodes. (b) This new system is formally decomposed into a perfect lattice + a perturbation responsible for scattering the incoming "plane waves" (Bloch waves).

Transmission coefficient

A natural quantity to address when discussing localization effects is to evaluate the conductance, or transmission coefficient of the sample. To measure this, an experimentalist dealing with electronic transport would have to connect the sample to electrodes and add an electrical potential. In optics, light would be sent on the sample, and the transmitted light would be measured. In this case, one has to take care of impedance mismatch problems on the interfaces, which tend to modify the measured transmitted signal.

We do exactly the same to calculate the transmission coefficient. A finite size system (say with N_s sites) is extended by connecting it to perfect lattices on both sides. They play the role of good conductors in electrical systems, or free space in optical systems. The Hamiltonian (4.6) is thus extended with identical sites (same on-site and hopping energies) of indices ranging from $-\infty$ to $+\infty$, as illustrated in Fig. 4.3a.

The Hamiltonian obtained is decomposed in the following manner

$$\underbrace{(\text{Sample} + \text{electrodes})}_{H} = \underbrace{(\text{Perfect lattice})}_{H^0} + \underbrace{(\text{Scatterers})}_{H^I} \tag{4.11}$$

as illustrated in Fig. 4.3b. For example, for the situation of Fig. 4.3

$$\begin{aligned} H^I = {} & (\epsilon_1 - \epsilon)|1\rangle\langle 1| + (\epsilon_2 - \epsilon)|2\rangle\langle 2| + (\epsilon_3 - \epsilon)|3\rangle\langle 3| \\ & + (t_1 - t)(|1\rangle\langle 2| + |2\rangle\langle 1|) + (t_2 - t)(|2\rangle\langle 3| + |3\rangle\langle 2|). \end{aligned} \tag{4.12}$$

The transmission or reflection coefficient are then given by standard scattering theory. If one considers an incoming plane wave $|k\rangle$ having a (dimensionless) wave vector k (i.e. an eigenstate of H^0) of the form

$$\forall n,\ \langle n|k\rangle = e^{ikn}, \tag{4.13}$$

the scattering of this state by the scatterer described by H^I yields the wave function

$$|\varphi\rangle = \left(\mathbb{1} + G^0 T\right)|k\rangle, \tag{4.14}$$

G^0 being the Green's function operator associated to H^0, and T the matrix defined by

$$T = H^I \left(\mathbb{1} - G^0 H^I\right)^{-1}. \tag{4.15}$$

Transmission and reflection coefficients

Any chain containing an arbitrary number of sites N_s can actually be reduced to an effective dimer, i.e. a chain with two sites $N_s = 2$ (cf. Sec. 4.2.3 and App. D). The calculation of the transmission of this chain is thus reduced to the calculation of the transmission through this effective dimer.

We thus need to evaluate the transmission and reflection coefficients of the amplitude for such a dimer. We assume it is positioned on the sites indexed by 0 and 1. H^I and T are thus 2×2 matrices. From the expression (4.14) of the wave function, and from the form of the Green's function G^0 of a perfect lattice given in App. D, the wave function takes the form $\langle n|\varphi\rangle = \tau e^{+ikn}$ in the forward direction ($n > N_s - 1$), where τ is the transmission coefficient

$$\tau = 1 + G^0_{0,0}T_{0,0} + G^0_{1,0}T_{0,1} + G^0_{0,1}T_{1,0}e^{-2ik} + G^0_{1,1}T_{1,1}. \tag{4.16}$$

Similarly, in the backward direction ($n < 0$) $\langle n|\varphi\rangle = e^{+ikn} + \rho e^{-ikn}$, ρ being the reflection coefficient

$$\rho = G^0_{0,0}T_{0,0} + G^0_{1,0}T_{0,1} + G^0_{0,1}T_{1,0} + G^0_{1,1}T_{1,1}e^{+2ik}. \tag{4.17}$$

When the scatterer is longer than a simple dimer, it is first renormalized and reduced to a dimer (cf. App. D). Then these expressions can be used to calculate the reflection and transmission coefficients of the full chain. In this case, the indices 1 in (4.16) and (4.17) correspond to the last site of the renormalized scatterer, i.e. the last site (index $N_s - 1$) of the initial scatterer. The exponents $+2ik$ and $-2ik$ are replaced by $+2ik(N_s-1)$ and $-2ik(N_s-1)$ respectively. Naturally the probability of transmission is $\mathcal{T} = |\tau|^2$.

4.2.3 Practical computation

In practice, the computation of the matrix elements entering the DOS, the Lyapunov exponent, and the transmission coefficient is performed using the renormalization and decimation procedures detailed in App. D. Schematically, it consists in recursively reducing the full lattice into a smaller, effective one (for instance with just two sites), whose Green's operator matrix elements are "selected elements" (i.e. a subset) of the original lattice's Green's operator matrix elements. This procedure is particularly efficient because the Hamiltonians considered are tridiagonal.

4.3 Correlation-induced delocalization in the dual random dimer model

Anderson localization is a single-particle effect, its two ingredients being a random medium and a wave governed by a linear equation trying to propagate in it. We saw in Sec. 4.1.3 that the important parameter is actually the correlations of the disordered medium. AL is often studied with delta-correlated potentials, and a natural question arising is: "How does AL survive the modification of the correlations?".

In this chapter, we address this problem on a simple model in which correlations are responsible for delocalization. We show that this interesting situation can be realized with an ultracold mixture of the kind discussed in Sec. 4.4.1.

4.3.1 The random dimer model and its "dual"

In 1D disordered systems, AL is known to occur at any energy when the disorder is delta-correlated [237, 263]. Nevertheless, if one introduces particular correlations, delocalization of a significant subset of the eigenstates can appear. This happens in the random-dimer model (RDM) [264], in which the sites of a lattice are assigned energies ϵ_a or ϵ_b at random, with the additional constraint that sites of energy ϵ_b always appear in pairs, or dimers. The same occurs in its dual counterpart (DRDM) [264], in which two lattice sites with energy ϵ_b never appear as neighbors. In these models, extended states arise from resonant modes of the (dual) dimers which present vanishing backscattering at an energy E_{res}. In the thermodynamic limit, the ratio $\sqrt{N_s}/N_s$ between the number of delocalized states and the total number of states vanishes, and there is no mobility edge separating extended and localized energy eigenstates [264–266]. However, in finite size systems, thus in real systems, a localization-delocalization transition can be induced by driving E_{res} inside the spectrum.

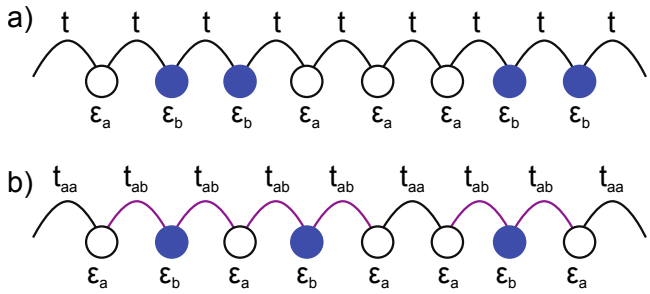

Figure 4.4: (a) In the random dimer model, the on-site energies ϵ_b always appear as pairs. (b) In the dual random dimer model, the on-site energies ϵ_b are forbidden to appear as pairs, and consequently the hoppings t_{ab} always appear as pairs.

This model was proposed to be the possible mechanism which leads to the insulator-metal transition in a wide class of conducting polymers such as polyaniline and heavily doped polyacetylene [267], and in some bio-polymers such as DNA [268]. The evidence of delocalized electronic states was experimentally demonstrated in a random-dimer GaAs-AlGaAs superlattices [269], while for photons, a RDM dielectric system was used [252]. Recently a RDM set-up has been proposed to demonstrate the delocalization of acoustic waves [270]. For polymers, semiconductor lattices, photonic crystals and elastic chains, the dimer resonant energies cannot be modified without changing the sample itself. Thus the localization-delocalization transition for a (D)RDM chain as a function of the relative position of the resonant modes with respect to the band modes cannot easily be studied using these physical systems. In this section, we show that ultracold mixtures are well suited to study the interplay between disorder and correlations, and we propose a realistic setup to study the DRDM.

The RDM was first introduced by Dunlap et al. [264]. It is a single-particle TB model describes by the Hamiltonian (4.6). The simplest example of disorder with this model consists in randomly attributing one of the two values ϵ_a or ϵ_b to the on-site energies, and to give the same value t for all the hopping energies, i.e. the probability law is

$$\forall n \in \mathbb{Z}, \begin{cases} P(\epsilon_n = \epsilon_a) = p, \\ P(\epsilon_n = \epsilon_b) = 1 - p, \\ P(t_n = t) = 1, \end{cases} \tag{4.18}$$

where $0 < p < 1$ and $P(X = x)$ is the probability of the random variable X to take on the value x. In other words, the on-site energies are simple random variables following a Bernoulli law. This does not give any information on

the conditional probabilities, i.e. on the correlations. This disorder is delta-correlated if, e.g., for all n, m such that $n \neq m$ the random variables ϵ_n and ϵ_m are independent and have the same law.

Random dimer correlations

The RDM consists in taking the same *single-site law* (4.18) but also impose the following correlations: one of the two energies, say ϵ_b, always appears as pairs, or dimers, i.e. the joint probability laws satisfy

$$\forall n \in \mathbb{Z},\ \forall \text{ odd } m$$
$$P[(\epsilon_n, \epsilon_{n+1}, \cdots, \epsilon_{n+m}, \epsilon_{n+m+1}) = (\epsilon_a, \underbrace{\epsilon_b, \cdots, \epsilon_b}_{m \text{ times } \epsilon_b}, \epsilon_a)] = 0. \quad (4.19)$$

It is important to specify this law precisely, because there seem to be confusion in the literature on what the RDM is. These correlations are the ones introduced by Dunlap et al. [264]. Other authors have used the term "random dimer model" but with other correlations (for instance, the two impurities always appear as dimers) [242, 265, 266].

The dual random dimer model

In real systems, it is generally rare to have the same hopping energies while the on-site energies are different. For instance, for the situation discussed in Sec. 4.4.1, changing the depth of a single well would also have a small effect on the energy needed to hop to neighbor sites. That is, generally there are correlations between the diagonal and off-diagonal terms of the Hamiltonian. For the simple situation of two possible values of the on-site energy, there can be three possible values for the hoppings: t_{aa} between two sites of energy ϵ_a, t_{bb} between two sites of energy ϵ_b and t_{ab} between two sites of different energies. The system is still disordered, and we will see that these additional correlations (between the ϵ's and the t's) are not sufficient to break AL.

The dual random dimer model (DRDM) consists in imposing that the ϵ_b's never appear as pairs (that is, never in succession), and consequently, the hoppings never take on the value t_{bb}. In this case, the correlation (4.19) are on the hoppings instead of being on the on-site energies [the ϵ_n's of (4.19) are replaced by t_n's, the ϵ_b's by t_{ab}'s, and the ϵ_a's by t_{aa}'s]. Examples of RDM and DRDM lattices are represented in Fig. 4.4.

4.3.2 Properties of a single dimer in a perfect lattice

In this section, we use the Green's function operator formalism introduced in Sec. 4.2.2 to calculate the properties of a single (dual) dimer $\ldots \epsilon_a \overset{t_{ab}}{\frown} \epsilon_b \overset{t_{ab}}{\frown} \epsilon_a \ldots$

positioned in an otherwise perfect, infinite lattice (on-site energies ϵ_a, hopping energies t_{aa}). The index of the only site having an energy ϵ_b is $n = 0$.

The Hamiltonian of the scatterer is

$$H^I = (\epsilon_b - \epsilon_a)|0\rangle\langle 0| + (t_{ab} - t_{aa})\left\{|-1\rangle\langle 0| + |0\rangle\langle 1| + \text{h.c.}\right\}. \tag{4.20}$$

The site $n = 0$ is removed by renormalizing the lattice. As explained in App. D, one has to separately renormalize H and H^0, obtaining the effective Hamilonians $\tilde{H}$ and $\tilde{H}^0$, in order to obtain the Hamiltonian of the new scatterer $\tilde{H}^I \equiv \tilde{H} - \tilde{H}^0$. Using the following notations for H

$$H = \ldots \epsilon_a \overset{t_{aa}}{\frown} \epsilon_a \overset{t_{ab}}{\frown} \epsilon_b \overset{t_{ab}}{\frown} \epsilon_a \overset{t_{aa}}{\frown} \epsilon_a \ldots$$

Renormalization

$$\Downarrow$$

$$\tilde{H} = \ldots \epsilon_a \overset{t_{aa}}{\frown} \tilde{\epsilon} \overset{\tilde{t}}{\frown} \tilde{\epsilon} \overset{t_{aa}}{\frown} \epsilon_a \ldots$$

we obtain

$$\tilde{\epsilon} = \epsilon_a + \frac{t_{ab}^2}{E - \epsilon_b}, \tag{4.21}$$

$$\tilde{t} = \frac{t_{ab}^2}{E - \epsilon_b}, \tag{4.22}$$

after renormalization, and for H^0

$$H^0 = \ldots \epsilon_a \overset{t_{aa}}{\frown} \epsilon_a \overset{t_{aa}}{\frown} \epsilon_a \overset{t_{aa}}{\frown} \epsilon_a \overset{t_{aa}}{\frown} \epsilon_a \ldots$$

Renormalization

$$\Downarrow$$

$$\tilde{H}^0 = \ldots \epsilon_a \overset{t_{aa}}{\frown} \tilde{\epsilon}_0 \overset{\tilde{t}_0}{\frown} \tilde{\epsilon}_0 \overset{t_{aa}}{\frown} \epsilon_a \ldots$$

the renormalization yields

$$\tilde{\epsilon}_0 = \epsilon_a + \frac{t_{aa}^2}{E - \epsilon_a}, \tag{4.23}$$

$$\tilde{t}_0 = \frac{t_{aa}^2}{E - \epsilon_a}. \tag{4.24}$$

It follows that the value of $\tilde{H}^I = \tilde{H} - \tilde{H}^0$ on the subspace $\{|-1\rangle, |1\rangle\}$ is simply

$$\tilde{H}^I = \alpha \begin{pmatrix} 1 & 1 \\ 1 & 1 \end{pmatrix}, \tag{4.25}$$

$$\text{with } \alpha = \frac{t_{ab}^2}{E - \epsilon_b} - \frac{t_{aa}^2}{E - \epsilon_a}. \tag{4.26}$$

This simple expression shows that there is a *resonant energy* $E_{\rm res}$ *for which the dimer is transparent* to incident waves (it does not scatter them because $\tilde{H}^I = 0$). This resonance is obtained for $\alpha = 0$ and is

$$E_{\rm res} = \frac{\epsilon_a t_{ab}^2 - \epsilon_b t_{aa}^2}{t_{ab}^2 - t_{aa}^2}. \tag{4.27}$$

4.3.3 What happens with many dimers?

The situation described above can be transposed to optics. In free space (i.e. without the dimer), the eigenstates are plane waves that propagate freely. The dimer discussed above is similar to a Fabry-Pérot cavity having a single resonant mode for which it is transparent. Adding many dimers to the underlying perfect lattice corresponds to aligning many such Fabry-Pérot cavities. Obviously, if the light is resonant with the first one, it will go through them all.

We now assume that there are few dimers in the lattice. If the disorder is not strong enough to significantly change the spectrum of the Hamiltonian, the lattice still exhibits a single band of allowed energies $\epsilon_a - 2|t_{aa}| \lesssim E \lesssim \epsilon_a + 2|t_{aa}|$, and *some states are expected to be delocalized if the resonant energy is inside this band*, i.e.

$$\epsilon_a - 2|t_{aa}| \leq E_{\rm res} \leq \epsilon_a + 2|t_{aa}|. \tag{4.28}$$

We introduce the dimensionless energy $\Delta\epsilon \equiv (\epsilon_b - \epsilon_a)/t_{aa}$ and hopping $t \equiv t_{ab}/t_{aa}$ characterizing this problem. The *delocalization condition* is obtained by combining (4.27) and (4.28) and is

$$\left|\frac{\Delta\epsilon}{t^2 - 1}\right| \leq 2. \tag{4.29}$$

This expression gives a kind of phase diagram of the DRDM in the limit of low disorder. It is not a phase diagram in the sense of statistical physics because it has been obtained from a single-dimer argument. Moreover, the transition from localization to delocalization is known not to be a phase transition. This phase diagram is represented in Fig. 4.5. The condition (4.29) for delocalization was already present in Ref. [264] despite the fact that the authors did not exhibit the resonance (4.27).

4.4 The dual random dimer model with an ultracold mixture

In this section, we show that an ultracold mixture is well suited to study this model. Indeed, with ultracold atoms, experimentalist have a good control on

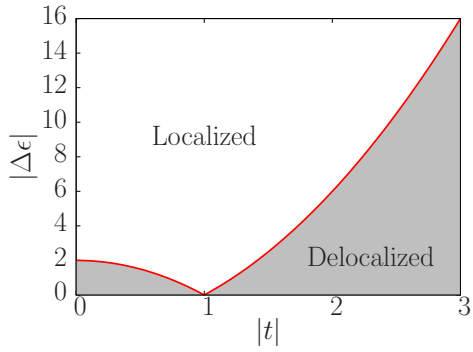

Figure 4.5: "Phase diagram" of the DRDM in the plane $(t, \Delta\epsilon)$ (see text). The red line is Eq. (4.29) and separates the existence of either no extended state (localized region), or of a few extended states (delocalized region).

many parameters. In our case, we will see that the DRDM can be studied in a unique way: the correlations can keep the same form (DRDM correlations) while the hopping and on-site energies can be tuned by playing on either the lattice depth, the transverse confinement, or the interspecies interaction. This enables us to cross the localization-delocalization transition of the DRDM. In the following, we will just give the example in which the transition is crossed by changing the interspecies interaction.

4.4.1 Anderson localization of matter waves with atomic impurities

After the first experiments on ultracold gases in optical lattices were realized [7, 271, 272], the idea of considering a mixture of two atomic species to study localization effects rapidly emerged [273, 274]. The idea is to use at least two species, i.e. either the same isotope in two different spin states, or two different kinds of atoms. By appropriately choosing either the polarization, and/or the laser frequency with respect to the atomic transitions, a single optical lattice can be deep for one species (species B_d) and relatively shallow for the other (species B_f). The first one can thus be seen as classically trapped in the potential wells (negligible tunneling) while the second is free to tunnel from site to site. The mutual interaction between the species locally modifies the potential landscape seen by B_f. If one is able to position B_d randomly in the lattice, this induces disorder for the "flying" species B_f. This is illustrated in Fig. 4.6.

In the following, we will illustrate the discussion taking ^{87}Rb as the "disorder species" B_d, and ^{41}K as the "flying species" B_f. These two atoms are bosons, and the mixture has been experimentally brought to degeneracy [275]. Because of a Feshbach resonance, the mutual interaction can be tuned by applying an external magnetic field [276]. This means that the scattering length can be changed from essentially $-\infty$ to $+\infty$. The gas can thus have attractive interactions ($a_s < 0$), be non-interacting ($a_s \simeq 0$), or have repulsive interactions ($a_s > 0$). This opens the possibility to continuously go from a situation

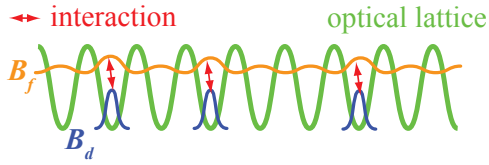

Figure 4.6: An atomic mixture in an optical lattice can be used to study localization effects [273]. A first species B_d is classically trapped in the potential wells, and interacts with a second one B_f, which can tunnel through the lattice. If B_d is randomly positioned, this is a realization of a disordered crystal in which species B_f play the role of electrons. With an appropriate choice of the mixture, the strength of the mutual interaction can even be continuously tuned from zero to infinity, and be attractive or repulsive.

of perfect order ($a_s \simeq 0$), to the disordered case ($a_s \neq 0$).

Reduction to a single-particle Hamiltonian

The properties of this system close to equilibrium can be studied in the following manner: since the impurities are classically trapped, we only take into account their mean-field repulsion (or attraction) with B_f and assume they do not tunnel through the lattice. An effective 1D single-particle Hamiltonian of the form (4.6) — describing the system close to a stationary state — can then be derived for the species B_f. This is done by using the procedures outlined in Sec. 1.2.4 for both species. We consider a situation with many B_f atoms per site such that a mean field treatment is appropriate for B_f. Additionally, in the longitudinal direction, the potential is a lattice sufficiently deep for a TB description to be valid (more precise conditions will be given in the following).

Evaluation of the on-site and hopping energies

The effective Hamiltonian (4.6) is thus obtained by a 1D reduction of the system Hamiltonian by introducing the transverse widths $\sigma_{\perp,B_f}$ of the condensate and $\sigma_{\perp,B_d}$ of the impurities wave functions in a cylindrical trap (cf. Ref. [70] and Sec. 1.2.4). We introduce the Wannier functions $\phi_n(z)$ approximated by the Gaussian functions

$$\phi_n(z) = \frac{\phi_n(0)}{\pi^{1/4}\sigma_{z,B_f}^{1/2}} \exp\left[-\frac{(z-z_n)^2}{2\sigma_{z,B_f}^2}\right], \tag{4.30}$$

where $|\phi_n(0)|^2$ is the number of bosons B_f in the nth lattice well. Similarly, the density of the impurities is $n_{B_d} \propto \sum_{n'} \exp[-(z-z_{n'})^2/\sigma_{z,B_d}^2]$. The

determination of the widths $\sigma_{\perp,B_f}$, $\sigma_{\perp,B_d}$, σ_{z,B_f}, and σ_{z,B_d} is carried out variationally [70, 273] assuming the system is at equilibrium. An orthonormalizing process similar to the Gram-Schmidt process is applied to this basis to obtain the new basis $\{\tilde{\phi}_n(z)\}$ satisfying $\int \tilde{\phi}_m(z)\tilde{\phi}_n(z) = \delta_{mn}$ [277].

We can now evaluate the parameters entering the effective Hamiltonian (4.6). The on-site energies are given by

$$\begin{aligned}\epsilon_n = \int \mathrm{d}z\, \tilde{\phi}_n(z) \Bigg[& -\frac{\hbar^2\nabla^2}{2m_{B_f}} + U_{B_f}(z) \\ & + \frac{1}{2}g|\phi_n(z)|^2 + g' n_{B_d}(z) \Bigg] \tilde{\phi}_n(z),\end{aligned} \tag{4.31}$$

where m_{B_f} is the mass of B_f, $U_{B_f}(z)$ is the lattice potential seen by B_f, and the parameters g and g' are the strengths of the 1D B_fB_f and B_fB_d interactions, which are given by (cf. Sec. 1.2.4)

$$g = \frac{2\hbar^2 a}{m_{B_f}\sigma^2_{\perp\, B_f}}, \tag{4.32}$$

$$g' = \frac{2\hbar^2 a'}{m_r(\sigma^2_{\perp\, B_f} + \sigma^2_{\perp\, B_d})}, \tag{4.33}$$

a and a' being respectively the B_fB_f and B_fB_d scattering lengths, and m_r the B_fB_d reduced mass. The hopping energies t_n are given by

$$t_n = \int \mathrm{d}z\, \tilde{\phi}_n(z) \left[-\frac{\hbar^2\nabla^2}{2m_{B_f}} + U_{B_f}(z) \right] \tilde{\phi}_{n+1}(z). \tag{4.34}$$

This completes the determination of the effective 1D Hamiltonian for bosons B_f.

4.4.2 Proposed setup

As explained in Sec. 4.4.1 the two-boson mixture $B_d = {}^{87}\mathrm{Rb}$–$B_f = {}^{41}\mathrm{K}$ is well suited to study localization effects because of the experimentally accessible interspecies Feshbach resonance. We will thus illustrate the following with this example. We assume the mixture is first brought to degeneracy in an optical trap, and that an external magnetic field can be applied to tune the interspecies interaction, as is Ref. [276].

General considerations

We propose to load the mixture in a 2D transverse lattice similar to the one of Paredes et al. [69]. This confines the atoms in a square array of parallel

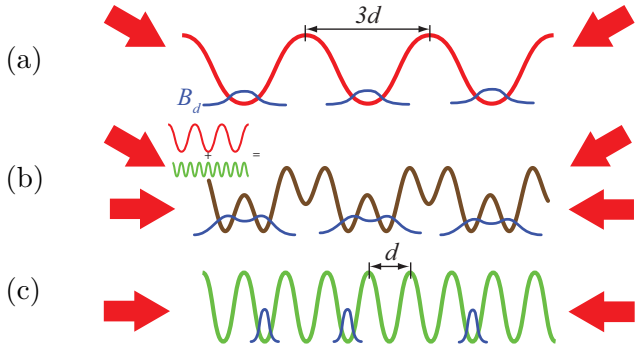

Figure 4.7: Experimental scheme to generate the correlated disorder. (a) Impurities are trapped in a lattice of step $3d$. (b) A second lattice of step d is switched on, and the first one turned off. In the final configuration (c), the impurities follow a DRDM distribution. The red arrows symbolize the laser beams of the lattices.

1D "tubes". By using far off-resonance lasers and playing on the power, the transverse confinement can be changed from 0 to high values in the range of a few tens of kHz. If the laser waists are sufficiently large, the longitudinal confinement can be low, ultimately limited by the underlying dipole force trap. In each 1D trap, the system is well described by the TB description if a third, much shallower optical lattice is added along the third, longitudinal direction (as in Ref. [69]).

Generation of the DRDM correlations

In order to arrange the ^{87}Rb disorder bosons such that two of them never stand in neighboring sites, one can first prepare a very dilute system in a first lattice of spacing $3d$ with less than one atom per site on average [69]. A second lattice with a spacing d is then adiabatically superimposed onto the first one. Finally, the first lattice is adiabatically turned off. This procedure is illustrated in Fig. 4.7. The two lattices can be created with the same laser by using an angle $\theta_1 = \arccos(1/3) \simeq 70.5°$ between the two beams of the first, while for the second the beams are counterpropagating ($\theta_2 = 180°$). The two pairs must not interfere with each other or with the transverse lattice. This can be done by introducing a detuning between them (a few tens of MHz [7]).

Experimental parameters

The atomic properties of ^{87}Rb and ^{41}K (and other isotopes) can be found respectively in Refs. [108] and [278–280].

The wavelengths of the two species are quite close to each other (the D_1

and D_2 lines of Rb are respectively at 795.0 nm and 780.2 nm, while for K they are at 769.9 and 766.9 nm). Their D_2 lines have the same linewidths $\Gamma_{\mathrm{Rb}}/2\pi \simeq 6.06$ MHz and $\Gamma_{\mathrm{K}}/2\pi \simeq 6.03$ MHz. Their saturation intensities are also the same $I_{\mathrm{sat}}^{\mathrm{Rb}} \simeq 1.67$ mW/cm^2 and $I_{\mathrm{sat}}^{\mathrm{K}} \simeq 1.75$ mW/cm^2.

We use $\lambda = 800$ nm for the longitudinal lattice, and a lattice potential depth $U_{\mathrm{Rb}}^{0,in} \simeq 30E_{\mathrm{Rb}}$, with $E_{\mathrm{Rb}} = \hbar^2k^2/2m_{\mathrm{Rb}}$ being the recoil energy for Rb, and k is the magnitude of the lattice's wave vector. This wavelength is sufficiently detuned from the atomic transitions to cause low spontaneous emission, and perform experiments that can last ~ 1 s.

The condition on the number of atoms needed to avoid double occupancy will depend on the external confinement. For instance, for an axial confinement of 60 Hz [69], double occupancy can be avoided if $N_{\mathrm{Rb}} \leq 20$ [281]. The number of impurities can be increased by increasing the lattice potential depth or by relaxing the axial confinement. In the rest, we neglect the effect of the axial confinement, and thus assume the system to be homogeneous. The influence of the axial confinement is currently being investigated in the group.

The potential depth U_{Rb}^0 of the final lattice $U_{\mathrm{Rb,K}}(z) = U_{\mathrm{Rb,K}}^0 \sin^2(\pi z/d)$ must be large compared to E_{Rb} to neglect the impurity mobility during the duration of the experiment (typically less than 1 second [142, 143]). This condition can be fulfilled at $U_{\mathrm{Rb}}^0 = 18E_{\mathrm{Rb}}$ in the presence of attractive interactions with K. Differently, the depth U_{K}^0 for the species K must be $\gtrsim 2\ E_{\mathrm{K}}$, the recoil energy for K, to guarantee the validity of the TB description. With $U_{\mathrm{Rb}}^0 = 18E_{\mathrm{Rb}}$, the wavelength chosen, and linearly polarized lattice beams we have $U_{\mathrm{K}}^0 = 2.5E_{\mathrm{K}}$. The tunneling time of the ^{87}Rb impurities is on the order of 1 s for all the points A to E in Fig. 4.8.

For the evaluation of the on-site and hopping energies, we consider a system of $N_{\mathrm{K}} = 1.3 \times 10^4$ ^{41}K atoms distributed in 200 wells, 10% of which are occupied by a ^{87}Rb atom. The effect of the mean-field interactions is enhanced by a tight radial confinement $\omega_{\perp\,\mathrm{K}}/2\pi = 60$ kHz (cf. Sec. 1.2.4).

4.4.3 Localization-delocalization transition

The influence of the various parameters (lattice depth, interaction, radial confinement) on the values of $\Delta\epsilon$ and t, which are the two dimensions of the (single-dimer) phase diagram, is not trivial. We thus use the numerical method described in Sec. 4.4.1 to evaluate the on-site and hopping energies. Of course, we make sure that the TB approximation is valid on the range of parameters explored.

For such a system, the phase diagram can be explored just by varying the K–Rb scattering length a' (lines in Fig. 4.8). The point (1,0) corresponds to $a' = 0$, in this case K atoms do not interact with the impurities, thus neither the on-site nor the hopping energies are modified by the presence of Rb atoms

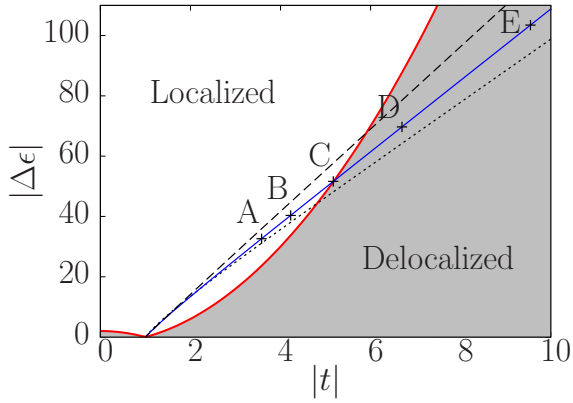

Figure 4.8: Calculated trajectories in the phase diagram for different number of atoms N_{K} obtained by varying the interspecies scattering length a'. Dashed line: $N_{\mathrm{K}} = 1.6 \times 10^4$, $a' \in [0, -87\,a_0]$. Continuous line: $N_{\mathrm{K}} = 1.3 \times 10^4$, $a' \in [0, -380\,a_0]$. Dotted line: $N_{\mathrm{K}} = 1.0 \times 10^4$, $a' \in [0, -570\,a_0]$. With 1.3×10^4 atoms, the localization-delocalization transition occurs for $a' = -346\,a_0$ (point C). Other points correspond to $a' = -316\,a_0$ (A), $-331\,a_0$ (B), $-361\,a_0$ (D) and $-376\,a_0$ (E) respectively, $a_0 \simeq 0.53$ Å being the Bohr radius.

and the lattice is not disordered. Higher points of the curve correspond to greater and greater attractive K–Rb interactions. Remember that this "phase diagram" actually corresponds to the presence of a single dimer in a perfect chain, and not to a full disordered chain.

To make sure that the single-dimer argument is sufficient to understand the physics, we numerically calculate the spectrum across the transition by evaluating the Lyapunov exponent, the transmission probability, and the DOS. This latter quantity is calculated to check that the localization observed is not a trivial effect such as that related to the opening of a band gap[4].

For this numerical calculation of the Lyapunov exponent $\gamma(E)$, we use the asymptotic expression (4.10) with $N_s = 1000$ lattice sites. The behavior of the Lyapunov exponent through the transition is shown in Fig. 4.9. The different lines, which correspond to the crosses in Fig. 4.8, show that the localization length is greater than the system size for points C, D, E, as expected from the single-dimer prediction. The location of the minima corresponds to the position of the resonance energy E_{res}, which moves inside the band for increasing values of $|a'|$. The non-zero value of γ in the delocalization regime is due to

[4]This is an important point. The DRDM correlations constraint the proportion of disordered sites (sites with an energy ϵ_b) to be $\leq 50\%$, but if this limit is reached, the system is actually not random anymore because one site over two is occupied by a ^{87}Rb atom. In this case, a band gap appears in the center of the spectrum.

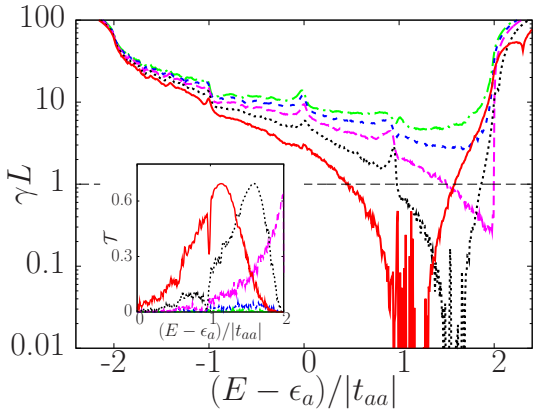

Figure 4.9: Lyapunov exponent γ in units of $1/L$, with $L = N_s d$ being the lattice length, as a function of the energy of the K atoms. The dot-dashed green line corresponds to point A in Fig. 4.8, the short-dashed blue line to point B, the long-dashed magenta line to point C, the dotted black line to point D and the solid red line to point E. The inset shows the corresponding behavior of the transmission probability $\mathcal{T}$.

the finite value of the number of sites in the computation.

The transmission probability $\mathcal{T} = |\tau|^2$, defined as the modulus square of the transmission coefficient, is calculated for different values of a' and is shown in the inset of Fig. 4.9. For $a' = -346\, a_0$ the resonance fits in the band-edge, and the corresponding transmission peak arises. For $a' = -361\, a_0$ and $a' = -376\, a_0$ the peak moves towards the center of the band in agreement with the position of the minimum of γ. The width of the peak decreases by increasing the system size, as the percentage of delocalized states scales as $\sqrt{N_s}/N_s$.

4.4.4 Effect of the additional correlations

Both the Lyapunov exponent and the transmission probability respectively show some small peaks and dips. These structures are due to an underlying order present in the procedure illustrated in Fig. 4.7. In fact, even if our proposition allows the distance between two subsequent impurities to be any integer > 1, still every three site is definitely without an impurity by construction. The evidence that this underlying order does not affect the DRDM physical effect is shown in Fig. 4.10. The transmission probability peak for the proposed DRDM pattern (Fig. 4.7) is in correspondence with the transmission probability peak of a genuine DRDM. Such a disorder pattern (i.e. without these supplementary correlations) could be generated by using a dipolar gas

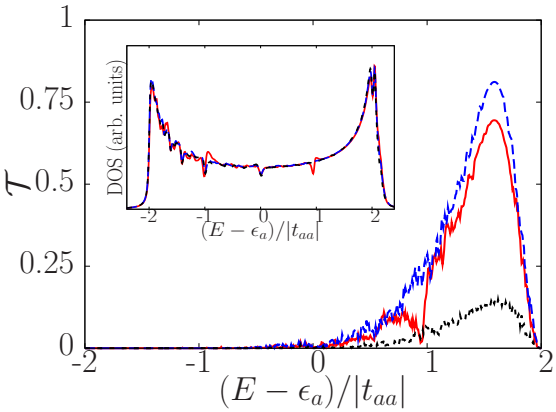

Figure 4.10: Transmission probability $\mathcal{T}$ for $N_{\rm K} = 1.3 \times 10^4$ and $a' = -361\, a_0$, and different disorder patterns: a genuine DRDM lattice (dashed-blue line), a DRDM lattice generated with the procedure illustrated in Fig. 4.7 (continuous-red line), and an uncorrelated lattice (dotted-black line). The inset shows the corresponding density of states.

for which repulsive interactions may avoid next-neighboring occupation [282]. However, at the moment, no dipolar gases have yet been cooled down to degeneracy in a mixture. For completeness of our analysis we compare the two DRDM models with a lattice where the position of impurities ϵ_b are delta-correlated [283], i.e. with a real Anderson model. In this case the transmission probability drops (Fig. 4.10), and becomes vanishing for longer chains. The residual peak is a signature of the presence of a few dual dimers, and we checked that it vanishes in an ordinary disorder model with uncorrelated on-site and hopping energies.

Finally, it is worth pointing out that the impurity distribution deeply modifies the nature of the states, but not the spectrum itself at this low impurity concentration. Indeed, the DOS is essentially the same for the three cases as shown in the inset of Fig. 4.10. When the percentage of impurities is increased, the underlying periodicity, which is different in the three models, leads to fragmentation of the DOS in either three, two or one bands. The DOS $\mathcal{N}(E)$ has been evaluated by using the Kirkman-Pendry relation introduced in Sec. 4.2.2.

4.4.5 Discussion

How to probe these properties in a real experiment?

Since the condensate energy corresponds to the lowest allowed energy (quasi-momentum $k = 0$, energy $(E - \epsilon_a)/|t_{aa}| = -2$ in the figures above), the region in the vicinity of the resonance is not directly probed by a BEC at equilibrium.

It could be explored by preparing Bloch states with an initial quasimomentum $k \neq 0$ by introducing a constant frequency shift between the two waves generating the lattice [284]. In the localized regime, we expect that for any $k \in [-\pi, \pi]$, the whole condensate stays at rest in the frame of reference of the moving lattice, while in the delocalized regime, at $k = k(E_{\mathrm{res}})$, the condensate stays at rest in the frame of reference of the laboratory. This should be done without dramatically changing the local densities such that the on-site and hopping energies (which are calculated at equilibrium and depend on the density) are not significantly modified.

What about the underlying confinement?

So far we have assumed the system to be finite ($N_s = 200$ sites) but with no longitudinal confinement. This can be done experimentally by using a box-like potential on top of the lattices (a box potential was done e.g. by Meyrath [179]). Nevertheless this is rarely the case in experiments because harmonic traps are easier to implement. The effect of the inhomogeneity is expected to be non-negligible because the on-site and hopping energies have a spatial deterministic dependence. For instance, the mean-field interaction of K with itself is smaller on the sides, where the density is lower than that in the middle of the trap. This issue is the object of current studies by our group. It is addressed by simulating the dynamics by a numerical integration of a 1D GPE.

4.5 Outlook

In this theoretical chapter we have addressed the problems of studying localization effects with ultracold gases. More precisely, we have assessed the feasibility of an experiment performed in the tight-binding regime (that is in a relatively deep lattice), and in which one atomic species is used to induce disorder for another through mutual interactions. We studied in details the dual random dimer model in which a localization-delocalization transition can be driven by tuning the mutual interaction. Our conclusion is that this transition should be observable in a ^{87}Rb–^{41}K mixture with realistic experimental parameters. Nevertheless, it is not yet clear what the most appropriate way to probe the system is, and this question is still the subject of current investigations involving the simulation of the dynamics with a numerical integration of the time-dependent Gross-Pitaevskii equation.

The recent success in studying such localization effects with ultracold atoms, performed in a variety of regimes — non-interacting bosons in a 1D tight-binding regime [143], bosons in a weak 1D disorder [142], non-interacting fermions in a weak 3D disorder [145], experiments in 2D [259], interplay with

superfluidity [285, 286] — suggest that these themes will keep developing in the near future. The very interesting regime of controlled correlations and controlled interactions will soon be accessible in experiments.

Conclusion

This dissertation has presented the work of three years at the Nonlinear Institute of Nice. I have taken part in the construction of the INLN BEC experiment, which is now up and running. This has been the subject of the first two chapters of this dissertation.

In the third chapter, we have focused on the realization of shortcuts to adiabaticity for quadratic Hamiltonians in two distinct limits: the 1D non-interacting case at finite temperature connecting two equilibrium states, and the 3D interacting BEC at $T = 0$ connecting two equilibrium states. We have seen that the performances of our method is limited by the trap anharmonicity and by the imperfect control we have over the fast dynamics of the time-dependent potential.

In the non-interacting case, it is clear that the methods should work equally to any initial state, i.e. even for non-equilibrium states. It may be useful to other fields of physics where adiabatic schemes are used. In the case of the BEC, it would be interesting to investigate the possibility of producing final states other than equilibrium states, by a modification of the methods presented in Chap. 3.

The possibility of performing shortcuts seems to be tightly connected to the existence of invariants of motions and it would be interesting to investigate the existence of such invariants for more complicated systems, such as other potentials, interacting systems, etc. This seems to be closely related to the integrability of the system. Since the classical definition of integrability is not easily extended to quantum systems — the quantum sense of "integrability" is not yet agreed upon — one may expect quantum systems to exhibit fundamentally different behaviors compared to their classical counterparts.

In the final chapter we have seen that a localization-delocalization transition can be crossed in a realistic experiment involving a mixture of ultracold gases loaded in optical lattices. One of the species is used as a source of disorder for the other which behaves like a wave in a disordered crystal. Since the disorder is synthetic, its correlation function can be engineered. We have proposed a realistic experimental scheme to create a correlated disorder which exhibits strong deviations from the standard AL. In particular, delocalization

can occur in this mixture. We have shown that this transition can be crossed by varying an external magnetic field to tune the interspecies collision cross-section through a Feshbach resonance without modifying the correlation of the disorder.

Appendix A

Technical drawings

This appendix gives the technical drawings of the main steel chamber, the Hellma glass cell and the magnetic trap.

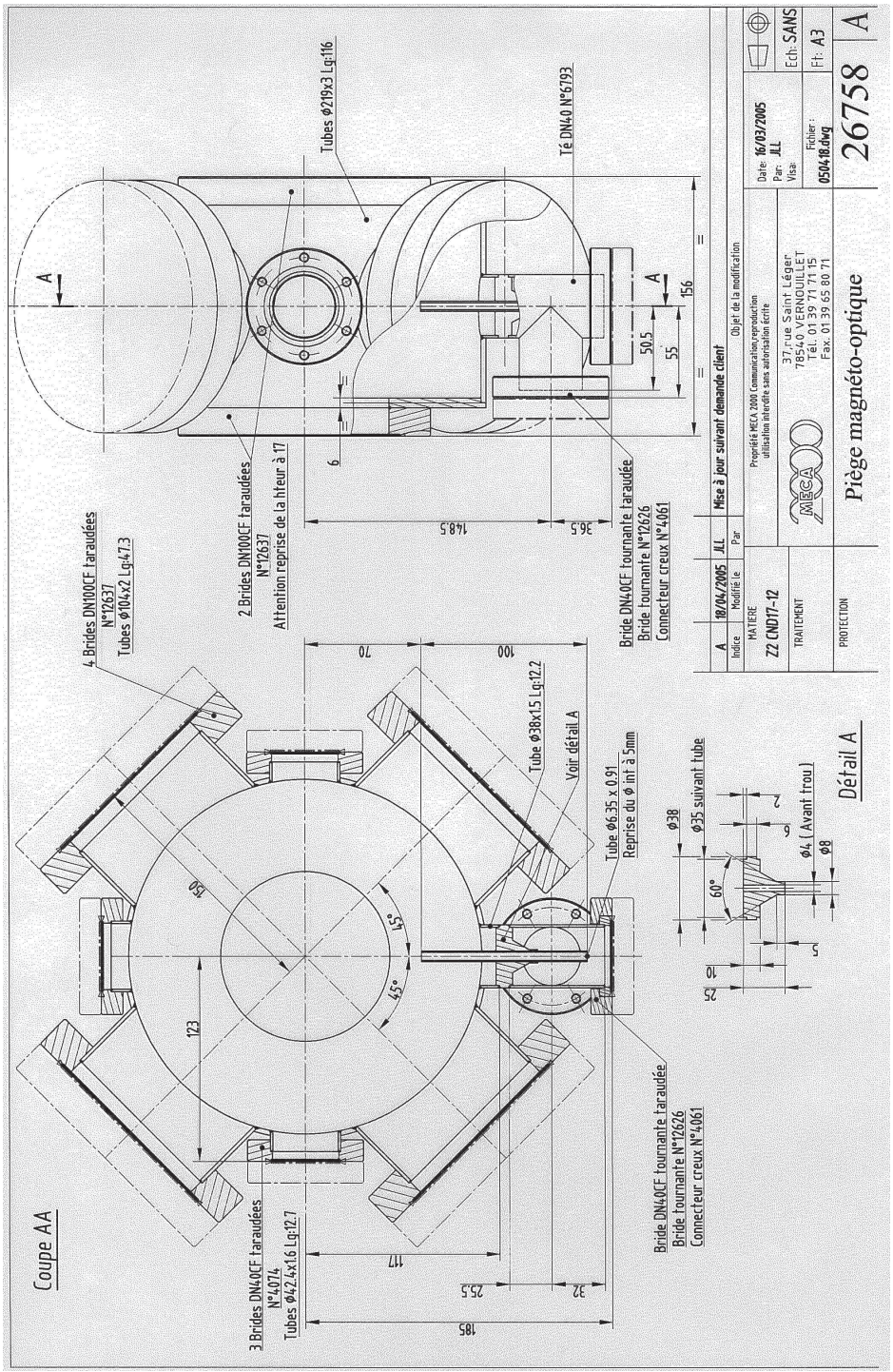

Figure A.1: Main steel chamber.

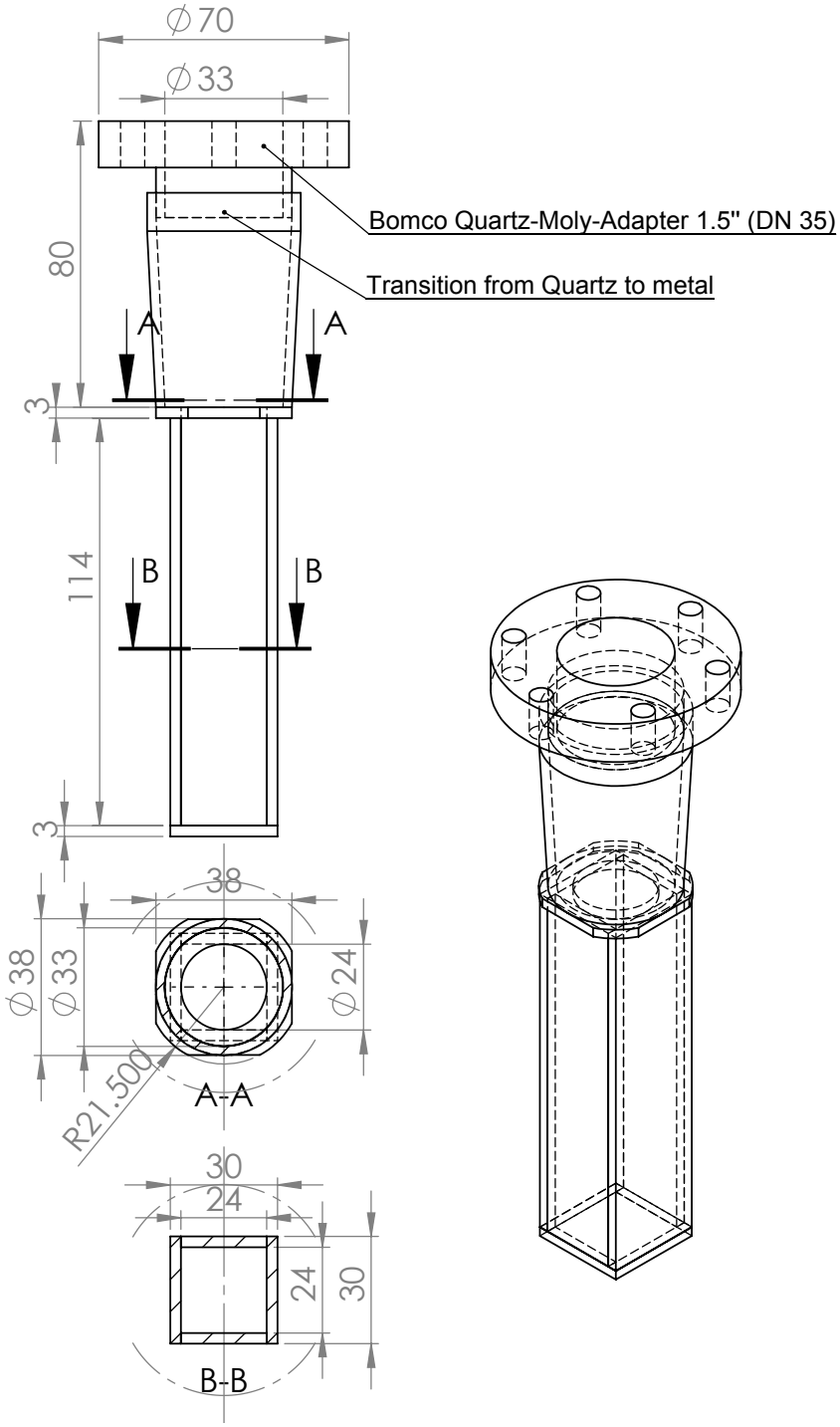

Figure A.2: Hellma glass cell.

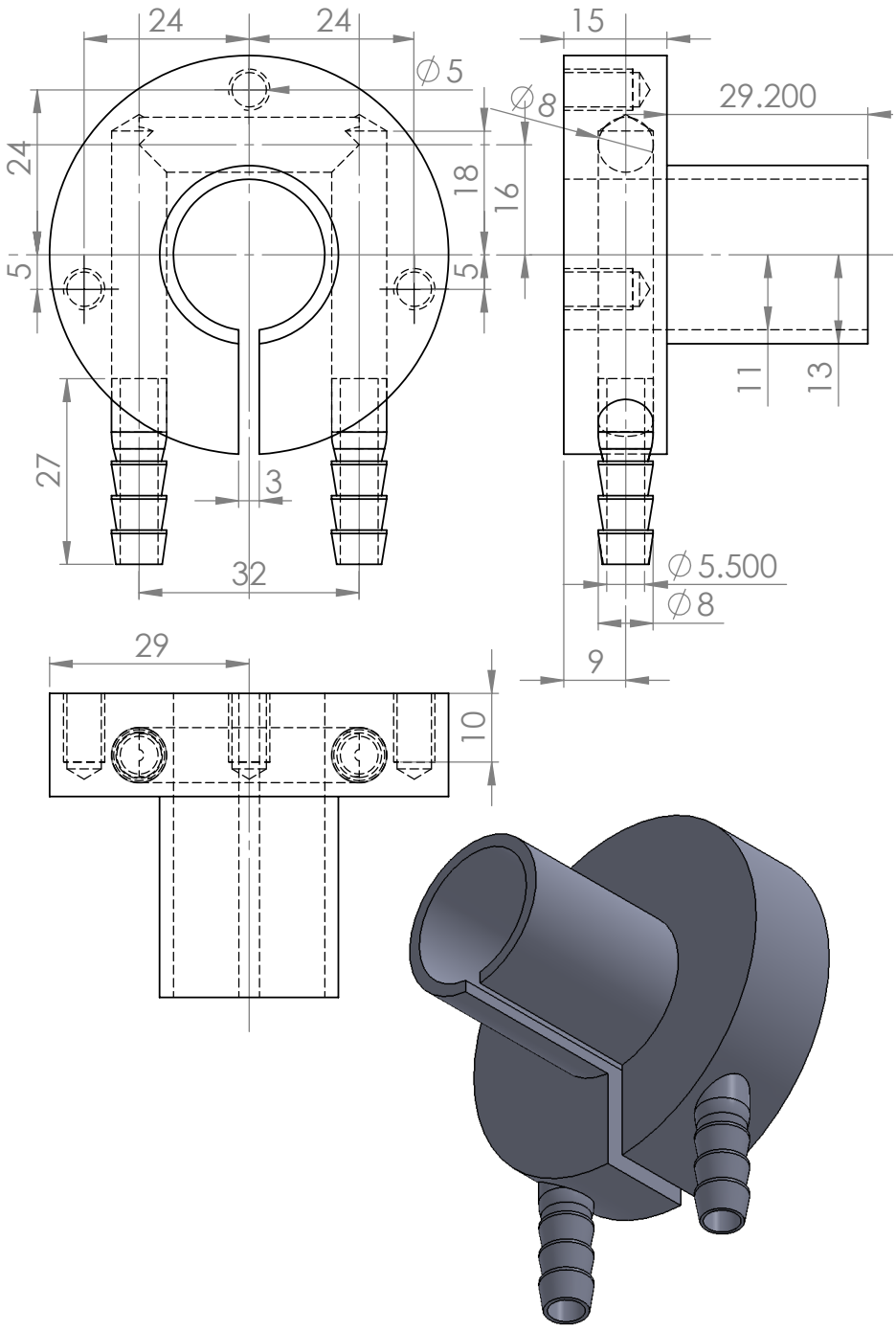

Figure A.3: Quadrupole coil support.

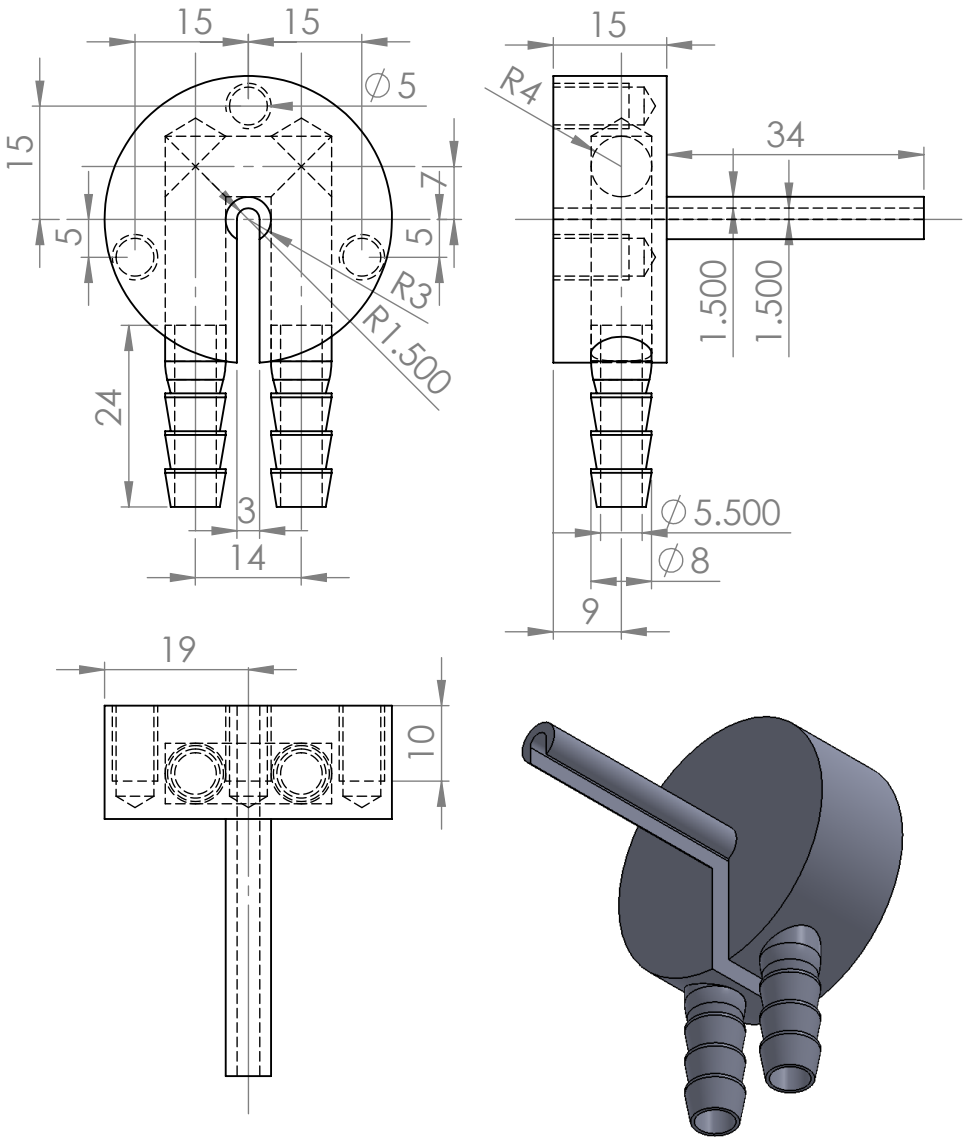

Figure A.4: Ioffe coil support.

Appendix B

Equipment

This appendix lists the key elements of the experiment. Standard electronics and optical elements such as the optical table, the lenses, the mirrors, the mountings, the cables, the oscilloscopes etc. are not listed.

Description	**Constructor**	**Part number (Model)**
Upper chamber 100 CF viewports (MOT1)	Torr Scientific	VPZ100BBAR
Upper chamber 38 CF viewports	Torr Scientific	VPZ38BBAR
Upper chamber ion pump	Varian	9191115 (VacIon Plus 20)
Lower chamber ion pump	Varian	9191213 (VacIon Plus 40)
Titanium sublimation pump	Varian	9160050
Mass spectrometer	Pfeiffer vacuum	Prisma 80, QMS 200
DFB 780 nm diodes	Eagleyard photonics	EYP-DFB-0780-00080-1500-SOT02-0000
DFB mounting and collimation lens	Thorlabs	LT230P-B
Tapered amplifier 780 nm (MOTs)	Sacher lasertechnik group	TEC-400-0780-2000
Individual polarization maintaining fibers (MOTs version 1)	OZ Optics	LPC-08-780-5/125-P-2.2-11AS-40-3A-3-3

One-to-six fibered splitters (MOTs version 2)	OZ Optics	FOBS-16P-1111111-5/125-P-780-16.66%-40-1AHPC,3A-3-1,3+LPC-08-P-2.2-11AS-40-1AHPC-3-1
ECDL diode (780 nm, pulled to 765 nm)	Eagleyard photonics	EYP-RWE-0780-02000-1300-SOT12-0000
Tapered amplifier 770 nm (dipole trap)	Sacher lasertechnik group	TEC-400-0770-1500
Band-stop filter 767-800 nm (dipole trap)	Semrock	NF01-785U-25
Aluminum-filled heat conducting epoxy	Cotronics corp.	Duralco 132
Magnetic trap power supply	CNB Electronique	CN7B-48-50 (48V/50A)
MOT1 power supply	Selectronic	SL1730SL20 (30V/20A)
Compensation coils power supplies	Selectronic	SL1730SB (30V/3A)
DDS function generator (rf source)	Tabor electronics	WW2571A
Rf amplifier	AR	25A250A (25 W)
Analog output card	National Instrument	778701-01 (NI PCI-6723)
Output card cables and BNC connectors	National Instrument	186381-02, 777643-01, 777807-01
CCD cameras	Point Grey Research	GRAS-20S4M-C, GRAS-03S3M-C, SCOR-20SOM

Appendix C

Scaling of Bose-Einstein condensates in harmonic traps

In this appendix, we first derived Eqs. (3.80)–(3.85), and then show that the general scaling equations obtained can be used to recover — by a perturbative approach — the dipole, quadrupole, and scissors modes discussed in Secs. 1.2.3 and 3.2.

C.1 Scaling

The starting point is the GPE (3.43) for the general harmonic potential (3.75). We look for a solution of the form

$$\psi(\mathbf{r},t) = \mathcal{A}(t)\chi(\boldsymbol{\rho},\tau)e^{i\phi(\mathbf{r},t)} \tag{C.1}$$

with

$$\boldsymbol{\rho} = B^{-1}\mathbf{r} + \boldsymbol{a}. \tag{C.2}$$

Equation (3.43) then takes the form

$$\begin{aligned} &i\hbar\left[\frac{\dot{\mathcal{A}}}{\mathcal{A}}\chi + \nabla_{\boldsymbol{\rho}}\chi\cdot\frac{\partial\boldsymbol{\rho}(B,\boldsymbol{a})}{\partial t} + \frac{\partial\chi}{\partial\tau}\frac{\partial\tau}{\partial t} + i\chi\dot{\phi}\right] = \\ &-\frac{\hbar^2}{2m}\left\{\sum_{i,j,k}[B^{-1}]_{ij}[B^{-1}]_{kj}\frac{\partial^2\chi}{\partial\rho_i\partial\rho_k} + 2i(B^{-1}\nabla_{\mathbf{r}}\phi)\cdot\nabla_{\boldsymbol{\rho}}\chi + i(\nabla^2_{\mathbf{r}}\phi)\chi - (\nabla_{\mathbf{r}})^2\chi\right\} \\ &+\frac{1}{2}m\left\{[B(\boldsymbol{\rho}-\boldsymbol{a})]^t W[B(\boldsymbol{\rho}-\boldsymbol{a})]\right\}\chi + \boldsymbol{u}^t B(\boldsymbol{\rho}-\boldsymbol{a})\chi + g_{3\mathrm{D}}|\mathcal{A}|^2|\chi|^2\chi. \end{aligned} \tag{C.3}$$

We look for the conditions that $\mathcal{A}$, B, and $\boldsymbol{a}$ have to satisfy in order to simplify Eq. (C.3) to the form

$$i\hbar\frac{\partial}{\partial\tau}\chi(\boldsymbol{\rho},\tau) = \left[U(\boldsymbol{\rho},0) + g_{3\mathrm{D}}N|\chi(\boldsymbol{\rho},\tau)|^2\right]\chi(\boldsymbol{\rho},\tau) \tag{C.4}$$

in the TF limit, namely, neglecting the kinetic term given by (3.78). We deduce immediately that (i) the second term of Eq. (C.3) has to be equal to the sixth, and (ii) the first to the seventh. Condition (i) leads to

$$\nabla_{\mathbf{r}}\phi = -\frac{m}{\hbar} B \left\{ [\dot{B^{-1}}]\mathbf{r} + \dot{\boldsymbol{a}} \right\}, \tag{C.5}$$

which has a solution if the matrix $B[\dot{B^{-1}}] = -\dot{B}B^{-1}$ is symmetric[1]. If this condition holds, we get Eq. (3.82) for the phase ϕ. Condition (ii) can be written as

$$\dot{\mathcal{A}}\mathcal{A}^{-1} = -\frac{1}{2}\mathrm{tr}(\dot{B}B^{-1}). \tag{C.6}$$

Using the invariance of the trace and determinant, the evolution of $\mathcal{A}$ can be written in term of the eigenvalues β_i of the matrix B as

$$\begin{gathered} \frac{\mathrm{d}}{\mathrm{d}t}\ln\mathcal{A} = \dot{\mathcal{A}}\mathcal{A}^{-1} = -\frac{1}{2}\sum_i \frac{\dot{\beta}_i}{\beta_i} = -\frac{1}{2}\frac{\mathrm{d}}{\mathrm{d}t}\ln\det B, \\ \text{that is} \quad \mathcal{A} = C\,(\det B)^{-1/2} \ \text{ with } C \in \mathbb{R}^+. \end{gathered} \tag{C.7}$$

If, e.g., at $t = 0$ we have $B = \mathbb{1}$ and $\mathcal{A} = 1$, equation (C.7) yields Eq. (3.84).

Moreover from the comparison between the third term in Eq. (C.3) and the nonlinear term [condition (iii)], we deduce Eq. (3.85). Taking into account (i)–(iii), Eq. (C.3) reduces to

$$\begin{aligned} i\hbar\frac{\partial\chi}{\partial\tau} &= \hbar\det B\frac{\partial\phi_0}{\partial t} \\ &\quad + \det B\Bigg\{\frac{m}{2}\left[\left(\dot{B}B^{-1}\mathbf{r} - B\dot{\boldsymbol{a}}\right)^2 + \mathbf{r}^t\ddot{B}B^{-1}\mathbf{r} + \mathbf{r}^t\dot{B}[\dot{B^{-1}}]\mathbf{r}\right] \\ &\quad + \frac{m}{2}\left\{[B(\boldsymbol{\rho}-\boldsymbol{a})]^t W[B(\boldsymbol{\rho}-\boldsymbol{a})]\right\} \\ &\quad - m\mathbf{r}^t\dot{B}\dot{\boldsymbol{a}} - m\mathbf{r}^t B\ddot{\boldsymbol{a}} + \boldsymbol{u}^t B(\boldsymbol{\rho}-\boldsymbol{a})\Bigg\}\chi \\ &\quad + g_{3\mathrm{D}}|\chi|^2\chi. \end{aligned} \tag{C.8}$$

By imposing the quadratic term in $\boldsymbol{\rho}$ to be equal to $\frac{1}{2}m\boldsymbol{\rho}^t W^0\boldsymbol{\rho}$, we get condition (iv), i.e., Eq. (3.80); the fifth condition is that the linear term in $\boldsymbol{\rho}$ vanishes and thus leads to (3.81); finally by requiring that the $\boldsymbol{\rho}$-independent term be null, we get (3.83) for ϕ_0.

[1] In a general case the matrix $\dot{B}B^{-1}$ can be split into a symmetric and an antisymmetric part. In the $\boldsymbol{\rho}$-frame of reference, the antisymmetric part gives rise to a rotational term proportional to the angular momentum and only the symmetric part of $\dot{B}B^{-1}$ contributes to the phase of the wave function. The rotational term can be neglected for nearly-isotropic traps or for small angular velocities of the trap.

C.2 Low-lying modes

Equation (3.81) describes the dipole mode for the center of mass and Eq. (3.80) the quadrupole and the scissors modes. The low-lying eigenfrequencies of these latter modes can be obtained by solving the equation of motion for the matrix B for the case of a tilt of the trap of a small angle α. At $t > 0$, the matrix W is constant and can be written as

$$W = \begin{pmatrix} \omega_\perp^2 & 0 & 0 \\ 0 & \omega_\parallel^2 & \alpha(\omega_\parallel^2 - \omega_\perp^2) \\ 0 & \alpha(\omega_\parallel^2 - \omega_\perp^2) & \omega_\perp^2 \end{pmatrix} = W^0 + \delta W, \tag{C.9}$$

where

$$W^0 = \begin{pmatrix} \omega_\perp^2 & 0 & 0 \\ 0 & \omega_\parallel^2 & 0 \\ 0 & 0 & \omega_\perp^2 \end{pmatrix}, \tag{C.10}$$

and

$$\delta W = \begin{pmatrix} 0 & 0 & 0 \\ 0 & 0 & \alpha(\omega_\parallel^2 - \omega_\perp^2) \\ 0 & \alpha(\omega_\parallel^2 - \omega_\perp^2) & 0 \end{pmatrix}. \tag{C.11}$$

We look for solutions of the form $B^t = 1 + \delta$. Equation (3.80) takes the form:

$$\ddot{\delta} \simeq -W^0\delta - \delta^t W^0 - (\mathrm{Tr}\delta)W^0 + \delta W, \tag{C.12}$$

up to the first order in δ. For the diagonal terms, we have

$$\ddot{\delta}_{ii} = -2\omega_i^2\delta_{ii} - (\mathrm{Tr}\delta)\omega_i^2. \tag{C.13}$$

Setting $\delta_{ii} = \Delta_i e^{i\Omega t}$, we obtain the following coupled equations

$$\begin{aligned} -\Omega^2\Delta_x &= -2\omega_\perp^2\Delta_x - (\Delta_x + \Delta_y + \Delta_z)\omega_\perp^2, \\ -\Omega^2\Delta_y &= -2\omega_\parallel^2\Delta_y - (\Delta_x + \Delta_y + \Delta_z)\omega_\parallel^2, \\ -\Omega^2\Delta_z &= -2\omega_\perp^2\Delta_z - (\Delta_x + \Delta_y + \Delta_z)\omega_\perp^2, \end{aligned} \tag{C.14}$$

whose solutions are the surface mode $\Omega = \sqrt{2}\omega_\perp$ for any values of $\omega_\perp$ and $\omega_\parallel$, and the breathing modes $\Omega \simeq 2\omega_\perp$ and $\Omega \simeq \sqrt{5/2}\omega_\parallel$ in the cigar-shape regime $\omega_\parallel \ll \omega_\perp$.

For the off-diagonal terms δ_{ij} ($\{i,j\} = \{2,3\}$ or $\{3,2\}$), Eq. (C.12) gives

$$\ddot{\delta}_{ij} = -\omega_i^2\delta_{ij} - \omega_j^2\delta_{ji} + \alpha(\omega_\parallel^2 - \omega_\perp^2), \tag{C.15}$$

namely

$$\ddot{\delta}_{ij} + \ddot{\delta}_{ji} = -(\omega_i^2 + \omega_j^2)(\delta_{ij} + \delta_{ji}) + 2\alpha(\omega_\parallel^2 - \omega_\perp^2), \tag{C.16}$$

which has the solution

$$\delta_{23} = \delta_{32} = \alpha \frac{(\omega_{\parallel}^2 - \omega_{\perp}^2)}{\Omega_s^2}[1 - \cos(\Omega t)], \tag{C.17}$$

with $\Omega_s = (\omega_{\perp}^2 + \omega_{\parallel}^2)^{1/2}$. This is a scissors mode with initial conditions $\dot{\delta}_{ij}(t = 0) = 0$ and $\delta_{ij}(t = 0) = 0$.

Appendix D

Renormalization

This appendix details the renormalization procedure used to calculate the density of states, the Lyapunov exponent, and the transmission coefficient in the case of one-dimensional tight-binding Hamiltonians (cf. Secs. 4.2 and 4.3). In the case of simple tridiagonal Hamiltonians, it provides a practical way to perform efficient numerical calculations. The procedure is illustrated with the example of a perfect lattice. The algorithm used to numerically calculate these quantities are also explained.

D.1 Renormalization

The Hamiltonian is assumed to be a sum of two terms, for instance a kinetic term and an interaction term

$$H = H^0 + H^I. \tag{D.1}$$

D.1.1 The Dyson equation

In the following, we will use the Dyson equation [287] which relates the Green's function operator $G^0(E) \equiv \left(E \cdot \mathbb{1} - H^0\right)^{-1}$ of H^0 to that of H, $G = (E \cdot \mathbb{1} - H)^{-1}$, by the relation

$$G = G^0 + G^0 H^I G. \tag{D.2}$$

The proof is a simple exercise of linear algebra.

D.1.2 The procedure

The idea of renormalization is to obtain an effective Hamiltonian describing the physics happening in a subspace $\mathcal{A}$ of the original Hilbert space $\mathcal{H}$. For this, $\mathcal{H}$ is decomposed into a direct sum of two subspaces $\mathcal{A}$ and $\mathcal{B}$:

$$\mathcal{H} = \mathcal{A} \oplus \mathcal{B}. \tag{D.3}$$

The projectors on these subspaces are written A and B, such that $A+B=\mathbb{1}$. The Hamiltonian is split into a sum of four terms

$$H=(A+B)H(A+B)=\underbrace{AHA}_{H_{AA}}+\underbrace{BHB}_{H_{BB}}+\underbrace{AHB}_{H_{AB}}+\underbrace{BHA}_{H_{BA}}, \tag{D.4}$$

which are grouped by two:

$$H=H^0+H^I, \tag{D.5}$$

$$\text{with } H^0=H_{AA}+H_{BB}, \text{ and } H^I=H_{AB}+H_{BA}, \tag{D.6}$$

such that the image of $\mathcal{A}$ (respectively $\mathcal{B}$) by H^0 is in $\mathcal{A}$ (respectively $\mathcal{B}$), while the image of $\mathcal{A}$ (respectively $\mathcal{B}$) by H^I is in $\mathcal{B}$ (respectively $\mathcal{A}$).

The idea of renormalization is to eliminate one of the two subspaces, and describe the physics in the remaining subspace by a new, effective, Hamiltonian. The cost of this procedure is that the new Hamiltonian is energy dependent. This is done by calculating the projection of the Green's operator on one of the subspaces:

$$G_{AA}\equiv AGA=\left[E\cdot\mathbb{1}-H_{\mathcal{A}}(E)\right]^{-1}, \tag{D.7}$$

where $H_{\mathcal{A}}(E)$ is the effective Hamiltonian on the remaining subspace, defined by

$$H_{\mathcal{A}}(E)=H_{AA}+H_{AB}G^0_{BB}(E)H_{BA}. \tag{D.8}$$

The proof makes use of the Dyson equation and is straightforward algebra.

D.2 An example: the perfect lattice

Let us illustrate the use of renormalization to calculate the Green's function of a perfect lattice described by the Hamiltonian

$$H=\sum_{n\in\mathbb{Z}}\Big\{\epsilon|n\rangle\langle n|+t\left(|n\rangle\langle n+1|+|n+1\rangle\langle n|\right)\Big\}. \tag{D.9}$$

To this purpose, we first need to calculate the expression of the Green's function of a semi-infinite lattice.

D.2.1 Green's function of a semi-infinite lattice

The Hamiltonian reads

$$H=\sum_{n=0}^{\infty}\Big\{\epsilon|n\rangle\langle n|+t\big(|n\rangle\langle n+1|+|n+1\rangle\langle n|\big)\Big\}. \tag{D.10}$$

It is renormalized using the subspaces $\mathcal{A} = \text{span}\{|0\rangle\}$ and $\mathcal{B} = \mathcal{H} - \mathcal{A}$, i.e. the Hamiltonian is split in the following manner:

$$H = \underbrace{\epsilon|0\rangle\langle 0|}_{H_{AA}} + \underbrace{t\left(|0\rangle\langle 1| + |1\rangle\langle 0|\right)}_{H_{AB}+H_{BA}} + \underbrace{\sum_{n=1}^{\infty}\left\{\epsilon|n\rangle\langle n| + t\big(|n\rangle\langle n+1| + |n+1\rangle\langle n|\big)\right\}}_{H_{BB}}. \tag{D.11}$$

The renormalization yields the equation

$$\frac{t}{2}g_{0,0}^2 - (\tilde{E} + ie)g_{0,0} + \frac{1}{2t} = 0 \tag{D.12}$$

for $g_{0,0} = \langle 0|G(E + i\delta)|0\rangle$, where $\tilde{E} = (E - \epsilon)/2t$ and $e = \delta/2t$. For $|\tilde{E}| < 1$, which defines the band of allowed energies, one defines the dimensionless wave vector k by $\cos k \equiv \tilde{E}$. This is the dispersion relation of this lattice. The solution of Eq. (D.12) is

$$g_{0,0}(E + i0^+) = \frac{1}{t}\left\{\tilde{E} - i\sqrt{1 - \tilde{E}^2}\right\} = \frac{e^{-i|k|}}{t} \quad \text{for } t > 0, \tag{D.13}$$

$$\text{and} \quad g_{0,0}(E + i0^+) = \frac{1}{t}\left\{\tilde{E} + i\sqrt{1 - \tilde{E}^2}\right\} = \frac{e^{i|k|}}{t} \quad \text{for } t < 0. \tag{D.14}$$

The sign of the root of (D.12) has been chosen such that the projected DOS

$$\mathcal{N}(E) = -\frac{1}{\pi}\lim_{\delta\to 0^+}\text{Im}g_{0,0} \tag{D.15}$$

is *positive* in the band.

D.2.2 Green's function of the infinite perfect lattice

The Hamiltaonian is given by (D.9). We want to calculate the matrix elements of the Green's function operator G^0 of this perfect lattice.

Diagonal matrix elements

The renormalization with $\mathcal{A} = \text{span}\{|n\rangle\}$ leads to

$$G_{n,n}^0 = \frac{1}{2t}\left(\frac{1}{\tilde{E} + ie - tg_{0,0}}\right) \tag{D.16}$$

for $G^0_{n,n} = \langle n|G^0(E+i\delta)|n\rangle$, where $g_{0,0}$ is the diagonal matrix element of the Green's function of a semi-infinite lattice on site 0. In the band ($|\tilde{E}| < 1$), using (D.16) and (D.14), one gets

$$G^0_{n,n}(E+i0^+) = -\frac{i}{2|t|}\frac{1}{\sqrt{1-\tilde{E}^2}} = -\frac{i}{2|t|\sin|k|}, \tag{D.17}$$

with the dispersion relation $\cos k \equiv \tilde{E}$. The density of states is obtained from (4.8),

$$\mathcal{N}(E) = \frac{1}{2\pi|t|}\frac{1}{\sqrt{1-\left(\frac{E-\epsilon}{2t}\right)^2}} \tag{D.18}$$

in the band, and $\mathcal{N}(E) = 0$ elsewhere.

Off-Diagonal matrix elements

By mathematical induction, one can show that

$$G^0_{0,n} \equiv \langle 0|G^0|n\rangle = (tg_{0,0})^{|n|}G^0_{0,0}. \tag{D.19}$$

In the band this gives

$$G^0_{0,n}(\tilde{E}+i0^+) = -\frac{i}{2t}\left[\tilde{E}-i\sqrt{1-\tilde{E}^2}\right]^{|n|}\frac{1}{\sqrt{1-\tilde{E}^2}}, \tag{D.20}$$

$$= -\frac{i}{2|t|}\frac{e^{-i|nk|}}{\sin|k|} \quad \text{for } t>0, \tag{D.21}$$

$$\text{and} \quad G^0_{0,n}(\tilde{E}+i0^+) = -\frac{i}{2|t|}\frac{e^{i|nk|}}{\sin|k|} \quad \text{for } t<0. \tag{D.22}$$

D.3 Numerical calculation of *G* for arbitrary chains: the decimation technique

This section gives the algorithm used to calculate the matrix elements of G entering the DOS, Lypunov exponent and transmission coefficient for a random chain, i.e. a chain in which the on-site and hopping energies have been randomly chosen.

D.3.1 Removal of one site

We now consider a lattice with a finite number of sites $|n\rangle$, $n \in [0, N_s-1]$. We will often use the renormalization procedure on tridiagonal Hamiltonians of the form (D.9), using a single site of the lattice as the subspace $\mathcal{B}$, in

order to reduce the dimensionality of the problem by 1. When removing one site, say the second site $|1\rangle$, the effective energy of the neighboring sites after renormalization are respectively

$$\tilde{\epsilon}_0 \equiv \langle 0|H_{\mathcal{A}}(E)|0\rangle = \epsilon_0 + \frac{t_0 t_1}{E - \epsilon_1}, \tag{D.23}$$

$$\text{and} \quad \tilde{\epsilon}_2 \equiv \langle 2|H_{\mathcal{A}}(E)|2\rangle = \epsilon_2 + \frac{t_1 t_2}{E - \epsilon_1}, \tag{D.24}$$

and the hopping energy between these two sites is

$$\tilde{t}_{0,2} \equiv \langle 0|H_{\mathcal{A}}(E)|2\rangle = \frac{t_0 t_1}{E - \epsilon_1}. \tag{D.25}$$

D.3.2 Calculation of $\langle 0|\boldsymbol{G}|\mathbf{N_s} - \mathbf{1}\rangle$

A renormalization removing the second site can be performed recursively to obtain partial information on a d-dimensional problem by reducing it to an effective 2D problem. The lattice is thus turned into an effective dimer (2 sites). This procedure is called "decimation" and was first described by Farchioni et al. [262] for solid-state physics. It can be sketched in the following way:

$$H = \epsilon_0 \overset{t_0}{\frown} \epsilon_1 \overset{t_1}{\frown} \epsilon_2 \overset{t_2}{\frown} \epsilon_3 \overset{t_3}{\frown} \cdots \overset{t_{N_s-2}}{\frown} \epsilon_{N_s-1}$$

Renormalization, removal of the second site

$$\Downarrow$$

$$\tilde{H} = H^{(1)} = \tilde{\epsilon}_0 \overset{\tilde{t}_{0,2}}{\frown} \tilde{\epsilon}_2 \overset{t_2}{\frown} \epsilon_3 \overset{t_3}{\frown} \cdots \overset{t_{N_s-2}}{\frown} \epsilon_{N_s-1}$$

Idem $(N_s - 3)$ times

$$\Downarrow$$

$$H^{(N_s-2)} = \bar{\epsilon}_0 \overset{\tilde{t}_{0,N_s-1}}{\frown} \bar{\epsilon}_{N_s-1}$$

The elements finally obtained are related to the Green's function matrix elements by $\langle 0|G|N_s - 1\rangle = 1/(E - \bar{\epsilon}_0)$, $\langle N_s - 1|G|0\rangle = 1/(E - \bar{\epsilon}_{N_s-1})$.

D.3.3 First and last diagonal matrix element

In order to compute the first and last diagonal matrix elements, one can simply renormalize the chain using $\mathcal{A} = \text{span}\{|0\rangle\}$, and $\mathcal{B} = \mathcal{H} - \mathcal{A}$. In this case H^I simply is $H^I = t_0(|0\rangle\langle 1| + |1\rangle\langle 0|)$. This yields

$$G_{0,0} = \frac{1}{E - \epsilon_0 + t_0^2 \langle 1|G_{BB}|1\rangle}. \tag{D.26}$$

Note that $\langle 1|G_{BB}|1\rangle$ is the first diagonal element of the Green's function of a new semi-infinite lattice. By applying the same renormalization recursively, we thus obtain $G_{0,0}$ as the continued fraction

$$G_{0,0} = \cfrac{1}{E - \epsilon_0 + \cfrac{t_0^2}{E - \epsilon_1 + \cfrac{t_1^2}{E - \epsilon_2 + \cdots}}}. \tag{D.27}$$

The simplicity comes from the fact that the Hamiltonian is tridiagonal. This algorithm for the calculation of the first diagonal matrix element of G is seen to be linear in the number of sites, it is thus efficient. Obviously, the same algorithm can be used for the last diagonal element G_{N_s-1,N_s-1}.

Appendix E

Publications

This appendix lists the articles published during this thesis.

[288] Shortcuts to adiabaticity for trapped ultracold gases
J.-F. Schaff, P. Capuzzi, G. Labeyrie, and P. Vignolo
New Journal of Physics **13**, 113017 (2011).

[209] Shortcut to adiabaticity for an interacting Bose-Einstein condensate
J.-F. Schaff, X.-L. Song, P. Capuzzi, P. Vignolo, and G. Labeyrie
Europhysics Letters **93**, 23001 (2011).

[208] Fast optimal transition between two equilibrium states
J.-F. Schaff, X.-L. Song, P. Vignolo, and G. Labeyrie
Physical Review A **82**, 033430 (2010),
and erratum, Physical Review A **83**, 059911(E) (2011).

[289] Localization-delocalization transition in the random dimer model
J.-F. Schaff, Z. Akdeniz, and P. Vignolo
Physical Review A **81**, 041604(R) (2010).

List of Figures

List of Tables

Bibliography

[1] T. Wilk, A. Gaëtan, C. Evellin, J. Wolters, Y. Miroshnychenko, P. Grangier, and A. Browaeys, *Entanglement of two individual neutral atoms using Rydberg blockade*, Physical Review Letters **104**, 010502 (2010).

[2] W. S. Bakr, J. I. Gillen, A. Peng, S. Fölling, and M. Greiner, *A quantum gas microscope for detecting single atoms in a Hubbard-regime optical lattice*, Nature **462**, 74 (2009).

[3] W. S. Bakr, A. Peng, M. E. Tai, R. Ma, J. Simon, J. I. Gillen, S. Fölling, L. Pollet, and M. Greiner, *Probing the superfluid-to-Mott insulator transition at the single-atom level*, Science **329**, 547 (2010).

[4] J. F. Sherson, C. Weitenberg, M. Endres, M. Cheneau, I. Bloch, and S. Kuhr, *Single-atom-resolved fluorescence imaging of an atomic Mott insulator*, Nature **467**, 68 (2010).

[5] C. Weitenberg, M. Endres, J. F. Sherson, M. Cheneau, P. Schauß, T. Fukuhara, I. Bloch, and S. Kuhr, *Single-spin addressing in an atomic Mott insulator*, Nature **471**, 319 (2011).

[6] T. Monz, P. Schindler, J. Barreiro, M. Chwalla, D. Nigg, W. Coish, M. Harlander, W. Hänsel, M. Hennrich, and R. Blatt, *14-Qubit Entanglement: Creation and Coherence*, Physical Review Letters **106**, 130506 (2011).

[7] M. Greiner, O. Mandel, T. Esslinger, T. W. Hänsch, and I. Bloch, *Quantum phase transition from a superfluid to a Mott insulator in a gas of ultracold atoms*, Nature **415**, 39 (2002).

[8] R. Gerritsma, G. Kirchmair, F. Zähringer, E. Solano, R. Blatt, and C. F. Roos, *Quantum simulation of the Dirac equation*, Nature **463**, 68 (2010).

[9] R. Gerritsma, B. Lanyon, G. Kirchmair, F. Zähringer, C. Hempel, J. Casanova, J. García-Ripoll, E. Solano, R. Blatt, and C. Roos, *Quan-*

tum Simulation of the Klein Paradox with Trapped Ions, Physical Review Letters **106**, 060503 (2011).

[10] A. Ekert and R. Jozsa, *Quantum computation and Shor's factoring algorithm*, Reviews of Modern Physics **68**, 733 (1996).

[11] X. Peng, Z. Liao, N. Xu, G. Qin, X. Zhou, D. Suter, and J. Du, *Quantum Adiabatic Algorithm for Factorization and Its Experimental Implementation*, Physical Review Letters **101**, 220405 (2008).

[12] D. Vion, A. Aassime, A. Cottet, P. Joyez, H. Pothier, C. Urbina, D. Esteve, and M. H. Devoret, *Manipulating the quantum state of an electrical circuit*, Science **296**, 886 (2002).

[13] A. D. O'Connell, M. Hofheinz, M. Ansmann, R. C. Bialczak, M. Lenander, E. Lucero, M. Neeley, D. Sank, H. Wang, M. Weides, J. Wenner, J. M. Martinis, and A. N. Cleland, *Quantum ground state and single-phonon control of a mechanical resonator*, Nature **464**, 697 (2010).

[14] Y. Makhlin, G. Schön, and A. Shnirman, *Quantum-state engineering with Josephson-junction devices*, Reviews of Modern Physics **73**, 357 (2001).

[15] T. Stöferle, H. Moritz, C. Schori, M. Köhl, and T. Esslinger, *Transition from a Strongly Interacting 1D Superfluid to a Mott Insulator*, Physical Review Letters **92**, 130403 (2004).

[16] T. Bourdel, L. Khaykovich, J. Cubizolles, J. Zhang, F. Chevy, M. Teichmann, L. Tarruell, S. J. J. M. F. Kokkelmans, and C. Salomon, *Experimental Study of the BEC-BCS Crossover Region in Lithium 6*, Physical Review Letters **93**, 050401 (2004).

[17] M. Köhl, H. Moritz, T. Stöferle, K. Günter, and T. Esslinger, *Fermionic Atoms in a Three Dimensional Optical Lattice: Observing Fermi Surfaces, Dynamics, and Interactions*, Physical Review Letters **94**, 080403 (2005).

[18] W. Ketterle and D. E. Pritchard, *Atom cooling by time-dependent potentials*, Physical Review A **46**, 4051 (1992).

[19] X. Chen, A. Ruschhaupt, S. Schmidt, A. del Campo, D. Guéry-Odelin, and J. G. Muga, *Fast Optimal Frictionless Atom Cooling in Harmonic Traps: Shortcut to Adiabaticity*, Physical Review Letters **104**, 063002 (2010).

[20] M. Fierz, *Über die relativistische Theorie kräftefreier Teilchen mit beliebigem Spin*, Helvetica Physica Acta **12**, 3 (1939).

[21] W. Pauli, *The Connection Between Spin and Statistics*, Physical Review **58**, 716 (1940).

[22] S. N. Bose, *Plancks Gesetz und Lichtquantenhypothese*, Zeitschrift für Physik **26**, 178 (1924); O. Theimer and B. Ram, *The beginning of quantum statistics: A translation of "Planck's law and the light quantum hypothesis"*, American Journal of Physics **44**, 1056 (1976).

[23] T. L. Hill, *Statistical mechanics* (McGraw-Hill Book Company, 1956).

[24] H. B. Callen, *Thermodynamics and an introduction to thermostatistics*, Second edition (John Wiley & Sons, 1985).

[25] B. Diu, C. Guthmann, D. Lederer, and B. Roulet, *Eléments de physique statistique* (Hermann, 1989).

[26] A. Georges and M. Mézard, *Physique statistique* (École Polytechnique, 2004).

[27] A. Einstein, *Quantentheorie des einatomigen idealen Gases*, Sitzungsber. Preuss. Akad. Wiss. Phys.-Math. Kl. page 3 (1924).

[28] M. Le Bellac, *Physique quantique* (EDP Sciences/CNRS Édition, 2007).

[29] D. Guéry-Odelin and T. Lahaye, *Basics on Bose-Einstein condensation*, in *Ultracold Gases and Quantum Information, Les Houches session XCI*, edited by C. Miniatura, L.-C. Kwek, M. Ducloy, B. Grémaud, B.-G. Engelert, L. F. Cugliandolo, A. Ekert, and K. K. Phua, pages 1–65 (Oxford University Press, 2011).

[30] F. Dalfovo, S. Giorgini, and S. Stringari, *Theory of Bose-Einstein condensation in trapped gases*, Reviews of Modern Physics **71**, 463 (1999).

[31] J. Weiner and P. S. Julienne, *Experiments and theory in cold and ultracold collisions*, Reviews of Modern Physics **71**, 1 (1999).

[32] C. Cohen-Tannoudji, B. Diu, and F. Laloë, *Mécanique quantique* (Hermann, 1973).

[33] J. Dalibard, *Collisional dynamics of ultra-cold gases*, in *Bose-Einstein Condensation in Atomic Gases, Proceedings of the international school of physics "Enrico Fermi", Course CXL*, edited by M. Inguscio, S. Stringari, and C. E. Wieman, pages 321–349 (IOS Press, 1999).

[34] E. G. M. van Kempen, S. J. J. M. F. Kokkelmans, D. J. Heinzen, and B. J. Verhaar, *Interisotope Determination of Ultracold Rubidium Interactions from Three High-Precision Experiments*, Physical Review Letters **88**, 093201 (2002).

[35] N. R. Thomas, N. Kjærgaard, P. S. Julienne, and A. C. Wilson, *Imaging of s and d Partial-Wave Interference in Quantum Scattering of Identical Bosonic Atoms*, Physical Review Letters **93**, 173201 (2004).

[36] C. Buggle, J. Léonard, W. von Klitzing, and J. Walraven, *Interferometric determination of the s and d-wave scattering amplitudes in* ^{87}Rb, Physical Review Letters **93**, 173202 (2004).

[37] M. Olshanii, *Atomic Scattering in the Presence of an External Confinement and a Gas of Impenetrable Bosons*, Physical Review Letters **81**, 938 (1998).

[38] K. Huang, *Statistical Mechanics* (Wiley, New York, 1987).

[39] P. Lepage, *How to Renormalize the Schrodinger Equation*, arXiv:nucl-th/9706029v1 (1997).

[40] H. M. J. M. Boesten, C. C. Tsai, J. R. Gardner, D. J. Heinzen, and B. J. Verhaar, *Observation of a shape resonance in the collision of two cold* ^{87}Rb *atoms*, Physical Review A **55**, 636 (1997).

[41] W. Ketterle and N. J. van Druten, *Evaporative cooling of trapped atoms*, Advances in Atomic, Molecular, and Optical Physics **37**, 181 (1996).

[42] J. Ensher, D. Jin, M. Matthews, C. Wieman, and E. Cornell, *Bose-Einstein Condensation in a Dilute Gas: Measurement of Energy and Ground-State Occupation*, Physical Review Letters **77**, 4984 (1996).

[43] I. Bloch, J. Dalibard, and W. Zwerger, *Many-Body Physics with Ultracold Gases*, Reviews of Modern Physics **80**, 885 (2008).

[44] F. Gerbier, *Condensats de Bose-Einstein dans un piège anisotrope*, Ph.D. thesis, Université Pierre et Marie Curie (2003).

[45] A. Aftalion, J. Dalibard, and C. Josserand, *Équation de Schrödinger non linéaire : des condensats de Bose-Einstein aux supersolides* (École Polytechnique, 2010).

[46] C. J. Pethick and H. Smith, *Bose-Einstein Condensation in Dilute Gases*, First edition (Cambridge University Press, 2002).

[47] S. Stringari, *Collective Excitations of a Trapped Bose-Condensed Gas*, Physical Review Letters **77**, 2360 (1996).

[48] Y. Kagan, E. Surkov, and G. Shlyapnikov, *Evolution of a Bose-condensed gas under variations of the confining potential*, Physical Review A **54**, R1753 (1996).

[49] Y. Castin and R. Dum, *Bose-Einstein Condensates in Time Dependent Traps*, Physical Review Letters **77**, 5315 (1996).

[50] Y. Kagan, E. L. Surkov, and G. V. Shlyapnikov, *Evolution of a Bose gas in anisotropic time-dependent traps*, Physical Review A **55**, R18 (1997).

[51] D. Jin, J. Ensher, M. Matthews, C. Wieman, and E. Cornell, *Collective Excitations of a Bose-Einstein Condensate in a Dilute Gas*, Physical Review Letters **77**, 420 (1996).

[52] M.-O. Mewes, M. Andrews, N. van Druten, D. Kurn, D. Durfee, C. Townsend, and W. Ketterle, *Collective Excitations of a Bose-Einstein Condensate in a Magnetic Trap*, Physical Review Letters **77**, 988 (1996).

[53] D. Jin, M. Matthews, J. Ensher, C. Wieman, and E. Cornell, *Temperature-Dependent Damping and Frequency Shifts in Collective Excitations of a Dilute Bose-Einstein Condensate*, Physical Review Letters **78**, 764 (1997).

[54] D. Stamper-Kurn, H.-J. Miesner, S. Inouye, M. Andrews, and W. Ketterle, *Collisionless and Hydrodynamic Excitations of a Bose-Einstein Condensate*, Physical Review Letters **81**, 500 (1998).

[55] O. Maragò, S. Hopkins, J. Arlt, E. Hodby, G. Hechenblaikner, and C. Foot, *Observation of the Scissors Mode and Evidence for Superfluidity of a Trapped Bose-Einstein Condensed Gas*, Physical Review Letters **84**, 2056 (2000).

[56] O. Maragò, G. Hechenblaikner, E. Hodby, and C. Foot, *Temperature Dependence of Damping and Frequency Shifts of the Scissors Mode of a Trapped Bose-Einstein Condensate*, Physical Review Letters **86**, 3938 (2001).

[57] M. Modugno, G. Modugno, G. Roati, C. Fort, and M. Inguscio, *Scissors mode of an expanding Bose-Einstein condensate*, Physical Review A **67**, 023608 (2003).

[58] S. E. Pollack, D. Dries, and R. G. Hulet, *Collective excitation of a Bose-Einstein condensate by modulation of the atomic scattering length*, Physical Review A **81**, 053627 (2010).

[59] S. Nascimbène, N. Navon, K. J. Jiang, L. Tarruell, M. Teichmann, J. Mckeever, F. Chevy, and C. Salomon, *Collective Oscillations of an Imbalanced Fermi Gas: Axial Compression Modes and Polaron Effective Mass*, Physical Review Letters **103**, 170402 (2009).

[60] A. Olivetti, J. Barré, B. Marcos, F. Bouchet, and R. Kaiser, *Breathing Mode for Systems of Interacting Particles*, Physical Review Letters **103**, 224301 (2009).

[61] W. Kohn, *Cyclotron Resonance and de Haas-van Alphen Oscillations of an Interacting Electron Gas*, Physical Review **123**, 1242 (1961).

[62] L. Jacak, P. Hawrylak, and A. Wojs, *Quantum Dots* (Springer, 1998).

[63] I. Bialynicki-Birula and Z. Bialynicka-Birula, *Center-of-mass motion in the many-body theory of Bose-Einstein condensates*, Physical Review A **65**, 063606 (2002).

[64] P. Vignolo, *Degenerate Fermi gases*, in *Ultracold Gases and Quantum Information, Les Houches session XCI*, edited by C. Miniatura, L.-C. Kwek, M. Ducloy, B. Grémaud, B.-G. Engelert, L. F. Cugliandolo, A. Ekert, and K. K. Phua, pages 66–104 (Oxford University Press, 2011).

[65] D. Guéry-Odelin and S. Stringari, *Scissors Mode and Superfluidity of a Trapped Bose-Einstein Condensed Gas*, Physical Review Letters **83**, 4452 (1999).

[66] L. Tonks, *The Complete Equation of State of One, Two and Three-Dimensional Gases of Hard Elastic Spheres*, Physical Review **50**, 955 (1936).

[67] M. Girardeau, *Relationship between Systems of Impenetrable Bosons and Fermions in One Dimension*, Journal of Mathematical Physics **1**, 516 (1960).

[68] A. Lenard, *One-Dimensional Impenetrable Bosons in Thermal Equilibrium*, Journal of Mathematical Physics **7**, 1268 (1966).

[69] B. Paredes, A. Widera, V. Murg, O. Mandel, S. Fölling, I. Cirac, G. V. Shlyapnikov, T. W. Hänsch, and I. Bloch, *Tonks-Girardeau gas of ultracold atoms in an optical lattice*, Nature **429**, 277 (2004).

[70] L. Salasnich, A. Parola, and L. Reatto, *Effective wave equations for the dynamics of cigar-shaped and disk-shaped Bose condensates*, Physical Review A **65**, 043614 (2002).

[71] R. Frisch, *Experimenteller Nachweis des Einsteinschen Strahlungsrückstoßes*, Zeitschrift für Physik A **86**, 42 (1933).

[72] A. Kastler, *Quelques suggestions concernant la production optique et la détection optique d'une inégalité de population des niveaux de quantification spatiale des atomes. Application à l'expérience de Stern et Gerlach et à la résonance magnétique*, Journal de Physique et le Radium **11**, 255 (1950).

[73] C. Cohen-Tannoudji, J. Dupont-Roc, and G. Grynberg, *Atom-Photon Interactions: Basic Processes and Applications* (Wiley, New York, 1992).

[74] B. R. Mollow, *Power Spectrum of Light Scattered by Two-Level Systems*, Physical Review **188**, 1969 (1969).

[75] J. Dalibard and C. Cohen-Tannoudji, *Atomes ultra-froids*, lecture notes at École Normale Supérieure (1999).

[76] R. Grimm, M. Weidemüller, and Y. B. Ovchinnikov, *Optical dipole traps for neutral atoms*, Advances in Atomic, Molecular, and Optical Physics **42**, 95 (2000).

[77] H. J. Metcalf and P. van der Straten, *Laser cooling and trapping of atoms*, Journal of the Optical Society of America B **20**, 887 (2003).

[78] C. Doppler, *Ueber das farbige Licht der Doppelsterne und einiger anderer Gestirne des Himmels* (K. Böhm, Prag, 1903).

[79] T. Hänsch, S. Lee, R. Wallenstein, and C. Wieman, *Doppler-Free Two-Photon Spectroscopy of Hydrogen 1S-2S*, Physical Review Letters **34**, 307 (1975).

[80] D. Wineland and H. Dehmelt, Bulletin of the American Physical Society **20**, 637 (1975).

[81] V. S. Letokhov, V. G. Minogin, and B. D. Pavlik, *Cooling and capture of atoms and molecules by a resonant light field*, JETP **45**, 698 (1977).

[82] D. J. Wineland and W. M. Itano, *Laser cooling of atoms*, Physical Review A **20**, 1521 (1979).

[83] J. P. Gordon and A. Ashkin, *Motion of atoms in a radiation trap*, Physical Review A **21**, 1606 (1980).

[84] V. S. Letokhov and V. G. Minogin, *Laser radiation pressure on free atoms*, Physics Reports **73**, 1 (1981).

[85] E. L. Raab, M. Prentiss, A. Cable, S. Chu, and D. E. Pritchard, *Trapping of Neutral Sodium Atoms with Radiation Pressure*, Physical Review Letters **59**, 2631 (1987).

[86] S. Chu, *Nobel Lecture: The manipulation of neutral particles*, Reviews of Modern Physics **70**, 685 (1998).

[87] C. N. Cohen-Tannoudji, *Nobel Lecture: Manipulating atoms with photons*, Reviews of Modern Physics **70**, 707 (1998).

[88] P. Lett, R. Watts, C. Westbrook, W. Phillips, P. Gould, and H. Metcalf, *Observation of Atoms Laser Cooled below the Doppler Limit*, Physical Review Letters **61**, 169 (1988).

[89] P. J. Ungar, D. S. Weiss, E. Riis, and S. Chu, *Optical molasses and multilevel atoms: theory*, Journal of the Optical Society of America B **6**, 2058 (1989).

[90] J. Dalibard and C. Cohen-Tannoudji, *Laser cooling below the Doppler limit by polarization gradients: simple theoretical models*, Journal of the Optical Society of America B **6**, 2023 (1989).

[91] Y. Castin, *Les limites du refroidissement laser dans les mélasses optiques à une dimension*, Ph.D. thesis, Université Pierre et Marie Curie (1991).

[92] Y. Castin and K. Mølmer, *Monte Carlo Wave-Function Analysis of 3D Optical Molasses*, Physical Review Letters **74**, 3772 (1995).

[93] J. Dalibard, *Laser cooling of an optically thick gas: The simplest radiation pressure trap?*, Optics Communications **68**, 203 (1988).

[94] T. Walker, D. Sesko, and C. E. Wieman, *Collective behavior of optically trapped neutral atoms*, Physical Review Letters **64**, 408 (1990).

[95] G. Labeyrie, F. Michaud, and R. Kaiser, *Self-Sustained Oscillations in a Large Magneto-Optical Trap*, Physical Review Letters **96**, 023003 (2006).

[96] T. Pohl, G. Labeyrie, and R. Kaiser, *Self-driven nonlinear dynamics in magneto-optical traps*, Physical Review A **74**, 023409 (2006).

[97] G. Gattobigio, F. Michaud, G. Labeyrie, T. Pohl, and R. Kaiser, *Long Range Interactions Between Neutral Atoms*, in *AIP Conference Proceedings Volume 862*, pages 211–220 (2006).

[98] J. T. Mendonça, R. Kaiser, H. Terças, and J. Loureiro, *Collective oscillations in ultracold atomic gas*, Physical Review A **78**, 013408 (2008).

[99] H. Terças, J. T. Mendonça, and R. Kaiser, *Driven collective instabilities in magneto-optical traps: A fluid-dynamical approach*, Europhysics Letters **89**, 53001 (2010).

[100] G. L. Gattobigio, T. Pohl, G. Labeyrie, and R. Kaiser, *Scaling laws for large magneto-optical traps*, Physica Scripta **81**, 025301 (2010).

[101] D. Wilkowski, J. Ringot, D. Hennequin, and J. C. Garreau, *Instabilities in a Magneto-optical Trap: Noise-Induced Dynamics in an Atomic System*, Physical Review Letters **85**, 1839 (2000).

[102] J. Tollett, C. Bradley, C. Sackett, and R. Hulet, *Permanent magnet trap for cold atoms*, Physical Review A **51**, R22 (1995).

[103] W. Petrich, M. H. Anderson, J. R. Ensher, and E. A. Cornell, *Stable, Tightly Confining Magnetic Trap for Evaporative Cooling of neutral Atoms*, Physical Review Letters **74**, 3352 (1995).

[104] K. Davis, M.-O. Mewes, M. Joffe, M. Andrews, and W. Ketterle, *Evaporative Cooling of Sodium Atoms*, Physical Review Letters **74**, 5202 (1995).

[105] M. H. Anderson, J. R. Ensher, M. R. Matthews, C. E. Wieman, and E. A. Cornell, *Observation of Bose-Einstein Condensation in a Dilute Atomic Vapor*, Science **269**, 198 (1995).

[106] C. Bradley, C. Sackett, J. Tollett, and R. Hulet, *Evidence of Bose-Einstein Condensation in an Atomic Gas with Attractive Interactions*, Physical Review Letters **75**, 1687 (1995), and erratum, Physical Review Letters **79**, 1170 (1997).

[107] K. B. Davis, M.-O. Mewes, M. R. Andrews, N. J. van Druten, D. S. Durfee, D. M. Kurn, and W. Ketterle, *Bose-Einstein Condensation in a Gas of Sodium Atoms*, Physical Review Letters **75**, 3969 (1995).

[108] D. A. Steck, *Rubidium 87 D Line Data*, revision 2.1, available online at http://steck.us/alkalidata (2008).

[109] W. H. Wing, *On neutral particle trapping in quasistatic electromagnetic fields*, Progress in Quantum Electronics **8**, 181 (1984).

[110] O. Luiten, M. Reynolds, and J. Walraven, *Kinetic theory of the evaporative cooling of a trapped gas*, Physical Review A **53**, 381 (1996).

[111] C. Cohen-Tannoudji, *Atomes ultrafroids, piégeage non dissipatif, et refroidissement evaporatif*, lecture notes of the 1996–1997 lectures at Collège de France.

[112] A. Moerdijk, H. Boesten, and B. Verhaar, *Decay of trapped ultracold alkali atoms by recombination*, Physical Review A **53**, 916 (1996).

[113] I. Bloch, T. Hänsch, and T. Esslinger, *Measurement of the spatial coherence of a trapped Bose gas at the phase transition*, Nature **403**, 166 (2000).

[114] M. Schellekens, R. Hoppeler, A. Perrin, J. V. Gomes, D. Boiron, A. Aspect, and C. I. Westbrook, *Hanbury Brown Twiss effect for ultracold quantum gases*, Science **310**, 648 (2005).

[115] E. Levich and V. Yakhot, *Time evolution of a Bose system passing through the critical point*, Physical Review B **15**, 243 (1977).

[116] E. Levich and V. Yakhot, *Time development of coherent and superfluid properties in the course of a λ-transition*, Journal of Physics A **11**, 2237 (1978).

[117] H. Stoof, *Formation of the condensate in a dilute Bose gas*, Physical Review Letters **66**, 3148 (1991).

[118] C. N. Weiler, T. W. Neely, D. R. Scherer, A. S. Bradley, M. J. Davis, and B. P. Anderson, *Spontaneous vortices in the formation of Bose-Einstein condensates*, Nature **455**, 948 (2008).

[119] W. Phillips and H. Metcalf, *Laser Deceleration of an Atomic Beam*, Physical Review Letters **48**, 596 (1982).

[120] C. Monroe, W. Swann, H. Robinson, and C. Wieman, *Very cold trapped atoms in a vapor cell*, Physical Review Letters **65**, 1571 (1990).

[121] D. Fried, T. Killian, L. Willmann, D. Landhuis, S. Moss, D. Kleppner, and T. Greytak, *Bose-Einstein Condensation of Atomic Hydrogen*, Physical Review Letters **81**, 3811 (1998).

[122] S. Doret, C. Connolly, W. Ketterle, and J. Doyle, *Buffer-Gas Cooled Bose-Einstein Condensate*, Physical Review Letters **103**, 103005 (2009).

[123] S. L. Cornish, N. R. Claussen, J. L. Roberts, E. A. Cornell, and C. E. Wieman, *Stable ^{85}Rb Bose-Einstein Condensates with Widely Tunable Interactions*, Physical Review Letters **85**, 1795 (2000).

[124] A. Robert, O. Sirjean, A. Browaeys, J. Poupard, S. Nowak, D. Boiron, C. I. Westbrook, and A. Aspect, *A Bose-Einstein condensate of metastable atoms*, Science **292**, 461 (2001).

[125] G. Modugno, G. Ferrari, G. Roati, R. J. Brecha, A. Simoni, and M. Inguscio, *Bose-Einstein condensation of potassium atoms by sympathetic cooling*, Science **294**, 1320 (2001).

[126] T. Weber, J. Herbig, M. Mark, H.-C. Nägerl, and R. Grimm, *Bose-Einstein condensation of Cesium*, Science **299**, 232 (2003).

[127] Y. Takasu, K. Maki, K. Komori, T. Takano, K. Honda, M. Kumakura, T. Yabuzaki, and Y. Takahashi, *Spin-Singlet Bose-Einstein Condensation of Two-Electron Atoms*, Physical Review Letters **91**, 040404 (2003).

[128] A. Griesmaier, J. Werner, S. Hensler, J. Stuhler, and T. Pfau, *Bose-Einstein Condensation of Chromium*, Physical Review Letters **94**, 160401 (2005).

[129] S. Kraft, F. Vogt, O. Appel, F. Riehle, and U. Sterr, *Bose-Einstein Condensation of Alkaline Earth Atoms:* ^{40}Ca, Physical Review Letters **103**, 130401 (2009).

[130] Y. N. Martinez de Escobar, P. G. Mickelson, M. Yan, B. J. DeSalvo, S. Nagel, and T. C. Killian, *Bose-Einstein Condensation of* ^{84}Sr, Physical Review Letters **103**, 200402 (2009).

[131] P. G. Mickelson, Y. N. Martinez de Escobar, M. Yan, B. J. DeSalvo, and T. C. Killian, *Bose-Einstein condensation of* ^{88}Sr *through sympathetic cooling with* ^{87}Sr, Physical Review A **81**, 051601 (2010).

[132] S. Stellmer, M. K. Tey, R. Grimm, and F. Schreck, *Bose-Einstein condensation of* ^{86}Sr, Physical Review A **82**, 041602 (2010).

[133] B. DeMarco and D. S. Jin, *Onset of Fermi Degeneracy in a Trapped Atomic Gas*, Science **285**, 1703 (1999).

[134] A. G. Truscott, K. E. Strecker, W. I. McAlexander, G. B. Partridge, and R. G. Hulet, *Observation of Fermi pressure in a gas of trapped atoms*, Science **291**, 2570 (2001).

[135] M. K. Tey, S. Stellmer, R. Grimm, and F. Schreck, *Double-degenerate Bose-Fermi mixture of Strontium*, Physical Review A **82**, 011608(R) (2010).

[136] I. Bloch, T. W. Hänsch, and T. Esslinger, *Atom Laser with a cw Output Coupler*, Physical Review Letters **82**, 3008 (1999).

[137] I. Bloch, M. Köhl, M. Greiner, T. W. Hänsch, and T. Esslinger, *Optics with an Atom Laser Beam*, Physical Review Letters **87**, 030401 (2001).

[138] W. Guerin, J.-F. Riou, J. Gaebler, V. Josse, P. Bouyer, and A. Aspect, *Guided Quasicontinuous Atom Laser*, Physical Review Letters **97**, 200402 (2006).

[139] M. Greiner, I. Bloch, O. Mandel, T. W. Hänsch, and T. Esslinger, *Exploring Phase Coherence in a 2D Lattice of Bose-Einstein Condensates*, Physical Review Letters **87**, 160405 (2001).

[140] Z. Hadzibabic, P. Krüger, M. Cheneau, B. Battelier, and J. Dalibard, *Berezinskii-Kosterlitz-Thouless crossover in a trapped atomic gas*, Nature **441**, 1118 (2006).

[141] Z. Hadzibabic, P. Krüger, M. Cheneau, S. P. Rath, and J. Dalibard, *The trapped two-dimensional Bose gas: from Bose-Einstein condensation to Berezinskii-Kosterlitz-Thouless physics*, New Journal of Physics **10**, 045006 (2008).

[142] J. Billy, V. Josse, Z. Zuo, A. Bernard, B. Hambrecht, P. Lugan, D. Clément, L. Sanchez-Palencia, P. Bouyer, and A. Aspect, *Direct observation of Anderson localization of matter waves in a controlled disorder*, Nature **453**, 891 (2008).

[143] G. Roati, C. D'Errico, L. Fallani, M. Fattori, C. Fort, M. Zaccanti, G. Modugno, M. Modugno, and M. Inguscio, *Anderson localization of a non-interacting Bose-Einstein condensate*, Nature **453**, 895 (2008).

[144] J. Simon, W. S. Bakr, R. Ma, M. E. Tai, P. M. Preiss, and M. Greiner, *Quantum simulation of antiferromagnetic spin chains in an optical lattice.*, Nature **472**, 307 (2011).

[145] S. S. Kondov, W. R. McGehee, J. J. Zirbel, and B. DeMarco, *Three-Dimensional Anderson Localization of Ultracold Matter*, Science **334**, 66 (2011).

[146] M.-O. Mewes, M. Andrews, N. van Druten, D. Kurn, D. Durfee, and W. Ketterle, *Bose-Einstein Condensation in a Tightly Confining dc Magnetic Trap*, Physical Review Letters **77**, 416 (1996).

[147] C. Myatt, E. Burt, R. Ghrist, E. Cornell, and C. Wieman, *Production of Two Overlapping Bose-Einstein Condensates by Sympathetic Cooling*, Physical Review Letters **78**, 586 (1997).

[148] L. V. Hau, B. D. Busch, C. Liu, Z. Dutton, M. M. Burns, and J. A. Golovchenko, *Near-resonant spatial images of confined Bose-Einstein condensates in a 4-Dee magnetic bottle*, Physical Review A **58**, R54 (1998).

[149] T. Esslinger, I. Bloch, and T. W. Hänsch, *Bose-Einstein condensation in a quadrupole-Ioffe-configuration trap*, Physical Review A **58**, R2664 (1998).

[150] S. Schneider, A. Kasper, C. vom Hagen, M. Bartenstein, B. Engeser, T. Schumm, I. Bar-Joseph, R. Folman, L. Feenstra, and J. Schmiedmayer, *Bose-Einstein condensation in a simple microtrap*, Physical Review A **67**, 023612 (2003).

[151] M. Fauquembergue, J.-F. Riou, W. Guerin, S. Rangwala, F. Moron, A. Villing, Y. Le Coq, P. Bouyer, A. Aspect, and M. Lécrivain, *Partially ferromagnetic electromagnet for trapping and cooling neutral atoms to quantum degeneracy*, Review of Scientific Instruments **76**, 103104 (2005).

[152] O. Zobay and B. M. Garraway, *Two-Dimensional Atom Trapping in Field-Induced Adiabatic Potentials*, Physical Review Letters **86**, 1195 (2001).

[153] Y. Colombe, E. Knyazchyan, O. Morizot, B. Mercier, V. Lorent, and H. Perrin, *Ultracold atoms confined in rf-induced two-dimensional trapping potentials*, Europhysics Letters **67**, 593 (2004).

[154] T. Schumm, S. Hofferberth, L. M. Andersson, S. Wildermuth, S. Groth, I. Bar-Joseph, J. Schmiedmayer, and P. Krüger, *Matter-wave interferometry in a double well on an atom chip*, Nature Physics **1**, 57 (2005).

[155] D. Stamper-Kurn, M. Andrews, A. Chikkatur, S. Inouye, H.-J. Miesner, J. Stenger, and W. Ketterle, *Optical Confinement of a Bose-Einstein Condensate*, Physical Review Letters **80**, 2027 (1998).

[156] M. Barrett, J. Sauer, and M. Chapman, *All-Optical Formation of an Atomic Bose-Einstein Condensate*, Physical Review Letters **87**, 010404 (2001).

[157] M. Falkenau, V. Volchkov, J. Rührig, A. Griesmaier, and T. Pfau, *Continuous Loading of a Conservative Potential Trap from an Atomic Beam*, Physical Review Letters **106** (2011).

[158] S. Inouye, M. R. Andrews, J. Stenger, H.-J. Miesner, D. M. Stamper-Kurn, and W. Ketterle, *Observation of Feshbach resonances in a Bose-Einstein condensate*, Nature **392**, 151 (1998).

[159] P. Courteille, R. S. Freeland, D. J. Heinzen, F. A. van Abeelen, and B. J. Verhaar, *Observation of a Feshbach Resonance in Cold Atom Scattering*, Physical Review Letters **81**, 69 (1998).

[160] J. Roberts, N. Claussen, J. P. J. Burke, C. H. Greene, E. Cornell, and C. Wieman, *Resonant Magnetic Field Control of Elastic Scattering in Cold ^{85}Rb*, Physical Review Letters **81**, 5109 (1998).

[161] H. J. Lewandowski, D. M. Harber, D. L. Whitaker, and E. A. Cornell, *Simplified System for Creating a Bose-Einstein Condensate*, Journal of Low Temperature Physics **132**, 309 (2003).

[162] C. J. Myatt, N. R. Newbury, R. W. Ghrist, S. Loutzenhiser, and C. E. Wieman, *Multiply loaded magneto-optical trap*, Optics Letters **21**, 290 (1996).

[163] G. Labeyrie, F. de Tomasi, J.-C. Bernard, C. A. Müller, C. Miniatura, and R. Kaiser, *Coherent Backscattering of Light by Cold Atoms*, Physical Review Letters **83**, 5266 (1999).

[164] G. Labeyrie, C. Miniatura, and R. Kaiser, *Large Faraday rotation of resonant light in a cold atomic cloud*, Physical Review A **64**, 1 (2001).

[165] G. Labeyrie, C. Miniatura, C. A. Müller, O. Sigwarth, D. Delande, and R. Kaiser, *Hanle Effect in Coherent Backscattering*, Physical Review Letters **89**, 14 (2002).

[166] C. Miniatura, R. Kaiser, G. Labeyrie, D. Delande, and C. A. Müller, *Coherent backscattering of light by an inhomogeneous cloud of cold atoms*, Physical Review A **67**, 033814 (2003).

[167] G. Labeyrie, E. Vaujour, C. A. Müller, D. Delande, C. Miniatura, D. Wilkowski, and R. Kaiser, *Slow Diffusion of Light in a Cold Atomic Cloud*, Physical Review Letters **91**, 1 (2003).

[168] G. Labeyrie, D. Delande, C. A. Müller, C. Miniatura, and R. Kaiser, *Coherent backscattering of light by an inhomogeneous cloud of cold atoms*, Physical Review A **67**, 033814 (2003).

[169] O. Sigwarth, G. Labeyrie, T. Jonckheere, D. Delande, R. Kaiser, and C. Miniatura, *Magnetic Field Enhanced Coherence Length in Cold Atomic Gases*, Physical Review Letters **93**, 143906 (2004).

[170] G. Labeyrie, D. Delande, R. Kaiser, and C. Miniatura, *Light Transport in Cold Atoms and Thermal Decoherence*, Physical Review Letters **97**, 013004 (2006).

[171] T. Pohl, G. Labeyrie, and R. Kaiser, *Self-driven nonlinear dynamics in magneto-optical traps*, Physical Review A **74**, 023409 (2006).

[172] G. Labeyrie, F. Michaud, and R. Kaiser, *Self-Sustained Oscillations in a Large Magneto-Optical Trap*, Physical Review Letters **96**, 023003 (2006).

[173] G. Labeyrie and U. Bortolozzo, *Light self-trapping in a large cloud of cold atoms*, Optics Letters **36**, 2158 (2011).

[174] W. Steckelmacher, *A review of the molecular flow conductance for systems of tubes and components and the measurement of pumping speed*, Vacuum **16**, 561 (1966).

[175] H. Lee, C. Adams, M. Kasevich, and S. Chu, *Raman Cooling of Atoms in an Optical Dipole Trap*, Physical Review Letters **76**, 2658 (1996).

[176] C. E. Wieman and L. Hollberg, *Using diode lasers for atomic physics*, Review of Scientific Instruments **62**, 1 (1991).

[177] M. Fauquembergue, *Réalisation d'un dispositif de condensation de Bose-Einstein et de transport d'un echantillon coherent d'atomes*, Ph.D. thesis, Université Paris-Sud (2004).

[178] K. B. MacAdam, A. Steinbach, and C. E. Wieman, *A narrow-band tunable diode laser system with grating feedback, and a saturated absorption spectrometer for Cs and Rb*, American Journal of Physics **60**, 1098 (1992).

[179] T. P. Meyrath, *Experiments with Bose-Einstein condensation in an optical box*, Ph.D. thesis, University of Texas at Austin (2005).

[180] N. R. Thomas, A. C. Wilson, and C. J. Foot, *Double-well magnetic trap for Bose-Einstein condensates*, Physical Review A **65**, 063406 (2002).

[181] W. Ketterle, D. S. Durfee, and D. M. Stamper-Kurn, *Making, probing and understanding Bose-Einstein condensates*, in *Bose-Einstein Condensation in Atomic Gases, Proceedings of the international school of physics "Enrico Fermi", Course CXL*, edited by M. Inguscio, S. Stringari, and C. E. Wieman, pages 67–176 (IOS Press, 1999).

[182] T. Bienaimé, S. Bux, E. Lucioni, P. W. Courteille, N. Piovella, and R. Kaiser, *Observation of a Cooperative Radiation Force in the Presence of Disorder*, Physical Review Letters **104**, 183602 (2010).

[183] E. Burt, R. Ghrist, C. Myatt, M. Holland, E. Cornell, and C. Wieman, *Coherence, Correlations, and Collisions: What One Learns about Bose-Einstein Condensates from Their Decay*, Physical Review Letters **79**, 337 (1997).

[184] B. D. Esry, C. H. Greene, and J. P. J. Burke, *Recombination of Three Atoms in the Ultracold Limit*, Physical Review Letters **83**, 1751 (1999).

[185] A. Norrie, R. Ballagh, C. Gardiner, and A. Bradley, *Three-body recombination of ultracold Bose gases using the truncated Wigner method*, Physical Review A **73**, 043618 (2006).

[186] S. Whitlock, C. F. Ockeloen, and R. J. C. Spreeuw, *Sub-Poissonian Atom-Number Fluctuations by Three-Body Loss in Mesoscopic Ensembles*, Physical Review Letters **104**, 120402 (2010).

[187] B. Jackson, P. Pedri, and S. Stringari, *Collisions and expansion of an ultracold dilute Fermi gas*, Europhysics Letters **67**, 524 (2004).

[188] T. Savard, K. O'Hara, and J. Thomas, *Laser-noise-induced heating in far-off resonance optical traps*, Physical Review A **56**, R1095 (1997).

[189] K. Dieckmann, *Bose-Einstein condensation with high atom number in a deep magnetic trap*, Ph.D. thesis, Universiteit van Amsterdam (2001).

[190] E. A. Cornell, J. R. Ensher, and C. E. Wieman, *Experiments in Dilute Atomic Bose-Einstein Condensation*, in *Bose-Einstein Condensation in Atomic Gases, Proceedings of the international school of physics "Enrico Fermi", Course CXL*, edited by M. Inguscio, S. Stringari, and C. E. Wieman (IOS Press, 1999).

[191] A. Minguzzi, S. Cont, and M. P. Tosi, *The internal energy and condensate fraction of a trapped interacting Bose gas*, Journal of Physics: Condensed Matter **9**, L33 (1997).

[192] M. Born and V. Fock, *Beweis des Adiabatensatzes*, Zeitschrift für Physik **51**, 165 (1928).

[193] T. Kato, *On the Adiabatic Theorem of Quantum Mechanics*, Journal of the Physical Society of Japan **5**, 435 (1950).

[194] D. Comparat, *General conditions for quantum adiabatic evolution*, Physical Review A **80**, 012106 (2009).

[195] A. Parkins, P. Marte, P. Zoller, and H. Kimble, *Synthesis of arbitrary quantum states via adiabatic transfer of Zeeman coherence*, Physical Review Letters **71**, 3095 (1993).

[196] J. I. Cirac, R. Blatt, and P. Zoller, *Nonclassical states of motion in a three-dimensional ion trap by adiabatic passage*, Physical Review A **49**, R3174 (1994).

[197] A. Sørensen, E. Altman, M. Gullans, J. Porto, M. Lukin, and E. Demler, *Adiabatic preparation of many-body states in optical lattices*, Physical Review A **81**, 061603 (2010).

[198] U. Hohenester, P. K. Rekdal, A. Borzì, and J. Schmiedmayer, *Optimal quantum control of Bose-Einstein condensates in magnetic microtraps*, Physical Review A **75**, 023602 (2007).

[199] G. De Chiara, T. Calarco, M. Anderlini, S. Montangero, P. Lee, B. Brown, W. Phillips, and J. Porto, *Optimal control of atom transport for quantum gates in optical lattices*, Physical Review A **77**, 052333 (2008).

[200] G. Vasilev, A. Kuhn, and N. Vitanov, *Optimum pulse shapes for stimulated Raman adiabatic passage*, Physical Review A **80**, 013417 (2009).

[201] M. Mundt and D. J. Tannor, *Optimal control of interacting particles: a multi-configuration time-dependent Hartree-Fock approach*, New Journal of Physics **11**, 105038 (2009).

[202] M. V. Berry, *Transitionless quantum driving*, Journal of Physics A **42**, 365303 (2009).

[203] J. E. Avron and A. Elgart, *Adiabatic Theorem without a Gap Condition*, Communications in Mathematical Physics **203**, 445 (1999).

[204] M. Sarandy and D. Lidar, *Adiabatic approximation in open quantum systems*, Physical Review A **71**, 012331 (2005).

[205] H. R. Lewis and W. B. Riesenfeld, *An Exact Quantum Theory of the Time-Dependent Harmonic Oscillator and of a Charged Particle in a Time-Dependent Electromagnetic Field*, Journal of Mathematical Physics **10**, 1458 (1969).

[206] L. Landau and E. Lifchitz, *Physique théorique, vol. 1. Mécanique* (MIR, Moscow, 1982).

[207] J. G. Muga, X. Chen, A. Ruschhaupt, and D. Guéry-Odelin, *Frictionless dynamics of Bose-Einstein condensates under fast trap variations*, Journal of Physics B **42**, 241001 (2009).

[208] J.-F. Schaff, X.-L. Song, P. Vignolo, and G. Labeyrie, *Fast optimal transition between two equilibrium states*, Physical Review A **82**, 033430 (2010), and erratum, Physical Review A **83**, 059911(E) (2011).

[209] J.-F. Schaff, X.-L. Song, P. Capuzzi, P. Vignolo, and G. Labeyrie, *Shortcut to adiabaticity for an interacting Bose-Einstein condensate*, Europhysics Letters **93**, 23001 (2011).

[210] M. Edwards, C. Clark, P. Pedri, L. Pitaevskii, and S. Stringari, *Consequence of Superfluidity on the Expansion of a Rotating Bose-Einstein Condensate*, Physical Review Letters **88**, 070405 (2002).

[211] M. Modugno, G. Modugno, G. Roati, C. Fort, and M. Inguscio, *Scissors mode of an expanding Bose-Einstein condensate*, Physical Review A **67**, 023608 (2003).

[212] K. Madison, F. Chevy, W. Wohlleben, and J. Dalibard, *Vortex Formation in a Stirred Bose-Einstein Condensate*, Physical Review Letters **84**, 806 (2000).

[213] A. Recati, F. Zambelli, and S. Stringari, *Overcritical Rotation of a Trapped Bose-Einstein Condensate*, Physical Review Letters **86**, 377 (2001).

[214] H. Hu, A. Minguzzi, X.-J. Liu, and M. Tosi, *Collective Modes and Ballistic Expansion of a Fermi Gas in the BCS-BEC Crossover*, Physical Review Letters **93**, 190403 (2004).

[215] *Numerical Recipes: The Art of Scientific Computing* (Cambridge University Press, 2007).

[216] Y. Li, L.-A. Wu, and Z. Wang, *Fast ground-state cooling of mechanical resonators with time-dependent optical cavities*, Physical Review A **83**, 043804 (2011).

[217] X. Chen, I. Lizuain, A. Ruschhaupt, D. Guéry-Odelin, and J. Muga, *Shortcut to Adiabatic Passage in Two- and Three-Level Atoms*, Physical Review Letters **105**, 123003 (2010).

[218] S. Ibáñez, S. Martínez-Garaot, X. Chen, E. Torrontegui, and J. G. Muga, *Shortcuts to adiabaticity for non-Hermitian systems*, Physical Review A **84**, 023415 (2011).

[219] A. Bulatov, B. Vugmeister, A. Burin, and H. Rabitz, *Nonadiabatic cooling and optimal control in off-resonance dipole optical potentials*, Physical Review A **58**, 1346 (1998).

[220] H. Mabuchi and N. Khaneja, *Principles and applications of control in quantum systems*, International Journal of Robust and Nonlinear Control **15**, 647 (2005).

[221] S. Schulz, U. Poschinger, K. Singer, and F. Schmidt-Kaler, *Optimization of segmented linear Paul traps and transport of stored particles*, Fortschritte der Physik **54**, 648 (2006).

[222] P. Salamon, K. H. Hoffmann, Y. Rezek, and R. Kosloff, *Maximum work in minimum time from a conservative quantum system*, Physical Chemistry Chemical Physics **11**, 1027 (2009).

[223] B. Andresen, K. H. Hoffmann, J. Nulton, A. Tsirlin, and P. Salamon, *Optimal control of the parametric oscillator*, European Journal of Physics **32**, 827 (2011).

[224] R. Bücker, J. Grond, S. Manz, T. Berrada, T. Betz, C. Koller, U. Hohenester, T. Schumm, A. Perrin, and J. Schmiedmayer, *Twin-atom beams*, Nature Physics **7**, 608 (2011).

[225] Y. Bidel, B. Klappauf, J.-C. Bernard, D. Delande, G. Labeyrie, C. Miniatura, D. Wilkowski, and R. Kaiser, *Coherent Light Transport in a Cold Strontium Cloud*, Physical Review Letters **88**, 203902 (2002).

[226] C. Kenty, *On Radiation Diffusion and the Rapidity of Escape of Resonance Radiation from a Gas*, Physical Review **42**, 823 (1932).

[227] P. Lévy, *Theorie de l'Addition des Variables Aléatoires* (Gauthier-Villiers, 1937).

[228] K. T. Compton, *Theory of Ionization by Cumulative Action and the Low Voltage Arc*, Physical Review **20**, 283 (1922).

[229] T. Holstein, *Imprisonment of Resonance Radiation in Gases*, Physical Review **72**, 1212 (1947).

[230] J.-P. Bouchaud and A. Georges, *Anomalous diffusion in disordered media: Statistical mechanisms, models and physical applications*, Physics Reports **195**, 127 (1990).

[231] E. Pereira, J. Martinho, and M. Berberan-Santos, *Photon Trajectories in Incoherent Atomic Radiation Trapping as Lévy Flights*, Physical Review Letters **93**, 120201 (2004).

[232] A. Fioretti, A. F. Molisch, J. H. Müller, P. Verkerk, and M. Allegrini, *Observation of radiation trapping in a dense Cs magneto-optical trap*, Optics Communications **149**, 415 (1998).

[233] P. Barthelemy, J. Bertolotti, and D. S. Wiersma, *A Lévy flight for light*, Nature **453**, 495 (2008).

[234] N. Mercadier, W. Guerin, M. Chevrollier, and R. Kaiser, *Lévy flights of photons in hot atomic vapours*, Nature Physics **5**, 602 (2009).

[235] E. Akkermans and G. Montambaux, *Mesoscopic Physics of Electrons and Photons* (Cambridge University Press, 2007).

[236] E. Akkermans, P. Wolf, and R. Maynard, *Coherent Backscattering of Light by Disordered Media: Analysis of the Peak Line Shape*, Physical Review Letters **56**, 1471 (1986).

[237] P. W. Anderson, *Absence of Diffusion in Certain Random Lattices*, Physical Review **109**, 1492 (1958).

[238] P. W. Anderson, *The question of classical localization: A theory of white paint?*, Philosophical Magazine B **52**, 505 (1985).

[239] C. A. Müller and D. Delande, *Disorder and interference: localization phenomena*, in *Ultracold Gases and Quantum Information, Les Houches session XCI*, edited by C. Miniatura, L.-C. Kwek, M. Ducloy, B. Grémaud, B.-G. Engelert, L. F. Cugliandolo, A. Ekert, and K. K. Phua, pages 441–533 (Oxford University Press, 2011).

[240] G. Lemarié, *Transition d'Anderson avec des ondes de matière atomiques*, Ph.D. thesis, Université Pierre et Marie Curie (2009).

[241] P. Lugan, *Ultracold Bose gases in random potentials: collective excitations and localization effects*, Ph.D. thesis, École Polytechnique (2010).

[242] F. Izrailev and A. Krokhin, *Localization and the Mobility Edge in One-Dimensional Potentials with Correlated Disorder*, Physical Review Letters **82**, 4062 (1999).

[243] R. L. Weaver, *Anderson localization of ultrasound*, Wave Motion **12**, 129 (1990).

[244] R. Dalichaouch, J. P. Armstrong, S. Schultz, P. M. Platzman, and S. L. McCall, *Microwave localization by two-dimensional random scattering*, Nature **354**, 53 (1991).

[245] A. Chabanov, M. Stoytchev, and A. Genack, *Statistical signatures of photon localization*, Nature **404**, 850 (2000).

[246] M. V. Berry and S. Klein, *Transparent mirrors: rays, waves and localization*, European Journal of Physics **18**, 222 (1997).

[247] D. S. Wiersma, P. Bartolini, A. Lagendijk, and R. Righini, *Localization of light in a disordered medium*, Nature **390**, 671 (1997).

[248] F. Scheffold, R. Lenke, R. Tweer, and G. Maret, *Localization or classical diffusion of light?* **398**, 206 (1999).

[249] M. Störzer, P. Gross, C. M. Aegerter, and G. Maret, *Observation of the Critical Regime Near Anderson Localization of Light*, Physical Review Letters **96**, 1 (2006).

[250] C. M. Aegerter, M. Störzer, and G. Maret, *Experimental determination of critical exponents in Anderson localisation of light*, Europhysics Letters **75**, 562 (2006).

[251] T. Schwartz, G. Bartal, S. Fishman, and M. Segev, *Transport and Anderson localization in disordered two-dimensional photonic lattices*, Nature **446**, 52 (2007).

[252] Z. Zhao, F. Gao, R. Peng, L. Cao, D. Li, Z. Wang, X. Hao, M. Wang, and C. Ferrari, *Localization-delocalization transition of photons in one-dimensional random n-mer dielectric systems*, Physical Review B **75**, 165117 (2007).

[253] C. M. Aegerter, M. Störzer, S. Fiebig, W. Bührer, and G. Maret, *Observation of Anderson localization of light in three dimensions.*, Journal of the Optical Society of America A **24**, A23 (2007).

[254] C. M. Aegerter, M. Störzer, W. Bührer, S. Fiebig, and G. Maret, *Experimental signatures of Anderson localization of light in three dimensions*, Journal of Modern Optics **54**, 2667 (2007).

[255] Y. Lahini, A. Avidan, F. Pozzi, M. Sorel, R. Morandotti, D. N. Christodoulides, and Y. Silberberg, *Anderson Localization and Nonlinearity in One-Dimensional Disordered Photonic Lattices*, Physical Review Letters **100**, 013906 (2008).

[256] J. Chabé, G. Lemarié, B. Grémaud, D. Delande, P. Szriftgiser, and J. C. Garreau, *Experimental Observation of the Anderson Metal-Insulator Transition with Atomic Matter Waves*, Physical Review Letters **101**, 255702 (2008).

[257] G. Lemarié, J. Chabé, P. Szriftgiser, J. C. Garreau, B. Grémaud, and D. Delande, *Observation of the Anderson metal-insulator transition with atomic matter waves: Theory and experiment*, Physical Review A **80**, 043626 (2009).

[258] G. Lemarié, H. Lignier, D. Delande, P. Szriftgiser, and J. C. Garreau, *Critical State of the Anderson Transition: Between a Metal and an Insulator*, Physical Review Letters **105**, 090601 (2010).

[259] M. Robert-de-Saint-Vincent, J.-P. Brantut, B. Allard, T. Plisson, L. Pezzé, L. Sanchez-Palencia, A. Aspect, T. Bourdel, and P. Bouyer, *Anisotropic 2D Diffusive Expansion of Ultracold Atoms in a Disordered Potential*, Physical Review Letters **104**, 220602 (2010).

[260] J. W. Goodman, *Speckle phenomena in optics: theory and applications* (Roberts and Company Publishers, 2007).

[261] P. D. Kirkman and J. B. Pendry, *The statistics of one-dimensional resistances*, Journal of Physics C **17**, 4327 (1984).

[262] R. Farchioni, G. Grosso, and G. Pastori Parravicini, *Electronic structure in incommensurate potentials obtained using a numerically accurate renormalization scheme*, Physical Review B **45**, 6383 (1992).

[263] E. Abrahams, P. W. Anderson, D. C. Licciardello, and T. V. Ramakrishnan, *Scaling Theory of Anderson Localization: Absence of Quantum Diffusion in Two Dimensions*, Physical Review Letters **42**, 673 (1979).

[264] D. H. Dunlap, H.-L. Wu, and P. W. Phillips, *Absence of Localizaztion in a Random-Dimer Model*, Physical Review Letters **65**, 88 (1990).

[265] S. De Bièvre and F. Germinet, *Dynamical Localization for the Random Dimer Schrödinger Operator*, Journal of Statistical Physics **98**, 1135 (2000).

[266] S. Jitomirskaya, H. Schulz-Baldes, and G. Stolz, *Delocalization in Random Polymer Models*, Communications in Mathematical Physics **233**, 27 (2003).

[267] P. Phillips and H. L. Wu, *Localization and its absence: a new metallic state for conducting polymers*, Science **252**, 1805 (1991).

[268] R. Caetano and P. Schulz, *Sequencing-Independent Delocalization in a DNA-Like Double Chain with Base Pairing*, Physical Review Letters **95**, 126601 (2005); A. Sedrakyan and F. Domínguez-Adame, *Comment on "Sequencing-Independent Delocalization in a DNA-Like Double Chain with Base Pairing"*, Physical Review Letters **96**, 059703 (2006); R. Caetano and P. Schulz, *Caetano and Schulz Reply*, Physical Review Letters **96**, 059704 (2006).

[269] V. Bellani, E. Diez, R. Hey, L. Toni, L. Tarricone, G. Parravicini, F. Domínguez-Adame, and R. Gómez-Alcalá, *Experimental Evidence of Delocalized States in Random Dimer Superlattices*, Physical Review Letters **82**, 2159 (1999).

[270] A. Esmailpour, M. Esmailpour, A. Sheikhan, M. Elahi, M. Tabar, and M. Sahimi, *Localization properties of acoustic waves in the random-dimer media*, Physical Review B **78**, 134206 (2008).

[271] B. P. Anderson and M. A. Kasevich, *Macroscopic Quantum Interference from Atomic Tunnel Arrays*, Science **282**, 1686 (1998).

[272] M. Greiner, I. Bloch, O. Mandel, T. W. Hänsch, and T. Esslinger, *Exploring Phase Coherence in a 2D Lattice of Bose-Einstein Condensates*, Physical Review Letters **87**, 160405 (2001).

[273] P. Vignolo, Z. Akdeniz, and M. P. Tosi, *The transmittivity of a Bose-Einstein condensate on a lattice: interference from period doubling and the effect of disorder*, Journal of Physics B **36**, 4535 (2003).

[274] U. Gavish and Y. Castin, *Matter-Wave Localization in Disordered Cold Atom Lattices*, Physical Review Letters **95**, 020401 (2005).

[275] G. Modugno, M. Modugno, F. Riboli, G. Roati, and M. Inguscio, *Two Atomic Species Superfluid*, Physical Review Letters **89**, 190404 (2002).

[276] G. Thalhammer, G. Barontini, L. De Sarlo, J. Catani, F. Minardi, and M. Inguscio, *Double Species Bose-Einstein Condensate with Tunable Interspecies Interactions*, Physical Review Letters **100**, 2 (2008).

[277] J. Larson, G. Morigi, and M. Lewenstein, *Cold Fermi atomic gases in a pumped optical resonator*, Physical Review A **78**, 023815 (2008).

[278] A. Sieradzan, P. Kulatunga, and M. Havey, *Hyperfine-structure measurements in the 4p $^2P_{3/2}$ state of ^{41}K using polarization quantum-beat spectroscopy*, Physical Review A **52**, 4447 (1995).

[279] D. Bloch, M. Ducloy, N. Senkov, V. Velichansky, and V. Yudin, *Doppler-Free Spectroscopy of the D_1 Line of Potassium*, Laser Physics **6**, 670 (1996).

[280] T. G. Tiecke, *Feshbach resonances in ultracold mixtures of the fermionic quantum gases ^6Li and ^{40}K*, Ph.D. thesis, University of Amsterdam (2009); T. G. Tiecke, *Properties of Potassium*, v1.0 (2010).

[281] V. N. Golovach, A. Minguzzi, and L. I. Glazman, *Dynamic response of one-dimensional bosons in a trap*, Physical Review A **80**, 043611 (2009).

[282] T. Lahaye, C. Menotti, L. Santos, M. Lewenstein, and T. Pfau, *The physics of dipolar bosonic quantum gases*, Reports on Progress in Physics **72**, 126401 (2009).

[283] K. Krutitsky, M. Thorwart, R. Egger, and R. Graham, *Ultracold bosons in lattices with binary disorder*, Physical Review A **77**, 053609 (2008).

[284] E. Peik, M. Ben Dahan, I. Bouchoule, Y. Castin, and C. Salomon, *Bloch oscillations of atoms, adiabatic rapid passage, and monokinetic atomic beams*, Physical Review A **55**, 2989 (1997).

[285] Y. Chen, J. Hitchcock, D. Dries, M. Junker, C. Welford, and R. Hulet, *Phase coherence and superfluid-insulator transition in a disordered Bose-Einstein condensate*, Physical Review A **77**, 033632 (2008).

[286] D. Dries, S. Pollack, J. Hitchcock, and R. Hulet, *Dissipative transport of a Bose-Einstein condensate*, Physical Review A **82**, 033603 (2010).

[287] F. J. Dyson, *The Radiation Theories of Tomonaga, Schwinger, and Feynman*, Physical Review **75**, 486 (1949).

[288] J.-F. Schaff, P. Capuzzi, G. Labeyrie, and P. Vignolo, *Shortcuts to adiabaticity for trapped ultracold gases*, New Journal of Physics **13**, 113017 (2011).

[289] J.-F. Schaff, Z. Akdeniz, and P. Vignolo, *Localization-delocalization transition in the random dimer model*, Physical Review A **81**, 041604(R) (2010).

Shortcuts to adiabaticity for ultracold gases

In this thesis I explore the possibility of accelerating adiabatic processes for quantum systems. Experiments are performed with a trapped ultracold gas of Rubidium-87 atoms in two distinct regimes: with a one-dimensional thermal gas that can be considered non-interacting, and with a three-dimensional Bose-Einstein condensate for which interactions are dominant.

In the first chapter, I recall some aspects of the theoretical description and important properties of such gases. The second chapter describes the Bose-Einstein condensation apparatus, mainly composed of two magneto-optical traps and a magnetic trap.

In the third chapter, this setup is used to demonstrate that adiabatic processes — in our case, the slow decompression and displacement of the gas — can be dramatically accelerated by using a proper design of the time-dependent parameters of the system. The theoretical treatment is detailed and is not restricted to trapped gases. It may be applied to other physical systems described by either a linear or nonlinear Schrödinger equation containing a time-dependent harmonic potential.

The final chapter is theoretical and not directly related to the others. In it I investigate the effect of disorder correlations on one-dimensional Anderson localization. I show that a degenerate mixture of Rubidium-87 and Potassium-41 atoms is well suited to study the localization-delocalization transition predicted by existing models of correlated disorder.

Keywords: degenerate ultracold gas, Bose-Einstein condensate, adiabatic transformation, harmonic oscillator, Lewis invariant, Anderson localization, random dimer model, delocalization.

Raccourcis aux transformations adiabatiques de gaz ultrafroids

Dans ce mémoire, j'étudie la possibilité d'accélérer les transformations adiabatiques de systèmes quantiques. Les expériences ont été réalisées avec un gaz ultrafroid de Rubidium-87 dans deux régimes différents : d'une part avec un nuage thermique uni-dimensionnel dans lequel les interactions sont négligeables, et d'autre part avec un condensat de Bose-Einstein tri-dimensionnel pour lequel les interactions sont prépondérantes.

Le premier chapitre de la thèse rappelle certains aspects théoriques ainsi que les principales propriétés des gaz ultrafroids. Le second chapitre décrit l'appareil expérimental de condensation de Bose-Einstein, principalement constitué de deux pièges magnéto-optiques et d'un piège magnétique.

Dans le troisième chapitre, cet appareil est utilisé afin de prouver que les transformations adiabatiques, dans notre cas, une décompression accompagnée d'un déplacement du gaz, peuvent être considérablement accélérées si les paramètres dépendant du temps du système suivent une trajectoire particulière. Le traitement théorique qui est détaillé n'est pas limité aux gaz froids, mais est également applicable à tout système décrit par une équation de Schrödinger, aussi bien linéaire que non linéaire, dans laquelle le potentiel dépendant du temps est harmonique.

Le dernier chapitre est théorique et quelque peu éloigné du reste du manuscrit. J'y étudie les effets des corrélations sur les systèmes désordonnés à une dimension dans lesquels la localisation d'Anderson est attendue. Je montre qu'un mélange dégénéré de Rubidium-87 et de Potassium-41 est adapté à l'observation de délocalisation induite par les corrélations du potentiel aléatoire.

Mots-clés : gaz ultrafroid dégénéré, condensat de Bose-Einstein, transformation adiabatique, oscillateur harmonique, invariant de Lewis, localisation d'Anderson, modèle aléatoire de dimères, délocalisation.